Downloaded from orbit.dtu.dk on: May 06, 2023

DTU Library

Vision Based Navigation Sensors for Spacecraft Rendezvous and Docking

Benn, Mathias

Publication date:
2011

Document Version
Publisher's PDF, also known as Version of record

Link back to DTU Orbit

Citation (APA):
Benn, M. (2011). *Vision Based Navigation Sensors for Spacecraft Rendezvous and Docking*. Technical University of Denmark.

General rights
Copyright and moral rights for the publications made accessible in the public portal are retained by the authors and/or other copyright owners and it is a condition of accessing publications that users recognise and abide by the legal requirements associated with these rights.

- Users may download and print one copy of any publication from the public portal for the purpose of private study or research.
- You may not further distribute the material or use it for any profit-making activity or commercial gain
- You may freely distribute the URL identifying the publication in the public portal

If you believe that this document breaches copyright please contact us providing details, and we will remove access to the work immediately and investigate your claim.

DTU Space
National Space Institute

Measurement & Instrumentation Systems
DTU Space - National Space Institute
2800 Kgs. Lyngby
DK - Denmark

Vision Based Navigation Sensors for Spacecraft Rendezvous and Docking

PhD Dissertation at the Danish Technical University - DTU

Mathias Benn

October 31st 2010

Colophon

The dissertation at hand has been typeset with LaTeX2e using the *memoir* documentclass and compiled by means of the MiKTeX Version 2.8 TeX implementation. Graphs, figures and diagrams have been produced using MatLab^{TM} R2007B from Math Works Inc., AutoCAD(R) by autodesk(R) and the Inkscape 0.47 and Dia 0.97.1 open source software packages.

The manuscript has been prepared for a 100% A4 format, two-side open-right printing.

Abstract

Space missions have recently entered a new stage where concerted mission, i.e. mission where multiple space segments cooperate in forming a combined platform on which improved or new physics or services can be achieved. The best-known existing example is probably the TDRSS constellation of 24 active spacecraft together providing the global positioning service dubbed GPS. However, several other present missions provide augmented performances based on multi space segment configuration, e.g. the GRACE twin spacecraft form together the world's hitherto most accurate gravitometer, which has provided new information and insight into gravitational related physics as diverse as dessert growth, ocean circulation, gravity anomaly mapping and precipitation and climate models. Plans and projects for future multi segment missions are plenty, with missions from all major space agencies in progress. Denmark has, with DTUs design of the Swarm mission, ESAs next Earth Observation Programme magnetic mapping mission, and DTUs participation in GRACE, ELISA and Alsat2, a leading role in designing and verifying sensor systems for this new class of spacecraft.

The Swedish led PRISMA mission is a technological demonstration mission, where all aspects of space rendezvous and docking to both a cooperative and a non-cooperative target is researched, with the use of novel methods, instruments and technologies. Amongst other equipment, DTU has delivered a vision based sensor package to the Main spacecraft of this constellation, providing both position and pose information for the Target vehicle. This dissertation will describe the study, implementation and verification methods that has led to the realization of this optical Vision Based Sensor (VBS), which is used on the PRISMA mission. On June 15^{th} 2010 the PRISMA satellites were launched successfully into orbit, and after the commissioning phase and system check-out the two joined satellites were separated August 9^{th}, initiating the operation phase of the mission. The Early Harvest started August 30^{th} for the Far Range VBS CHU and September 9^{th} for the Short Range VBS CHU, from where the first in-flight data and analysis will be presented and discussed in this dissertation. While writing, the PRISMA mission is continuously providing new VBS data on a daily basis.

Project supervisor:
Head of Department, Professor John Leif Jørgensen,
Measurement and Instrumentation Systems, DTU Space

Resumé

Indenfor de seneste årtier har rumfarten påbegyndt en ny fase hvor konstellationer rumfartøjer arbejder sammen, for derved at skabe en kombineret platform som kan realisere videreudvikling eller nyskabelse af fysiske egenskaber og ydelser. Bedst kendt er givetvis TDRSS konstellationen der består af de 24 aktive satellitter som leverer det globale positioneringssystem, GPS.

Flere andre missioner består af rumfartøjer som supplerer hinanden i en kombineret platform, f.eks. GRACE tvillinge-satellitterne der tilsammen danner verdens hidtil mest præcise gravitometer, som har leveret banebrydende information og indsigt i gravitationsrelateret tilstande såsom ørkenbevægelser, havstrømme og klimamodeller. Mange fremtidige rumfartsmissioner omhandlende flere rumfartøjer er enten planlagt eller igangsat, og involverer alle større rumfartsorganisationer. Danmark har, med sit design af Swarm missionen, ESAs næste mission for kortlægning af jordens magnetfelt, og DTUs deltagelse i GRACE, ELISA og Alsat2, en ledende rolle i både design og verificering af sensorsystemer tilhørende den nye klasse af rumfartøjer.

Den svensk ledte PRISMA satellitmission er en teknisk demonstrationsmission, hvor alle aspekter omhandlende rendezvous og sammenkobling til både et passivt og et kooperativt rumfartøj er undersøgt, ved brug af nyudviklede metoder, instrumenter og teknologier. Heriblandt, en kamerabaseret sensor leveret af DTU, til brug på hovedsatellitten for at levere både position og orientering af Target satellitten baseret på billedinformation. Denne afhandling vil beskrive studiet, implementerings- og verificeringsmetoderne som har resulteret i fremstillingen af den kamerabaserede sensor (Vision Based Sensor - VBS), som er integreret i PRISMA missionen. Den 15.juni blev PRISMA satellitterne sendt i kredsløb rundt om Jorden, og efter den indledende fase og følgende systemverifikation blev de to satellitter separeret den 9. august 2010, hvilket påbegyndte den operationelle fase. De indledende målinger for VBS systemets dele blev påbegyndt den 30. august og den 9. september for henholdsvis Far Range VBS CHU og Short Range VBS CHU, hvorfra det første data og dets analyse vil blive præsenteret og diskuteret i denne afhandling. Under skriveforløbet af denne afhandling leverer PRISMA missionen dagligt ny VBS data.

Projektvejleder:
Sektionsleder, Professor John Leif Jørgensen,
Måling og Instrumentering, DTU Space

Preface

This dissertation is submitted in partial fulfillment of the requirements for achieving the PhD degree at the Danish Technical University - DTU. The work described herein has been conducted in cooperation with the Space Instrumentation Group (SIG) at DTU Space - National Space Institute.

Acknowledgements

Throughout the work of this dissertation great support and guidance have been available from the Space Instrumentation Group of DTU Space which I owe a great thanks. Especially a thanks to my project supervisor, John L. Jørgensen, for making this project study feasible, and for providing me with ideas and challenges throughout the PhD study.
Furthermore, a thanks to my friend and PhD colleague Jonas B. Bjarnø for sharing his expertise in the field of space and for his involvement in the PRISMA mission, a thanks to Troelz Denver for sharing his expertise in programming and algorithm implementation, and a thanks to my fellow PhD students at DTU Space for their involvement and interest in the PRISMA mission.
Finally, deep gratitude goes to family, friends and closest for their continuous support throughout my studies.

Contents

Abstract . . . . . **iv**

Resumé . . . . . **v**

Preface . . . . . **vi**

Acknowledgements . . . . . **vi**

Contents . . . . . **vii**

List of Figures . . . . . **x**

List of Tables . . . . . **xiv**

Nomenclature . . . . . **xv**
Typographical Conventions xv
Acronyms and Abbreviations xv
Terminology and Definitions xviii

1 Introduction **1**
1.1 Background 1
1.2 Future Perspectives 3
1.3 Scope of Dissertation 6
1.4 Summary 7

2 System Description **9**
2.1 VBS Functionalities 9
2.2 μASC Description 13
2.3 μASC Adaption of VBS Functionality 15
2.4 VBS Solution Information 16
2.5 Summary 18

3 Flight System **19**
3.1 Cooperative Target Feature Points 19
3.2 CHU Design 29
3.3 Summary 33

4 Far Range . . . 35
4.1 Scenario for Far Range Mode . . . 35
4.2 Implementation . . . 38
4.3 Verification . . . 44
4.4 Summary . . . 50

5 Short Range - Cooperative . . . 51
5.1 Scenario for Short Range Mode . . . 51
5.2 Implementation . . . 55
5.3 Verification of SR-Coop Mode . . . 64
5.4 Summary . . . 74

6 Mode Switching . . . 75
6.1 Far ↔ Intermediate Range . . . 75
6.2 Intermediate ↔ Short Range . . . 79
6.3 Summary . . . 82

7 In-flight Experience . . . 83
7.1 AGC/Shutter Settings . . . 83
7.2 Far Range Mode . . . 88
7.3 Intermediate Range Mode . . . 96
7.4 Short Range Mode . . . 100
7.5 Mode Switching . . . 102
7.6 Summary . . . 106

8 Concluding Comments . . . 107
8.1 Future Work . . . 107

Bibliography . . . 111

Appendices . . . 115

A Datasheet of LED SMC735 . . . I

B Characterization of LED SMC735 . . . III

C PRISMA FM LEDs . . . XI

D LED Placement on STEP Model . . . XXIII

E μASC CHU Timing . . . XXIX

F P4P Solution Method . . . XXXI

G Short Range Cooperative LED Fitting . . . XXXVII

H PPS vs. LED Pulsing . . . XLI

I Notes on Noise Measurements of the VBS Mockup XLV

J Test Report of the Final PRISMA SW Load Campaign LXXIII

K Docking Pattern Calibration LXXXIX

L Inflight Data Analysis XCIII
L.1 FR AGC and Detection Threshold Settings XCIII
L.2 IR Mode Validation for FR CHU XCVII
L.3 IR Mode Validation for SR CHU CVI
L.4 CHU Alignment CX

M FR Bandpass and Edge Stray Analysis CXIII

N VBS Performance During Orbit Correction CXVII

List of Figures

1.1 Gemini-7 pictured during rendezvous approach with Gemini-6A . . . 2
1.2 Progress supply vehicle . . . 3
1.3 Details of the PRISMA satellites . . . 4
1.4 Limitations for flight operations . . . 6

2.1 Estimate of accuracy for mode overlapping . . . 12
2.2 System elements of the μASC . . . 13
2.3 Reference frames used by the μASC . . . 14
2.4 Functionality of CHU cross strapping in the μASC . . . 15
2.5 Modes of μASC including VBS mode . . . 16
2.6 Data flow structure for the VBS algorithm . . . 17

3.1 Temperature relation between I-V for the SMC735 LED. . . . 20
3.2 Thermal analysis of solar panel . . . 21
3.3 LED housing elements. . . . 22
3.4 Radiation pattern of the LED SMC735. . . . 22
3.5 LED overlapping in between intersecting panels. . . . 23
3.6 Movement of LED detection center. . . . 24
3.7 Final Approach and Recede side of the Target satellite. . . . 25
3.8 Collimator L-bracket as mounted on Target satellite. . . . 25
3.9 Placement of collimator beams at a distance of 2 meters. . . . 26
3.10 Tractor beam detected from PRISMA FM Collimator II by FM FR CHU. . . . 26
3.11 Mounting of LED housings directly mounted to the spacecraft. . . . 27
3.12 Mounting of LED housings mounted on an angle bracket and then to the spacecraft. . . . 28
3.13 Animated view of Target with visible LEDs. . . . 28
3.14 Verification of camera shutter system. . . . 30
3.15 Spectral sensitivity characteristics of the CCD and SR lens transmission profile. . . . 31
3.16 Relative lens transmission and CCD response combined. . . . 32
3.17 Relative lens transmission and CCD response combined with LED variations. . . . 32
3.18 The coated Short Range lens. . . . 33

4.1 Projection geometry of pinhole camera 36
4.2 Line of sight between Main and Target - Max. distance 36
4.3 Orbit pointing illustration 37
4.4 Mode diagram for the Far Range CHU. 39
4.5 Vector rotation description 42
4.6 Data flow structure for the Far Range mode algorithm 43
4.7 The Pharos module. 44
4.8 Detected centroids from the Pharos module 45
4.9 Linked centroids from the Pharos module 46
4.10 Test setup for the FR-IR testing on the real night sky. 47
4.11 Results from the Far Range VBS with a controllable moving Target. 47
4.12 Prediction trajectories from HeavensAbove. 48
4.13 All centroids recorded during tracking of satellite A and B. 49
4.14 Angular velocities with respect to CHU sphere. 50

5.1 Short range approach configuration 52
5.2 Pixel size of diodes vs range. 53
5.3 Signal to noise ratio of detected LED and background of Target. . . 53
5.4 Pinhole projection of four points 56
5.5 Mapping between frames 56
5.6 Fitting of the Target translation 59
5.7 Mode diagram for the Short Range CHU. 60
5.8 Data flow structure for the Short Range mode algorithm 61
5.9 Placement of end-of-integration in relation to the PPS pulse. 63
5.10 True PPS and LED timing. 63
5.11 Dolly test bench for Short Range cooperative mode. 64
5.12 Noise in VBS determined position of Target Mock-up. 66
5.13 Noise in VBS determined orientation of Target Mock-up. 67
5.14 Target rotation positions. 68
5.15 Example of correlation between Pose and Position. 70
5.16 Detected centroids during full rotation. 70
5.17 Target Position of the VBS output at rotation of Target. 71
5.18 Target Pose of the VBS output at rotation of Target. 72
5.19 Detected centroids during test of Exceeding Edge flag. 72
5.20 Brought daylight test of LED system and Short Range CHU. 74

6.1 View from the FR CHU. 76
6.2 Detected and linked centroids in the time domain. 78
6.3 Links found in FR and IR mode, respectively. 78
6.4 Test setup for the SR-IR switching. 79
6.5 View from SR CHU. 80
6.6 R.A. given in VBS outputs when switching between SR and IR. . . 81
6.7 Declination given in VBS outputs when switching between SR and IR.81

7.1 First Light image from the Far Range CHU. 84

7.2 Shutter time variations for the FR CHU. 85
7.3 Image segment for AGC setting 20. 85
7.4 First Light image from the Short Range CHU. 87
7.5 Close-up of Target at 15m. 87
7.6 Logarithmic histogram of Target view. 88
7.7 Thresholded Target images 88
7.8 First FR VBS results having false links. 89
7.9 True FR linking of Target. 90
7.10 VBS solutions omitting Target. 91
7.11 VBS solutions omitting Target and Edge Stray. 91
7.12 Influence of hotspot filtering on VBS FR solutions. 93
7.13 Noise in angle difference between CHU B and CHU C. 94
7.14 Angular velocity for Target pointing. 96
7.15 IR mode solutions with invalid output for multiple detected objects. 97
7.16 Zoomed area of detected Target 99
7.17 Target pointing given in the internal camera coordinate system of CHU C. 99
7.18 Target pointing given in inertial coordinates. 100
7.19 Shutter time during SR-Coop operations. 101
7.20 Valid SR solutions from the VBS system. 102
7.21 Inflight IR→FR mode transition. 103
7.22 Inflight SR↔IR mode transition. 105
7.23 Shutter time during mode transition. 105

8.1 View of Target from SR CHU 109

A.1 Datasheet of LED SMC735 II

B.1 Test bench for thermal characterization of the SMC735. IV
B.2 LED characterization 1. V
B.3 LED characterization 2. V
B.4 LED characterization 3. VI
B.5 LED characterization 4. VI
B.6 LED characterization 5. VII
B.7 LED characterization 6. VII
B.8 LED characterization 7. VIII
B.9 LED characterization 8. VIII
B.10 LED characterization 9. IX
B.11 LED characterization 10. IX

E.1 μASC Center of Integration Timing XXX

F.1 Pinhole projection of four points. XXXI
F.2 Mapping between frames XXXIV

G.1 Fitting of the Target rotation XXXIX

G.2 Fitting of the Target translation XL

H.1 PPS pulse vs. LED pulse. XLII
H.2 PPS and LED frequency. XLII
H.3 Leading edge of PPS and LED pulses. XLIII
H.4 Trailing edge of LED pulse. XLIII

K.1 Docking Pattern captured normal to boresight. LXXXIX
K.2 Docking Pattern captured at 45deg pitch to boresight. XC
K.3 Docking Pattern captured at 45deg turn to boresight. XC
K.4 Full $-Y$ panel of Target captured XCI

L.1 Image segment for AGC setting 5000. XCIV
L.2 Image segment for AGC setting 400. XCIV
L.3 Image segment for AGC setting 40. XCIV
L.4 Image segment for AGC setting 20. XCV
L.5 Image segment for AGC setting 10. XCV
L.6 Image segment for AGC setting 5. XCV
L.7 Inverted image illustrating the Earth Shine in the left side. . . . XCVI
L.8 Valid flags for IR mode on FR CHU. XCVIII
L.9 Info flags for IR mode on FR CHU. XCIX
L.10 Solution info fields for IR mode on FR CHU. C
L.11 Apparent Direction marked valid for IR mode on FR CHU. CI
L.12 CCD positions marked valid for IR mode of FR CHU. CII
L.13 CCD positions marked valid for IR mode of FR CHU. CIII
L.14 Target dimensions marked valid for IR mode of FR CHU. CIV
L.15 Shutter times for the FR CHU. CV
L.16 CCD positions marked valid for IR mode of SR CHU. CVI
L.17 CCD positions marked valid for IR mode of SR CHU. CVII
L.18 Dimensions marked valid for IR mode of SR CHU. CVIII
L.19 Shutter times for the SR CHU. CIX
L.20 Tracked Target for the FR CHU. CXI
L.21 Tracked Target for the SR CHU. CXI

M.1 All detected centroids. CXIII
M.2 VBS FR solutions with Target. Bandpass:150-290"/s CXIV
M.3 VBS FR solutions omitting Target. Bandpass:150-290"/s CXIV
M.4 VBS FR solutions omitting Target.. Bandpass:150-1000"/s . . . CXIV
M.5 VBS FR solutions omitting Target and Edge Stray. Bandpass:15-290"/s CXV
M.6 VBS FR solutions omitting Target and Edge Stray. Bandpass:150-290"/s CXV
M.7 VBS FR solutions omitting Target and Edge Stray. Bandpass:150-500"/s CXV
M.8 VBS FR solutions omitting Target and Edge Stray. Bandpass:150-1000"/s CXVI

N.1 Detected Target in CCD Coordinates CXVIII
N.2 Shutter time of the FR CHU CXVIII
N.3 Zoomed area of detected Target CXIX
N.4 Pointing attitude of CHU B and CHU C. CXXI
N.5 Target pointing given in the internal camera coordinate system of CHU C. CXXII
N.6 Target pointing given in inertial coordinates. CXXIII

List of Tables

1.1 Modes of operation of the VBS system 6
1.2 Orbit parameters of the PRISMA Target satellite 7

2.1 Data field validity vs. reported mode. 17

5.1 Standard deviation values for the different measurement positions. . 69

G.1 Real minimum vs. estimated VBS minimum. XXXVIII

Nomenclature

Typographical Conventions

Bibliographic references are given in square brackets denoting author surname and publication year e.g. [Abidi1990]. For multiple publications from the same author and year an additional alphabetic designator is added e.g. [Benn2009a]. For multiple citations in the same reference, each citation will be separated by a comma e.g [Abidi1990, Benn2009a].
References to sections uses Chapter.Section notation e.g. (see Section 1.1).
Figures, Tables and Equations are numbered with incremental numbers in reference to the chapter number. In equations, letters with *italic* notation will be representing variables, e.g. x, $\overrightarrow{u_i}$ and $\underline{\underline{R}}_{\phi}$, and roman letters will be representing units, e.g. $\frac{\mathrm{W}}{\mathrm{m}^2}$ and $\frac{^\circ}{\mathrm{s}}$.
Moreover, the introduction of new variables by the declaration of an equation will be implemented as exemplified:

$$E = m \cdot c^2 \tag{0.1}$$

where:
E: describes the energy equivalent to the mass.
m: describes the mass.
$c = 3.00 \cdot 10^8 \frac{\mathrm{m}}{\mathrm{s}}$: denotes the velocity of light in vacuum.

In number notifications all commas(,) and periods(.) symbolize decimal separators throughout the dissertation, i.e. no 1000 separators are used.

Acronyms and Abbreviations

The following list contains acronyms and abbreviations used throughout the dissertation:

AFF Autonomous Formation Flying

ASC Advanced Stellar Compass

CAD Computer-Aided Design

CC Camera Center

CCD Charge-Coupled Device

CCRG Collimated Close Range Group

CDR Critical Design Review

CDS Correlated Double Sampling

CHU Camera Head Unit

CMOS Complementary Metal oxide Semiconductor

CoC Circle of Confusion

COI Center Of Integration

COTS Commercial Off The Shelf

CRG Close Range Group

DART Demonstration for Autonomous Rendezvous Technology

DTU Danish Technical University

DoF Degrees of Freedom

DPU Data Processing Unit

EFL Effective Focal Length

EGSE Electrical Ground Support Equipment

ELISA Electronic Intelligence Satellite

EM Engineering Model

EOI End of Integration

ESA European Space Agency

ETS Engineering Test Satellite

FARM Final Approach/Recede Manoeuvres

FFRF Formation Flying Radio Frequency

FM Flight Model

FOV Field of View

FR Far Range

FWHM Full Width at Half Maximum

GCRG Geometric Close Range Group

GMT Greenwich Mean Time

GNC Guidance, Navigation and Control

GPS Global Positioning System

GRACE Gravity Recovery and Climate Experiment

IR Intermediate Range

ISS International Space Station

LED Light Emitting Diode

LTAN Local Time of Ascending Node

MIS Measurement and Instrumentation Systems

MUX Multiplexer

NASDA National Space Development Agency of Japan

NSO Non-Stellar Objects

OBC On-Board Computer

OGSE Optical Ground Support Equipment

PnP Perspective-n-Point

PCB Printed Circuit Board

PPG Position and Pose Group

PPS Pulse Per Second

PRISMA Prototype Research Instruments and Space Mission technology Advancement

PROX Proximity Operations

SFS Star Field Stimulator

SIG Space Instrumentation Group

STR Star Tracker

SMD Surface Mount Device

SN Signal-to-Noise

SPENVIS The Space Environment Information System [Spenvis2007]

SR Short Range

SR-c Short Range - cooperative

SR-n Short Range - noncooperative

SSC Swedish Space Corporation

STEP Standard for the Exchange of Product model data

TC Telecommand

TDRSS Tracking and Data Relay Satellite System

TM Telemetry

uASC micro Advanced Stellar Compass

VBS Vision Based Sensor

Terminology and Definitions

A selection of applied notation and parameters used in the following chapters are shortly summarized in this section.

Arcseconds: is a unit of angular measurement, defined as $\frac{1}{3600}$ of a degree, or $\frac{\pi}{648000}$ radians, and will be represented with the unit ["].

Centre Of Integration and End Of Integration: or COI and EOI. COI describes the time of which an image is referred to, stamped in the center of integration during image capture, where EOI refers to the end of the image capturing which is used as a fixed synchronization point for the VBS system.

Gravitational parameter (μ): is a combination of the Universal Gravitational Constant and the Mass of the Earth determined with high precision to be [Fortescue2003, Hansen2004b]:

$$\mu = G \cdot M_{Earth} = 3.986004418 \cdot 10^{14} \frac{\mathrm{m}^3}{\mathrm{s}^2}$$

Hotspots and Hotlines: These expression refers to radiation damage that have occurred on the CCD sensor. Hotspots occur due to crystal defects in the depletion region of the photo diode, seen as bright pixels in the image field. Hotlines occurs when crystal defects exists in the vertical CCD channel, causing entire lines to occur bright [Ochi1996].

Inertial Reference Frame: The reference frame of which the μASC is determining the attitude pointings of a CHUs boresight is given in relation to the J2000 inertial reference frame. Therefore, the use of inertial reference frame throughout the dissertation relates to the J2000.

Lifetime: The lifetime of electric components used in space refers to the time into the mission where a component can be expected to function properly. This lifetime is often controlled by the radiation shielding provided around the component or how well derated the component is.

Main and Target: The name 'Main' refers to the Main spacecraft of two satellites flying in formation which is capable of taking images and manoeuvre around the second spacecraft denoted 'Target'. 'Target' thus refers to the passive satellite of the two. These definitions are used throughout the report.

Quaternion: Rotations and Attitude pointing outputs delivered by the μASC and the VBS system are given in quaternion representations. Throughout this dissertation the quaternions are defined as:

$$\begin{aligned} q_1 &= e_x \sin(\tfrac{\phi}{2}) \\ q_2 &= e_y \sin(\tfrac{\phi}{2}) \\ q_3 &= e_z \sin(\tfrac{\phi}{2}) \\ q_4 &= \cos(\tfrac{\phi}{2}) \end{aligned} \tag{0.2}$$

where:
e_x, e_y, e_z : describes the direction cosines of the rotation axis.
ϕ : describes the rotation angle.

R_{Earth}: describes the radius of the Earth. In this project an average value usually applied when describing satellite orbits has been used. In [Murray2001] this is defined to be:

$$R_{Earth} = 6.3781 \cdot 10^6 \text{m}$$

Visible Spectrum: The human eye only responde to a small part of the wavelengths in the electromagnetic spectrum. This range is said to vary from human to human in the wavelengths from the violet values $390 \leftrightarrow 455nm$ to the red values $620 \leftrightarrow 780nm$. A standardized version of the human eye states that the relative responsiveness is smaller than 10^{-3} outside the range of $390 \leftrightarrow 720nm$ [Schubert2006]. As such, this range is applied as the visible spectrum throughout this dissertation.

Chapter 1

Introduction

This chapter will describe the background history of rendezvous and docking missions in spaceflight, detailing what has presently been achieved and lesson learned. Afterwards some future missions with mission objectives involving rendezvous and docking will be discussed, in addition to the requirements needed for making these missions feasible. An introduction to the PRISMA mission will be given together with a description of the involvement of this dissertation. Lastly, the scope of this dissertation will be given, including the aspects and suspected outcome of the work performed.

1.1 Background

Since the very beginning of the spaceage, the principles of rendezvous flights and docking of two spacecraft have shown their importance and necessity in different space missions. These have involved a wide range of objectives such as vehicle servicing/inspection, technical demonstrations, supply deliverance and lunar landing.
The first successful rendezvous approach conducted between two spacecraft in the same orbit around the Earth was performed in 1965. The two manned spacecraft consisted of Gemini-6A and Gemini-7, where Gemini-6A was manually maneuvered into a distance of only 30cm to the meanwhile passively orbiting Gemini-7 [NASA1966]. Subsequently, the first rendezvous approach with a docking was successfully conducted in the same Gemini space program by the Gemini-8 vehicle being manually docked to the unmanned Agena-8 target vehicle.

These demonstration missions lead to the start of realizing the lunar landings, where these kind of maneuvers were essential in order to transfer crew between the vehicles and ensuring their safe return to Earth. Many other

Figure 1.1. *Gemini-7 pictured during rendezvous approach with Gemini-6A at a distance of 7 meters. (Image: PD NASA Photo)*

manned spaceflights involving rendezvous and docking have been achieved. Included here are the more known missions such as the servicing missions of the Hubble space telescope and the many dockings achieved with the space stations by vehicles bringing both crew and supplies.

The main part of successful dockings have been relying on the presence of man in order to navigate the two spacecraft together, based on different visual aspects or features of the Target spacecraft. One spacecraft type has though distinguished itself, namely the Progress supply vehicle, which has been used since 1978 and up to the present day when supplying different space stations. The Progress vehicle is able to dock autonomously using a sophisticated radar system called Kurs, where a passive antenna system has to be placed at the docking port, and a active antenna system placed on the Progress vehicle [Portree1995]. The docking maneuver is supervised by both space station crew and ground personnel, all capable of aborting the current docking maneuver.

Autonomous rendezvous and docking between two unmanned spacecraft was first achieved in 1997 by NASDA with their Engineering Test Satellite ETS-7. This mission consisted of two satellites, a Chaser and a Target, where the Target acted as a passive spacecraft only equipped with basic attitude stabilization capabilities, and the Chaser being a full manoeuvrable spacecraft using propulsion to move in all 6 degrees-of-freedom (6DoF) [Inaba2000, Kasai1999]. Different navigation instruments where used during rendezvous and docking with the Target, involving laser, GPS and a proximity sensor. The proximity sensor was used for final approach and docking, and consisted of a 3D shaped marker placed on Target that was lighted up by 100 light emitting diodes placed on Chaser. The reflected light from the

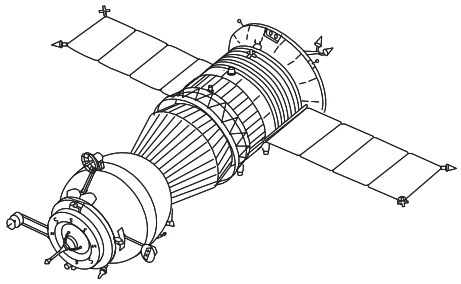

(a) Progress-M logistics resupply spacecraft.

(b) Approaching ISS prior to docking.

Figure 1.2. *Progress supply vehicle. (Images: [Portree1995] and PD NASA Photo)*

marker was captured with a camera, allowing distance and pose between the two spacecraft to be derived, resulting in a successful docking.
Later followed the successful Orbital Express mission by NASA, also performing rendezvous and docking between a Chaser and a Target satellite. This mission carried an optical bench mounted with three optical systems and a laser ranger, and was the first to achieve autonomous refueling and hardware exchange between two spacecraft while in-orbit [Rotenberger2008, Leinz2008].

Performing rendezvous and docking in space between spacecraft moving with velocities greater $7\frac{\text{km}}{\text{s}}$ have shown their difficulties. This has been well illustrated by both the mishap in the DART mission in 2004, the collision between Mir and Progress M-34 supply vehicle, and the mishap during docking of Progress M-58 supply vehicle to the ISS.

1.2 Future Perspectives

Future missions with rendezvous, docking and precision formation flying as primary objectives are already in development or in search of financing. One of these are the ESA led Darwin mission where a constellation of satellites, each mounted with a telescope, is flying in a circular formation. Combining the functionalities of the individual telescopes allow interferometer measurements to be made, although this entails the need of knowing the telescope positions with sub-millimeter precision for the data to be merged. The Darwin mission is scheduled for launch in 2015

The Darwin missions need for high accuracy determination of the positioning in between the telescopes, has initialized the demonstration satellite missions called PROBA3 and PRISMA. The PROBA3 mission has completed the preparatory phase and is going to demonstrate precise formation flying

and collision avoidance technologies.
The PRISMA mission is the first of the three missions, and has been launched mid 2010. This mission has direct relation to this dissertation and will therefore be described in greater detail.

1.2.1 PRISMA Mission

The Prototype Research Instruments and Space Mission technology Advancement (PRISMA) mission is led by the Swedish Space Corporation (SSC) in cooperation with different countries and institutions. PRISMA is a technical demonstration satellite mission and consists of two satellites which from launch were coupled together. Once in orbit the two satellites were separated where the one, known as the Main spacecraft, has full 6DoF maneuverability and uses this functionality to perform different maneuvers around the passive spacecraft known as the Target satellite.

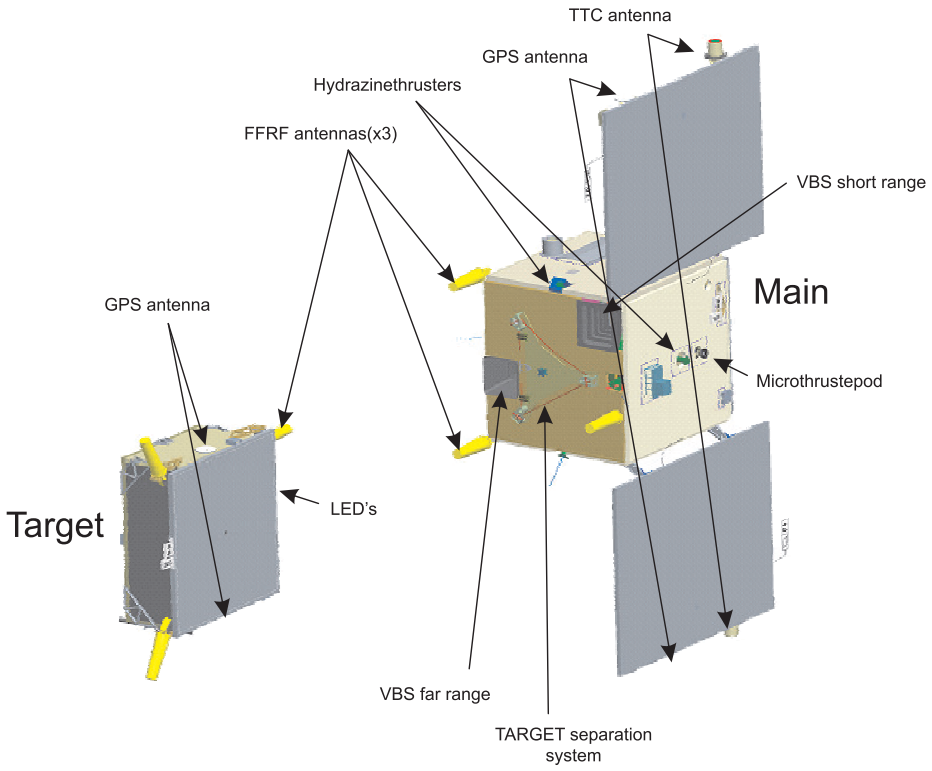

Figure 1.3. *Details of the PRISMA satellites. The two CHUs meant for VBS are indicated. (Image: SSC)*

The Main spacecraft is equipped with different sensor technologies which can determine the position and/or pose of Target in relation to Main. The onboard sensors are as follows:

GPS: A GPS based navigation system with sensors onboard both Main and Target.

FFRF: Formation Flying RF sensor with antennas and transceiver equipment onboard both Main and Target.

VBS: A Vision Based Sensor consisting of cameraes on Main picturing Target, where Target has included ability to provide feature point markings.

Placement of these sensors and a general description of the two satellites are illustrated in Figure 1.3, showing the situation where the spacecraft are separated flying in Short Range formation.

Different maneuvers and approaches of Main around Target have been defined, based on the use of the different sensor instruments running either solo or in cooperation with one another. The sensors and their interactions are controlled by the Guidance, Navigation and Control (GNC) system of the Main spacecraft which has the following modes incorporated [Persson2006b]:

AFF: Autonomous Formation Flying based on the GPS system and the FFRF sensor system.

H&R: Homing and Rendezvous based on VBS only.

PROX: Proximity Operations based on the GPS and VBS systems.

FARM: Final Approach and Recede Operations based on VBS only.

The four denoted modes each highlight common maneuvering scenarios and important aspects of formation flying experiments. The maneuvering around Target has though a limited field of operation. This is due to the two spacecraft constant need for power, resulting in a minimum tilt angle requirement of the solar panels with respect to the sun vector. The maneuverability of Target is limited by the use of magnetorquers, implemented for detumbling control and to align its solar panel side with the sun vector. This control method enables a stability of the sunvector-pointing within $\pm 10°$ for the Target satellite.

The minimum angle of the Main approach has been set to $45°$ and the resulting field of operation for Main is as illustrated in Figure 1.4.

The VBS system of the three sensors used in the PRISMA mission is to be delivered by the Space Instrumentation Group (SIG) of DTU Space in coordination with a micro-Advanced Stellar Compass (μASC). This sensor has to produce reliable information on the positioning of Target in reference to the Main spacecraft, enabling Main to perform its maneuvers for the different formation flying experiments. SSC and SIG have from meetings and short feasibility studies found the need of splitting the VBS system into modes of operations, based on the distance between Target and Main. These modes are

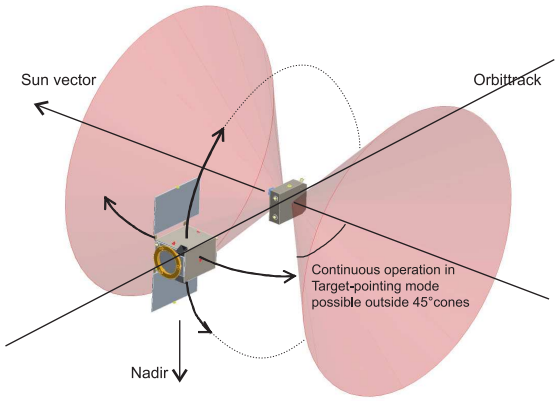

Figure 1.4. *Limitations for continuous flight operations. The angle to the sun shall not exceed 45° in order to satisfy the power specifications of Main. (Image: SSC)*

listed in Table 1.1, where Cooperative/Non-cooperative denotes if the Target spacecraft is providing feature points of its own or not.
Further description of each of these modes are given in Section 2.1.

Mode	Range	Position	Pose
Far Range	1000km-500m	Inertial, pointing only	-
Intermediate Range	2km-30m	Relative, pointing only	-
Short range Non-cooperative	200m-2m	Relative, pointing and distance	3 DOF
Short range Cooperative	200m-20cm	Relative, pointing and distance	3 DOF

Table 1.1. *Modes of operation of the VBS system, including approximated ranges between Target and Main, and which Target information that can be determined.*

During the design and development phase of the VBS instrument, the planned orbit parameters were used to describe the scenario analysis pre-launch. In Table 1.2 the planned orbit parameters are compared with the actual orbit parameters achieved by the launch provider.

The resulting Sun-synchronous Dawn-Dusk orbit is at a greater altitude than what was originally planned but at a similar inclination. The difference in the design and actual orbit parameters are taken into consideration when the scenarios for the various VBS modes are described in the related chapters.

1.3 Scope of Dissertation

The work in this dissertation is based on the development, integration and verification of the VBS system for the PRISMA mission. The work has been

Parameter	Design	Actual
Orbit type	Heliosynchronous	Heliosynchronous
Altitude	700km	740-800km
Inclination	98.2°	98.338°
Eccentricity	0.001	0.002 - 0.005

Table 1.2. *Orbit parameters of the PRISMA Target satellite. [Eberhard2007, Granholm2007, Persson2006b]*

based on, and is a continuation of, the scene analysis and proof of concept as presented in [Benn2007], which used the PRISMA missions requirements as guidelines for the capability and functionality requirements of the VBS system. The fully functional and space-qualified μASC navigation instrument are used as the design platform, extending its capabilities with VBS functionality.

The scope of this dissertation is to describe the implementations, verifications and qualification methods conducted to evolve the VBS system from its proof-of-concept state into realization of a Flight Model for the PRISMA mission. This includes both hardware and software development and modifications directly linked to the system, which encompass both the full Flight Model VBS system and the systems used for VBS system verification.

The two main modes of VBS operation, denoted Far Range (FR) mode and Short Range (SR) mode, are described in great details within this dissertation. Whereas elaboration of the transition mode between the FR and SR modes, denoted Intermediate Range (IR) mode, is merged into the sections regarding the FR and SR modes.

The PRISMA satellites were launched June 15$^{\text{th}}$ 2010 and the VBS system has subsequently passed the Commissioning Phase and Early Harvest Phase, wherefore the first in-flight results will be presented and discussed in this dissertation.

1.4 Summary

Descriptions of previous rendezvous and docking spaceflight missions, starting back from the very first successful attempts, have been explained and shortly analyzed. This was transitioned into description of present and future spaceflight missions with similar mission objectives, which included a closer descriptions of the PRISMA mission and what relevance this mission has for the project leading to this dissertation.

Lastly the scope of this dissertation has been presented, regarding both description of the work structure and the expected outcome of the project.

Chapter 2

System Description

In order to clarify the overall needed functionalities of a Vision Based Sensor (VBS) system, the following chapter will describe the scenarios that the system has to cope with and which parameters that are available for describing position of a Target spacecraft. Furthermore, a description of the μASC instrument is given into which the VBS system has to be implemented. Finally it is outlined which requirements of the μASC system that have to be taken into consideration when adapting it to function as a VBS instrument, and which output information that will be available from the VBS system. The information regarding the system functionality and requirements presented in this chapter are extracted from information given in i.a. [Benn2007, Denver2006b, Persson2006a, Persson2006b]

2.1 VBS Functionalities

The design of the Vision Based Sensor (VBS) system has primarily been based on the scenario analysis performed in [Benn2007]. Here the PRISMA mission has been used as guidelines describing the needed performance requirements of the VBS system, and has been thoroughly used during design and development of the VBS to μASC implementation.

The physical operating range required by the PRISMA mission has lead to the division of the possible scenarios into three main groups, namely Far Range, Intermediate Range and Short Range. In short, the three modes cover the following scenarios:

- **Far Range mode:** Where stars are detectable in the background in conjunction with the Target spacecraft.

- **Intermediate Range mode:** Where the Target spacecraft appears to bright, disabling detection of stars and no features of the Target spacecraft distinctly are visible.

- **Short Range mode:** Where features of the Target spacecraft are visible based on two subscenarios:

  - **Cooperative:** The Target spacecraft provides feature points in form of LEDs placed in predefined patterns,
  - **Non-cooperative:** The Target spacecraft have the fixed structure and outer elements illuminated only by the ambient surroundings.

Each of these modes of the VBS are capable of delivering different solution parameters, which are further described in the following subsections along with a clarification of the modes and their characteristics.

2.1.1 Far Range

Since the Far Range mode will be able to detect stars in coordination with detection of Target, the attitude of the CHU can on this basis be determined with high accuracy. The Target is detected as a dot in the image, enabling determination of a pointing direction towards Target in the inertial reference frame.

From [Benn2007] it is known that the Target spacecraft can be detected by looking at the angular velocity of the objects passing by relative to the CHU pointing. Based on the build-in star catalogue in the DPU, a list of all the Non-Stellar Objects (NSO) detected on the starry sky can be created. The list of NSOs is provided to the FR algorithms which tracks all objects, filtering out the objects moving in a certain angular velocity interval and announces the object which has the best solution based on the filters. Track history is kept for all linked objects, enabling the system to estimate the stability and the precision of the tracked object.

In order for the VBS mode to announce the correct pointing towards the Target spacecraft, the Target satellite has to be detectable as a centroid by the FR CHU. If the Target is not visible, the object with the next-best track record will be announced, if any. In conjunction with the announcement history and precision numbers will tell that the object has changed.

This approach requires that the Target satellite is visible in three subsequent image frames in order for a track record to be initialized.

2.1.2 Intermediate Range

The upper/far limit of the IR mode is set by the scenario where the Target spacecraft is detected so bright that the starry background is not visible, which disables the attitude determination for the FR CHU. The Target satellite will in this case be seen as a Big-Bright-Object (BBO), from where an apparent pointing towards the Target spacecraft can be provided.

Since the attitude cannot be determined on the stars, the attitudes of the VBS CHUs are based on mapping of the attitudes provided from the two standard CHUs, if applicable.

The lower/near limit of the IR mode is set by the scenario where the SR CHU is not capable of distinguishing features on the Target spacecraft. Likewise, the Target spacecraft will here be seen as a BBO from where an apparent pointing can be determined.

2.1.3 Short Range

In distances where features of the Target are detectable additional information can be analyzed, thus providing the ability to determine multiple degrees-of-freedom (DoF) resulting in both pose and position determination of the Target spacecraft in reference to the CHU [Abidi1990, Benn2007, Benn2008a, Bjarnoe2005]. Again the highly accurate pointing knowledge of the CHU boresight based on the stars as reference cannot be determined, though mapping from the attitude determined by the standard startrackers can be used.

For the PRISMA mission, the Target spacecraft is capable of operating in two different modes which become effective at Short Range distance:

2.1.3.1 Non-cooperative Mode

When Target is in Non-cooperative mode it will act as any other passive spacecraft, where normal imaging of the Target has to be analyzed for feature detection corresponding to already known features of the spacecraft. From good quality images, with respect to sharpness, resolution and proper illumination of the object under review, 6DoF positioning and orientation can be determined.

2.1.3.2 Cooperative Mode

The Cooperative mode of Target takes into advantage that the Target spacecraft is designed for this type of mission. Here, Target is capable of delivering clearly marked feature points, realized by LEDs placed on Target. Based on centroiding of these points and the fact that their positions on Target are already known, the pose and positioning of Target can be determined in 6DoF.

This mode provides the ability to derive pose and positioning knowledge at distances even closer than what is possible in Non-cooperative mode, due to the fact that the entire Target does not have to be in FOV, but only a portion of the feature points.

2.1.4 Mode Transitions

The different modes of operation, described in Section 2.1.1 to 2.1.3, have to be linked together in order to provide functionality in the entire range of detection required by the PRISMA mission. Enabling a seamless transition in between each mode requires that two adjoining modes can overlap into each others range of operation, giving the ability to provide two solutions from where the most accurate can be used.

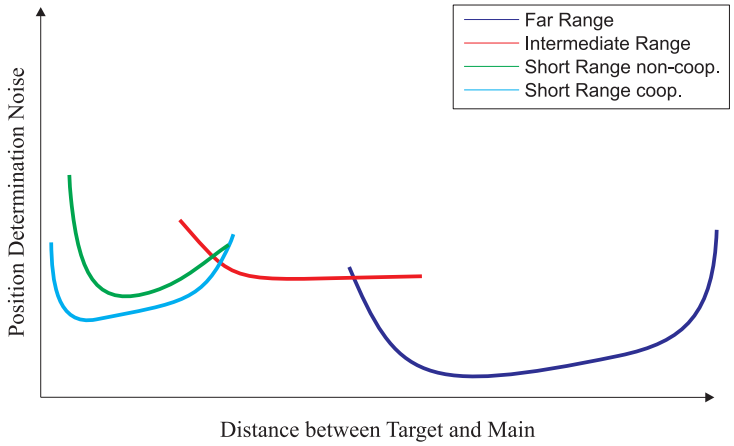

Figure 2.1. *Estimate of accuracy for mode overlapping.*

Based on the analysis and description of the modes given, an estimate of how each mode will operate is illustrated in Figure 2.1. The Far Range mode is illustrated as the one with highest accuracy due to the fact that the stars are visible, providing a reference of pointing. The Intermediate Range mode is illustrated as the least accurate due to the fact that the determinable parameters are based on the limited amount of information the image is capable of providing. The two Short Range modes are illustrated with the Cooperative mode providing higher accuracy than the Non-cooperative mode, since clear feature points are provide. Furthermore, the Cooperative mode is capable of getting results at the shortest distance.
This illustration should only be seen as a weak comparison between the different modes. This is due to the fact that each main mode will provide different parameters of Target, such as 6DoF positioning for Short Range modes and only pointing towards Target in Far Range mode.

The mode switching of the VBS system is implemented to function autonomously based on the scenario, the detected image information and previous solution availability. The mode switching is determined independently between the FR and SR CHU, and is discussed in Chapter 4 and 5 describing the functionality of the two CHUs, respectively.

2.2 μASC Description

The Space Instrumentation Group (SIG) at DTU Space has for a decade been developing a star sensor instrument. The present version is called the micro-Advanced Stellar Compass (μASC) and constitutes the fourth generation in a row of star sensor instruments. This instrument is capable of determining pointing attitude of the sensor instrument based on recognition of star patterns on the sky, and its primary application is on-board attitude determination for spacecraft. The μASC is designed to withstand the harsh environment of space and has proven its worth on several satellite missions, resulting in a continuous growth in demand for future satellite missions.

The μASC instrument consists of two main elements, namely a Camera Head Unit (CHU) and a micro-Data Processing Unit (μDPU) which both are depicted in Figure 2.2 along with a baffle system of the CHU.

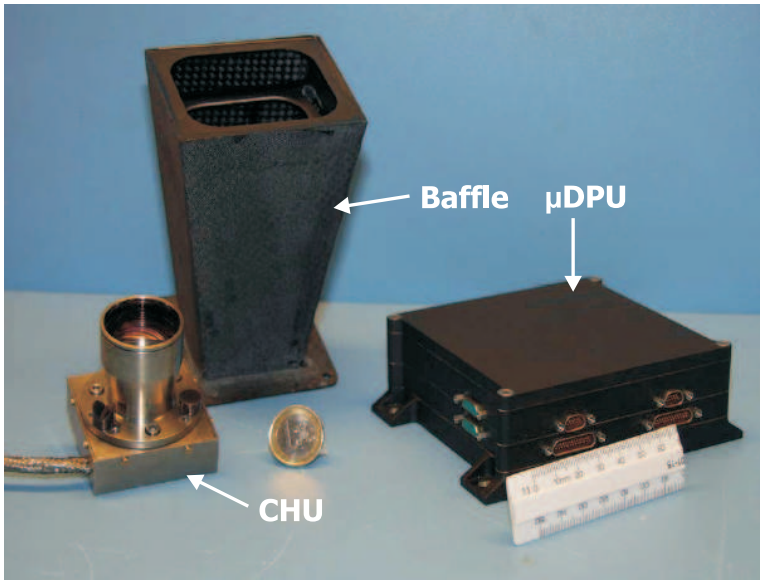

Figure 2.2. *System elements of the μASC, depicting a CHU, a Baffle and a double μDPU. (Image: [Mortensen2005])*

The star sensor of the instrument is based on a CCD image sensor chip with a lens frontend designed for low-light situations. The image captured by the CCD is subsequent analyzed for presence of stars, based on highly accurate

centroiding of spots available in the image. The positions of these centroids are compared with positions of stars represented in an on-board star catalog, from where the attitude pointing can be determined. Through testing and data collected from flight it has been confirmed that the μASC is capable of detecting a wide range of illumination intensities. Objects from a magnitude of +7 to a magnitude of -4 are generally detectable, giving a dynamic range above 10000, based on the definition of the Magnitude scale [Rasc2007].
Furthermore, the CCD used in the CHU has a full well capacity of 170000e^- photons per pixel, with an additional factor of 2^8 before overblooming in the pixels occur.

Pointing accuracy estimation for the μASC instrument has been based on data recorded from flight and real-sky tests performed from ground. The values of accuracy are given as Noise Equivalent Angle (NEA) which is the noise experienced with the boresight of the camera looking at the same star pattern over time. Accuracy estimations have shown that an accuracy better than 2 arcseconds for the X- and Y- axis directions can be achieved and an accuracy around 15-20 arcseconds in the roll direction around the boresight can be achieved [Michelsen2006].

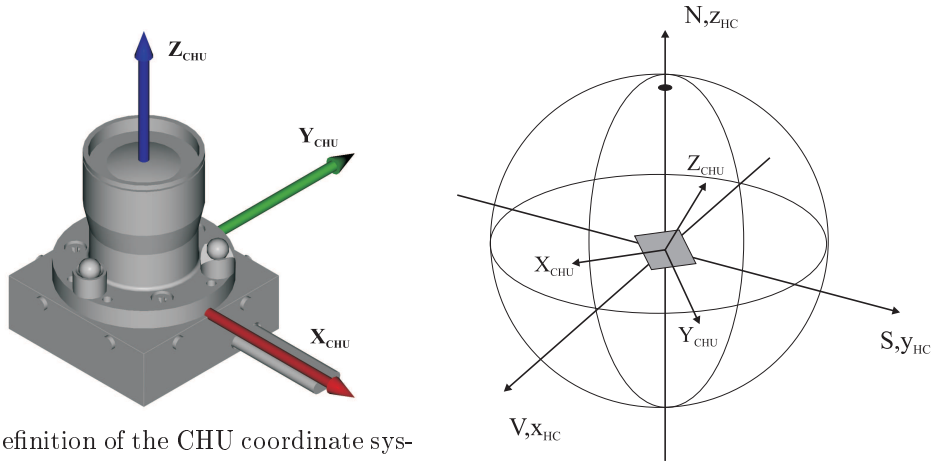

(a) Definition of the CHU coordinate system.

(b) CHU reference frame in J2000.

Figure 2.3. *Reference frames used by the μASC. (Images: [Bjarnoe2007, Mortensen2005])*

The pointing determined by the instrument is referring to the pointing of the CHU boresight, which in the definition of the CHU coordinate system corresponds to the pointing of the Z-axis. The definition of the CHU reference frame is illustrated in Figure 2.3(a), where the XY-plane is in the CCD-plane of the CHU and the Z-axis describes the optical center of the lens.
The attitude solution provided by the μASC system describes the boresight pointing of the defined CHU frame in the J2000 inertial reference frame, as illustrated in Figure 2.3(b).

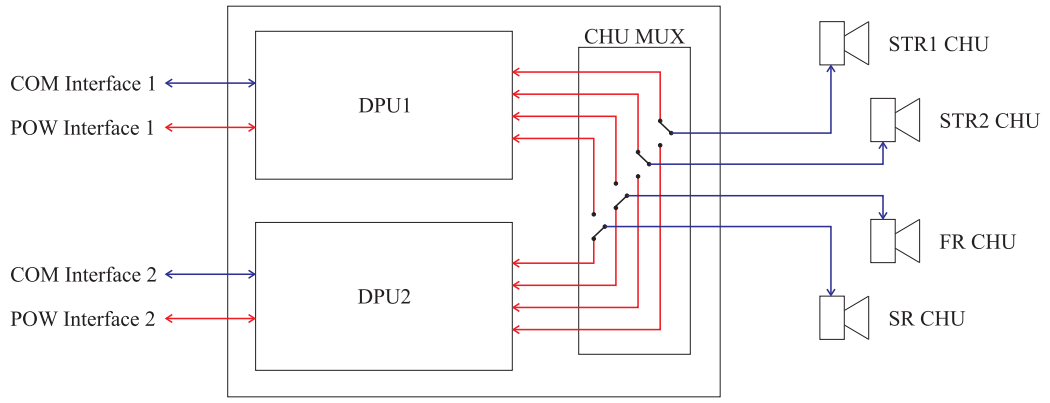

Figure 2.4. *Functionality of CHU cross strapping in the μASC in the situation of STR CHUs are controlled by DPU1 and VBS CHUs are controlled by DPU2.*

The configuration of the μASC consists of a single or a double μDPU which can have up to four CHUs connected, providing control of all CHUs individually. In the configuration using two μDPUs a cross strapping interface between the two allows individual access to the CHUs. The functionality of the cross strapping is illustrated by the CHU MUX in Figure 2.4.

The attitude update frequencies the μASC instrument is capable of delivering are: 4Hz, 2Hz, 1Hz, ..., $\frac{1}{16}$Hz, which are directly related to the integration time used for the CCD, giving times of: 250ms, 500ms, 1s, ..., 16s. Furthermore, the system provides the ability to control the integration by triggering on a flank of an externally applied pulse. Usually a PPS pulse from a GPS receiver is used for the purpose.

The software processing hardware of the μASC consists of a 100Mhz processor, 16MB RAM and 5.5MB Flash, where the STR only uses a minor percentage of the full hardware capabilities in its standard configuration. The operating system is written in `C` code, and compiled with a `GNU C` compiler. The communication interface of the μASC consists of a RS-422 link using a packet utilization standard protocol for exchange of telemetry (TM) and telecommands (TC). Control of the instrument is realized using a range of TCs which are all described in [Denver2006a] together with descriptions of TM data interpretation.

2.3 μASC Adaption of VBS Functionality

In order to realize the implementation of VBS functionality to the μASC several modifications and issues has been processed. It is known that for close range operations the FOV and focus distance of the standard CHU will not

be able to deliver reasonable imaging, due to the fact that the original design has been optimized towards the instruments primary purpose, namely the detection of distant stars in low light situations. Therefore, the lens design has been up for re-design.
Furthermore, the electronic design of the CHU is based on use of the standard lens and low light situations. This leads to the need of modifications of gain and integration time control, providing adjustment capabilities of the image capture system in order to enable picturing of Target. The necessary hardware modifications to the μASC are discussed in Section 3.2.

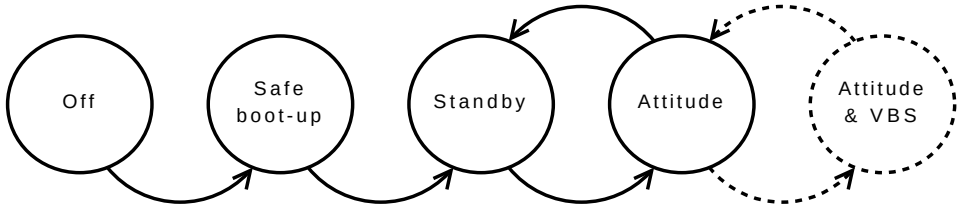

Figure 2.5. *Modes of μASC including the additional VBS mode.*

Since the μASC has to be able to perform as a normal star tracker, the VBS functionality has been implemented as an additional mode to the range of already existing modes of the μASC. The predefined modes are depicted in Figure 2.5 [Mortensen2005], including a mode for the VBS illustrated by the dotted lines.
Any VBS software, such as pose and position algorithms, have been implemented in the operating system of the μASC, where necessary parameters and variables are exchanged with the already existing star tracking system. Furthermore, the TM/TC interface of the μASC has been extended to provide control of the additional functionalities that the VBS system provides, as well as handling of the data created by the VBS system.

2.4 VBS Solution Information

Based upon the operating mode of the VBS system, different outputs are determinable by the VBS system. The mode is based on the scenario, which CHU is activating the VBS routine, previous available VBS solutions and input information, all determined autonomously.

In order to illustrate the input and output data of the VBS system, the data flow is given in Figure 2.6. The listed input information is as provided by the μASC system to the VBS system, from which the VBS system relies upon to function as desired.

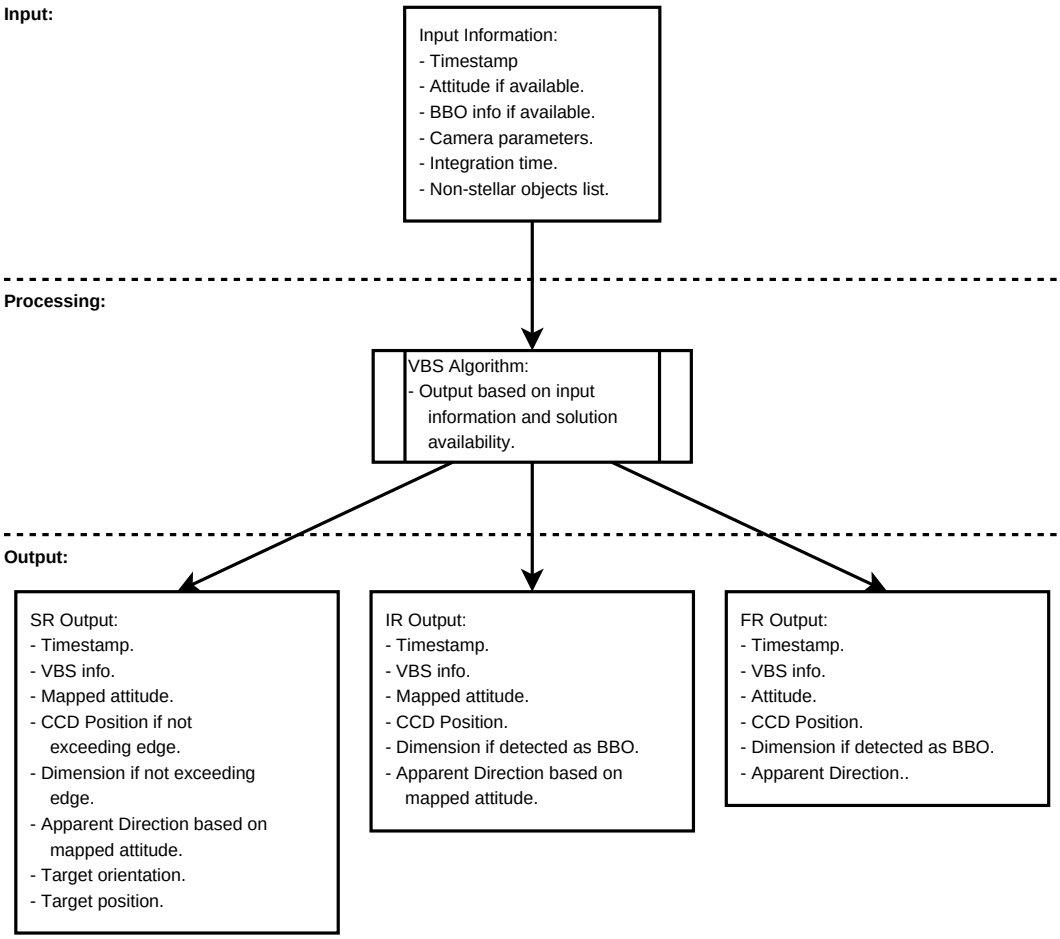

Figure 2.6. *Data flow structure for the VBS algorithm. Shown output data fields assumes that a solution has been determined for the given mode.*

VBS Mode \ Data Field	Timestamp	VBS Info	Attitude	CCD Pos.	Dimension	App.Dir.	Orientation	Position
Far Range	✓	✓	✓	✓		✓		
Intermediate Range	✓	✓		✓				
Short Range	✓	✓					✓	✓

Table 2.1. *Data field validity vs. reported mode. Green indicates the data fields that can be considered valid in each respective solution mode. Blue indicates fields that can be valid and needs verification based on VBS Info field. Red indicates data fields that cannot be resolved for the current mode.*

The output information from the data flow diagram have been aggregated in Table 2.1, which clearly illustrates the differences between each of the modes

by comparing the valid output fields. Additionally, the fields that might be determinable for the mode are highlighted. This goes for e.g. the success of the attitude mappings when the CHU is not able to determine its own pointing.

2.5 Summary

The scenario in which the VBS system has to be operational has been split up into three different modes, namely Far Range, Intermediate Range and Short Range, with two additional submodes of the Short Range mode denoted Cooperative and Non-cooperative. A description of each of these modes and the expected determinable parameters of Target have been given together with an estimate of their precision capabilities. Along with the precision estimates an illustration of how the overlapping in between the modes is thought to be functioning has been provided.
Furthermore, an introduction and a description of the μASC instrument is given, along with a discussion of which requirements are needed in order to implement VBS functionality into the instrument.

Chapter 3

Flight System

In order to realize the VBS system on the μASC, small hardware changes to the system and external support hardware are needed. This chapter will describe the external support hardware, consisting of LEDs placed on Target for providing cooperative feature points, and the μASC hardware changes, consisting of modifications to the optical system and the camera shutter control. This chapter will describe the design and verification of the VBS related hardware modifications/developements used for the PRISMA mission.

3.1 Cooperative Target Feature Points

As described in Section 2.1, the Target spacecraft of the PRISMA mission is to deliver cooperative feature points for the Short Range Cooperative mode of the VBS system. These feature points are designed, assembled and verified by the DTU Space, and this section will describe the different aspects.

The initial investigation of how to realize the Target feature points are discussed in [Benn2007], where the selected approach uses light-emitting diodes in the near-infrared spectrum.

3.1.1 LED

The chosen LED for the Target feature points are the SMC735, issuing a surface mount ceramic structure with a peak wavelength of 735nm. The datasheet for the SMC735 LED is given in Appendix A where the following specifications are given:

Chip Material:	AlGaAs
Power Dissipation:	200mW
Pulse Forward Current:	500mA
Forward Voltage:	1.85V
Total Radiated Power:	10.0mW
Peak Wavelength:	735nm
Half Width (FWHM):	30nm
Rise/Fall Time:	80ns/80ns

The SMC735 component has undergone the standard space qualification test for electrical components at DTU Space, including irradiation, thermal cycling, etc., and has proven qualified for the use on the PRISMA mission with respect to meeting the mission requirements.

Additional verifications has been carried out in order to analyze the behavior of the SMC735 at different scenarios, especially with respect to the peak wavelength and FWHM. Appendix B describes the characterization of the peak wavelength with respect to LED temperature and pulse-powering, mainly used during the design of the CHU lens system described in Section 3.2.2.

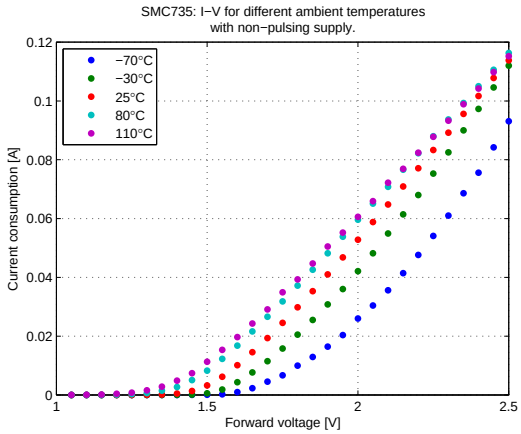

Figure 3.1. *Temperature relation between I-V for the SMC735 LED.*

Additionally, measurements are taken from a steady powered LED in a thermal controlled environment resulting in the dataset presented in Figure 3.1, illustrating that the power-dissipation of the LED is decreasing at low temperatures, resulting in lower radiated light. The LED powering described in Section 3.1.7 utilize a voltage limited supply, giving that the radiated power will vary with temperature.

From a thermal analysis of Target performed by SSC it is known that the body structure of the Target satellite is estimated to be within a few degrees from 0°C[Hellman2007], except for the solar cell panel denoted as +Z panel. The thermal model of the +Z panel is depicted in Figure 3.2,

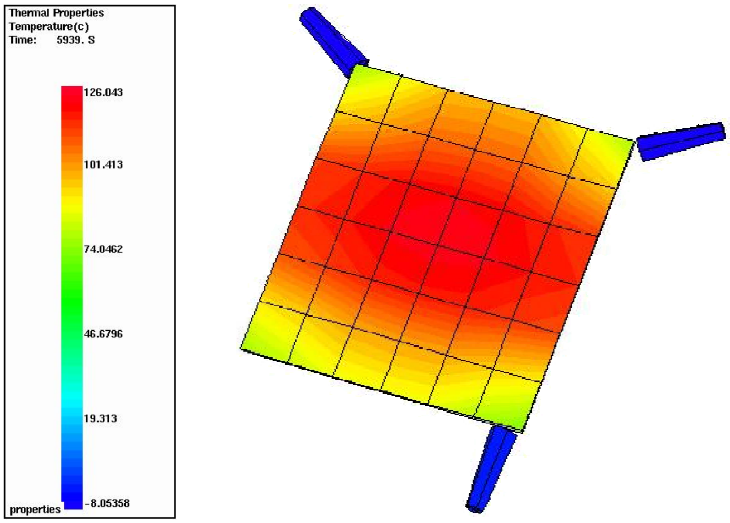

Figure 3.2. *Thermal analysis of solar panel side of Target corresponding to the +Z panel. (Image: SSC)*

where only the outermost edges are within the maximum limits of 80°C for the SMC735 denoted in its associated datasheet. This temperature knowledge is used in both the design of the LED housing, described in Section 3.1.2, and the placement patterns on Target, described in Section 3.1.6.

3.1.2 LED Housing

From [Johnston2000] it is known that radiation damage of LEDs have direct influence performance changes such as light output and the forward voltage. Therefore, special housing of the LED is designed, providing shielding protection and thermal stability.

In Figure 3.3 is the subelements of the LED assembly illustrated. Here the lens is designed to provide shielding to the LED in combination with the surrounding black-anodized aluminium housing. The full assembly of the LED system is described in [Benn2008d].

Based on irradiation tests of the SMC735 it is known that the housing design provides significant protection for the PRISMA mission requirements and lifetime [Thuesen2007].

3.1.3 LED Lens

The Lens system placed in front of the Target LEDs is designed such that it will support in the irradiation protection of the LED, which due to the exposed

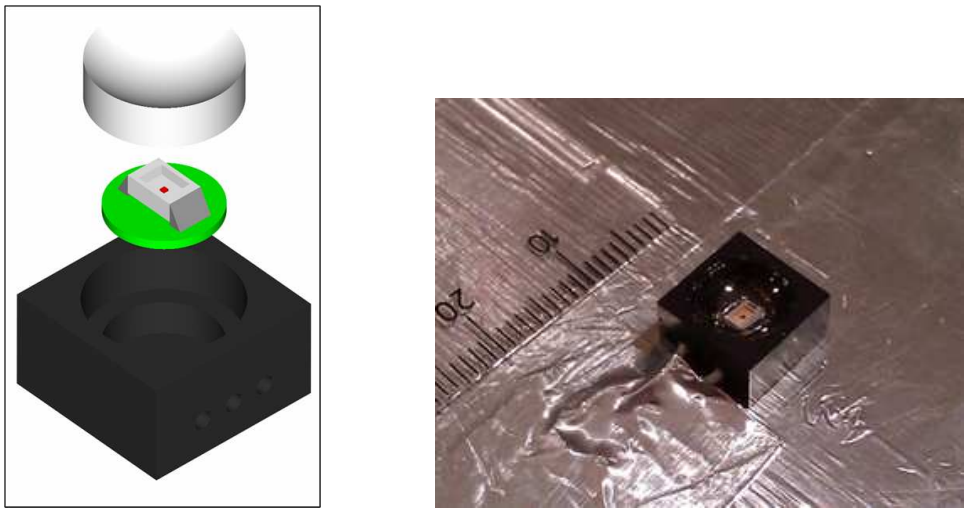

Figure 3.3. *LED housing elements. Left: Exploded view of the CAD drawing. Right: Assembled LED mounted on a Target mock-up.*

placement is designed in quartz structure[1]. Additionally, the lens is designed such that the light emitted by the LED forms a 60° evenly distributed cone around the boresight.

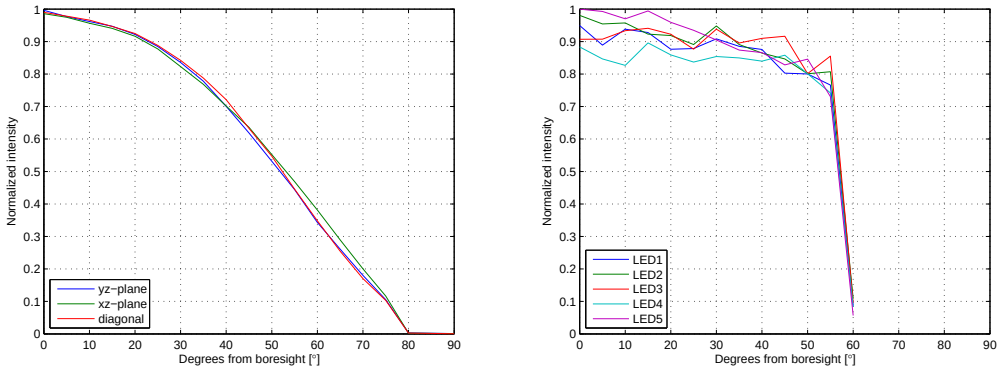

Figure 3.4. *Radiation pattern of the LED SMC735 based on centroid intensities measured using the μASC. Left plot illustrates the radiation pattern of the LED without lens elements in front of the die, and the right plot illustrates the radiation pattern in the yz-plane of the first five prototypes with the Lens system in front of the die.*

Figure 3.4 illustrates the measurements taken prior to the lens design versus the results of the final lens design, showing that the desired angle of 60° is almost achieved with an even distribution of the emitted light.

[1] Quartz is used instead of glass, since glass is known to darken in radiation environments [Hedden1960].

The final full assembly of all the LEDs used for the PRISMA mission showed great variance in the radiation pattern of the emitted light, though kept within tolerances for the performance analysis of the VBS Short Range cooperative mode. The variances in between the LEDs are illustrated in Appendix C as given in [Benn2008c].

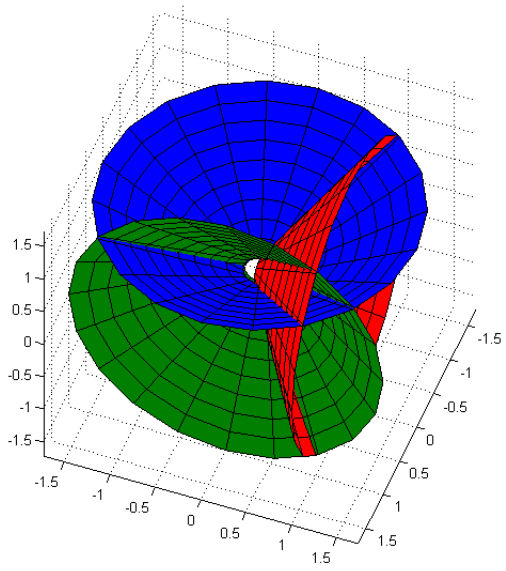

Figure 3.5. *LED overlapping in between intersecting panels illustrated by the 60° cones for the radiation pattern.*

The reason for a spanning of 60° around the LED boresight is given from the fact that a smooth transition in between view of adjoining panels is desired for the SR-Coop mode. By spanning 60° at least one panel is visible at any pose of the Target spacecraft. This is illustrated in Figure 3.5, showing the overlapping from the radiated patterns.

By placing a lens in front of the LED the outside view of the optical center will vary from the true center due to the lens diffractions. In order to estimate the true center based on the optical center, measurements were taken which illustrates the significance of the differences. These measurements are given in Figure 3.6 showing that the optical center can be corrected for between -30° to 30° by readjusting the physical center of the die. Beyond these limits a standard deviation profile has been created which will be used by the SR-Coop mode to correct the detected center based on the detected viewing angle.

3.1.4 Docking Pattern

The docking pattern serve to provide position and pose determination once the Main and Target satellites are closer than about 10 m, and all way into about

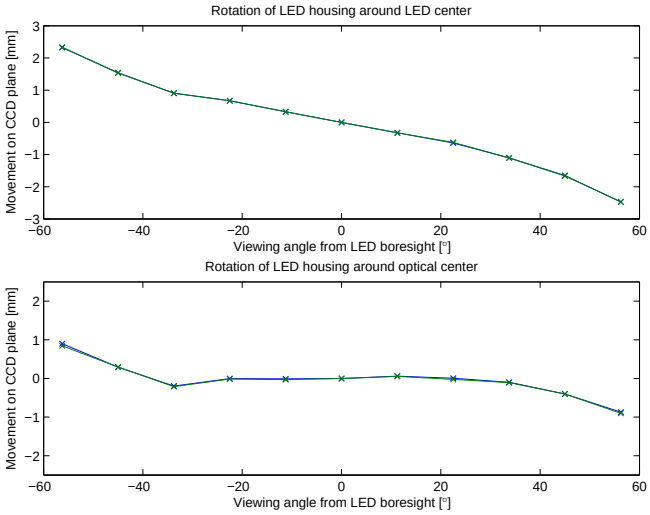

Figure 3.6. *Movement of LED detection center when rotating around the LED, measured with the μASC system. Top: Rotation around physical center of the die. Bottom: Rotation around the optical center.*

40cm. This is planned for during the Final Approach and Recede Manoeuvre (FARM).

The docking pattern consists of five spatial placed LEDs on a fixed structure. This structure is placed on only one panel of the target S/C in accordance with the panel planned for docking simulation approach flight, pointing the same direction as the pointing of the collimated LEDs[2].

In Figure 3.7 is shown how the Docking panel is mounted on Target. Note the middle LED is lifted above the plane of the other LEDs, which aid the VBS solution when the CHU is normal to the panel.

3.1.5 Tractor Beams

Five LEDs on Target differs in design and functionality than the others. These are placed in aluminium tubes with a hole pattern and a collimating lens system in front of the LED.
The Collimated LEDs form a well-defined beam containing a geometric pattern suitable for recovery of Target pose. The governing principle is that a lens converts a micro-meter hole pattern into a collimated beam, which can then be focused on by any camera and, in principle, at any distance. Each Collimated LED is enclosed in a cylindrical housing that is mounted to an L-bracket located externally on Target as illustrated in Figure 3.7 and 3.8. The placement of the L-bracket on Target is defined such that, when the SR

[2]Discussed in Section 3.1.5

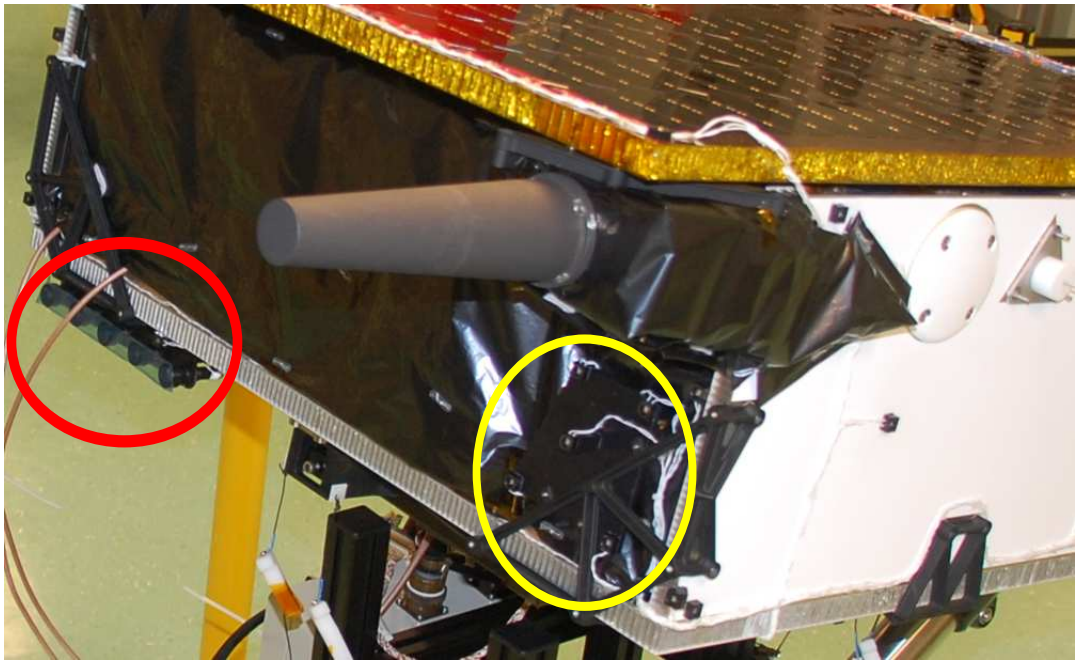

Figure 3.7. *Final Approach and Recede side of the Target satellite (-Y panel). The LED docking panel is marked with yellow and the collimator bracket is marked with red.*

CHU is aligned with the Docking Pattern, the FR CHU will be aligned with the center collimated LED beam when Main is rotated accordingly.

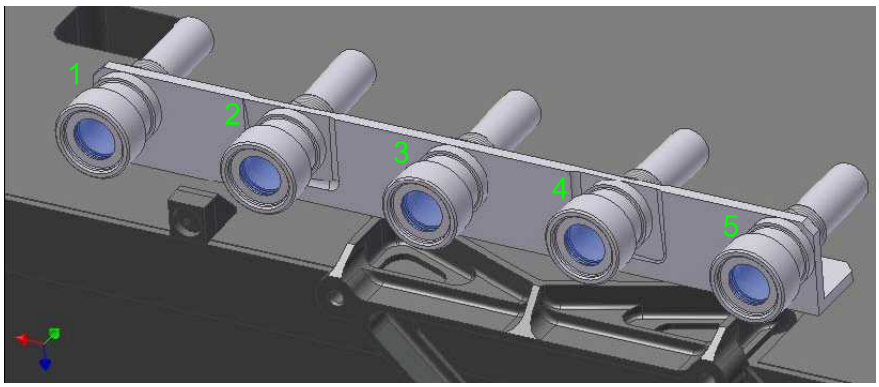

Figure 3.8. *Collimator L-bracket as mounted on Target satellite.*

In order to define a search area for the collimated beams, the second and fourth collimator tubes are angled such that they point inwards the center collimator and respectively upwards and downwards. At a distance of 2 meters the placement of the collimated beams will be located in a pattern as shown in Figure 3.9, creating a search area for the FR camera at this distance.

Each collimator will provide a star pattern of 9 to 10 stars and will be detected as the image given in Figure 3.10. By having the different star pat-

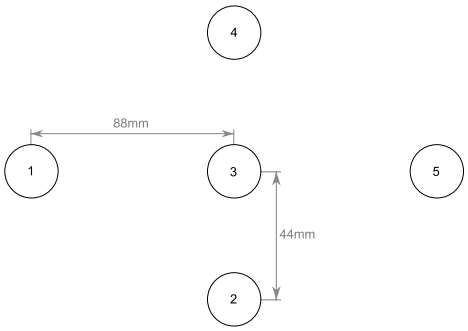

Figure 3.9. *Placement of collimator beams at a distance of 2 meters.*

terns from the collimators included in the star catalogue of the μDPU, enables pointing towards the collimator to be determined.

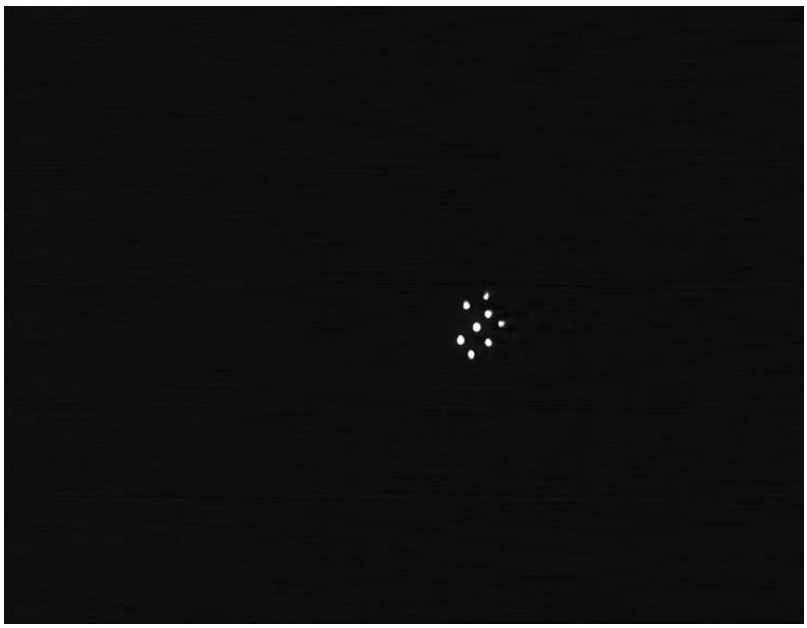

Figure 3.10. *Tractor beam detected from PRISMA FM Collimator II by FM FR CHU.*

Due to the limited manoeuvrability of the two FM satellites, Main and Target, detection of the collimator beams from Target to Main was not accomplished during the integration and verification campaigns of the VBS system at SSC. Though, calibration images have been taken of the FM L-bracket which will be used to create a user-defined star catalog which will be uploaded to the PRISMA satellites during the mission. Since the search for the collimator tractor beams is not seen as a standard manoeuvre of the VBS system, the routine for detecting the collimator beams is not included in the automatic algorithm control of the VBS system.

3.1.6 LED Placement

The LEDs are placed on the Target spacecraft by hand based on coordinates given in the Target reference frame. Due to the fact that the LEDs have axial symmetry of the light emitted, the rotations around their individual boresights are based on the ease of harness layout on the spacecraft. Therefore, the final mounting was performed by SSC.

Two different mechanical interfaces for the LED housings exist. First is based on the housing having the bottom surface glued directly to the surface of the spacecraft. The center of the mounting interface is here defined as the center of the housing surface touching the spacecraft. This mounting type is illustrated in Figure 3.11.

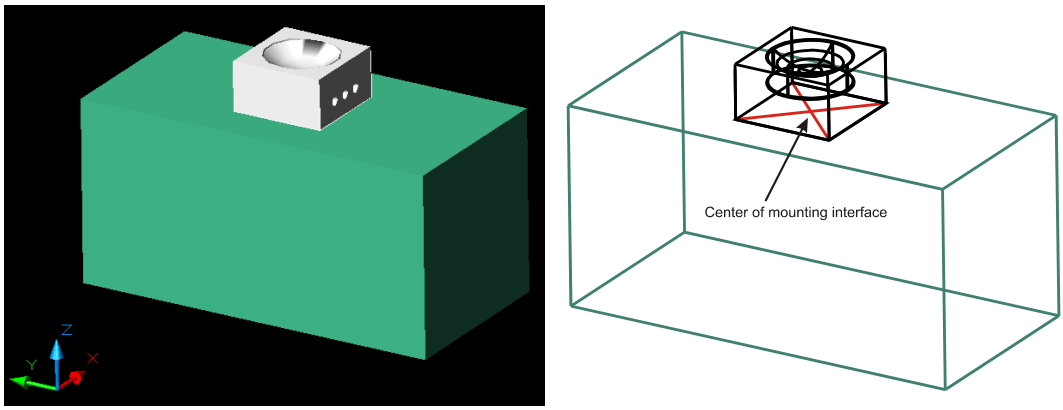

Figure 3.11. *Mounting of LED housings directly mounted to the spacecraft.*

The second mounting type includes an angle bracket, where the LED housing is mounted on the angle bracket and thereafter is the angle bracket mounted on the spacecraft. This mounting type is used in situations where direct mounting on the top surface of the spacecraft is unfeasible, but stable side panels are available as mounting surfaces. When placing the angle brackets on the spacecraft the LED housing shall be free of the spacecraft structure, which gives that the bottom of the LED housing and the top of the spacecraft surface is planar. The angle bracket mounting is illustrated in Figure 3.12.

The lens element and housing are designed such that it will provide an evenly distributed light cone of 60 degrees around boresight. This gives an undisrupted overlapping from panel to panel, including rotations directly over the corners. The overlapping is discussed in Section 3.1.3, where Figure 3.5 illustrates how 60 degrees cones overlap each other in the corners.

Each of the six panels on the spacecraft have five LEDs placed in same plane and in unique patterns from panel to panel. The final positions of all the LEDs and the docking pattern are given in [Benn2009b] which are illustrated in Appendix D.

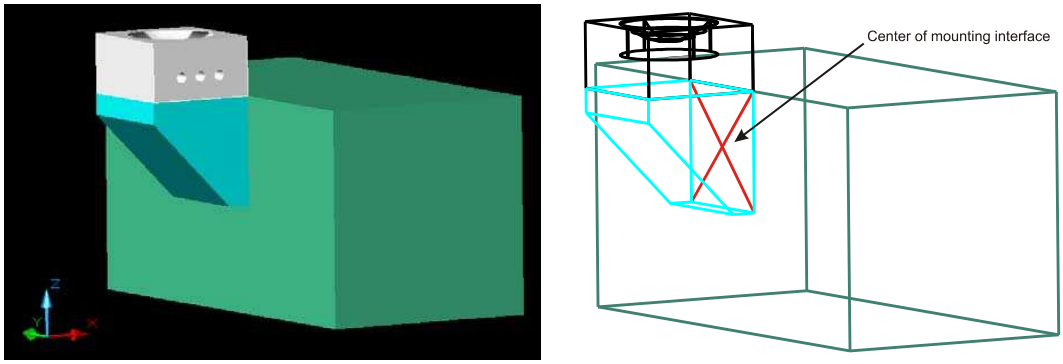

Figure 3.12. *Mounting of LED housings mounted on an angle bracket and then to the spacecraft.*

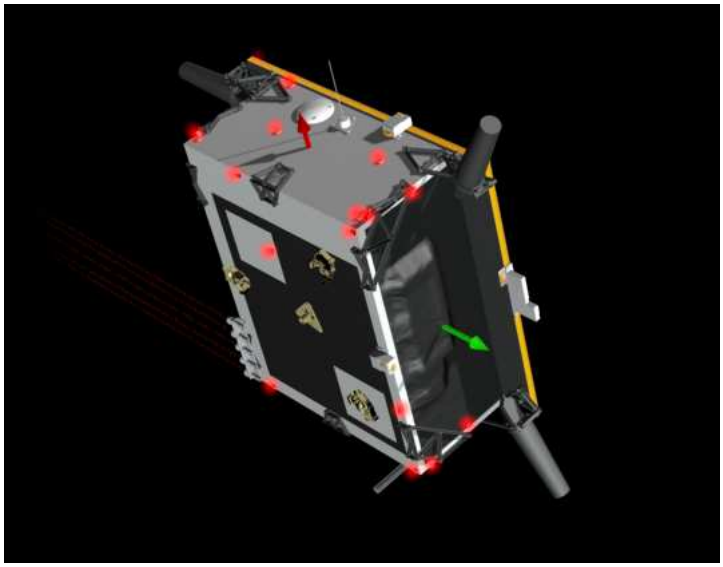

Figure 3.13. *Animated view of Target with visible LEDs.*

3.1.7 LED Powering

The total of 40 LEDs comprising the cooperative feature points and tractor beams of the Target spacecraft are wired in strings of eight. Each string is routed such that if one LED fails, only one panel or the fifth redundant on all panels are lost. This design interfaced with the LED powering circuit as designed by the SSC.

The LED powering is operated in pulses utilizing a voltage limited supply and has the following specifications:

Pulse rising edge: Synchronous with 1-PPS rising edge (camera integration locked).

Pulse duration: Standard 5ms, with commandable variations from 1ms to 31ms in steps of 1ms.

Current (pr. LED): Normal at 180mA, minimum 120mA.

Frequency: 1Hz.

The synchronization between the LED blinking on Target and the camera integration on Main is discussed in Section 3.2.1.

3.2 CHU Design

The Camera Head Unit (CHU) of the μASC is originally designed for the purpose of detecting stars on the starry sky, and is therefore extremely light sensitive together with a focus set to infinity. Due to the fact that the VBS system is desired to work out from distances where Target is as faint as a mv7 star in magnitude and into close-up between the two satellites. This required an extended dynamic range for the CHU in order to cope with the scenarios where Target reflects enough light to blind the CHU.

Additionally, the SR CHU shall be able to distinguish the cooperative feature points on the Target spacecraft from the rest of the structure.

This section describes the modifications needed in order to address the two mentioned issues.

3.2.1 Shutter Control

In order to extend the dynamic range of detection levels for both the SR and FR CHU an electronic shutter circuit was developed for each of their CHUs.

At time of development the flight unit of the μASC DPU was already delivered to SSC for integration on the Main satellite. Therefore, all hardware changes were limited to the CHU electronic, including control lines from the DPU.

In order to electronically control the integration time of a CCD, two methods can be used. One method utilize the speed of which the CCD timing signals are running to control how fast each image is read from the detection layer to the read-out layer, where the second method utilizes the clearing of the substrate of the detection diodes which clears out the detection layer [Janesick2001]. Since the CHU control is running at fixed clock speeds set by the DPU the first method can not be realized. The second method only involves an extra control to the CCD and its timing generator which both is placed in the CHU, enabling realization of a shutter.

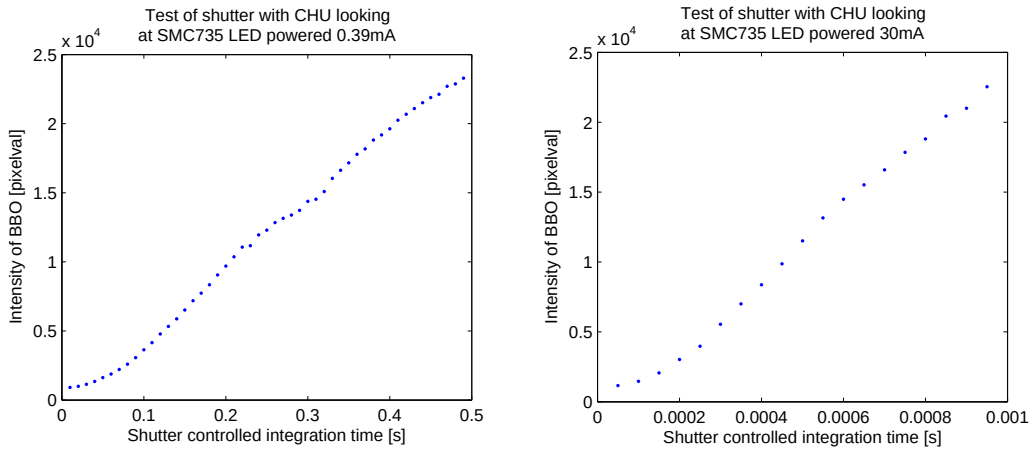

Figure 3.14. *Verification of camera shutter system. The graphs illustrate the integration time vs. the brightness of the detected Big-Bright Object. Left going from full integration and downwards on a faint low-powered LED. Right going from 1ms and downwards on a bright high-powered LED.*

A thorough analysis of the CCD timing signals provided an overview of the different trigger signal, especially the two signal denoted XSG1 and XSG2 which controls the dispatching of the detection layer to the read-out layer, and thereby setting the end-of-integration (EOI). The timing overview is given in Appendix E.

The electronic shutter is implemented such that a micro-controller is placed inside the CHU, sniffing the control lines from the DPU to the CCD timing generator, and through these acquire information of when to clear the substrate (i.e. set start-of-integration). Thereby, the integration time can be controlled from the DPU, only by modifying the software that handles the CCD control lines.

The shutter implementation has thereby been verified on the full system by letting the CHU view at a constant powered LED and note the detected intensity level versus integration time. This data is presented in Figure 3.14, illustrating correct behavior of the implementation method.

The shutter control software implemented in the DPU is designed such that the integration period can be synchronized with the LED blinking, realized by feeding a PPS signal to both systems. The synchronization of the two systems and its verification are descirbed later in Section 5.2.4.

3.2.2 Lens System

As described in Section 2.1 the FR CHU shall be able to detect stars in coherence with the Target satellite, giving that no lens modifications are needed from the standard design.

Though, from the description in Section 2.1 it is given that modifications to the SR CHU are needed. This is due to the fact that the incoming light needs to be limited around the LEDs in order to provide a significant signal-to-noise ratio (SNR) for enabling correct detection. Additionally, the focus point has to be adjusted for close range operations.

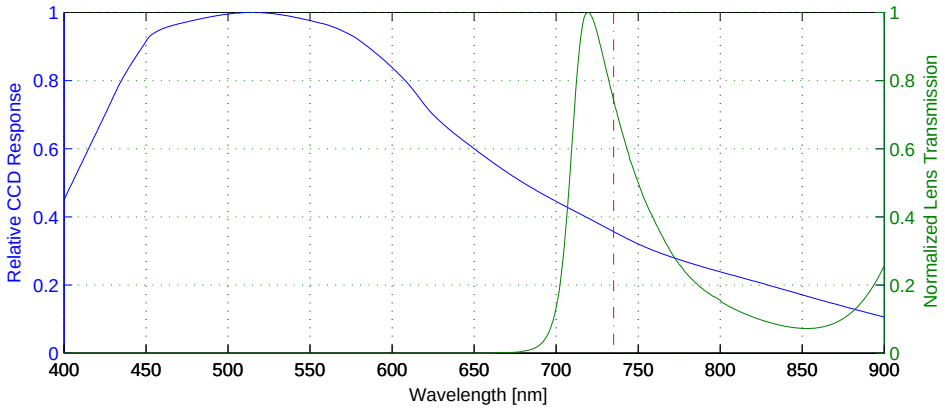

Figure 3.15. *Spectral sensitivity characteristics of the CCD used in the μASC (Information provided by SIG - DTU Space) together with normalized SR lens transmission spectrum from measurements.*

It was desired to design a band-pass filtering of the SR CHU lens system, such that the wavelength of the LED would pass through, rejecting the unwanted background light reflected from Target. Based on the theoretical VBS SR performance analysis given in [Joergensen2008] the width of the band-pass filter was designed for ±30nm around the peak wavelength of the SMC735 at 735nm. The final lens transmission profile resulted in the band-pass seen in Figure 3.15 which had a lower red-stop limit than anticipated, which is believed to be caused by the natural IR stop given in quartz [Soda1961].

In figure 3.15 is given both the lens and the CCD response in relation to the wavelength of the light. The combined lens transmission and CCD response is given in Figure 3.16, illustrating that the response for the peak wavelength is at $\sim$ 66% of the full response. Revision of the performance analysis [Joergensen2008] showed that these values lie within the margins.

In Appendix B is given a later characterization of the SMC735 and how they perform at different ambient temperatures and powering methods. The results from this characterization are plotted into Figure 3.17, where the PT100 temperature sensor has measured the structure of which the LED has been placed. It is seen that at increasing temperatures the peak wavelength of the emitted light also increases, thus shifting the output to wavelengths with less than 50% responsiveness for the CCD and lens system.

Based on the temperature information given in Section 3.1.1, the change in peak wavelength can be an issue for the LEDs placed on the solar panel.

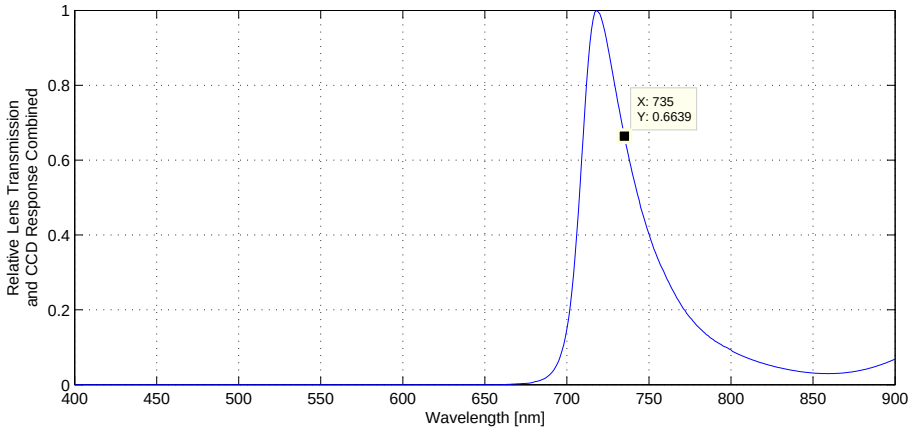

Figure 3.16. *Relative lens transmission and CCD response combined. Peak wavelength of LED is marked.*

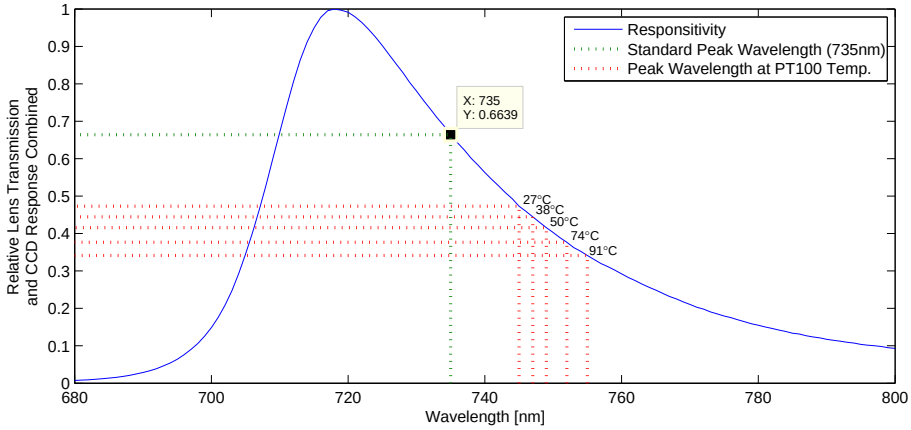

Figure 3.17. *Relative lens transmission and CCD response combined. The green line indicates the point of the defined peak wavelength of the LED. The red lines are the readings of the PT100 element from the test described in Appendix B*

Whereas the rest of the structure is varying with a few degrees around 0°C, and the pulse-powering of the LEDs, provide a stable wavelength close to the peak of 735nm, enabling detection by the SR CHU. This has been verified using the Engineering Model of the flight system and is described later in Chapter 5.

Figure 3.18. *The coated Short Range lens is giving a blue shine due to the red-pass filter.*

3.3 Summary

In order to extend the μASC system with VBS functionality, additional hardware and hardware modifications are necessary. This chapter has described the design and functionality of the support hardware for enabling a cooperative Target, namely the LEDs providing detectable feature points. Additionally, the needed design modifications of the standard CHU system has been described. Both with respect to realizing a FR CHU, by adding shutter capabilities, and with respect to realizing a SR CHU, by adding shutter capabilities and a modified lens system.

Chapter 4

Far Range

This chapter deals with the Far Range mode by describing the scenario regarding orbit and the interactions in between the Main and Target spacecraft. Analysis of the scenario will be followed by description of solution implementation into the VBS system on the μASC and the on-ground verification methods used for characterization of the FR performance.

4.1 Scenario for Far Range Mode

The Far Range mode is defined by the scenario where stars are detectable in the background in conjunction with the Target satellite. This enables the CHU to determine the boresight attitude based on the stars, while detecting Target as a non-stellar object in the FOV.

During the Far Range mode it is desired to determine which of the visible objects seen by the FR CHU represents the Target. Following the requirements given in Section 1.2.1 the distance between Main and Target can vary between 500m to 1000km for the FR mode if the light conditions allow this.

During this section a pinhole representation will be used in order to describe the geometric aspects of the system. This pinhole model is depicted in Figure 4.1. (x, y, z) coordinates represents a point in the camera coordinate system and (x', y') coordinates represent the projected point into a CCD plane at a distance of f from the pinhole.

Two CCD planes are placed in the figure where the real CCD plane is placed in the negative direction of z, but to simplify calculations and for keeping monotonous definition throughout the report the CCD plane is placed in the positive direction of z resulting in projection of (x, y, z) coordinates into similar signed (x', y') coordinates.

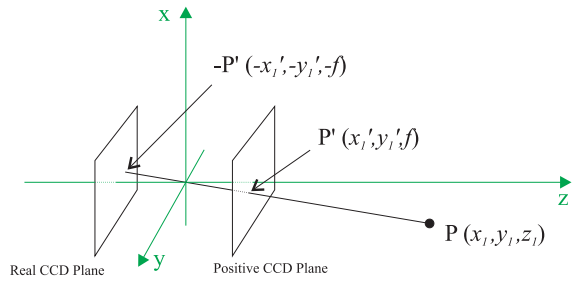

Figure 4.1. *Projection geometry of pinhole camera assuming pinhole is placed at* $(0, 0, 0)$ *with boresight pointing in the direction of z-axis. The focal length of the camera is denoted f.*

Using this camera model the projected coordinates of a point P can be calculated as follows:

$$x_1' = x_1 \cdot \frac{f}{z_1}, \; y_1' = y_1 \cdot \frac{f}{z_1} \tag{4.1}$$

where:
f: describes the focal length of the camera, i.e. the distance from the pinhole to the CCD plane.
x_1, y_1, z_1: describes the coordinates of the point P.
x_1', y_1' describes the projected coordinates on the CCD.

Based on the simplified pinhole model of the CHU, it has been estimated that the detected size of Target in FR mode is approximately 5 pixels, i.e. the Target will be detected as a centroid by the μASC system [Benn2007]. The FR mode of the VBS is therefore based on the centroids detected by the μASC.

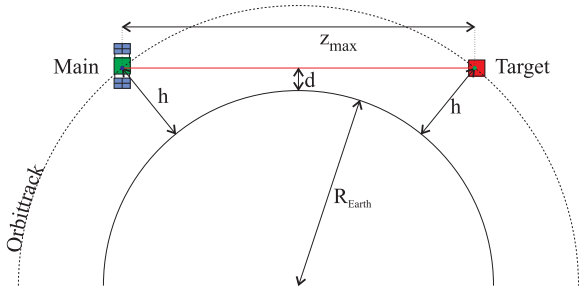

Figure 4.2. *Line of sight between Main and Target at maximum length.*

When the PRISMA satellites are orbiting the Earth, Main will chase Target, following the orbit trajectory of Target.

The chasing is illustrated in Figure 4.2 where the line-of-sight between Main and Target is shown with a red line, indicating the maximum distance z_{max} where Target is detectable by Main. Since the atmosphere of the Earth

will cause deflection of the actual position of Target detected by Main due to the refraction of the light, the lowest allowed limit of d is set to be above the atmosphere at a 100km where the atmosphere density is adequately low [Fortescue2003]. The longest allowable distance is determined using Pythagoras' theorem as follows:

$$(R_{Earth} + d)^2 + \left(\frac{z_{max}}{2}\right)^2 = (R_{Earth} + h)^2 \tag{4.2}$$

$$\Rightarrow z_{max} = 5.704 \cdot 10^6 \text{m} \tag{4.3}$$

where:
$h = 700 \cdot 10^3$m: denotes spacecraft altitude as described in Section 1.2.1.
$d = 100 \cdot 10^3$m: describes the thickness of the earths atmosphere [Fortescue2003].

This distance is above the limits stated in the requirements for the Far Range mode defined in Section 1.2.1 to be 1000km, meaning that Target will be in line of sight at all time when inside FOV of the Far Range CHU. Due to the fact that when the Earth is in FOV its albedo can over-bloom the CCD, making Target undetectable, it is assumed that the Far Range CHU is pointing in such a manner that the Earth is outside the FOV, i.e. shaded by the baffle system.

In [Benn2007] is described how two Earth orbiting satellites with similar orbit parameters can detect one another based on line-of-sight. The concept is, that based on the angular velocity in reference to the inertial coordinate frame, the Target will move at a certain band-gap given by the orbital parameters of both Main and Target.

This pointing and circular movement is illustrated in Figure 4.3.

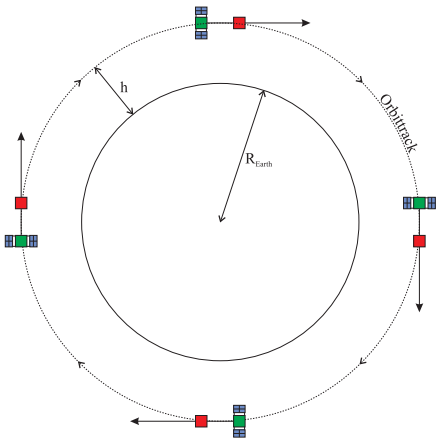

Figure 4.3. *Illustration of pointing direction of Main and Target during one orbit.*

In order to determine the angular velocity of the Target object, it is desired to determine the moving speed of the satellites for the current orbit. Based on the altitude information given in Section 1.2.1 the mean value is set to $h = 770$km and by assuming an eccentricity of $e = 0.0$, the moving speed of the satellites can be estimated by using the Keplarian equations for an elliptical LEO [Fortescue2003, Hansen2004b, Wertz2002]:

$$v = \sqrt{\frac{\mu}{r} \cdot (1 + e \cdot \cos(\theta))} = \sqrt{\frac{\mu}{r}} \tag{4.4}$$

where:
μ: describes the gravitational parameter.
r: describes orbital separation. Here given as $r = R_{Earth} + h$.
e: describes the eccentricity, which determines how elongated the orbit ellipse is. Circular orbit assumed $\Rightarrow e = 0.0$.

Thereby the angular velocity, ω, can be determined from the following expression:

$$\omega = \frac{d\theta}{dT} = \frac{360^\circ}{\left(\frac{2\pi \cdot r}{v}\right)} = \frac{360^\circ \sqrt{(\mu)}}{2\pi \cdot r\sqrt{(r)}} = 59.86 \cdot 10^{-3} \tfrac{^\circ}{\mathrm{s}} = 215.5 \tfrac{''}{\mathrm{s}} \tag{4.5}$$

The Target will then appear as an object moving within a certain angular velocity bandpass around the value determined in Equation (4.5) and can thereby be pointed out. Detection of objects with this value of movement with respect to the background is detectable using the μASC due to its abilities of determining centroid positioning down to subarcsecond accuracy.

4.2 Implementation

The Far Range VBS mode function as the main mode of the FR CHU, mainly due to the fact that the highest level of precision can be obtained when Target is detected in coherence with the starry background, i.e. the FR CHU is capable of determining its attitude pointing.

When the attitude pointing can not be determined, usually due to Target blinding the CHU and thereby forcing the camera shutter downwards, the Intermediate Range VBS mode is called instead. This mode-switching behavior is illustrated in Figure 4.4, which gives that the IR mode is a fallback mode for the FR mode.

The input for the FR mode given by the μASC consists of the following elements:

- Timestamp.

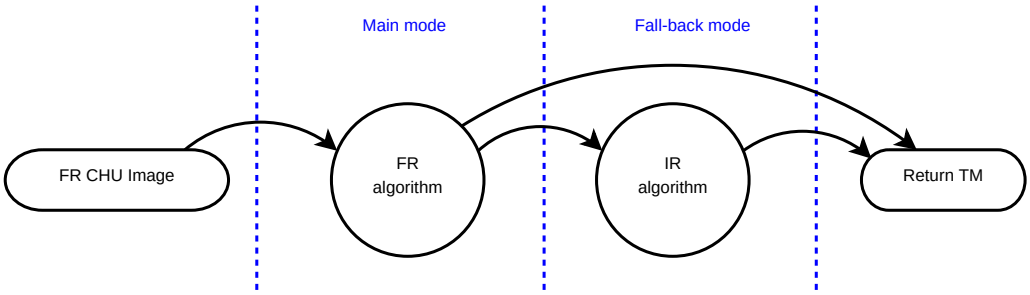

Figure 4.4. *Mode diagram for the Far Range CHU.*

- Attitude pointing.
- Non-stellar objects (NSO).
- Big-bright-object (BBO) information

The timestamp is given as the Center of Integration (COI) of the image for which the attitude and centroiding information is based upon, where the adjustable shutter time has been taken into account. Due to this implemented electronic shutter in the CHU, the sampling period of centroid data is not occurring with a fixed frequency, given that all comparison with previous data needs to be aligned with the timestamp.

The attitude pointing is based on the centroids recognized as stars. therefore, only non-stellar objects are forwarded to the VBS system, from where the Target candidate needs to be located.

Additionally, if any BBO is detected in the FOV, data such as width, height and position are forwarded to the VBS system as well.

From each centroid in the NSO list a unit vector describing the pointing of the object can be determined. Centroid representation in unit vectors will describe each object as a point on a unit sphere of the CHU in reference to the inertial coordinate system, simplifying angle calculations and attitude determination due to the fact that the angle between two vectors can be determined using the dot product definition [Adams2006]:

$$\vec{u} \bullet \vec{v} = |\vec{u}| \cdot |\vec{v}| \cdot \cos\theta = u_1 v_1 + u_2 v_2 + u_3 v_3 \tag{4.6}$$

where:
θ: describes the angle between the two vectors.
$\vec{u}$, $\vec{v}$: are vectors in a xyz-coordinate system where subscript 123 respectively denotes the xyz elements.

Using unit vector representation of the centroids reduces Equation (4.6) to determine the angle θ to the following:

$$\theta = \arccos\left(\vec{u} \bullet \vec{v}\right) = \arccos\left(u_1 v_1 + u_2 v_2 + u_3 v_3\right) \tag{4.7}$$

From the information provided in two consecutive NSO lists, the following data can then be calculated:

- $\boldsymbol{\omega}$ - describing the angular velocity between two centroids in each their list
- **Direction** - indicating the direction of which the rotation was performed

By having the bandpass of the Target movement[1], the centroid candidates can be picked, and a result list will be at hand whenever all centroids in two NSO lists have been compared. This result list, containing timestamp, xyz-coordinates of the centroid, angular velocity and direction, can then be compared to subsequent NSO lists provided.

Knowing the timespan, the angular velocity and turning direction the xyz pointing can be predicted, telling the expected pointing of subsequent centroids. Due to noise influence from different sources such as precision in centroiding, uniformity of reflected light from Target and variations in between the two orbit trajectories a deviation between the predicted pointing and the pointing of potential centroids in following NSO lists is applied. This deviation is referred to as the Search Area around the predicted pointing, and if the pointing of a centroid in the subsequent NSO lists lies within the threshold limited by the Search Area, the centroid can be linked to the record in the result list.

This filtering is described in greater details in [Benn2007].

The xyz pointing unit vector is determined using Equation (4.8), where the projection geometry used is described in Figure 4.1.

$$\begin{bmatrix} x_{unit} \\ y_{unit} \\ z_{unit} \end{bmatrix} = \frac{1}{F} \begin{bmatrix} x_{ccd} \\ y_{ccd} \\ f \end{bmatrix} \tag{4.8}$$

where:
$x_{unit}, y_{unit}, z_{unit}$: describes the xyz pointing unit vector.
x_{ccd}, y_{ccd}: describes the point on the CCD plane.
f: describes the focal length.
F: describes the distance from the pinhole center $(0, 0, 0)$ to the point on the CCD plane, defined by $F = \sqrt{x_{ccd}^2 + y_{ccd}^2 + f^2}$.

Determination of the angle between the two vectors has already been described using Equation (4.7), which can be used to determine the angular velocity. The equation for calculating the angular velocity is then given by:

[1] The bandpass of Target movement is discussed in Section 4.1

$$\omega = \frac{d\theta}{dT} \tag{4.9}$$

where:
$d\theta$: is the moved angle calculated using Equation (4.7).
dT: is the timespan defined by the difference in the two timestamps.

The direction of rotation is described by a second xyz unit vector with similar reference to the inertial reference system. The rotation of a pointing vector can therefore be rotated around such a direction rotation vector in an angle corresponding to θ. This vector has to be perpendicular to the two pointing vectors creating the examined angle, leading to the use of the cross-product between the two vectors which is defined for two vectors in $\mathbb{R}^3$ [Adams2006]. The rotation unit vector is determined using the following equation:

$$\vec{d} = \frac{\vec{u} \times \vec{v}}{|\vec{u} \times \vec{v}|} = \frac{1}{\sqrt{(u_2v_3 - u_3v_2)^2 + (u_3v_1 - u_1v_3)^2 + (u_1v_2 - u_2v_1)^2}} \cdot \begin{bmatrix} u_2v_3 - u_3v_2 \\ u_3v_1 - u_1v_3 \\ u_1v_2 - u_2v_1 \end{bmatrix} \tag{4.10}$$

where:
$\vec{u}$, $\vec{v}$: is vectors in a xyz-coordinate system where subscript $_{1,2,3}$ respectively denotes the xyz elements.
$\vec{d}$: describes the rotation direction vector.

The reason for unifying the rotation vector lies in its further use. In order to predict future points it is desired to rotate the latest used pointing vector an angle corresponding to $\alpha = \omega \cdot dT$ around the rotation direction vector. It is defined that any set of successive rotations using rotation matrices, can be replaced by a single equivalent rotation matrix [Baker2007]. Thus a rotation of α degrees around a unit vector can be performed using a rotation matrix performing a right-hand rotation, which is defined as follows:

$$\underline{\underline{R}} = \begin{bmatrix} 1 + (1-c)(d_x^2 - 1) & -d_z s + (1-c)d_x d_y & d_y s + (1-c)d_x d_z \\ d_z s + (1-c)d_x d_y & 1 + (1-c)(d_y^2 - 1) & -d_x s + (1-c)d_y d_z \\ -d_y s + (1-c)d_x d_z & d_x s + (1-c)d_y d_z & 1 + (1-c)(d_z^2 - 1) \end{bmatrix} \tag{4.11}$$

where:
c, s: describes $\cos\alpha$ and $\sin\alpha$, respectively.

If the rotation direction vector is not unified a scaling will occur as well, which is undesired. Using this rotation matrix, the predicted point can be expressed as:

$$\vec{p} = \underline{\underline{R}}\ \vec{u} \tag{4.12}$$

where:
$\vec{p}$: denotes the expected direction to the following point.

Figure 4.5 illustrates the rotation performed on the $\vec{u}$ vector around the $\vec{d}$ vector in the $\mathbb{R}^3$ environment.

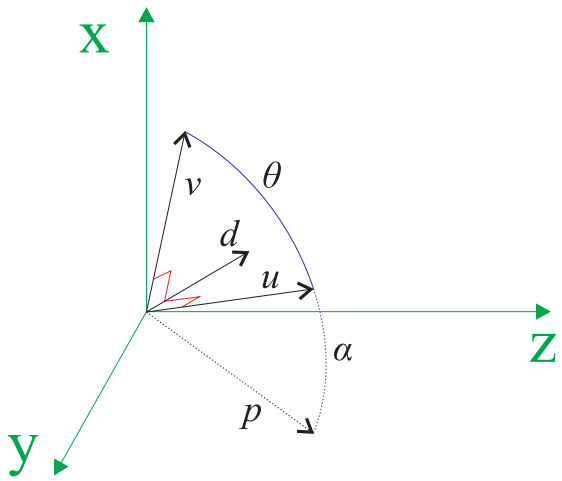

Figure 4.5. *Vector rotation description in the $\mathbb{R}^3$ space.*

The entire unit pointing and prediction system has been implemented in the μASC DPU, written in the C-syntax used for the software compilation. Clear restrictions and interfaces between the standard startracker software and the VBS software, have been handled during the software development and implementation. Thus a stable solution is provide which does not influence the high-priority startracker routines to be executed.

The dataflow for the FR mode internal to the VBS system is depicted in Figure 4.6, illustrating the input information of the algorithms, the internal processing, and the output information in conjunction with needed history information for subsequent executions.

The "Result History" contains information about the average angular velocity for all objects following the bandpass limits, average pointing vectors towards the objects, link history of the objects, average rotation vectors describing the movement of the linked object and last the timestamp representing the saved elements.

Combining this data with the timestamp received at the next execution of the FR algorithms, the expected pointing of all objects in the "Results History" can be predicted using Equation 4.12, and thereby compared to the list of current NSOs at the following execution.

The total output information from the μASC during FR VBS mode is as described in Figure 2.6.

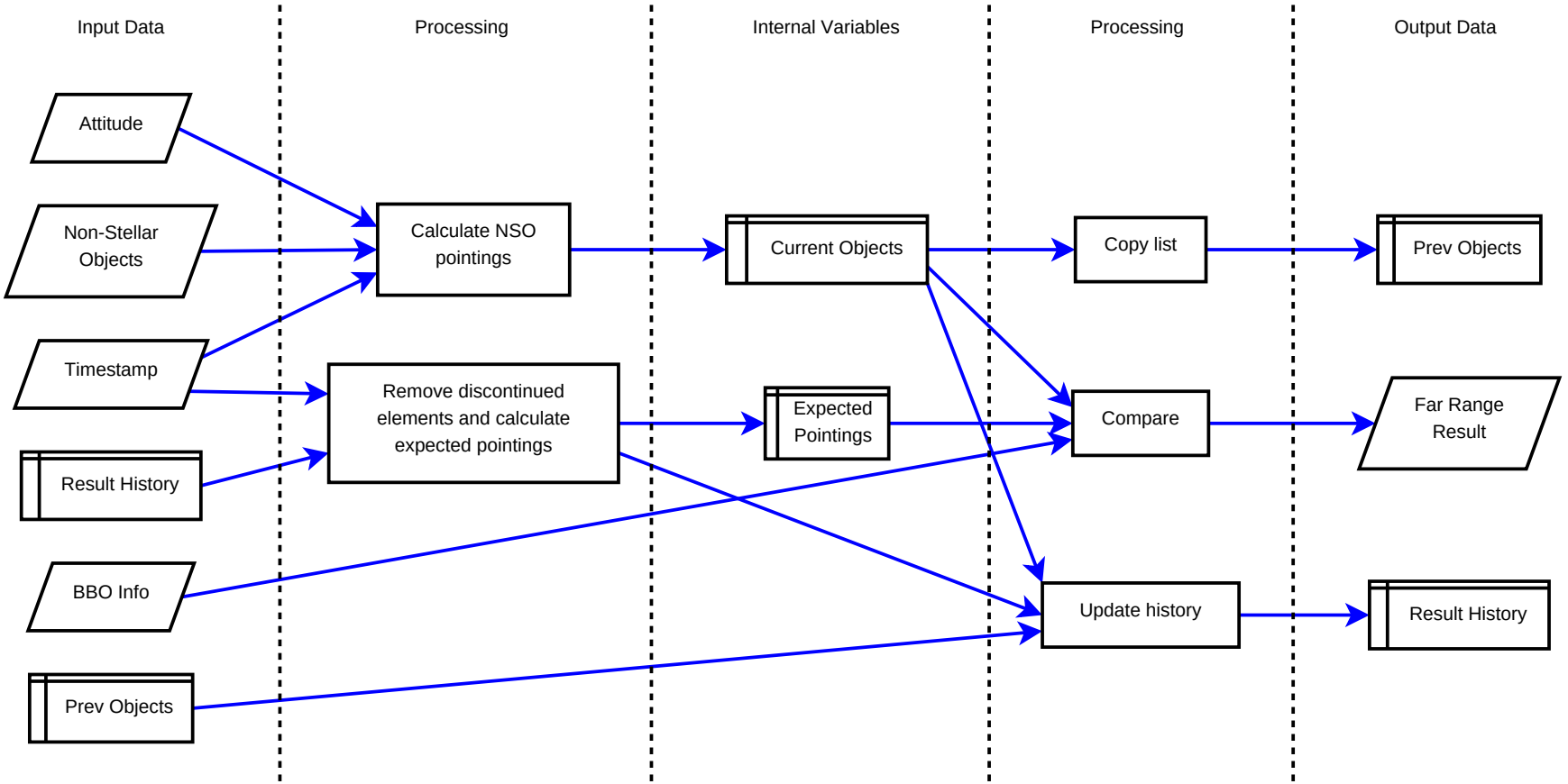

Figure 4.6. *Data flow structure for the Far Range mode algorithm.*

4.3 Verification

Varies methods have been used in order to verify the functionality of the VBS Far Range mode. This section describes the different verification methods and test setups developed for test and integration of the FR mode.

4.3.1 Pharos Module

Based on the description in Section 4.1 of the Far Range mode and its field of operation, it is given that two constraints are needed for the VBS system to provide a FR VBS solution: Namely, the FR CHU needs to be able to detect stars for attitude determination, and a non-stellar object needs to move inside the velocity bandgap relative to the stars.

During normal laboratory tests of the μASC system, a star field stimulator (SFS) is used in front of the CHU, providing imaginary stars based on collimated LED patterns. Based on the star pattern, the μASC is able to determine an attitude pointing of the CHU.

PhD student A. Massaro, DTU Space, has modified such a star field stimulator to enable an additional controllable moving "star", using an additional collimated LED with a piezo-motor controlled mirror system in front [Massaro2010a].

The Pharos module is pictured in Figure 4.7.

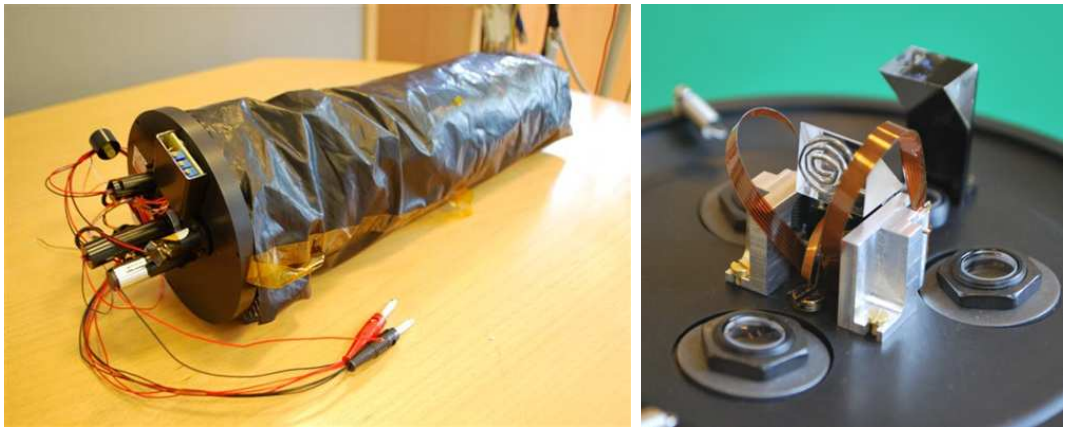

Figure 4.7. *The Pharos module. To the left is the module mounted on the darkened plexiglas tube. To the left is a close-up of the Pharos interior, including the motor-controlled mirror system. (Image: [Massaro2010b]).*

During operation of the Pharos module, centroids detected by the FR CHU is as illustrated in Figure 4.8.

The SFS consists of nine "stars" placed in groups of three which are shown in the periphery of the illustrated CCD area. These stars are used by the μASC to determine an attitude pointing of the FR CHU. Likewise, the moving "Target" centroid is seen in the middle of the CCD area, performing a linear movement with a fixed speed relative to the stationary stars.

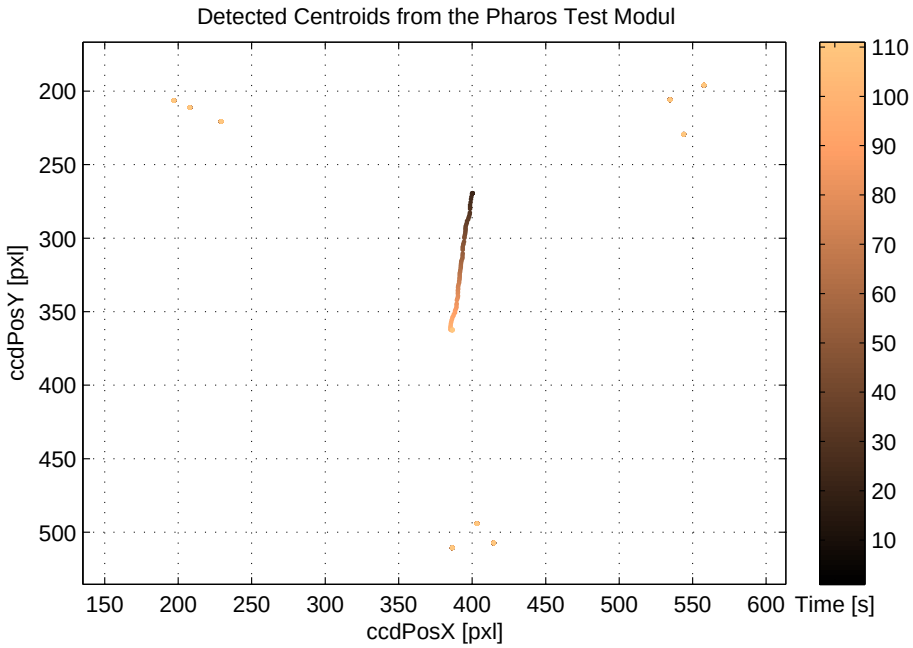

Figure 4.8. *Detected centroids from the Pharos module. The nine stationary "stars" are seen in the periphery, and the moving "Target" is seen as the centroid sequence in the middle. (Data: [Massaro2010b])*

The centroids presented in Figure 4.8 are fed to the VBS system, from where the Target centroid is pointed out as a linked object. In Figure 4.9 illustrates the links established of the detected centroids.

The Target centroid is moving in downwards direction, from where it is seen that three to five centroids are needed in order to commence determination of links, just as described in Section 4.2.

This correct linking is used to deduce correct behavior of the VBS system on the given scenario.

The Pharos module has been used both during software development and integration, as well as verification of the FM VBS system as mounted on the PRISMA satellites.

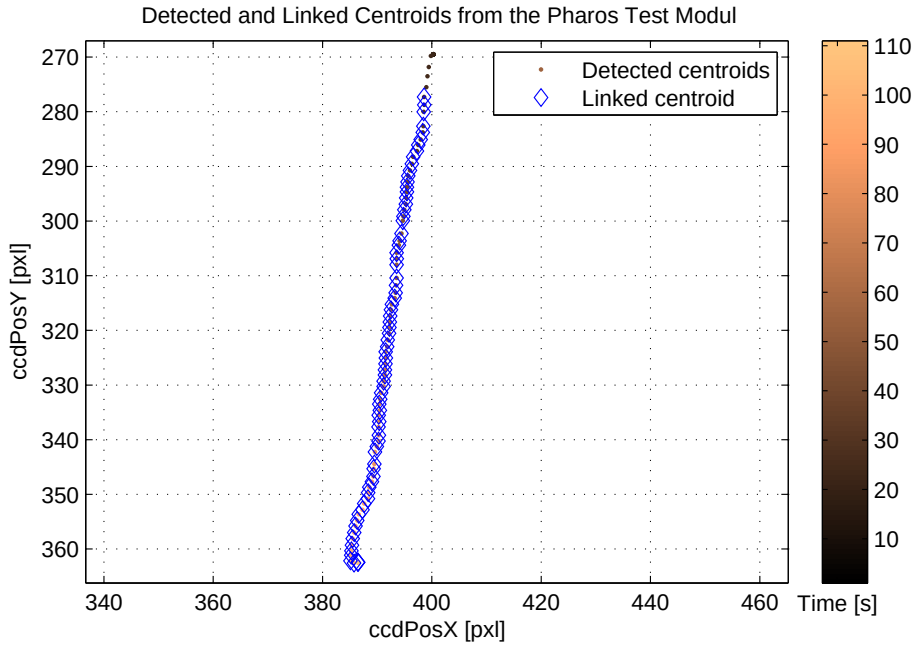

Figure 4.9. *Linked centroids of the Pharos module from the data presented in Figure 4.8. (Data: [Massaro2010b])*

4.3.2 Real Sky Verification - Seeded Target

It was desired to qualify the FR mode on the real night-sky in order to have a more realistic scenario. In order to realize a setup with a controllable light source moving with a certain speed, a LED has been put on a black-covered linear guider. Having the boresight of the FR CHU pointing upwards and the linear guider placed over it, the FR CHU can see the LED while having the starry sky in the background. This test setup is illustrated in Figure 4.10.

The test setup showed instabilities in windy weather resulting in only linear movements for short periods. Even though, the VBS system shows good performance since it is clearly able to point out the moving Target as soon as a linear movement is detected in the centroids for more than three frames. In Figure 4.11 is the output from the VBS system illustrated in coordination with the detected centroids. It is seen that three subsequent centroids creates the link of the moving object and lock on to this until it differs from the predicted moving path. Furthermore, from the sequence 39 to 44 it is seen that no Target lock is achieved due to the irregular movements of the centroids.

By stabilizing the test setup additionally, tests for the FR and IR switching could proceed. The test had its main focus on the mode switching between the FR and IR modes, wherefore the results are discussed further in Section 6.1.

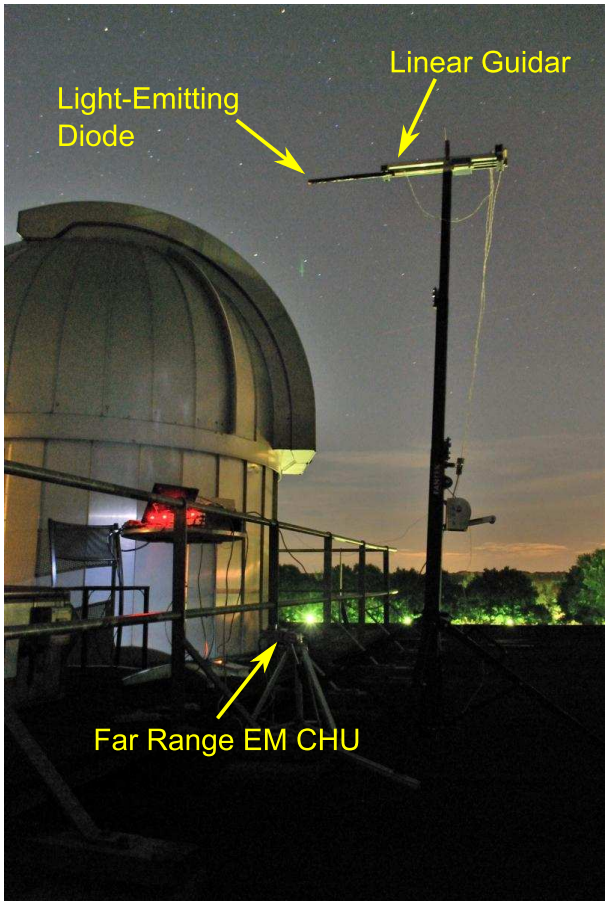

Figure 4.10. *Test setup for the FR-IR testing on the real night sky.*

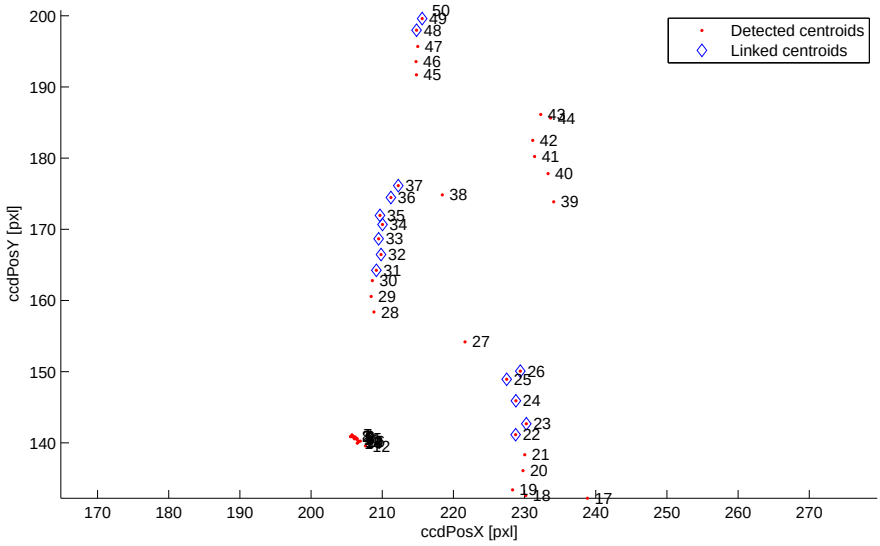

Figure 4.11. *Results from the Far Range VBS with a controllable moving Target. The numbers illustrate the sequence of detection of the centroids.*

4.3.3 Real Sky Verification - Satellite Tracking

In order to verify the FR VBS algorithms on an orbit-like scenario with the starry sky in the background, the VBS system was tested on image data captured from ground of Low Earth Orbiting satellites. The data was captured from Hawaii, which enables viewing of stars close to the horizon. By knowing the trajectory of bright satellites, a standard startracker CHU was set to capture the image data of the detected centroids when pointing certain directions. The system captured all detected centroids, and not only the Non-Stellar Objects which are usually used for input to the VBS system.

Two satellites of interest were found crossing each others paths in almost same time span. These were:

A: Cosmos 1980 Rocket with a magnitude of 4.4 in brightness.

B: Cosmos 2227 Rocket with a magnitude of 3.4 in brightness

The predicted trajectories were found using Heavens Above, and is illustrated in Figure 4.12 for the two referred satellites.

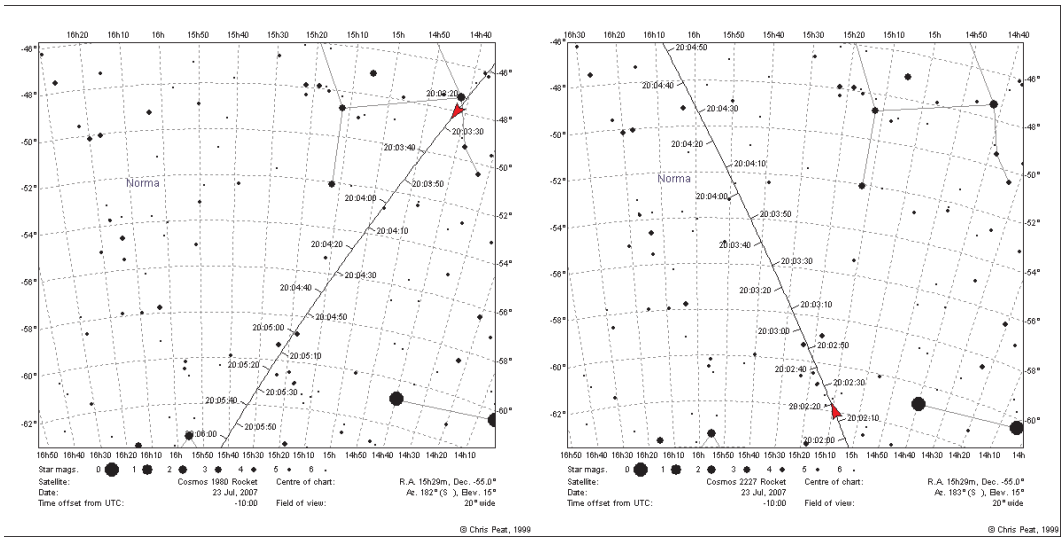

Figure 4.12. *Prediction trajectories from HeavensAbove. Left image is for satellite A and right image is for satellite B.*

Feeding the captured centroid files to the FR VBS system, the algorithms were capable of linking the movement of two simultaneously visible objects separately, the result of which are plotted in Figure 4.13 together with all detected centroids. It is seen that other linking occurred, which in several cases are due to the distance between stars can match the search bandpass for angular velocities, creating additional linked objects. These false links are

though lost very fast, clearing its propagation history and marking it as a weak link. Due to the fact that the μASC is capable of filtering out centroids recognized as stars, thus only providing NSO lists, links created from stars are not considered as a problem.

In order to visually compare Figure 4.12 with Figure 4.13, the movement direction of the stars can be said to follow the lines of Declination in the grid.

The VBS system was not executed directly during capturing of the datasets, but the gathered data files have subsequently been fed to the VBS system in order to verify the algorithms.

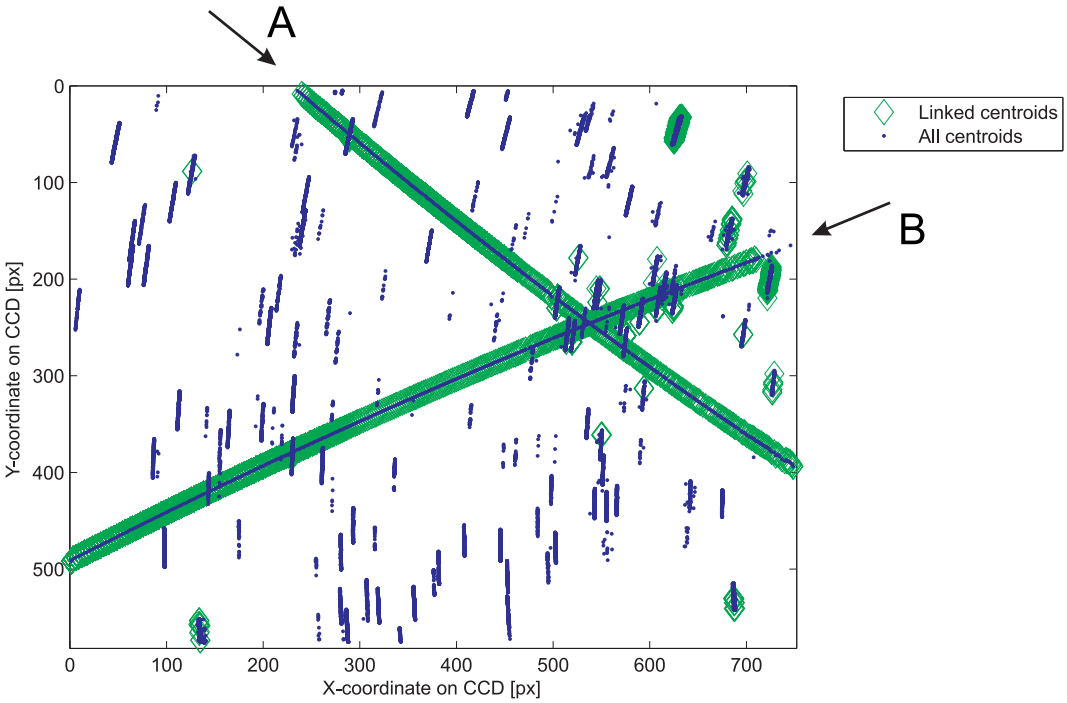

Figure 4.13. *All centroids recorded during tracking of satellite A and B. The arrows indicate directions of the satellite trajectories. All internally linked centroids in the VBS algorithms are illustrated.*

Based on Figure 4.12 and the orbit parameters, an assumption was made of what angular velocities of the two objects could be expected in the time of flying through FOV. These expected velocities are plotted as solid lines in Figure 4.14 together with all calculated velocities of linked centroids, showing that the calculated velocities are following the expected line of Object A and B. Velocities related to Object A have a tendency to be more noisy than the ones related to Object B. The increased noise level is likely due to the fact that the brightness of Object A is low seen from its magnitude level, hence making it more difficult for the μASC to determine the correct centroid point.

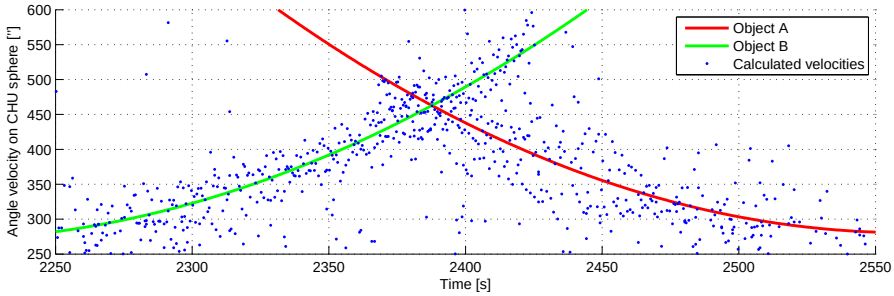

Figure 4.14. *Angular velocities with respect to CHU sphere calculated from detected centroids together with the expected velocities of Object A and B.*

4.4 Summary

A scenario analysis for the Far Range mode has been outlined together with the problem description of the Target tracking. Algorithm implementation into the μASC system has been outlined together with the dataflow and mode switching strategy. Finally, the implemented FR mode of the VBS system has been verified both using test benches and real-sky setups, together with performance analysis of the VBS output.

The performed verification methods have illustrated correct behavior of the VBS system for the FR scenario.

Chapter 5

Short Range - Cooperative

The Short Range Cooperative mode involves the Targets ability to provide detectable feature points, thus making it the cooperative part in the mode. In this mode the VBS system is able to deliver pose and position information of the Target satellite. The concept of having a cooperative Target is to ease detection of known feature points and to increase accuracy of pose and position determination. This chapter will describe the implementation of the Short Range cooperative method into the VBS system and the following verification and performance analysis.

5.1 Scenario for Short Range Mode

The Short Range cooperative mode is available in the situations where Target is in close distance to Main and high precision is needed with respect to both pose and position. These situations concern the two flying scenarios called Proximity Operations (PROX) and the Final Approach/Recede Manoeuvres (FARM) which both are outlined in Section 1.2.1. The distance ranges of the scenarios are limited from where the feature points on Target are fixable and into a distance simulating a docking manoeuvre, i.e. the spacecraft are touching if possible. The cooperative feature points of Target will be detected by the Short Range CHU, while the final approach manoeuvres will be aided from use of the Far Range CHU viewing the collimated beam pattern emitted from Target during the Cooperative mode. An illustration of the docking manoeuvre is available in Figure 5.1 where the collimated tractor beam is seen as the red line. Later revisions have changed the design of the boom fixture for the collimated tractor beams and is described in Section 3.1.5.

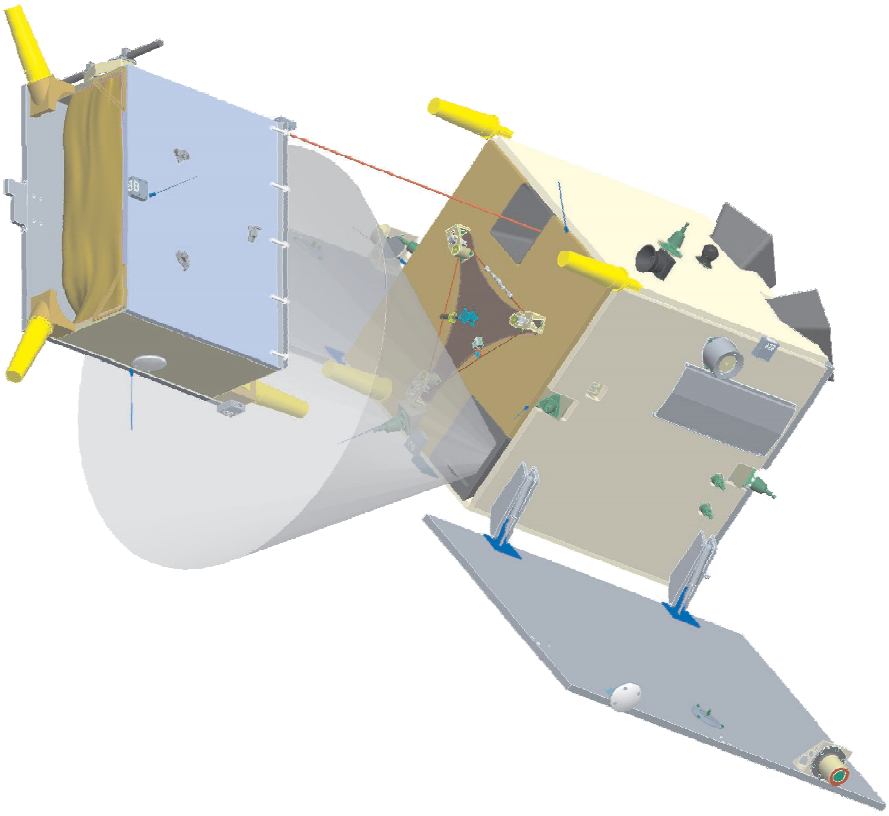

Figure 5.1. *Short range approach configuration. The red line indicates the line-of-sight between the Far Range CHU and one of the collimated tractor beam LEDs. (Image: SSC)*

5.1.1 SR-Coop Operating Range

Outer detection limit:

The SR cooperative mode is limited by the fact that the diodes have to be visible and the systems ability to distinguish two detected centroids from each other. A performance analysis of the Short Range cooperative mode with respect to emitted and detected LED light, LED spot size on CCD, Signal-to-noise rate and distance limitations, has been prepared in [Joergensen2008] taking the scenario, LED and camera parameters into consideration.

In order to estimate the SNR ratio of the detected light from the LEDs vs. the background level, the spot size of the detected LED onto the CCD is essential. In Figure 5.2 illustrates the estimated spot size of the three main contributions for the given scenario, namely Circle of Confusion, Diffraction and Geometrical spot size [Joergensen2008].

Based on the spot size knowledge and the knowledge of radiated light from the LEDs at any given distance, the SNR between the LEDs and the spacecraft body has likewise been estimated.

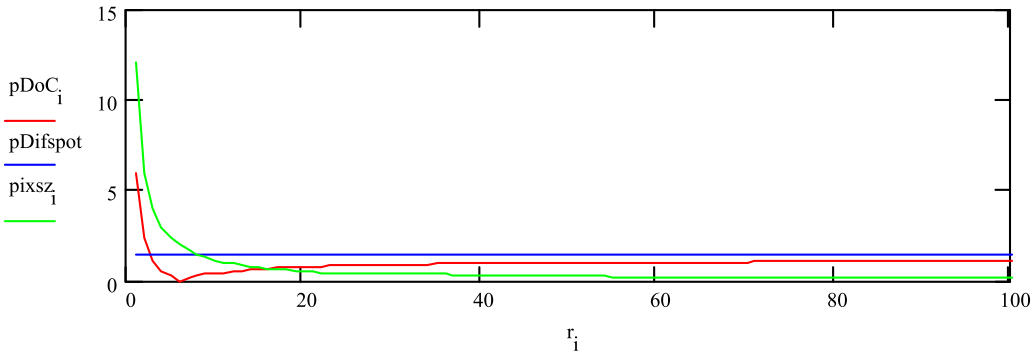

Figure 5.2. *Pixel size of diodes vs range. Red is the Circle of Confusion spot size, blue is the Diffraction spot size and green is the Geometrical spot size. X-axis given in meters and Y-axis given in pixels. [Joergensen2008]*

It is known that the μASC is able to perform centroiding on images with a SNR level above 10 which gives the limit of where LEDs can be detected on the Target satellite. Figure 5.3 shows the SNR vs distance, illustrating that the SNR level is above 10 to a distance of more than a 100m.

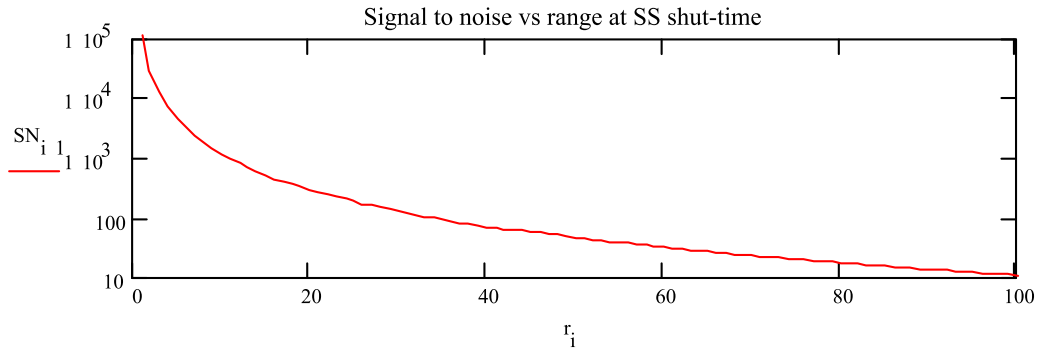

Figure 5.3. *Signal to noise ratio of detected LED and background of Target. X-axis given in meters and Y-axis represent the signal-to-noise ratio in logarithmic scale. [Joergensen2008]*

The outer detection range of the SR-coop mode is set by the SNR of the LEDs vs the background level as well as the ability to separate the centroids from each other. The geometrical outer limit is set where the CHU is still able to distinguish the centroids from each other.

The maximum distance from where the CHU can distinguish all the LEDs of one panel, when viewing from the panels normal, can be estimated based on the previous mentioned pinhole representation of the CHU[1], the knowledge

[1] Illustrated in Figure 4.1.

that the closest placed LEDs[2] on a given panel equals $LED_{Min} = 0.1\text{m}$ and that the μASC needs a separation of minimum 3 pixels in between centroids. Using Equation 4.1 for the pinhole camera model, the maximum detection distance can be estimated by the following expression:

$$Z_{Max} = \frac{EFL}{3 \cdot p_H} \cdot LED_{Min} = \frac{20 \cdot 10^{-3}\text{m}}{3 \cdot 8.3 \cdot 10^{-6}\text{m}} \cdot 0.1\text{m} \approx \underline{\underline{80\text{m}}} \tag{5.1}$$

where:
Z_{Max}: describes the maximum detectable distance between Main and Target.
EFL: describes the effective focal length of the camera, standard value for a CHU is $20 \cdot 10^{-3}$m.
p_H: describes the physical pixel height on the CCD.

This gives that the upper detection distance, Z_{Max}, is controlled by the geometrical approach, where as the SNR approach has a margin > 20m for the light conditions.

Inner detection limit:

The inner detection limit for the SR-coop mode is confined by the fact that a minimum of four coplanar LEDs[3] needs to be in the FOV of the CHU.

From the LED placement model, given in Section 3.1.6, it is known that the largest distance between coplanar LEDs for any given panel is given as $LED_{Max} = 0.7\text{m}$.

Using the pinhole representation of the CHU, the minimum distance between Main and Target can be approximated, viewing any given Target panel.

$$Z_{Min} = \frac{EFL}{CCD_W} \cdot LED_{Max} = \frac{20 \cdot 10^{-3}\text{m}}{6.502 \cdot 10^{-3}\text{m}} \cdot 0.7\text{m} \approx \underline{\underline{2.15\text{m}}} \tag{5.2}$$

where:
Z_{Min}: describes the minimum detectable distance between Main and Target for any given panel.
CCD_W: describes the physical width of the CCD sensor area.

Due to the fact that proximity and docking maneuvers are desired for the PRISMA test platform, one panel of the Target satellite has been equipped with a Docking Pattern consisting of five LEDs placed in close proximity. This Docking Pattern is placed on the $-Y$ panel of Target and has a maximum LED distance of: $LED_{DockMax} = 0.13\text{m}$, which gives an approximation of the minimum detectable distance expressed by:

[2]The closest LED distance exclude the docking pattern on panel $-Y$. LED placement on Target is discussed in Section 3.1.6.

[3]The four coplanar LEDs are limited by the P4P-problem described in Section 5.1.

$$Z_{DockMin} = \frac{EFL}{CCD_W} \cdot LED_{DockMax} = \frac{20 \cdot 10^{-3}\text{m}}{6.502 \cdot 10^{-3}\text{m}} \cdot 0.13\text{m} \approx \underline{\underline{0.40\text{m}}} \quad (5.3)$$

where:
$Z_{DockMin}$: describes the minimum detectable distance between Main and Target for any given panel.

Implemented shutter described in Section 3.2.1 and implemented lens system for the SR CHU described in Section 3.2.2 have enabled a great dynamic range for the SR-coop mode, enabling a clear and forthright detection of the Docking Pattern even at the closest distance which physically can be obtained between the satellites.

5.2 Implementation

5.2.1 Short Range Algorithms

[Benn2007] discusses which solution method for determining pose and position is most efficient for the PRISMA Short Range scenario, utilizing the μASC instrument.

The chosen method is based on solution of the Perspective-4-Point (P4P) Problem, which take advantage of the fact that only one perspective solution is present for four coplanar, non-collinear points, when observed from one single position in the $\mathbb{R}^3$ environment. This representation is similar to that of a camera system.

The P4P problem can be solved using a geometric model based on volume calculations of the four tetrahedra defined by the Camera Center, C_C, and three of the four points [Abidi1990]. Taking the previously discussed pinhole projection from Section 4.1 into consideration, the projection of four points, P_i for $i = 1..4$, are as described in Figure 5.4 where the points on the CCD are described by P_i', assuming that the projected points have been corrected for lens distortion. The C_C indicates the center of the camera and f describes the focal length.

The solution method of the P4P-problem used by the VBS system is presented in Appendix F. Here is described how the x, y, z positions in $\mathbb{R}^3$ of the projected points, based on a minimum of inputs.

The inputs for the P4P method is

- $s_{12}, s_{13}, s_{14}, s_{23}, s_{24}, s_{34}$, where s_{ij} describes the distance from P_i to P_j
- P_1', P_2', P_3', P_4', describing the xy-coordinates of the detected projections given in CCD coordinates.

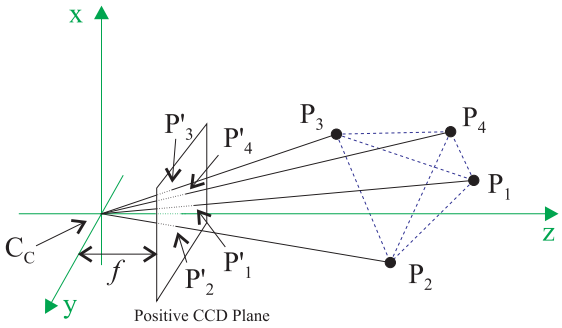

Figure 5.4. *Definition of pinhole projection of four points*

Based on this input the P4P method returns the xyz-coordinates P_1, P_2, P_3, P_4 together with a precision estimate based on the variance, σ^2, of the different distance calculations for $\overrightarrow{C_C P_1}$.

If the noise precision estimate is acceptable, the Rotation and Translation description of the plane of the points can be determined based on geometrical approaches. This is illustrated in Figure 5.5.

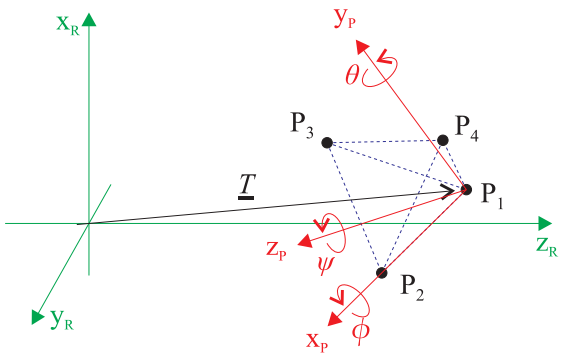

Figure 5.5. *Mapping between frames performed by a translation and rotations.*

The presented P4P solution method presented in Appendix F assumes that the reference between the projected points and which point is projected are known beforehand.
Since the sequence of the four chosen centroids is undefined, the relations between the projected points and the LEDs are unknown. This gives $4! = 24$ combination possibilities, but by assigning the LEDs in a counterclockwise direction, the combination possibilities has been reduced to four. The assignment of the LEDs is further described in Section 3.1.6. Therefore, the application has been designed to solve the P4P problem four times for each possible combination.

The centroid selection and LED interlinking have direct relation to the performance optimization of solving the P4P-problem. This is directly seen if all possible combinations have to be analyzed. For example, if 12 feature points are detected and 4 feature points have to be selected, the following number of combinations are possible:

$$C(n,r) = \binom{n}{r} = \frac{n!}{r! \cdot (n-r)!} = \frac{12!}{4! \cdot (12-4)!} = 495 \tag{5.4}$$

From these combination possibilities of selection of four points, an additional four is possible using a clockwise, mean-centered selection method, resulting in $495 \cdot 4 = 1980$ possible combinations for only matching of one side.

Therefore, a solution has been implemented which performs a greedy sorting of the centroids before calling the P4P solution method, when numerous centroids are detected. The following sorting methods has been used, based on the fact that five LEDs are present on each panel, with additional five on the $-Y$-panel in the form of the Docking Pattern:

Nearest Neighbor: When centroids from two panels of the Target satellite are visible for the VBS camera, then choosing a centroid in the perimeter and select the four nearest neighbors will have the ability to split up the centroids to their respective panels.

Angle around Mean Point: When centroids from three panels of the Target satellite are visible for the VBS camera, then by rotating around the Mean Point of the centroids, selecting five consequent centroids at a time, will likewise have the ability to split up the centroids to their respective panels.

Distance from Mean Point: The last routine is based on the fact that $-Y$-panel of Target has the Docking Pattern in place. Centroids representing this panel can be separated from the remaining LEDs, by sorting the centroids based on their distance from the Mean Point of the centroids.

Using these procedures, running the P4P-method based on many infeasible combinations have been avoided. By choosing five centroids at a time and running the P4P-method based on these has reduced the execution time enormously.

The three mentioned methods also use the fact that only four centroids out of the five chosen needs to relate to co-planar LEDs in order for the P4P-method to estimate a solution.

Through vigorous testing of the SR-Coop system, this greedy sorting approach has showed that the VBS algorithm is able to determine the Pose and

Position of the Target satellite independently of the viewing angle. The solution can even be given when glints are detected from the Target satellite, which is realistic for the given scenario.

Due to the fact that greedy sorting method 1 and 2 has one sorting for each of the detected centroids, the number of possible combinations are limited to:

$$C(n,4) = n \cdot \frac{5!}{4! \cdot (5-4)!} = n \cdot 5 \tag{5.5}$$

3rd greedy sorting method is limited by the inner and outer boundaries, giving that the number of possible combinations are limited to:

$$C(n,4) = (n-4) \cdot \frac{5!}{4! \cdot (5-4)!} = (n-4) \cdot 5 \tag{5.6}$$

5.2.2 Solution Fitting

The solution based on the discussed P4P method is very susceptible to even small noise variations from the centroids, and are usually only based on a minimum number of total detected centroids. Therefore, the P4P solution is only used as an initial guess for Pose and Position determination, denoted "Lost In Space" for the VBS system.

By subsequently fitting the P4P solution to a minimum error of the system, the 6 degrees-of-freedom can be determined based on all available centroid information.
This is performed by back-projecting the LED-model onto the CCD for the current Pose and Position, and thereby iteratively rotate the Target satellite to the minimum error fit in its 6DoF.

In order to perform the best fitting of Pose and Position, optimization and data fitting methods has been investigated.

In general for optimization and data fitting routines applies that different properties of the function for optimization are needed [Nocedal2006, Madsen2008]. These includes: The Jacobian, which describes the first order derivatives, and the Hessian, which describes the second order derivatives. When the derivatives can not be described based on a function, they can be estimated by multiple function evaluations.

This approach is not directly applicable for the Target fitting, simply due to the fact that the function that needs to be optimized will change dramatically in between each execution, and be unique for each given scenario. The changes are influenced by the number of linked LEDs and centroids, whereas several function evaluations are needed to describe the function properties before a minimization can be estimated.

A simpler approach is taken based on the knowledge of the fitting behavior for the present scenario. Namely, that each of the 6DoF elements will behave as a parabola fit due to the method used for residual calculation.

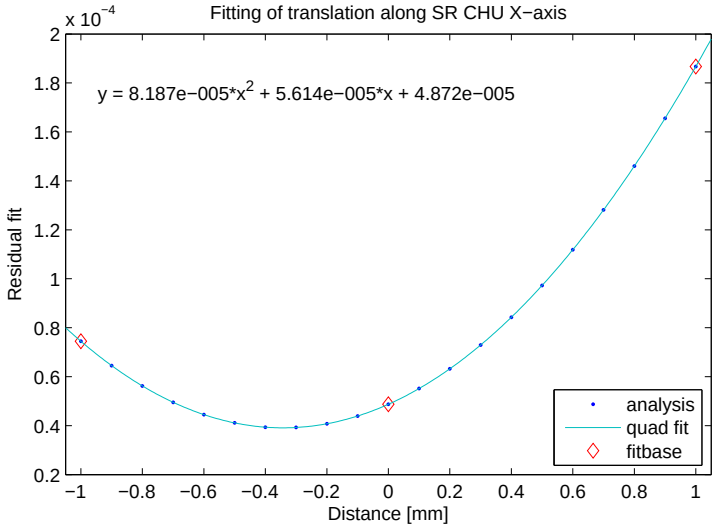

Figure 5.6. *Fitting of the Target translation along the x-axis of the SR CHU coordinate frame.*

In Figure 5.6 is illustrated how the fitting of the position along one axis can be estimated by fitting a quadratic function to this. Additionally, the VBS system determines the fitting using only three points of the system in order to minimize the calculation time, where these three points are illustrated as `'fitbase'`.

Optimization of all 6DoF of the Target Pose and Position, and the reliance of the implementation in the SR-Coop VBS method is described in greater details in Appendix G.

The implemented iterative fitting method uses three general stop conditions in order to determine optimized fitting and not to exceed its execution slot:

- **Error:** The residual error is at a tolerated minimum level.
- **Convergency:** The fitting solution is not converging any longer.
- **Iterations:** A maximum number of iteration runs have been reached.

At any subsequent execution of the SR-Coop function where a previous solution is available, this fitting method is used directly on the detected centroids versus the back-projected LEDs for the Target spacecraft, which has included any drifting information. Succeeding will provide a solution fast, whereas a fitting failure will trigger the "Lost In Space" P4P method which requires longer execution time.

5.2.3 Short Range on μASC

Implementation of the VBS SR-Coop algorithms and methods into the μASC system has included a mode switching control based on both available input information and output from each submode.

The main mode for the SR CHU is the SR-Coop mode in cooperative execution of Target, and SR-Noncoop mode when Target is not providing feature points.

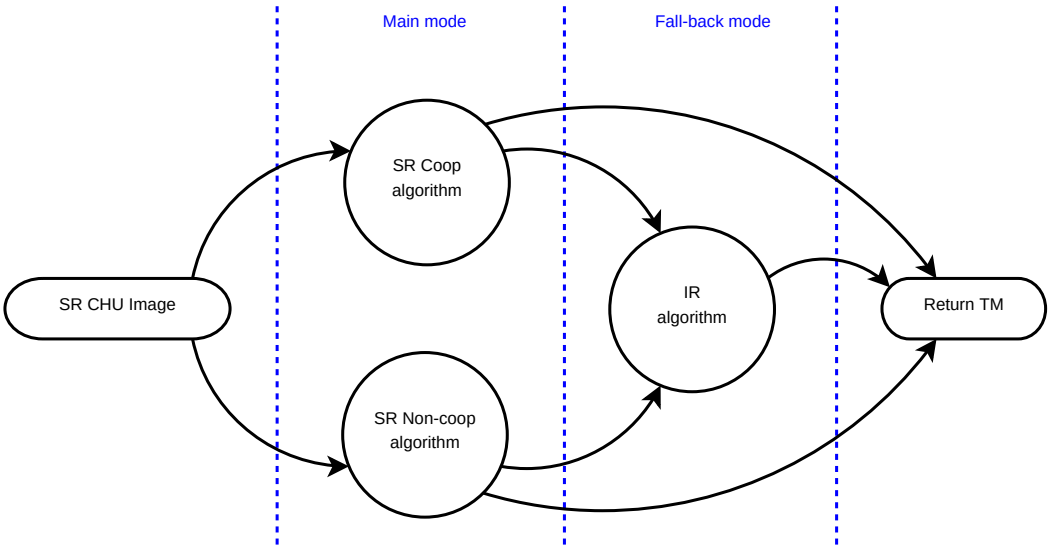

Figure 5.7. *Mode diagram for the Short Range CHU.*

Common for the two modes is the determination of all 6DoF of Target relative to the SR CHU. Though, if they fail to provide a solution, the IR mode is used as a fallback mode, providing pointing direction only.

This mode switching structure is illustrated in Figure 5.7 and is discussed in details in Section 6.2

Figure 5.8 illustrates the dataflow through the implemented SR-Coop mode of the VBS system. It is seen that the iterative fitting method is called first if any previous solution is available for the Target Pose and Position. If the fitting fails or the previous data is unavailable, the "Lost In Space" routine is called.

The total output information from the μASC during SR-Coop VBS mode is as described in Figure 2.6.

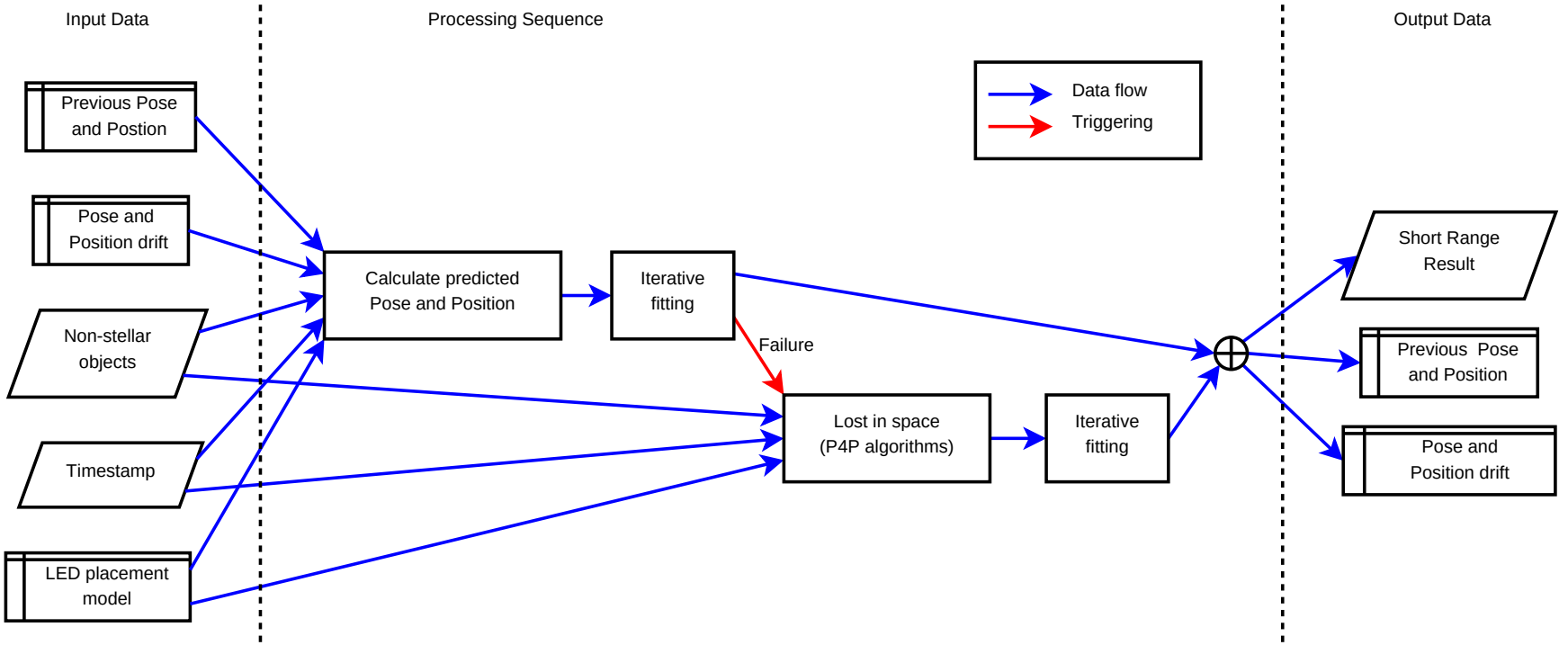

Figure 5.8. *Data flow structure for the Short Range mode algorithm.*

5.2.4 Shutter vs. LED Synchronization

The cooperative Short Range mode of the VBS system is dependent on detection of the LEDs placed on the Target spacecraft. As described in Section 3.1, the LEDs are pulsed-powered at a certain interval. This LED system on the Target S/C and the camera system on the Main S/C needs to be synchronized in order for the camera to capture the light emitted from the LED during the pulse period.

The two PRISMA satellites both comprise GPS instruments[4], which are capable of delivering a Pulse-Per-Second (PPS) signal that runs synchronous on both satellites.

The μASC instrument has the functionality of synchronizing the center of integration (COI) with a PPS pulse provided to it. Furthermore, the COI can be placed at any point in between two PPS pulses with a resolution of 1/65536 sec. Since the camera is continuously adjusting its integration time based on the incoming light, it needs to be synchronized with the LED pulsing. Basing the LED pulsing on the PPS signal will enable this synchronization between the two systems, and thereby realize that the camera integration period is lying within the time period where the LED is powered on.

The integration time of the camera is set to synchronize with the PPS pulse, such that the end-of-integration (EOI) is fixed in relation to the PPS pulse. For the PRISMA mission the LED pulse length is set to 5.0ms, meaning that the EOI is placed at $PPS + T_{LED}$. In Figure 5.9 is illustrated how the LED pulsing is synchronized to the PPS pulse and where the EOI is placed.

The EOI has to occur while the LEDs are still in full power. Therefore, the LED pulse has to be equal to or longer than the EOI. The shutter settings are controlled by the Automatic Gain Control (AGC) in the μDPU, discussed in Section 3.2.1.

During a software upload campaign at SSC in Stockholm, the PPS pulses vs. the LED pulsing were measured in order to verify the relation, LED pulse length and the amount of light emitted from the LEDs. The measurements from the campaign are presented in Appendix H.

The campaign showed that the PPS signal on Main controlling the μASC and the PPS signal on Target controlling the LEDs was drifting up to 1ms in difference on the Flight Models. Furthermore, the LED pulse length had a variance of $(-1.0/+0.0$ms) from the programmable value. This gave a timing sequence as illustrated in Figure 5.10.

Since the minimum integration period of the camera can be set as low as 1us, it is essential that the LED pulse is ON all the way down to end-

[4]The GPS instruments are part of the DLR contribution to the PRISMA mission [Eberhard2007].

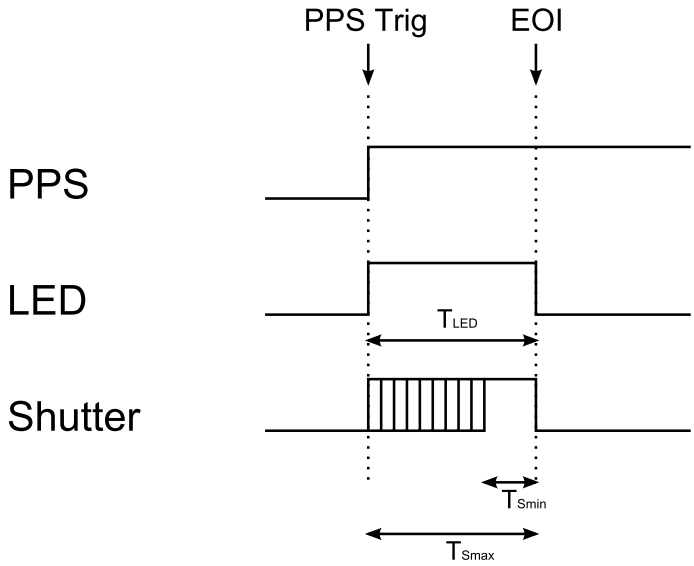

Figure 5.9. *Placement of end-of-integration in relation to the PPS pulse.*

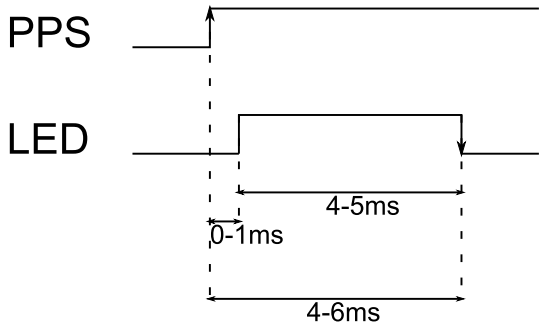

Figure 5.10. *True PPS and LED timing between Main PPS signal and Target LED pulsing, as measured on FM.*

of-integration. Otherwise, the incoming light is not linearly scaled and the camera AGC will not function as intended.

Based on the measurements performed at the campaign, the requirements for the LED pulsing has been changed from having a minimum LED pulse length of 5ms to have a minimum of 4ms. The AGC and shutter control of the VBS system has therefore been adapted to the following requirements: The LED pulse is to start at $PPS(-0.0/+1.0\text{ms})$ and end at $PPS+4.00\text{ms}(-0.00/+1.0\text{ms})$. Compliance with these requirements has ensured correct AGC functionality with respect to capturing the emitted light from the LEDs.

In Section 5.1 it is concluded that the geometric restrictions of centroid separations sets the upper limit of the SR-coop operation envelope. This still holds true with the reduction in the detected light, in form of the shorter pulse length, and has been verified using the performance analysis given in [Joergensen2008].

5.3 Verification of SR-Coop Mode

Figure 5.11. *Dolly test bench for Short Range cooperative mode.*

Development of the Short Range algorithms has had main focus on the cooperative mode, where Target provides feature points using a LED system. This subsection will discuss the test and verification of the Short Range cooperative mode.

In order to verify the Short Range cooperative algorithms, the VBS system has been tested in different flight-like scenarios. This includes using both the EM VBS system on the target mockup as well as the FM system on the Main and Target satellites in maneuverable laboratory configurations.

5.3.1 Noise Characterization

During development of the VBS system and its algorithms the EM Short Range CHU and the Target mockup model were used. Figure 5.11 shows the Target mockup on its rotating stand and the SR CHU on the linear guided dolly. This setup has been used in order to verify that the SR cooperative mode is functioning as expected for a wide range of scenarios, showing the systems capabilities and verifications of algorithm adjustments.

Furthermore, the setup has been used in order to describe the noise characteristics of the SR cooperative mode. By providing VBS position solutions at different fixed distances and on a stable Target, the x-, y- and z-position values given in Figure 5.12 and the yaw, pitch and roll orientation values given in Figure 5.13 are outputted by the VBS. The VBS system gave a valid solution at all the tested distances, and it is seen that the noise increases as the distance increases.

The standard deviation of the noise figures can be approximated with an exponential rising function, given in the form of ae^{bx}. The noise distribution of the z-position is approximately 10 times larger than the noise distribution for both the x- and y-positions, which correspond to the theoretically capabilities of the μASC system.

At close-up between Main and Target the noise distribution is not directly exponential increasing. This is due to the fact that at close distances different optical effects occur in the system, introduced from both the CHU lens, the LED lens et al. Further investigations of this effect is planned in order to map the close distance noise characteristics.

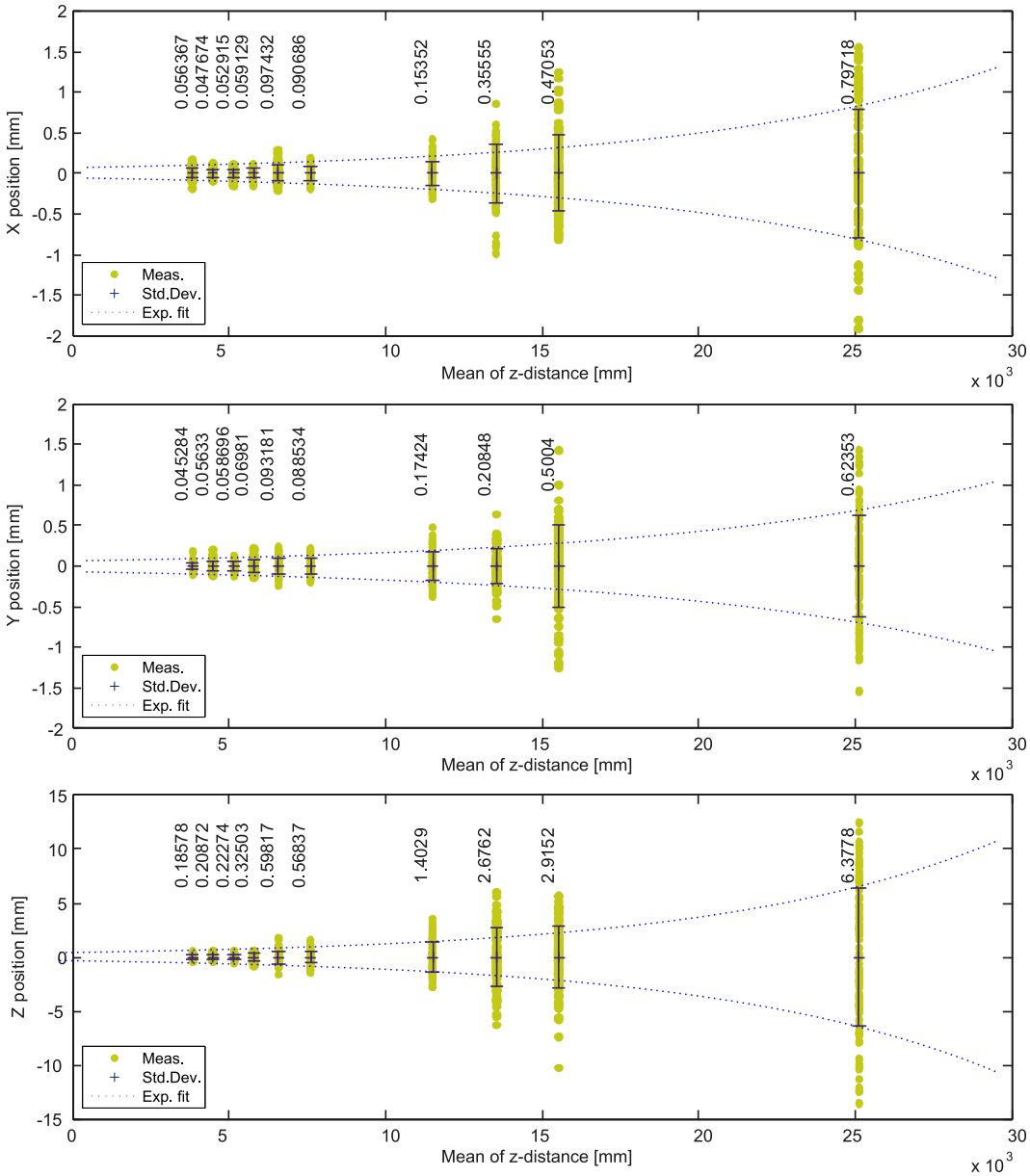

Figure 5.12. *Noise in VBS determined position of Target Mock-up. Measurements have been plotted as difference from the mean value for each distance. The numbers describes the value of the standard deviation at the given distance. The exponential fit is based on the standard deviation values for each of the measured distances. Note that the scale for "Z position" is ∼10 times that of "X-" and "Y position".*

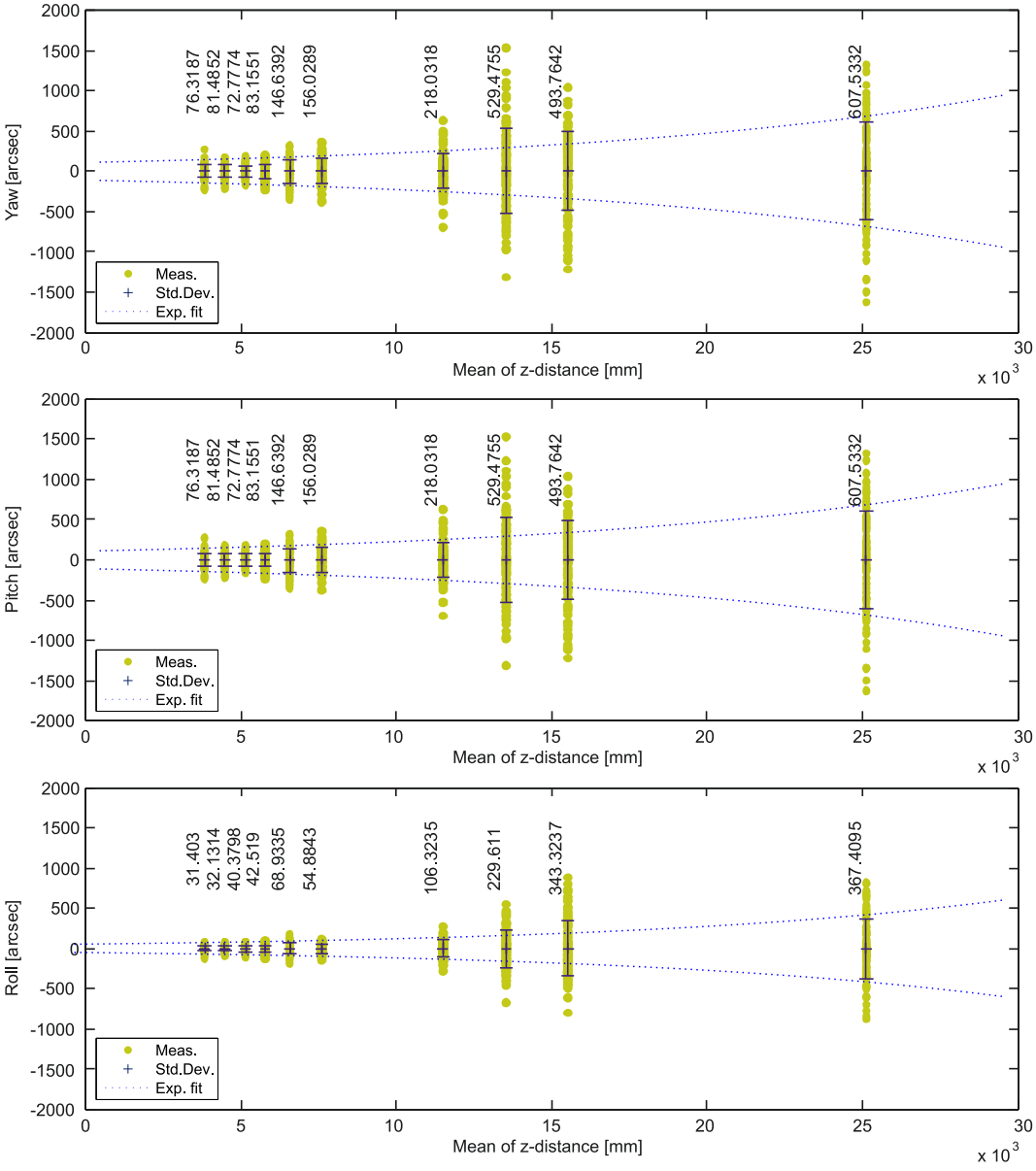

Figure 5.13. *Noise in VBS determined orientation of Target Mock-up. Measurements have been plotted as difference from the mean value for each distance. The numbers describes the value of the standard deviation at the given distance. The exponential fit is based on the standard deviation values for each of the measured distances.*

Due to the fact that the VBS system, the μASC AGC control and the μASC centroiding algorithms have been continuously improved during the development and verification phase of the VBS, the noise characteristics have changed as well. The latest noise characteristics of the Short Range Cooperative mode have been performed on the Target mock-up with similar settings as just discussed, though with focus on viewing angle of the Target spacecraft and the difference in wide and narrow panels of Target. These measurements have lead to the release of [Benn2010a] and is presented in Appendix I.

The four Target rotation positions used during the measurements are illustrated in Figure 5.14, where each of these positions were measured at four different distances, approximately given as 5.2m, 8.2m, 11.2m and 15.2m.

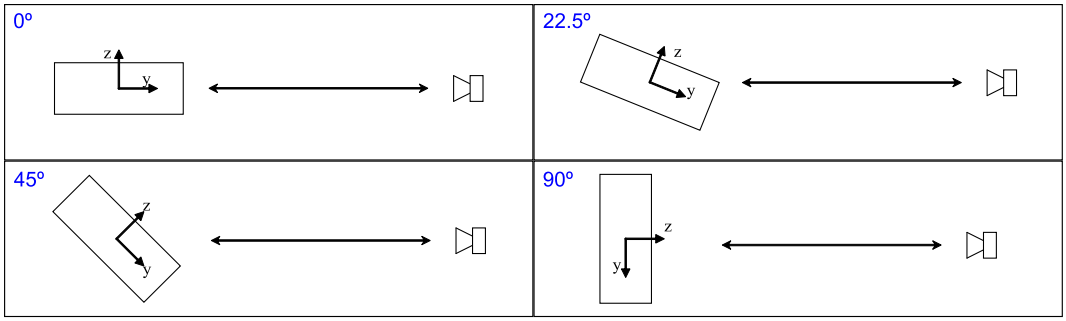

Figure 5.14. *Target rotation positions as defined by the Target reference frame. Rotation positions used are* 0°, 22.5°, 45° *and* 90°, *respectively.*

Based on the presented measurements in Appendix I, the standard deviation values for each of the different measured positions are given in Table 5.1. It is seen that the noise distribution of the normal view on +Y panel (0°) is notably greater than for the other measured panel views. It is believed that this effect is due to a combination of the narrow spacing between the LEDs and the influence of centroiding noise when viewing from normal. Similar effect is for example not seen at same level when viewing the +Z panel from its normal, nor seen when +Y panel is slightly slanted.

Not all the plotted standard deviations in Appendix I follow the exponential growing as would be expected. It is believed that several additional measurements are needed in order to make a clearer assumption on such a distribution of all the standard deviations.

It has to be noted that cross correlation between the position values and the pose values have been observed for a main part of the measurements and can give an increase in the standard deviation results.

During software integration on the FM satellites the included testing of the VBS system showed a clear relation in between pose and position. This correlation occur when a panel is normal to the CHU boresight, and dependent on the orientation a position value corresponds to a respective angle value in pose. This effect is illustrated in Figure 5.15 which displays the VBS results when

Ori	Dist	PosX [mm]	PosY [mm]	PosZ [mm]	Yaw ["]	Pitch ["]	Roll ["]
0°	Dist1	0,763	0,728	0,815	10,783	530,432	507,062
	Dist2	2,396	2,269	3,947	29,858	1414,285	1659,188
	Dist3	2,875	2,444	9,557	55,547	1752,901	1969,919
	Dist4	2,648	2,744	16,341	40,476	1963,994	1768,507
22.5°	Dist1	0,236	0,759	0,845	15,582	434,924	147,047
	Dist2	0,724	0,735	1,133	22,243	513,676	475,110
	Dist3	0,363	0,680	2,463	17,018	438,005	231,292
	Dist4	0,605	1,241	4,097	20,837	835,524	391,715
45°	Dist1	0,044	0,097	0,473	43,601	39,123	43,384
	Dist2	0,051	0,068	0,691	17,389	47,301	36,376
	Dist3	0,130	0,107	1,786	31,160	139,614	67,345
	Dist4	0,082	0,220	4,202	31,569	117,874	54,536
90°	Dist1	0,346	0,226	0,614	10,918	171,195	230,341
	Dist2	0,745	0,720	0,666	16,299	459,545	489,119
	Dist3	1,196	0,846	2,241	41,938	551,414	803,172
	Dist4	1,457	1,371	2,306	37,838	928,311	940,587

Table 5.1. *Standard deviation values for the different measurement positions.*

having the +Y panel normal to the camera, where the x-position corresponds to q2 and the y-position corresponds to -q1.

The Pose and Position relation is mainly due to the fact that the Target coordinate reference point is placed on the outside of the satellite, away from the optical center and the center of gravity. This leads to false noise characteristics if Pose and Position is not correlated to each other.

5.3.2 LED Model

In order for the SR cooperative mode to function optimally, a correct model describing the LED placements on Target is crucial. The current model is based on the descriptive STEP file for LED placement as starting point, and has been reworked based on measurements performed using the Flight VBS system. A number of campaigns have shown an incomplete LED model, though improving the performance, panel overlapping and locking capabilities of the VBS system from time to time.

During the last software upload to the PRISMA FM[5], the latest LED model was uploaded to the VBS system of the Main satellite and tested with the Target satellite in FOV, enabling full test of the FM VBS. The Target satellite was rotated around one axis while the VBS system provided solutions, from

[5]Test report for final FM software upload is given in Appendix J

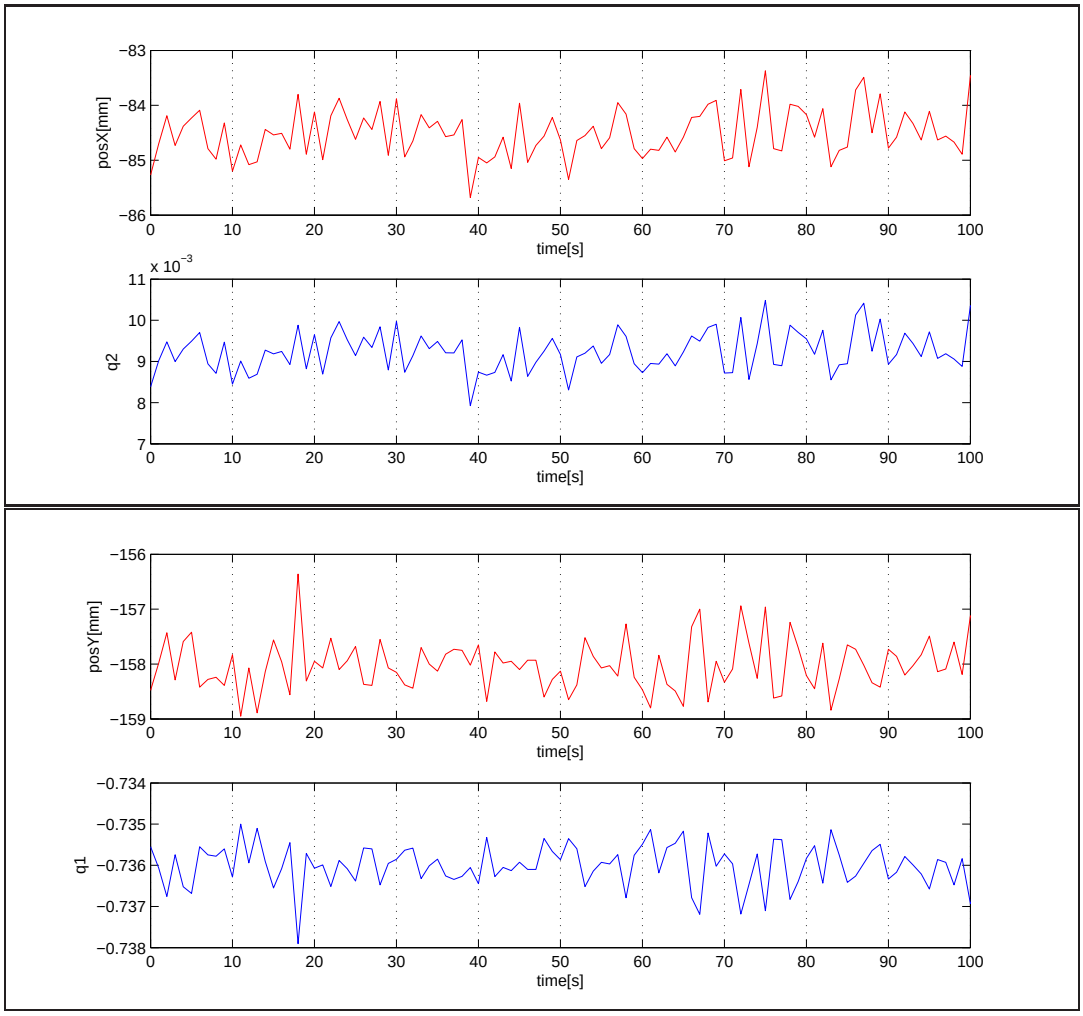

Figure 5.15. *Example of correlation between Pose and Position.*

where all centroids detected during the rotation are illustrated in Figure 5.16 given in CCD coordinates for x and y respectively.

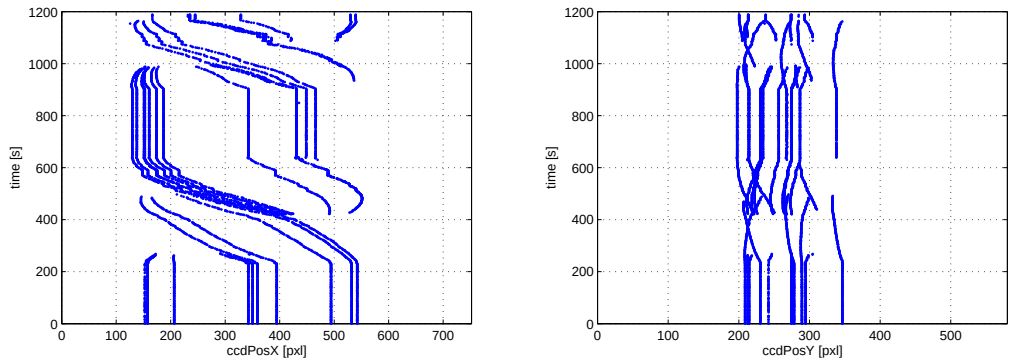

Figure 5.16. *Detected centroids during full rotation.*

The VBS output during this rotation is illustrated in Figure 5.17 and 5.18. During the measurements it was observed that using newest calibrated LED model, the mapping between panel $-Y \rightarrow +X$ and $+X \rightarrow +Y$ went smoother compared to previous models, while the mapping between panel $+Y \rightarrow -X$ and $-X \rightarrow -Y$ were uneven and provided noisy results. This indicates that the -X panel is not correctly aligned to the other panels in the used LED model. The newest model suffers from the fact that the measurements used for building it was taken while there were issues with correct PPS synchronization and an unstable AGC shutter control. New measurements with a final stable and synced system were taken during the last campaign, and will be used in correlation with the Early Harvest phase of the satellite mission to optimize the next LED model for release. This issue is discussed further in Chapter 7 regarding the first in-flight experience of the PRISMA VBS system.

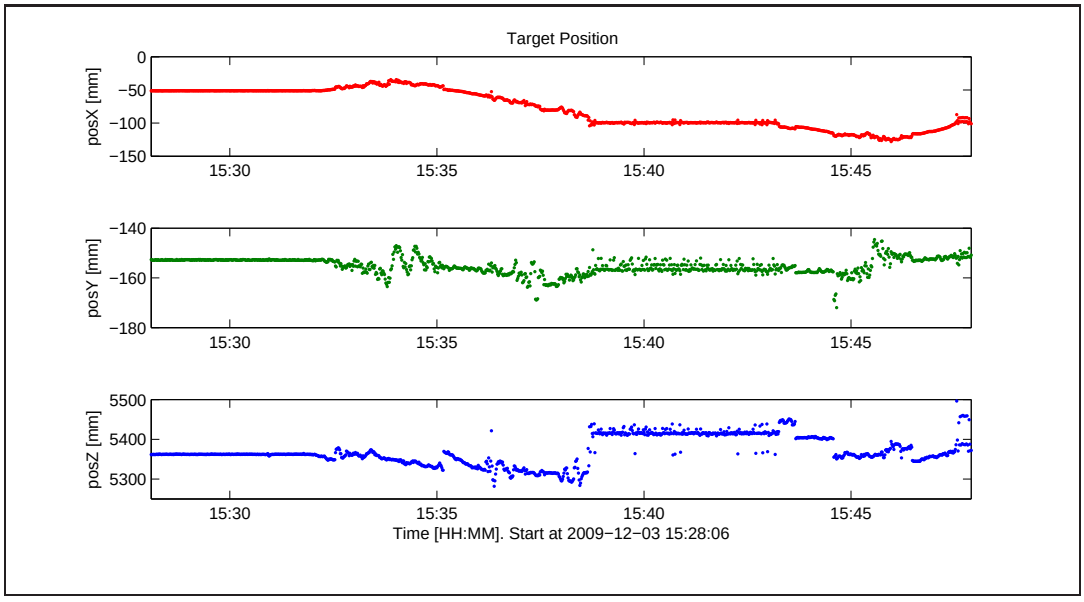

Figure 5.17. *Target Position of the VBS output at rotation of Target.*

5.3.3 Exceeding Edge

The Short Range cooperative mode is capable of determining the pose and position even when part of Target exceeds the FOV. The requirement for acquiring a VBS solution in this scenario is that at least four co-planar LEDs are in FOV of the SR CHU.

Information regarding VBS solutions based on exceeding edge of the FOV is flagged in the VBS TM package. Verification of Exceeding Edge solutions have been verified on the FM VBS system as described in the test report given in Appendix J.

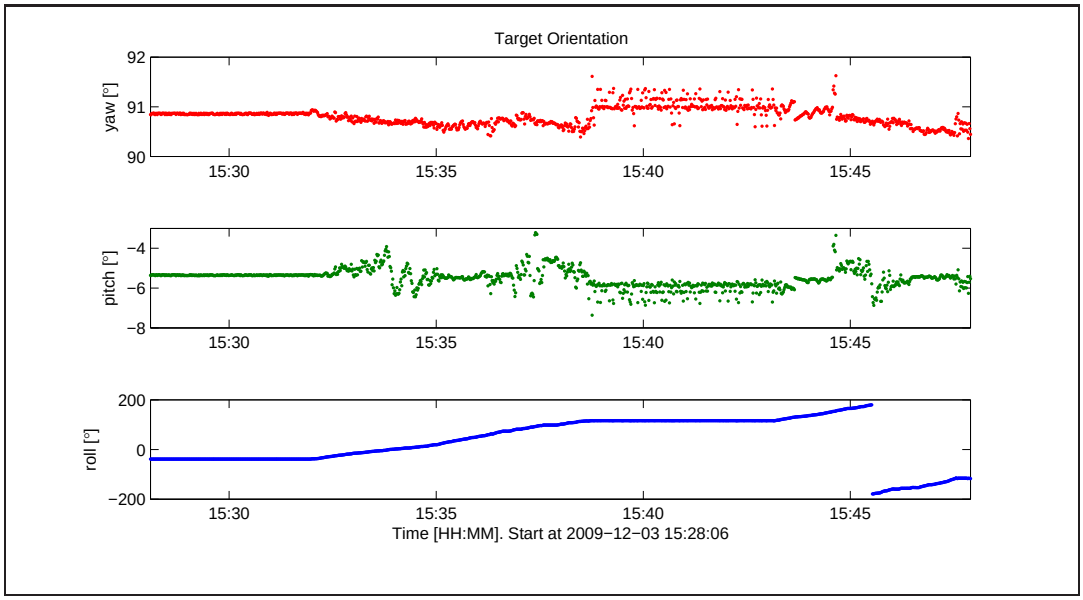

Figure 5.18. *Target Pose of the VBS output at rotation of Target.*

The test sequence consisted of having full Target in FOV showing that the Exceeding Edge flag was not set. Thereafter the SR CHU was blinded, forcing it out of lock, and the Target satellite moved to a position where at least one LED is out of the FOV of the SR CHU. The blinding cover was thereby removed, and it was observed that a solution was acquired as soon as the AGC levels had adjusted, and that the Exceeding Edge flag was correctly set. The centroids taken during the test setup is illustrated in Figure 5.19, where the blue centroids indicate invalid VBS solutions, green centroids indicate valid VBS solution without Exceeding Edge flag and the red centroids indicate valid VBS solution with the Exceeding Edge flag.

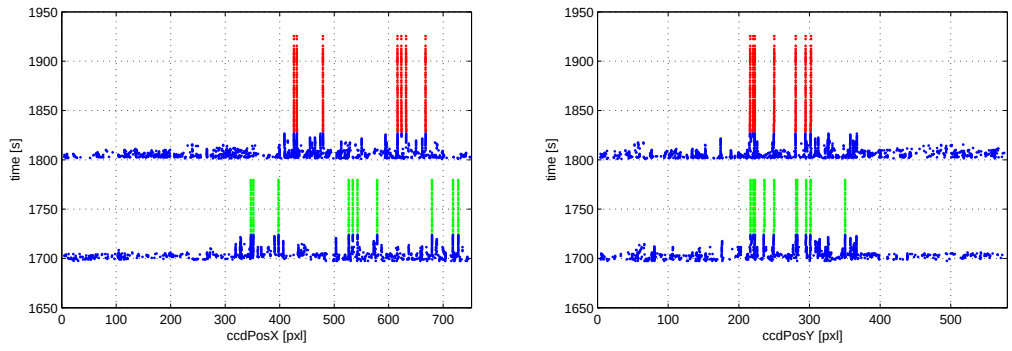

Figure 5.19. *X- and Y-coordinates of detected centroids during test of Exceeding Edge flag. Blue = invalid VBS solution, Green = valid VBS solution and no flag, Red = valid VBS solution and flag.*

5.3.4 Target Photometric Validation

In order to enable the great dynamic distance of the visual system an electrical shutter control has been implemented in the VBS CHUs. Design and validation of the shutter control and synchronization are discussed in Chapter 3, where the photometric validation has been performed on the LED lens and diode level in comparison with the CHU lens system. As discussed, the lens of the SR CHU has been optimized for transmission of the wavelength of the LED, cutting off a significant part of the suns spectrum. The desired transmission profile of the lens has been verified using a spectrometer, mapping the transmission profile of the lens from varying wavelengths.

Furthermore, the LED system has been analyzed for the radiation profile as well as its radiated spectrum in relation to temperature changes.

In order to verify the designed Signal-to-Noise ratio for the lens and LED system, the EM system and Target mockup was tested in brought daylight. Figure 5.20 illustrates the view from the SR CHU of the Target mockup with the LEDs on. The SNR level clearly enables detection of the LED points, enabling the VBS system to come up with a solution for the current setup.

Due to heavy wind, no noise performance characterization was conducted on the daylight test setup. This is desired information and is discussed further in Chapter 8.1.

The shutter implementation and docking maneuvers onwards Target has likewise been tested for. Section 5.1.1 describes the distance limitations based on the Docking Pattern on the $-Y$ panel on Target which gives a minimum distance of $Z_{DockMin} \approx 0.40$m between Target and CC of the CHU. This distance is smaller than what is physically possible between the satellites due to antennas and gauges mounted on their body frame.

During a test campaign at SSC the FM satellites were placed in close proximity with clearing for maneuverability in order to calibrate the Docking Panel LEDs. The images captured during the campaign is presented in Appendix K and verifies that the VBS system is capable of detecting the LEDs in close proximity and, from this, determine Pose and Position of Target.

From the images the interlaced operation of the CCD is clearly illustrated on the blinking LEDs, as well as the extended center LED and how the Circle of Confusion is described when an LED is closer than the focus point of the camera system.

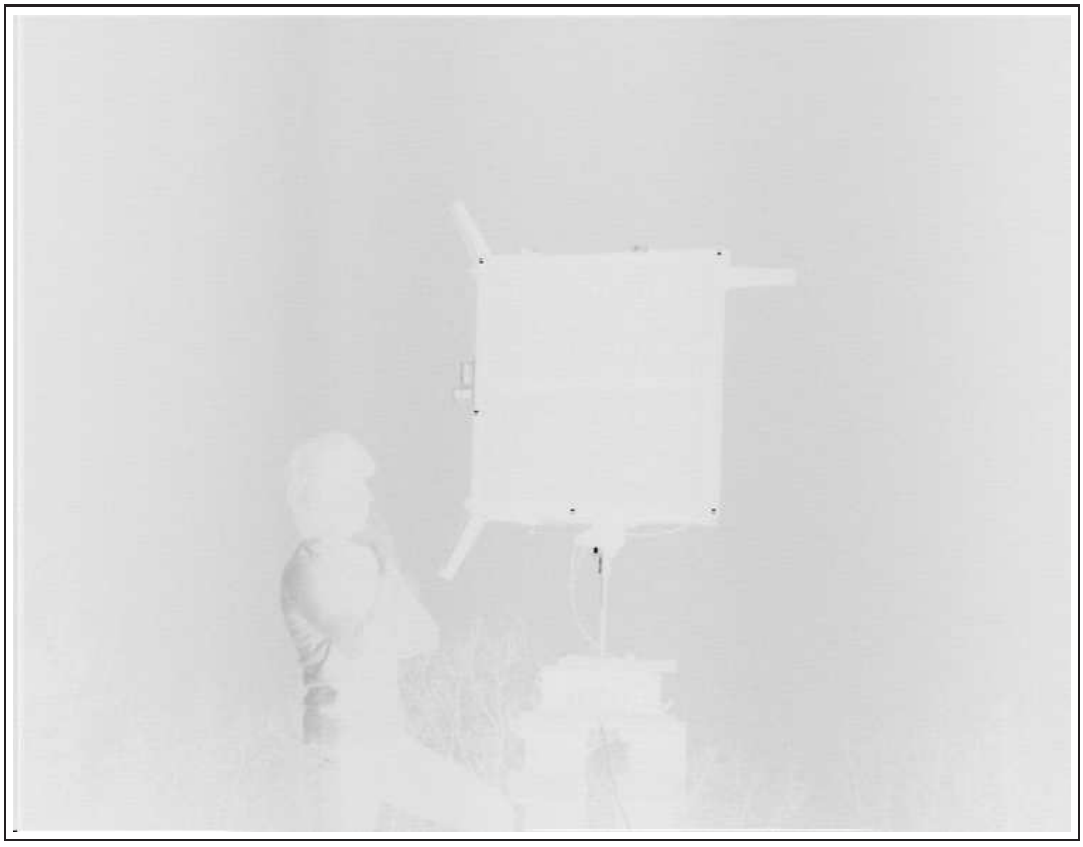

Figure 5.20. *Brought daylight test of LED system and Short Range CHU. Image inverted for ease of view.*

5.4 Summary

The scenario of the Short Range Cooperative mode has been outlined and analyzed in order to define the design parameters of the mode. Furthermore, the implementation of the mode behavior into the μASC VBS system has been described, followed by the verification methods, performance analysis and noise behavior of the VBS output data.

The implemented SR-Coop VBS mode has shown reliable and robust capabilities for a line of different scenarios, following the theoretical assumptions made during the design phase.

Chapter 6

Mode Switching

From Chapter 4 and 5 it is known that the VBS system provides different Target solution information based on the VBS mode. The Far- and Intermediate Range modes will provide information about the pointing direction towards the Target spacecraft, whereas the Short Range Mode will provide both pose and position information of the Target spacecraft. Since the VBS system has to cover the range from a Mv7 star down to close-up, the solution information has to overlap when switching from one mode to another.

Based on the knowledge of the different modes and their capabilities in various scenarios a set of mode switching rules has been designed. Running the VBS system based on the designed set of rules provides autonomous mode switching and control, producing smooth transition in between each of the overlapping modes.

This chapter will describe the design of the mode transition rules and present test results proofing correct mode switching behavior, resulting in a stable VBS system providing high precision pointing or pose and position information of a Target spacecraft in the entire transition range.

6.1 Far $\leftrightarrow$ Intermediate Range

Based on the FR and IR mode descriptions, given in Chapter 4, an expected mode-switching behavior can be realized. The FR CHU will run in both FR mode and IR mode dependent on the given scenario between Main and Target, and therefore needs to handle the switching in between FR and IR mode. For the FR$\leftrightarrow$IR mode switching case two main different scenarios are available, namely going from FR to IR mode and going from IR to FR mode.

For both the FR and IR mode goes that the automatic gain and shutter control of the VBS CHUs needs time to settle whenever the lightning in the scenario changes. It is therefore given that the worst-case for the FR-IR

switching will be when moving from an Mv7 star to a BBO object from one frame to another. It is therefore desired to realize such a scenario in order to analyze the performance of the VBS system.

6.1.1 Test Setup

In order to execute the FR mode, the startracker system needs to determine the attitude based on the detected centroids in the CHU image. Therefore, the test setup includes viewing of the starry sky while an interjected light source behave as the Target spacecraft. The imitated Target needs to be controllable both in luminosity and movement velocity, and is therefore realized using a LED on a black-covered linear guider. Having the boresight of the FR CHU pointing upwards and the linear guider placed over it, the FR CHU is able to detect the LED while having the starry sky in the background.

This test setup is the same used for validating the FR mode as described in Section 4.3.2, and the setup is illustrated in Figure 4.10.

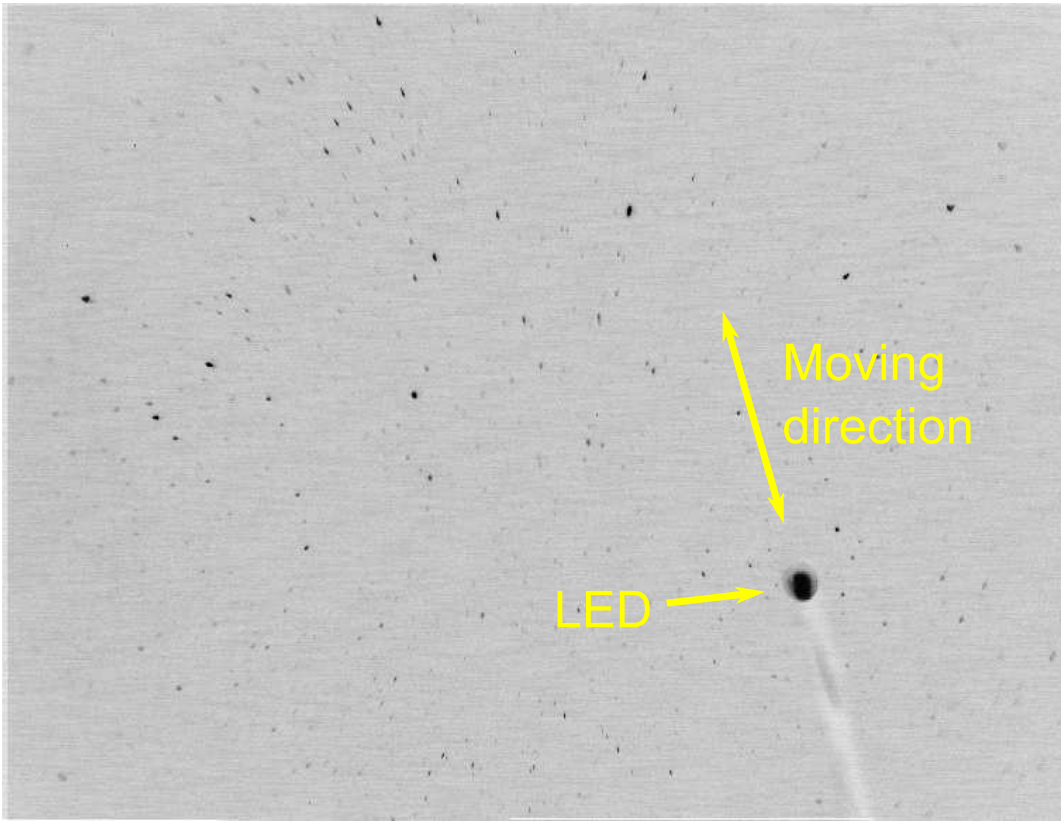

Figure 6.1. *View from the FR CHU. Image is inverted and enhanced for printing.*

The linear guider is set to move with an average speed of 300-350 "/s relative to the CHU in a planar motion over the CCD. This rate is realistic to

what is encountered in space on most 3axis stabilized satellites in Low Earth Orbit [Benn2007]. The view from the FR CHU is imaged in Figure 6.1 where the linear guider, the LED and the starry background is seen.

The LED is powered such that it varies from an Mv7 star to a BBO in pulses. For this test the LED is powered high two times with a pulse length of 10 seconds. First pulse at T=100s and next at T=136s.

6.1.2 Results

Figure 6.2 shows all the non-stellar object centroids tracked by the VBS system. Furthermore, the linked centroids pin-pointed by the VBS system are illustrated both for FR mode and IR mode. Figure 6.3 illustrates the CCD coordinates of these linked centroids in the plane of the CCD, again both for FR and IR mode.

It is seen that the tracking of the correct object is resumed only two to four image frames after the gain and shutter levels has settled and where the stars have become visible again. This shows that the automatic gain and shutter control fast and reliably settles on a new stable level after being blinded, and thereby re-enables tracking of the Target spacecraft.

The linking is operating as designed since going from FR to IR holds track of the centroids while going from IR to FR (powering down the LED) forces the gain and shutter control to stabilize before any objects can be detected again. Four to five frames are taken before the levels are settled.

Furthermore, the lowest level of the LED lies on the detection limit for the CCD. This is seen when the link is lost, causing interruptions in the linking when running in FR mode. The VBS system though re-links as soon as the LED is detected and the noise level is still within the track history tolerances.

Additionally to the real-sky verification of the mode switching, the Pharos Module has been used for laboratory testing enabling easier test setup and extended controllability for determining mode switching behavior during algorithm development. The Pharos module is described in Section 4.3.1.

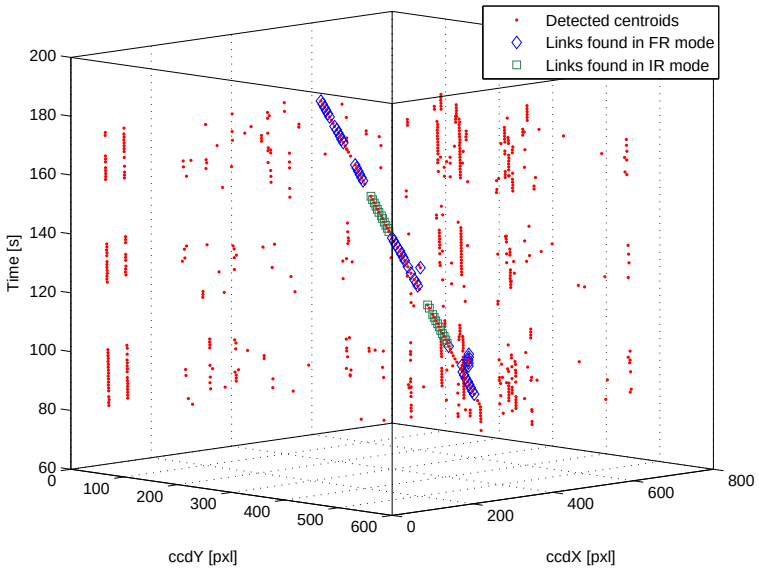

Figure 6.2. *Detected and linked centroids in the time domain.*

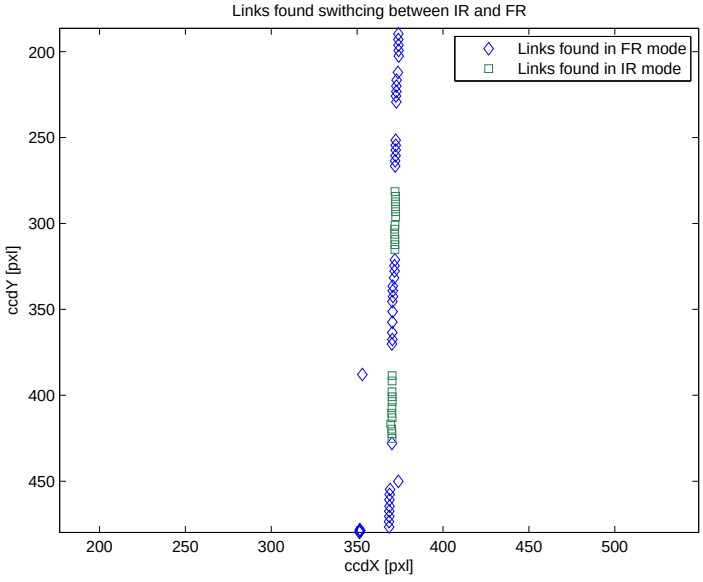

Figure 6.3. *Links found in FR and IR mode, respectively.*

6.2 Intermediate ↔ Short Range

Similar mode switching has been tested for when going from the SR to IR mode and back again. This switching involves only the SR CHU, which is able to determine Target pose and position in SR mode. It is known that the SR Cooperative submode is the mode which needs to be the high reliability mode for the PRISMA mission. Therefore, this cooperative VBS mode is subject to the mode-switching test.

The SR CHU naturally establishes a strong fix onto the detected LEDs on the Target spacecraft when running the SR-cooperative mode. Due to this fact the solution has to be forced away from the true solution by creating a very bright BBO, which will force the gain and shutter values to re-adjust.

Due to the fact that it is near impossible to provide a BBO object exactly in the origo of the Target reference frame, the two solutions will differ depending on which mode are the active. Therefore, this test will illustrate the settle time and the pose and position determination refix when switching mode.

6.2.1 Test Setup

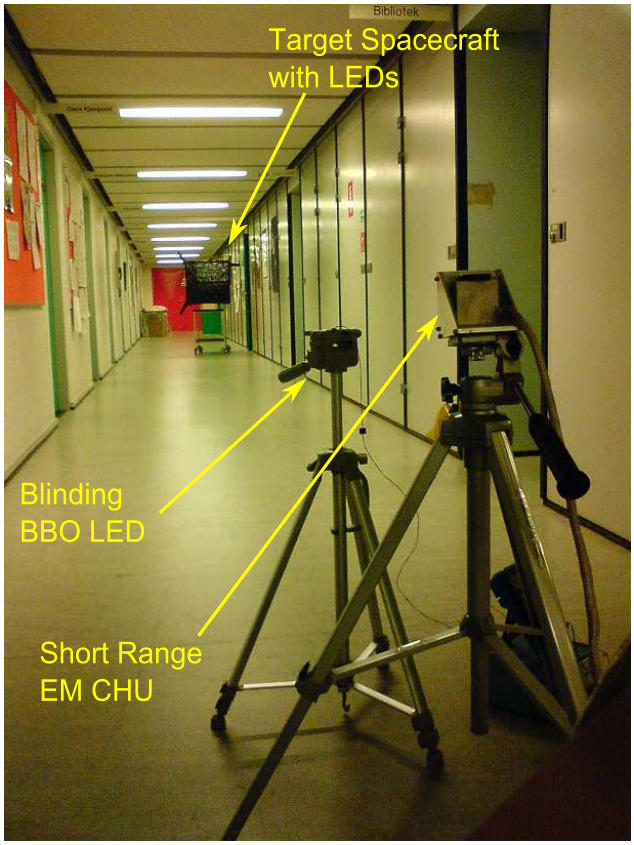

Figure 6.4. *Test setup for the SR-IR switching.*

The test setup consists of a SR CHU with the cooperative Target spacecraft in field of view. In order to create the BBO, an LED is used again and placed in close proximity of the CHU in order to generate a signal much stronger than the Target LEDs. This test setup is illustrated in Figure 6.4.

During the test the LED used for creating the BBO is pulsed three times, and is held high for each pulse until the gain and shutter levels have re-adjusted to the BBO created.

6.2.2 Results

Figure 6.5 shows the view from the CHU when the BBO LED has just been powered on and before the gain and shutter levels have started adjusting. It is seen that lens flares and vertical CCD overblooming is present which can lead to imprecise centering of the BBO until the gain and shutter control removes these unwanted effects. The red arrows show the LEDs on Target and illustrates where the Target satellite is placed in relation to the BBO.

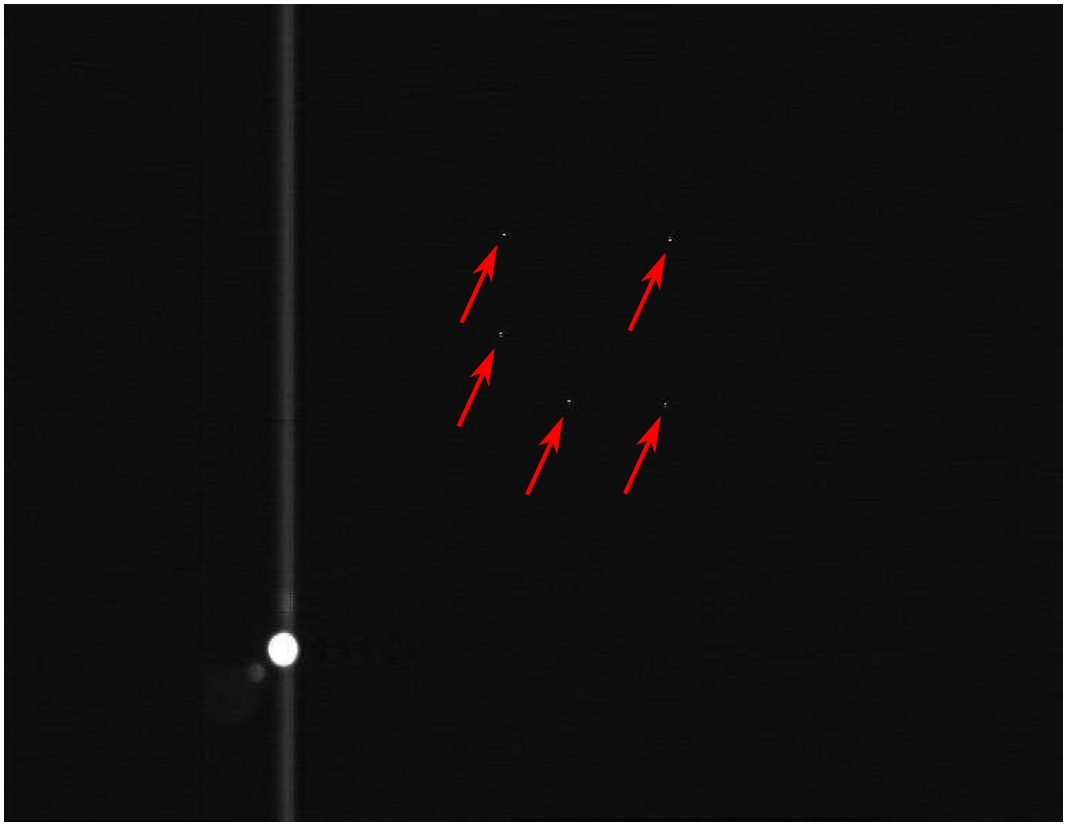

Figure 6.5. *View from SR CHU directly after powering on the blinding LED. The red arrows illustrate the five visible LEDs on the Target spacecraft.*

The output of the VBS system is illustrated in Figure 6.6 and Figure 6.7

given in Right Ascension and Declination values in the CHU reference system, assuming an attitude pointing of $q = [0, 0, 0, 1]$ during testing.

It is seen that the switch going from SR to IR has a lock directly on to the new Target from frame to frame. The new lock drifts while the gain and shutter values re-adjust, but this was to expect by seeing the blooming level of the BBO shown in Figure 6.5.

Additionally, for the switch going from IR to SR the Target LEDs are not visible due to the fact that the gain and shutter control needs to re-adjust for the intensity. As soon as the intensity levels of the LEDs are detectable again a solution is provided by the VBS system. This transition takes about 10 frames for the gain and shutter control to adjust.

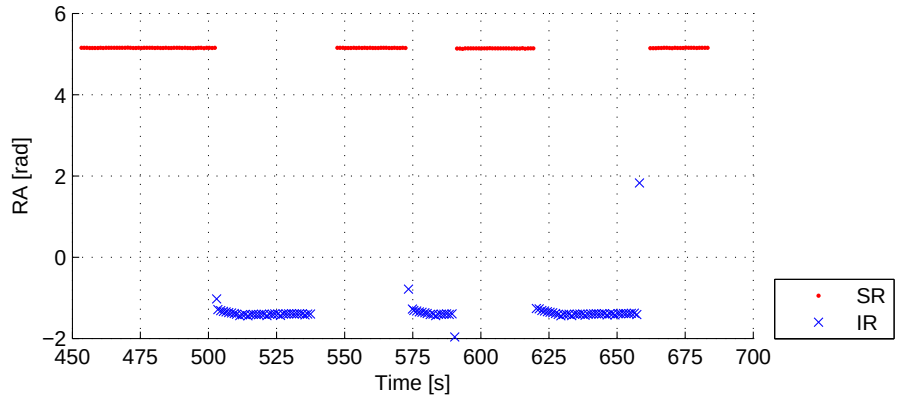

Figure 6.6. *R.A. given in VBS outputs when switching between SR and IR.*

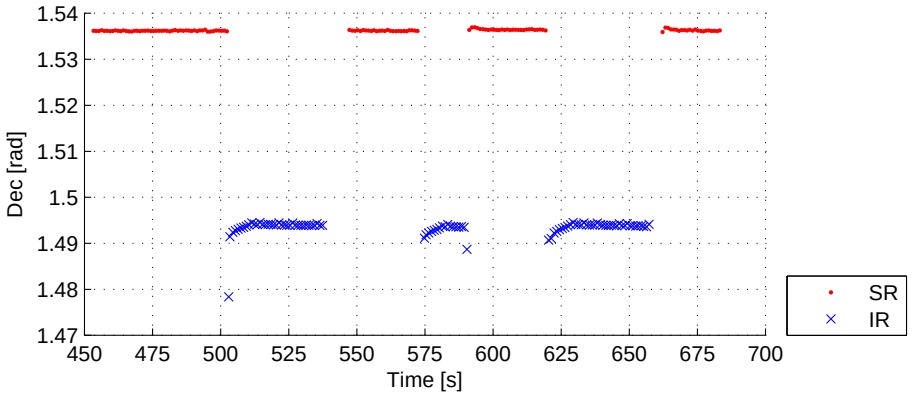

Figure 6.7. *Declination given in VBS outputs when switching between SR and IR.*

6.3 Summary

It has been shown that the implementation of the Vision Based Sensor system onto the generic μASC instrument is able to determine the pointing or pose and position for a Target satellite for a rendezvous and docking mission. This has been shown by having the system exposed to scenarios similar to the three different main modes, namely Short Range, Intermediate Range and Far Range mode.

By changing the different scenarios in worst-case manner has shown how the VBS system correctly changes the respective mode in order to enable solution determination, and that the correct solution is obtained in the different modes. The transitions between the different modes are clearly dependent on the settling time of the gain and shutter control, though the used worst-case scenarios has shown that the solutions will provide smooth transitions in between modes since the determined solution was correct at each mode. The parameters for the gain and shutter control are adjustable, and will be optimized in-flight during the mission based on how the system reacts with the current parameter settings.

The described FR$\leftrightarrow$IR and IR$\leftrightarrow$SR mode switches are revisited in Section 7.5 regarding in-flight experience with the VBS instrument.

Chapter 7

In-flight Experience

The PRISMA satellites were launched June 15th 2010 with the VBS system integrated. After a successful commissioning phase the mission entered the operational phase, including initiation of the VBS system. This chapter will describe the first initial calibration steps and discuss the performance analysis for each mode based on the data collected during Early Harvest for the VBS. Due to the fact that inflight VBS data is acquired continuously during writing, analyzed data is partly included as Appendices in order to keep this chapter flexible.

7.1 AGC/Shutter Settings

The performance of optical systems for spaceflight are difficult to fully verify using on-ground test-benches. This is due to the fact that realistic sun-simulators are needed for having the full spectrum and the correct power per square-meter. Optical systems are therefore often only partly verified, where the full performances are theoretically outlined.

The VBS system of PRISMA is reliant on detection of Target in a broad range of different scenarios. Therefore, the performance of the VBS camera and lens systems is essential and is verified as an initial stage of activating the VBS system.

This section will describe the "First Light" images of the inflight optical verification and needed AGC tunings for the two different VBS CHUs.

7.1.1 First Light from FR CHU

The Far Range CHU of the VBS system is capable of functioning as a standard startracker CHU due to its minimal design changes from the standard. Due to

this fact, the optical system of the FR CHU was verified before the initiation of the VBS system.

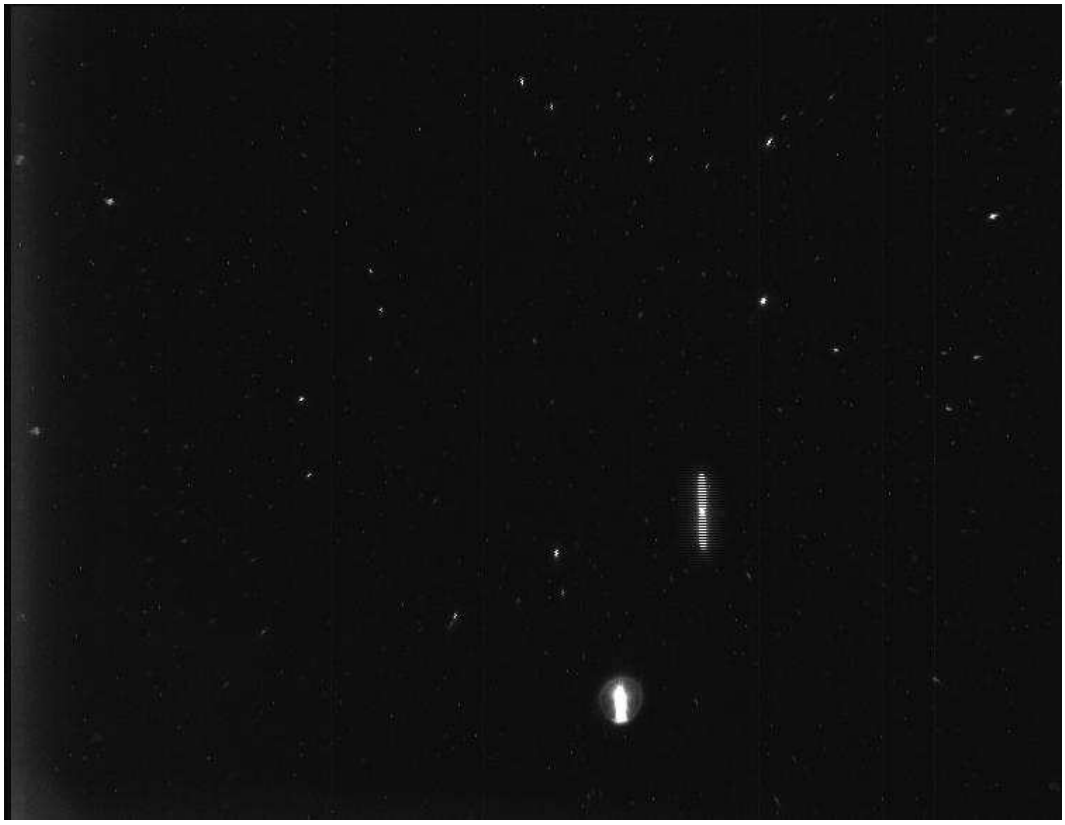

Figure 7.1. *First Light from the Far Range CHU. Target is the brightest object in the bottom of the photo and the extended object is a cross-passing orbiting satellite. Earth is at the right (+X direction) for the FR CHU.*

The "First Light" image captured by the FR CHU is depicted in Figure 7.1, with boresight pointing towards orbit trajectory while chasing Target. A sequence of images were captured from where it is known that Target is the bright object in the bottom of the image. In the sequence, Target is moving in an elliptical shape in the image field, due to the difference in the orbit trajectories of Main and Target.

Additionally illustrated in Figure 7.1 is a distinct secondary non-stellar object passing in the FOV. Based on the interlacing effect the object speed is approximated to $\sim 10 \cdot 10^3$"/s relative to the CHU pointing. This object moves faster than what is accepted by the FR mode, which is discussed in details in Section 7.2 for similar cross-passing objects.

The automatic shutter control of the VBS CHUs are activated as soon as the μASC is commanded into VBS mode. Based on image properties and visible features the shutter time is set accordingly. In Figure 7.2 is illustrated the automatic shutter control in function while Target pointing. The current

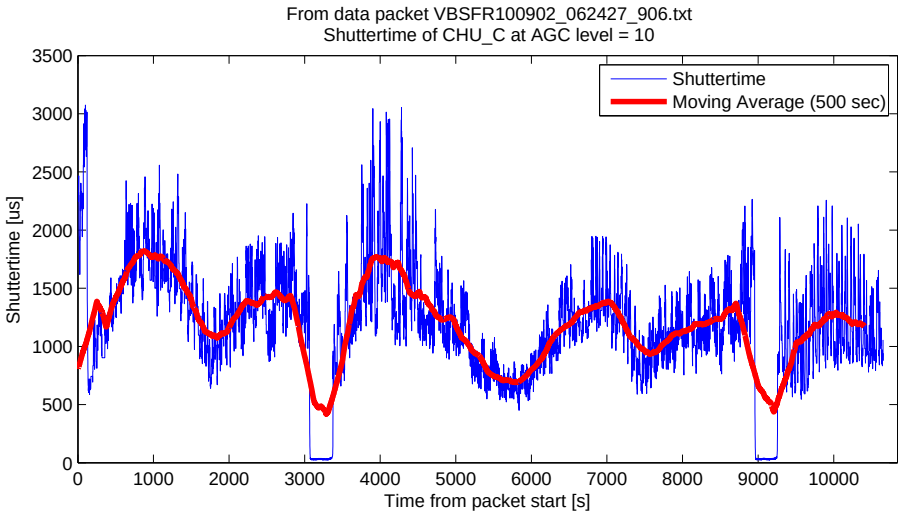

Figure 7.2. *Shutter time variations for the FR CHU including moving average of the ±250 samples. The moon is parsing through FOV at T≈3100s and T≈8900s.*

orbit trajectory featured that the moon entered the FOV, for which the shutter correctly readjusts at $T \approx 3100$s and $T \approx 8900$s.

The low frequency oscillation, illustrated by the moving average, follows the luminosity of Target depending on the sun-pointing angle[1] and clearly shows the variations over an orbit. The high-frequency oscillations are believed to be caused by instabilities in the shutter control and the PPS synchronization pulses, and is under investigation.

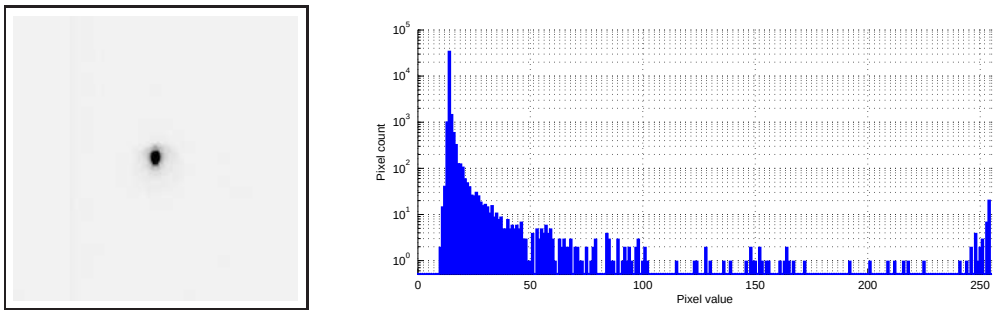

Figure 7.3. *Image segment for AGC setting 20 from inverted image IMC_967387390.878632.jpg, together with the belonging logarithmic histogram.*

During the Early Harvest phase the parameters for the AGC and the shutter control were adjusted in order to determine the optimal settings for Target detection. This procedure is presented in Appendix L, Section L.1, from where

[1] According to Target description in Section 1.2.1 the attitude pointing of Target is stable down to ±10°

the result is illustrated in Figure 7.3.

It was ascertained that the halo effect of Target reflections in the lens system should be avoided in order to enable determination of Target only. Additionally, the AGC settings should still allow star detection. Based on these two facts the final AGC and shutter parameters were set in accordance with the information given in Figure 7.3, with an addition of increasing the centroid detection threshold such that the halo effect was removed which is seen as pixel values up to 100 in the illustrated histogram.

Based on the First Light image sequence for the FR CHU, i.a. Figure 7.1 and Figure L.7, Edge Stray detection of the inflow of light from the Sun and reflections from the Earth caused problems by adding an arbitrary big-bright-object in the image field. The root cause for this event is due to shortened baffles for the two VBS CHUs mounted on PRISMA.

The Edge Stray BBO caused the FR mode to malfunction and is discussed in details in Section 7.2. An Edge Stray removal filtering has therefore been implemented in the μASC image processing before feeding centroid information to the VBS algorithms.

7.1.2 First Light from SR CHU

The First Light image sequence from the Short Range CHU demonstrated acceptable performance of the AGC and shutter control utilizing the standard flight parameters. One of these images is depicted in Figure 7.4 where the Target satellite is captured at a distance of $\sim$ 30m to Main, with the Earth and clouds as background. The image clearly illustrates the distinct appearance of the LED feature points compared with the overall noisy background, from where the Short Range Cooperative mode was able to provide VBS solutions. This scenario is discussed further in Section 7.4.

Even though the AGC and shutter values for the SR CHU seemed reasonable in the First Light series of images, closer operations showed difficulties for LED screening when the solar panel was visible for the camera. This effect is illustrated in Figure 7.5 depicting a region-of-interest image of Target, resulting in the entire solar panel being detected as centroids due to a standard centroid threshold of 50.

The histogram for the ROI image is given in Figure 7.6, showing that a great part of the image information lies above the threshold of 50. From this histogram a new value of 150 is of better choice in order to reduce the number of detected features.

In order to verify that the LEDs are still detected with the new centroiding threshold, the difference between the two thresholds are illustrated in Figure 7.7. The threshold of 150 reduces the number of feature points heavily, enabling the SR-Coop mode to determine a solution with a minimum of false

Figure 7.4. *First Light from the Short Range CHU. The LEDs are visible on Target with the Earth in the background.*

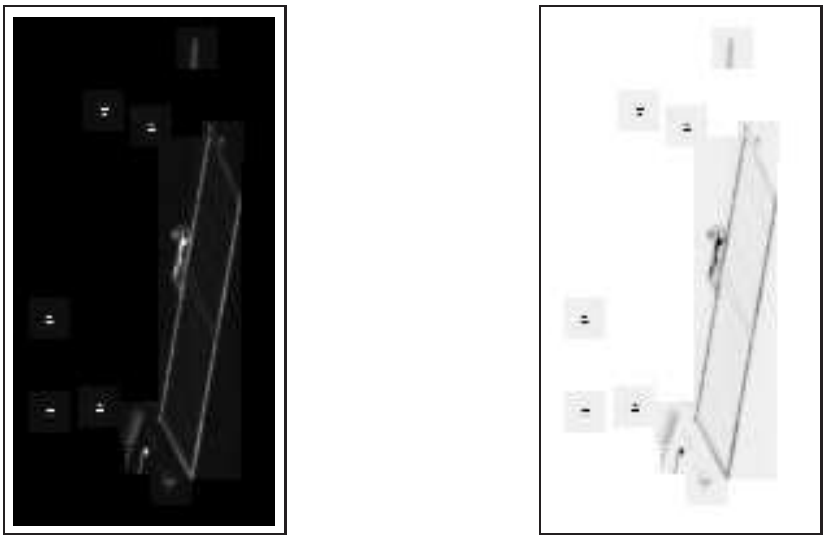

Figure 7.5. *ROI image of close-up of Target at ∼15m, with centroiding threshold set at 50. Left is the original image, right is the inverted view.*

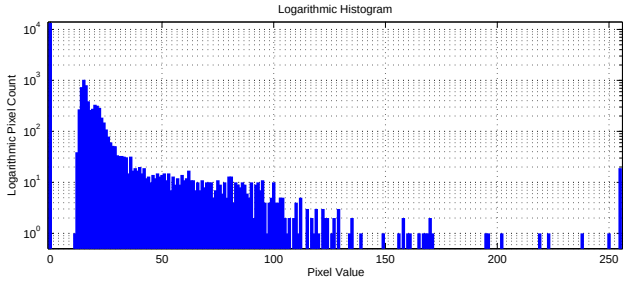

Figure 7.6. *Logarithmic histogram of the Target view given in Figure 7.5.*

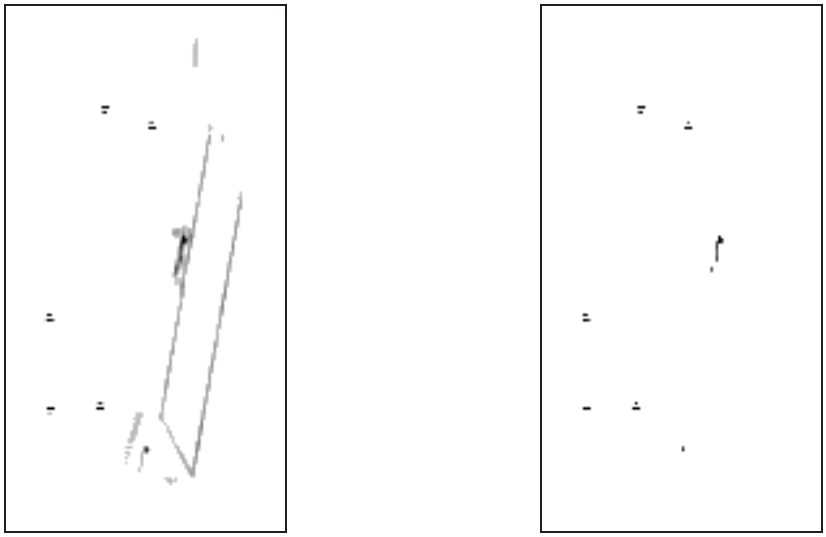

Figure 7.7. *Thresholded Target images illustrating only the values above the threshold. Left is threshold = 50, and right is threshold = 150.*

objects. This configuration is currently under evaluation on the PRISMA mission.

7.2 Far Range Mode

The Far Range CHU was the first VBS CHU to be activated for acquiring Early Harvest VBS data. Based on the image information acquired in the "First Light" image sequence for the AGC initialization, it was ascertained that the FR CHU could easily determine its attitude based on the stars, while having Target in FOV.

Additionally, from the two moon blinding events illustrated by the shutter time in Figure 7.2, a direct measure of the angular velocity of Mains orbit trajectory can be estimated to $\omega = 220.0\frac{''}{s}$, which corresponds to the design angular velocity for the Far Range mode as given in Section 4.1 to be $\omega = 215.5\frac{''}{s}$.

Knowing that the Far Range conditions were available, the VBS system was initialized. This section will describe the initial inrun problems, lessons learned regarding on-ground testing and performance estimate for the FR mode.

7.2.1 Initial Revisions

For the first initialization of FR mode, several unforseen problems turned up. These included the following:

- Attitude mappings not converging.
- Edge Stray effect in the baffle system.
- Sign problem in Right Ascension and Declination calculations.
- False VBS lockings due to hotspots.

Attitude Mappings:
From the first FR VBS data it was clearly seen that the solutions were only sporadic marked valid, and that all solutions were not linked to the true Target centroid. This is depicted in Figure 7.8, illustrating that the few available links are either marking stars or the edge stray BBO in the image. The true Target is highlighted, showing that the centroid is steady in the picture field due to boresight pointing towards Target along the orbit track.

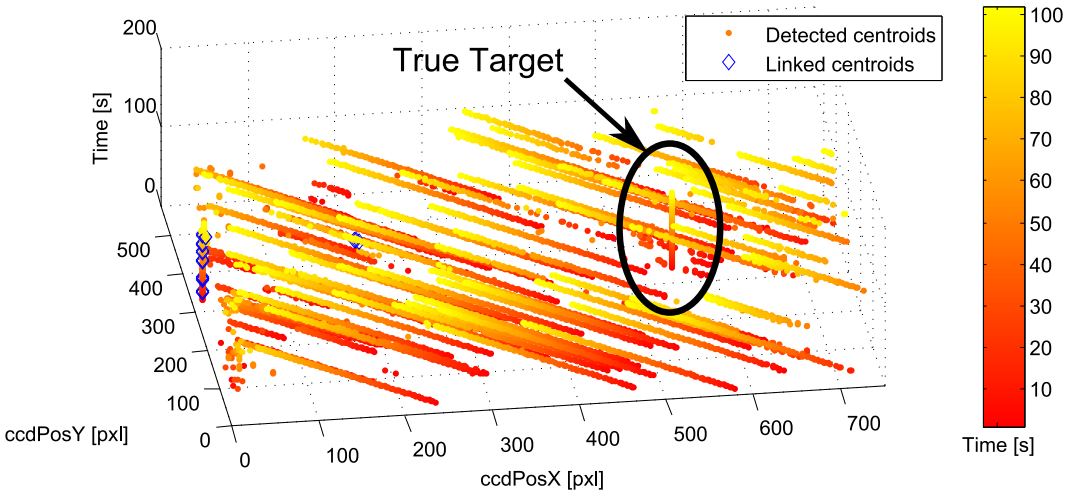

Figure 7.8. *First FR VBS results having false links together with all detected centroids. The true Target centroid is highlighted as the steady object.*

These first VBS results with false linking led to running the same scenario on the Engineering Model of the VBS system for debugging. The problem was clearly seen and rooted to the fact that a link between the determined FR CHU attitude and the attitude used for the FR algorithms was missing, resulting in the FR algorithms being seeded with a unit pointing $q = [0, 0, 0, 1]$. For

the given scenario where the CHU boresight is Target pointing during orbit and the missing mapping of centroids into inertial coordinates, results in that Target is detected as a stationary object where as all the star centroids are seen as moving objects, making them candidates for the VBS solution.

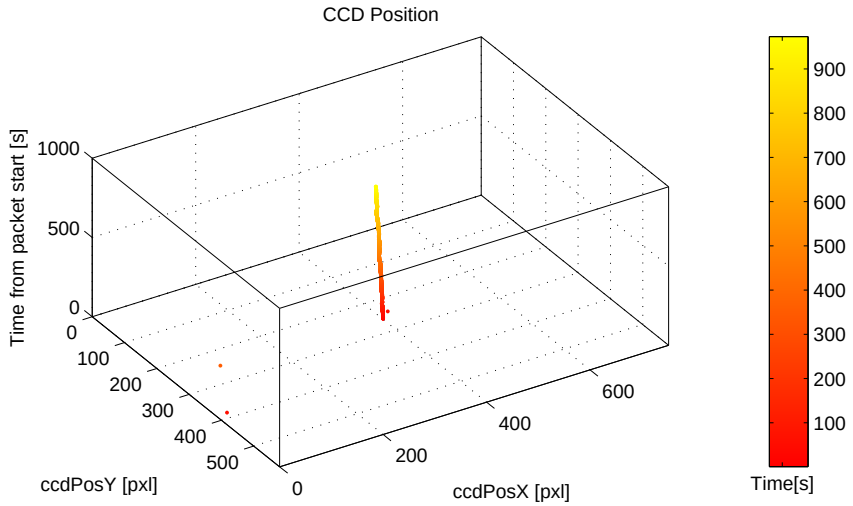

Figure 7.9. *True FR linking of Target. The plot illustrate the CCD Position field of the VBS solution output, giving coordinates of Target.*

After correcting the missing link in the attitude mapping, the FR mode was able to acquire the correct Target centroid in subsequent runs in similar scenarios. These correct links are depicted in Figure 7.9 illustrating the CCD coordinate field from the VBS output packets, i.e. only showing the solution among all detected centroids. It is noted that two false links are acquired, which are associated to the Edge Stray effect discussed later in the current section.

The reason for not discovering the missing attitude mapping in the verification phase is due to the fact that all testing methods have utilized a steady-pointing CHU, relative to the stars, while detecting a moving Target. Not vice versa, which is the inflight configuration for PRISMA. The onground verification methods are up for a revisit in design, and is discussed in Section 8.1

Edge Stray:

The baffle system for the VBS CHUs on the PRISMA mission has been shortened from the standard baffle length, due to changes in volume requirements from SSC. This shortening has, as discussed in Section 7.1.1, given rise to Edge Stray detection from the Earth and Sun, marking a BBO in the list of detected centroids.

An analysis of which objects the FR system is able to lock onto was performed on inflight data seeded to the EM VBS system, providing different

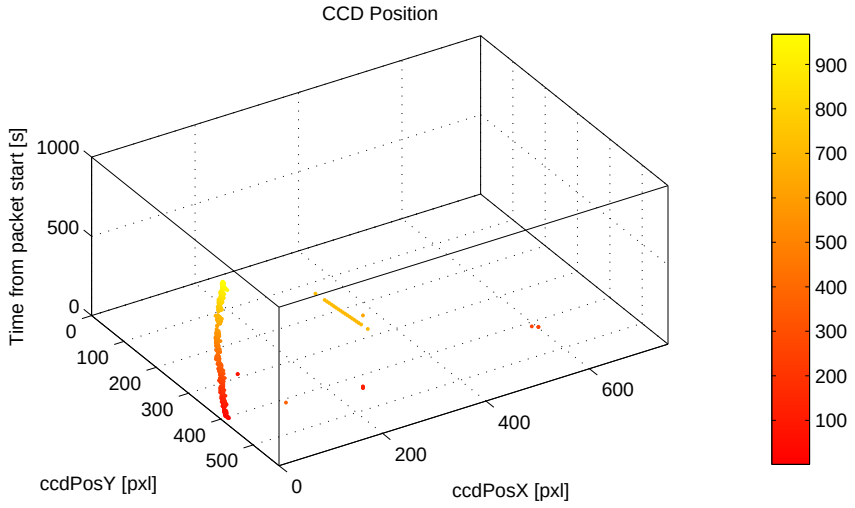

Figure 7.10. *VBS output solutions when Target is not contained in the centroid list. Edge Stray is locked onto instead.*

settings and scenarios depending on analysis. The full analysis is given in Appendix M, where all the different scenarios are given. One scenario involve detection of the Edge Stray object while having the true Target centroid neglected from the centroid list. The VBS solution output is given in Figure 7.10, clearly illustrating the detection of the Edge Stray.

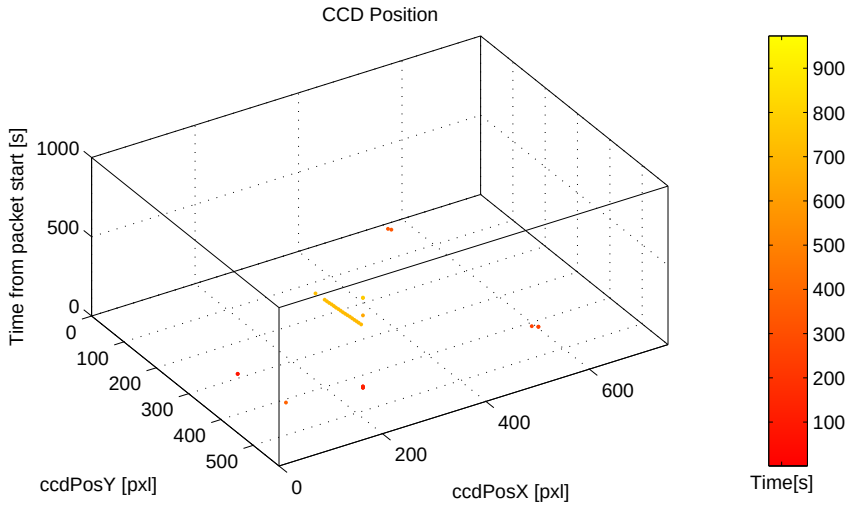

Figure 7.11. *VBS output solutions when Target and Edge Stray are not contained in the centroid list. Cross-passing objects are locked onto instead.*

The reason that the FR mode locks onto the Edge Stray, is simply due to the scenario where the boresight is steady pointing towards Target. All objects that for the CHU appear stationary are potential Target objects, giving high

confidence to the false Edge Stray.

An Edge Stray filter has been implemented into the centroiding algorithm of the μASC, which disables detection of the Edge Stray BBO and removes it from the centroid list. The result enables the VBS solution outputs given in Figure 7.11, where only a cross-passing object and hotspots are locked onto.

The locking of cross-passing objects are related to the functionality of the FR algorithms, which needs a minor redesign if such objects are to be neglected. This is discussed further in Section 8.1 regarding future work.

Apparent Direction:
During inflight, the GNC-module onboard PRISMA reported invalid Apparent Direction as determined by the VBS system, even though these datafields were marked as valid in the VBS telemetry packet.

This divergency was addressed in the first Inflight Data Analysis given in Appendix L, and has been identified to be a conversion based on a left-hand rotation system instead of the right-hand rotation system, as goes for the equatorial coordinate system on the celestial sphere.

The reason that this reversed rotation was not seen in the verification phase is due to fact that the VBS EGSE data analysis tool took the reversed rotation into account.
Both the VBS software and the VBS EGSE has been corrected, and has been verified on inflight data, as well as by the PRISMA GNC module.

Hotspots:
The locking of hotspots is due to the fact that these, similarly to the Edge Stray, are steady in the image field. Based on inflight data an analysis were initiated in order to tune the aggressiveness of hotspot filtering.

One specific part of inflight data illustrates clearly the influence of hotspots in the FR mode, and is given in Figure 7.12. At this given scenario the Main is reacquiring Target pointing, whereas a hotspot is locked onto before the Target centroid. Full Target lock is first acquired when the detection history of Target is above the detection history of the hotspot, which in this case takes several seconds.

To avoid false locks at such scenarios, the hotspot filtering is tuned aggressively in accordance with the given dataset and inflight experience. The final result is likewise illustrated in Figure 7.12, showing correct behavior for locking on to Target after Main has performed a maneuver.

Verification on inflight performance of the tuned hotspot filtering is currently pending.

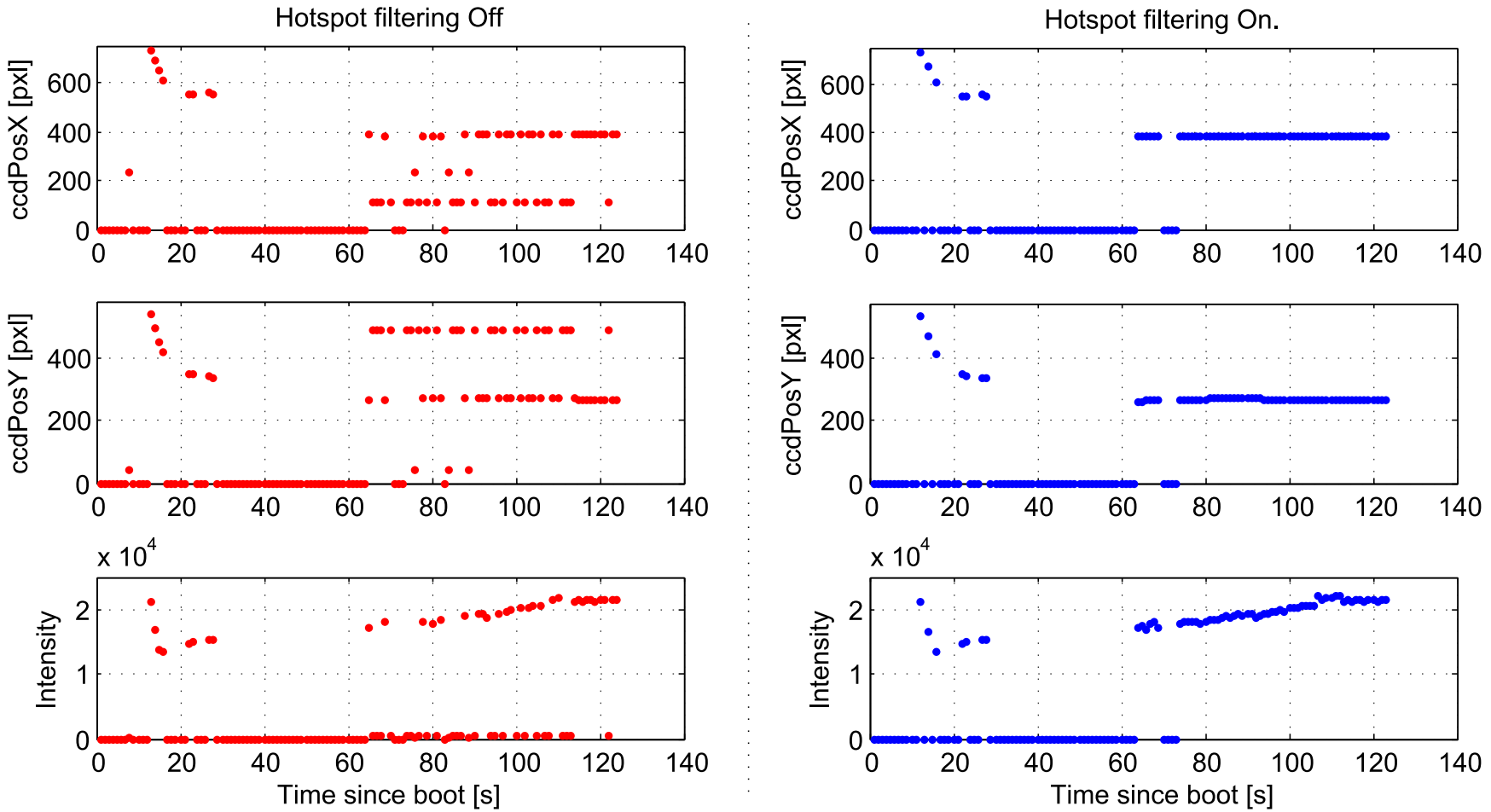

Figure 7.12. *Influence of hotspot filtering on VBS FR solutions. Left column illustrates the CCD centroid datafield of the VBS packet with hotspot filtering Off, and the right column with the hotspot filtering On.*

7.2.2 Alignment of Startrackers

One of the goals for the Early Harvest phase of the PRISMA mission was to determine the interalignment between the three startrackers, namely the standard startrackers CHU A and B versus the FR CHU of the VBS system denoted CHU C. At such, the attitude pointing of the FR CHU can be available, even when Target is blinding for the stars, by mapping the valid attitude from either of the two standard startrackers. Determination of this interalignment is likewise described in the first inflight data analysis presented in Appendix L.

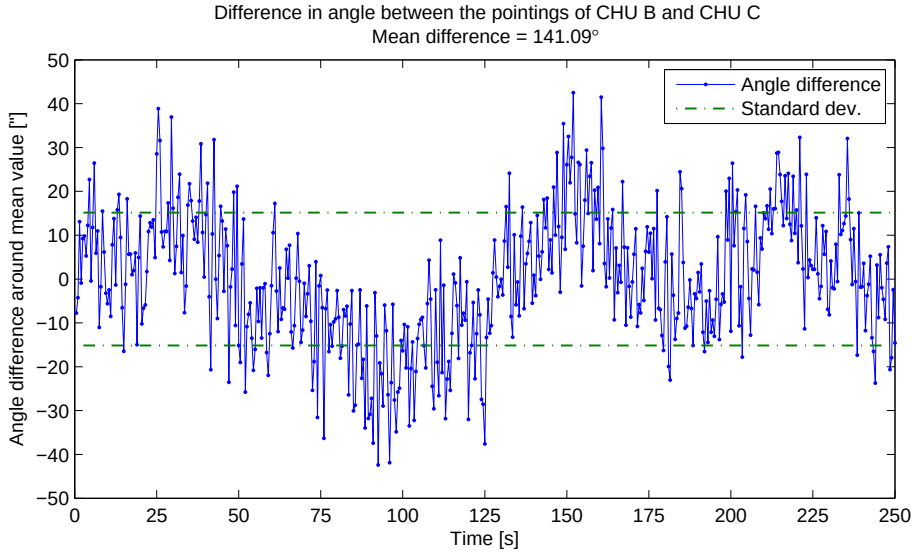

Figure 7.13. *Noise in angle difference between CHU B and CHU C attitudes over time.*

In Figure 7.13 is illustrated the noise in the angle difference between the attitudes of CHU B and CHU C, both giving vibration noise and time variance. The standard deviation for the 500 given sample points shows a standard deviation of $\sim 15''$ which for the mounting configuration of the CHUs is acceptable, namely the mount on two different panels with active reaction wheels included in the design of the Main satellite.

Based on the valid attitude data retrieved from the Early Harvest phase, two rotation quaternions have been created:

$$q_{B2C} = \begin{bmatrix} 0.892648 \\ 0.108352 \\ -0.283797 \\ 0.333012 \end{bmatrix} \Rightarrow \begin{array}{rcl} rot_z & = & 0.3112^\circ \\ rot_y & = & 35.3674^\circ \\ rot_x & = & 139.1821^\circ \end{array} \tag{7.1}$$

$$q_{A2C} = \begin{bmatrix} 0.891719 \\ -0.105216 \\ 0.285599 \\ 0.334960 \end{bmatrix} \Rightarrow \begin{array}{rcr} rot_z & = & 0.2597° \\ rot_y & = & -35.4387° \\ rot_x & = & 138.7412° \end{array} \tag{7.2}$$

By enabling mapping of the valid attitudes into the FR CHU will support the FR algorithms in scenarios, where Target is blinding for the stars in FOV of the FR CHU. Thus, extending the working area of the FR mode into the IR mode. This configuration is currently uploaded to the inflight PRISMA system, pending verification.

7.2.3 Performance

For the FR VBS mode, several performance parameters exists. These includes i.a. robustness of the Target lock, Target reacquiring and noise in the Target pointing. The robustness and Target reacquiring are touched in Section 7.2.1, showing continuous improvements during the data analysis of the Early Harvest. Especially the described analysis with Target vs No Target denoted by Figure 7.9, 7.10 and 7.11, given in Appendix M.

In order to describe the noise in the Target pointing, the previous analyzed dataset used in Figure 7.9 is considered, where the distance between Main and Target is between 9.5km to 10.5km. The noise of the Target pointing can be described by analyzing the angular velocity (ω) of the R.A. and Dec.

It applies that the R.A. and Dec. can be converted to a unit pointing vector by [Sidi2002]:

$$p = \begin{bmatrix} \cos(RA)\cos(Dec) \\ \sin(RA)\cos(Dec) \\ \sin(Dec) \end{bmatrix} \tag{7.3}$$

From where the angular velocity can be determined by:

$$\omega = \frac{\arccos(p_i \cdot p_{i+1})}{dT} \tag{7.4}$$

The angular velocity of the Target pointing in inertial coordinates are given in Figure 7.14, together with the mean value and standard deviation of ω. The mean value equals $mean(\omega) = 215.15"/s$ which corresponds directly to the estimated design value for the FR mode described in Section 4.1.

Additionally, the noise figure for the FR mode can be described by the standard deviation of the angular velocity, given by $std(\omega) = 6.91"/s$.

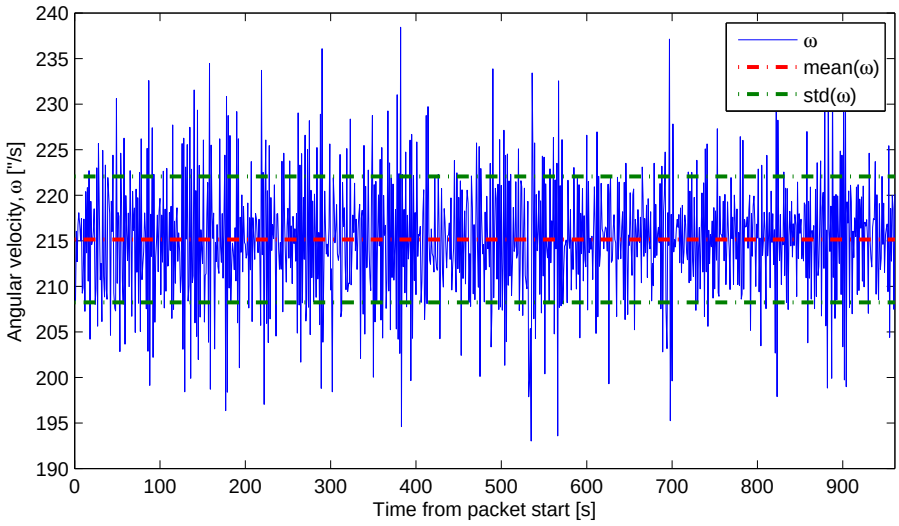

Figure 7.14. *Angular velocity for Target pointing with the standard deviation.*

7.3 Intermediate Range Mode

The Intermediate Range mode of the VBS system is functioning as the fallback mode for both FR and SR mode, and as an overlap during transit from the one mode to the other. The first activation of the IR mode took place during the AGC and shutter parameter adjustment as described in Section 7.1. Starting in FR mode with long exposures and from here revert into IR mode as soon as the shutter time decreased such that stars no longer could be detected.

This section will describe the first results acquired for the IR mode from the FR CHU and the following revisions with respect to performance adjustments. Additionally, the alignment determination between the two VBS CHUs are discussed, and finally a performance analysis of the IR mode for both the FR CHU and the SR CHU.

7.3.1 Initial Revisions

For the Early Harvest phase involving the Intermediate Range mode, three performance issues were addressed. One regarding multiple detected objects, the other regarding detection of Edge Stray effects, and the last regarding the Apparent Direction.

Multiple Detected Objects:

The IR mode is designed to point out the best Target candidate among the detected centroids. During Early Harvest the IR mode gave correct Target solution when Target was detected as a BBO or as a single centroid, but when

multiple centroids were detected in coherence with the Target centroid, the IR reported no objects detected instead of choosing the best candidate.

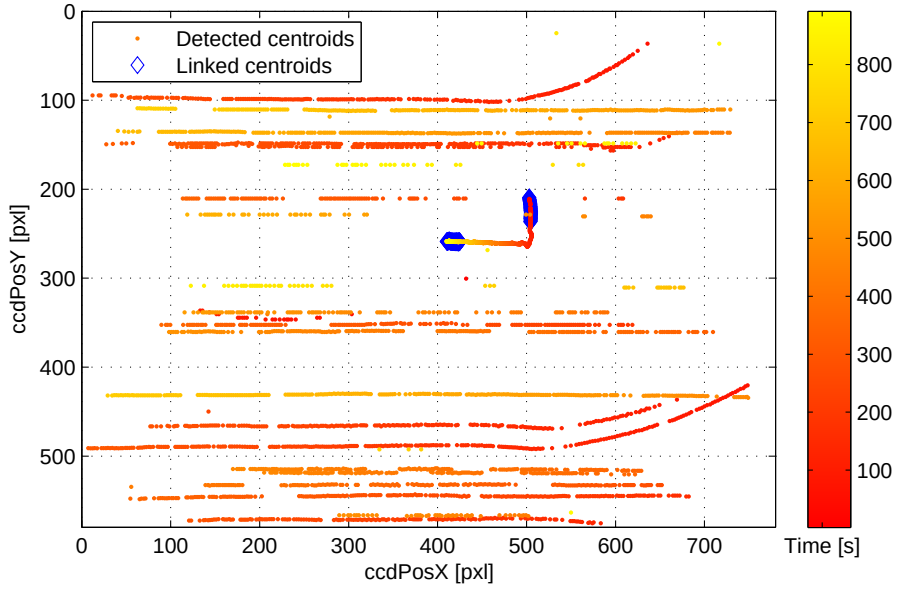

Figure 7.15. *IR mode solutions with invalid output for multiple detected objects. The gap between the valid solutions illustrates performance issue.*

This scenario is illustrated in Figure 7.15 where the IR mode has acquired Target, thereby loses it as soon as multiple objects are detected, and finally it easily reacquires when object count decreases. This undesired behavior were found to be a missing linkage between the internal variables of the IR algorithm and the telemetry packet, and was corrected in the software releases during Early Harvest phase.

The verification methods of the IR mode have only involved realizing the Target as either a single centroid or as a BBO among centroids, which led to this inflight misbehavior of the VBS system during IR mode. The verification methods will be taken up for revision and are discussed further in Section 8.1.

Edge Stray and Apparent Direction:

The two additional performance issues regarding IR mode involves detected of Edge Stray and Apparent Direction calculations.

These are directly related to the already addressed and clarified issues presented in the subsections of Section 7.2.

7.3.2 Alignment of VBS CHUs

The two VBS CHUs are mounted onto Main with a rotation of $\sim 90°$ relative around their boresight, such that their axes are aligned in the following manner:

$$\begin{aligned} X_{FR} &\approx -Y_{SR} \\ Y_{FR} &\approx X_{SR} \\ Z_{FR} &\approx Z_{SR} \end{aligned} \tag{7.5}$$

During the Early Harvest phase, Intermediate Range data was gathered from both the FR CHU and the SR CHU, with Target $\leftrightarrow$ Main distances $>$ 1km in order to perform an interalignment calibration in between the two VBS CHUs. By acquiring data at such great distances, the relative small translation between the two CHUs can be neglected.

Based on chosen data from i.a. the IR data illustrated in Figure L.12 and L.16, given in Appendix L, the inter-alignment can be estimated. The 90° rotation inbetween the two VBS CHUs is clearly illustrated in Figure L.20 and L.21. Final optimization of alignment between the two boresight pointings is an ongoing process at the time of writing.

7.3.3 Performance

The performance of the IR VBS mode has been analyzed based on the Early Harvest phase, and is presented in both Appendix L, regarding validity and robustness, and Appendix N, regarding performance while Main is performing orbit maneuvers.

The data presented in Appendix L formed the basis for the VBS CHU alignment discussed in Section 7.3.2 and shows that stable VBS solutions are available for IR mode as soon as Target is in FOV for any of the two VBS CHUs.

A snippet of the analyzed dataset from Appendix N is depicted in Figure 7.16, illustrating the scenario where Main is performing an orbit correction for its current trajectory.

Based on these CCD coordinates of the Target centroid, the Apparent Direction towards Target in reference to the CHU coordinate system has been calculated and is given in Figure 7.17

Due to the fact that the IR mode is unable to determine the attitude pointing of the current CHU, the dataset analyzed in Appendix N has been mapped based on attitude data derived from the standard startracker CHUs.

In Figure 7.18 is given the result of the Target pointing in inertial coordinates based on the mapped attitude data. Based on the shown result it is given that the orbit correction performed by Main is neglectable when this mapping procedure is used.

This processed and adapted data from Appendix N enables the fact that the functionality of the FR mode can be executed on the FR CHU even when

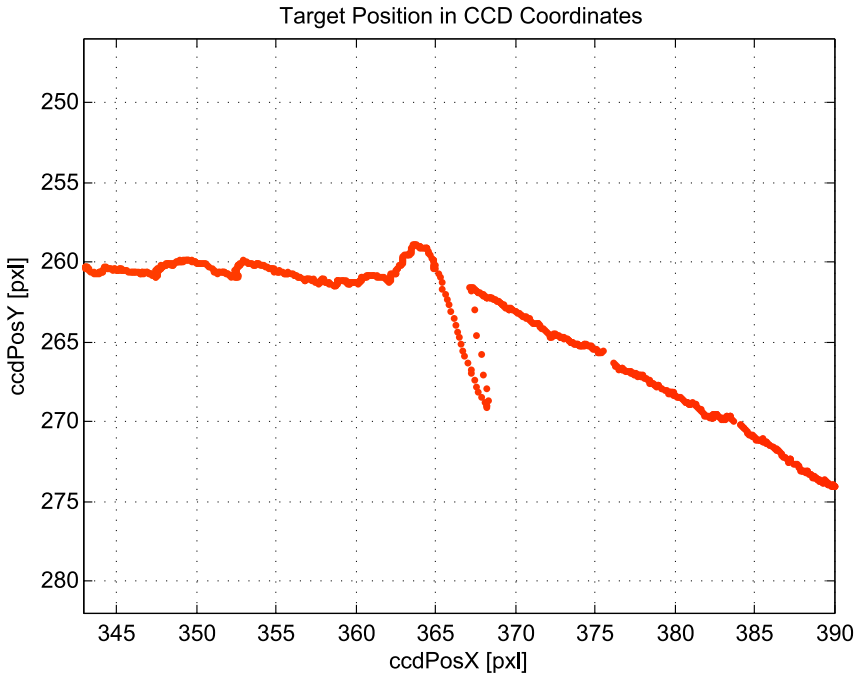

Figure 7.16. *Centroid snippet of zoomed area of detected Target from Figure N.1, where Main satellite performs orbit correction.*

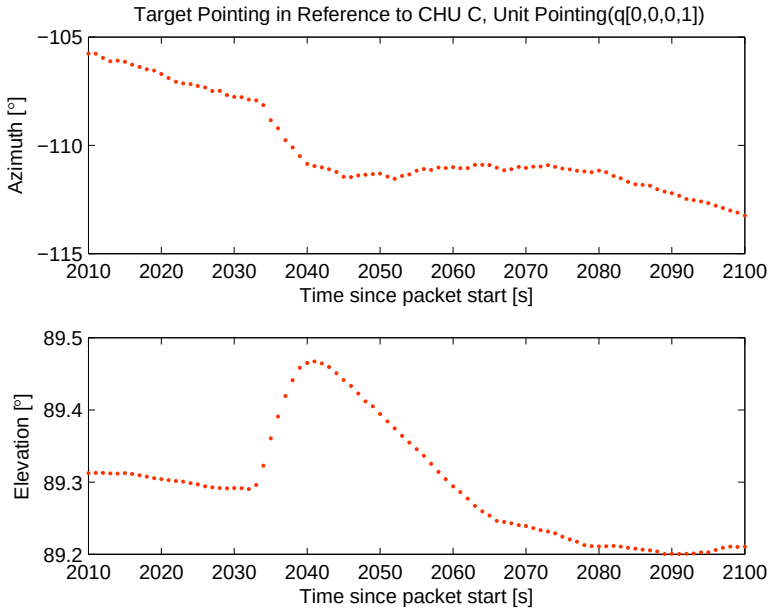

Figure 7.17. *Target pointing given in the internal camera coordinate system of CHU C.*

its attitude can not be determined by detected stars. By using the mapping introduced in Equation (7.1) and (7.2) the FR mode will be able to extend

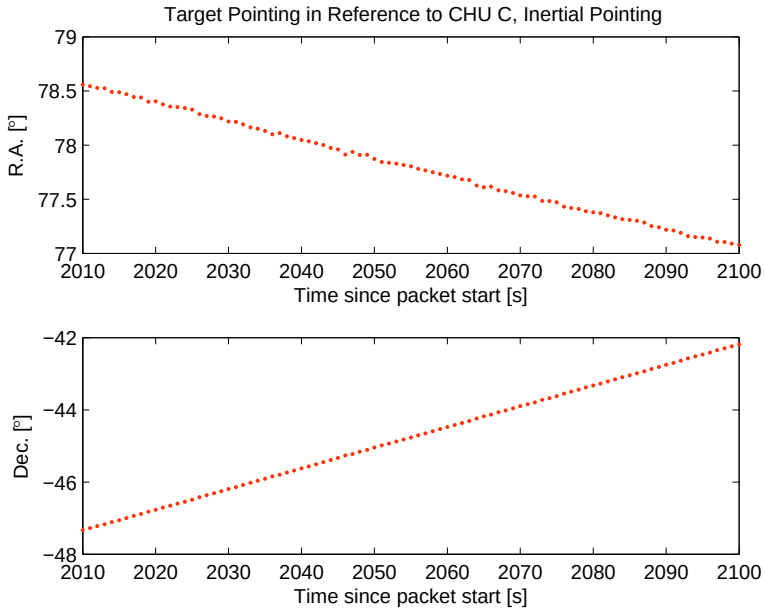

Figure 7.18. *Target pointing given in inertial coordinates.*

its field of operation into the IR mode, enabling neglection of falsely detected Target objects such as Moon blindings etc.

7.4 Short Range Mode

The Short Range mode of the VBS system is the latest to be activated on the PRISMA mission. At the time of writing the initial proximity operations[2] are carried out on the inflight PRISMA mission, having the VBS system activated as passenger.

The data from the close-up operations are currently being processed, thus no direct performance analysis of the inflight Short Range mode exists. Therefore, this section will mainly concern the initial observations on the ongoing data processing.

7.4.1 Initial Revisions

The Short Range mode is deeply reliant on the LED model, describing the placement of the LEDs in the Target reference frame with high accuracy. The role as passenger in PROX has therefore been focussed on gathering centroid data of the LEDsm in order to prepare for a re-calibration of the LED model based on the inflight configuration.

[2]Known as the PROX mode of the PRISMA mission, as described in Section 1.2.1.

No revisions of the Short Range mode algorithms and parameters have been performed yet, though the first revision has been planned following the PROX and will mainly concern upload of a re-calibrated LED model.

During the initial PROX operations, deviations has been experienced with the PPS-signal, used for synchronizing the LED pulsing and the integration time, and has resulted in the LEDs not being pulsed during image integration. This problem lies outside the VBS and μASC system, but has great influence on the system performance. This is especially seen on the AGC and shutter control, where a snippet is depicted in Figure 7.19.

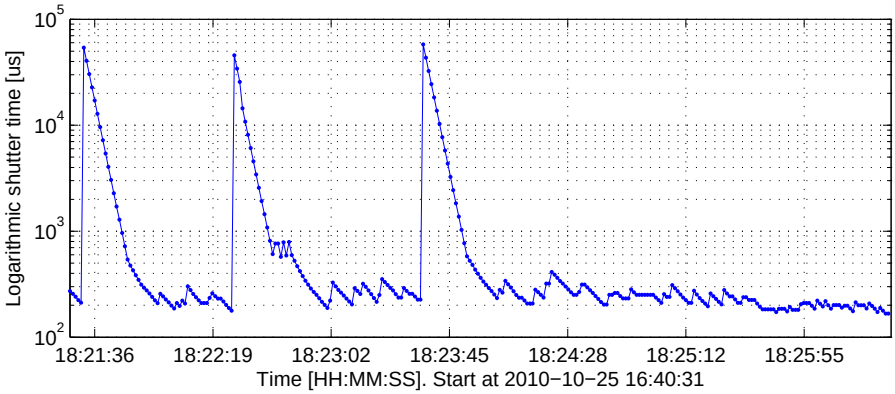

Figure 7.19. *Shutter time during Short Range Cooperative operations.*

The AGC and shutter control expects the LEDs to be present during integration and regulates thereafter from image to image. If the LEDs suddenly are not present the shutter time expands, and afterwards rolls back. In order to cope with the experienced outer PPS deviations a revision of the AGC and shutter control, with a less aggressive regulation, is currently pending inflight qualification.

7.4.2 Performance

The first SR-Coop solutions were achieved during an approach maneuver by Main, where the VBS system locked on to the Target satellite at a distance of 47m.

During PROX the Main↔Target distance has been as short as 10m while providing VBS data from the SR CHU.

As mentioned, the analysis of inflight SR VBS data is pending finalization of the PROX operations. Though, data snippets from the SR mode have been achieved. During the shutter time data given in Figure 7.19 the concurrent VBS data is illustrated in Figure 7.20, showing the determined Target position in reference to the SR CHU coordinate frame.

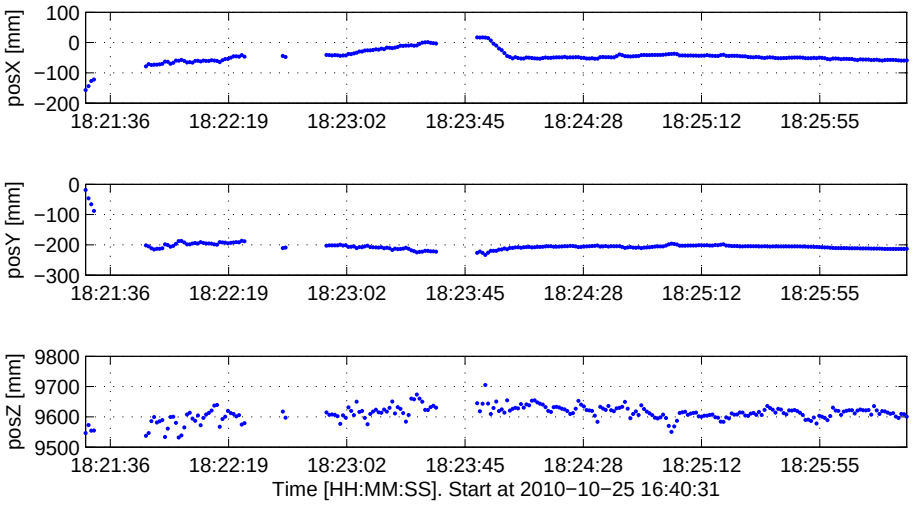

Figure 7.20. *Valid SR solutions from the VBS system with the integration times given in Figure 7.19.*

The influence of the unsteady integration time is clearly indicated in the dataset, seen both as invalid data sections and increased position noise.

Besides the unstable AGC and shutter control, one additional performance issue has been noted. It has been ascertained that the Target mock-up differs from the FM Target satellite regarding one specific characteristic with respect to light reflections, the honeycomb structured panels.

The cut edges of the honeycomb plates, that comprise the satellite panels, are only covered with clear capton tape, enabling view of the aluminium fractured surface which can create intense glints when the sun is at certain angle of incident. This effect has given rise to multiple false centroids detected besides the LED centroids, providing noise and instability to the system. Therefore, the additional glints in the SR scenarios are taken into consideration during data analysis and future tuning of the SR algorithms.

7.5 Mode Switching

In order to enable the entire dynamic range of the VBS system, correct overlapping in between the modes are necessary for having a smooth transition while Main performs approach or retried maneuvers in respect to Target.

The functionality and verification of the mode transitions for the VBS system are described in Chapter 6. This section will described the inflight experience with the VBS system during mode switching and its performance.

7.5.1 Far ↔ Intermediate Range

During the Early Harvest phase several maneuvers between Main and Target has been carried out, providing different scenarios for the VBS system. For the FR CHU, the transitional phases have resulted in mode switchings between IR and FR mode.

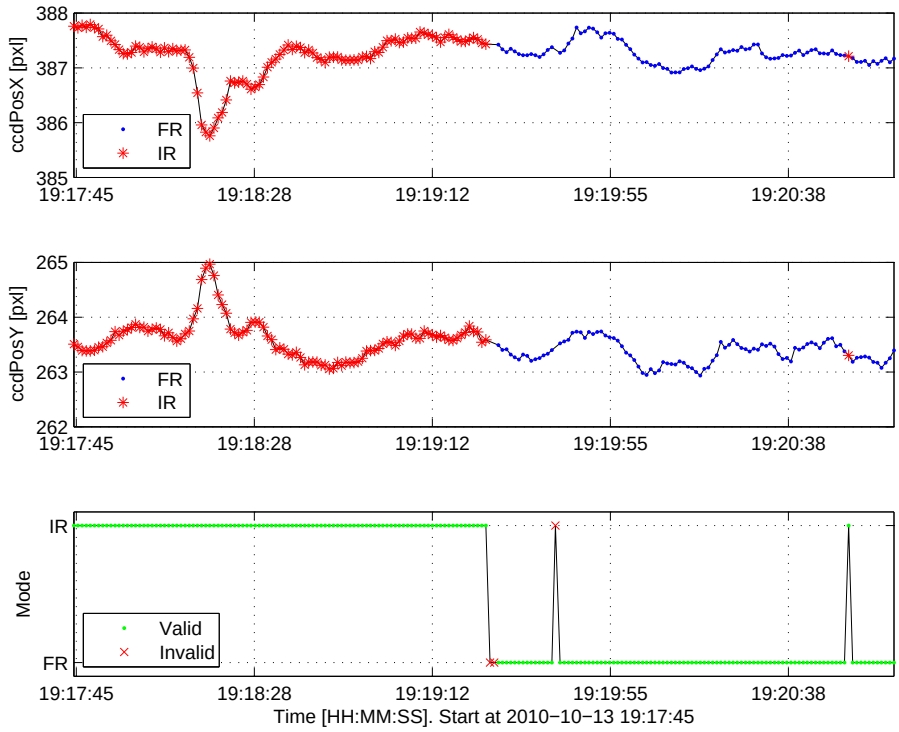

Figure 7.21. *Inflight IR→FR mode transition. The two top plots illustrates the CCD position result from the VBS packet, and the bottom plot illustrates the mode and validity flags from the VBS packet.*

Figure 7.21 illustrates the performance of the VBS system during a mode switch between IR mode to FR mode. During the dataset, the Main satellite performs a recede maneuver from $\sim$ 4km to $\sim$ 5km, resulting in correct hand-over from one mode to another.

The first two datapoints after the mode switch are expectedly marked as invalid. This is due to the fact that SSC has requested the VBS system only to execute the FR algorithms as long as an attitude can be determined by the FR CHU. The two invalid datapoints marks the run-in of the FR algorithm.

Subsequently, two single-pointed mode switches are occuring. The first is marked as an invalid solution given by the fact that neither FR or IR mode are able to determine a correct pointing, though the successive datapoint is

marked as valid.

The second single-pointed mode switch illustrates the scenario where the FR CHU attitude looses its attitude, and thereby cannot determine Target pointing. The FR mode falls back to IR mode which provides the correct Target pointing, creating a contiguous data series around the point.

7.5.2 Intermediate $\leftrightarrow$ Short Range

During PROX several mode switchings for the SR CHU have been experienced, where one example is given in Figure 7.22. Due to the fact that the CCD position during SR mode was marked as invalid, the Apparent Direction values are compared instead. Though, for IR mode the Apparent Direction points to the optical center, and for the SR mode it points to the origo of Target reference frame. Therefore, the depicted dataset is given in order to illustrate the stability of the two solution methods.

In the scenario for the given dataset, the mode switching is not caused by approach and recede maneuvers, but as an outcome due to the unstable shutter time as discussed in Section 7.4.1. The dataset clearly illustrates the SR modes ability to fall back as soon as the shutter time readjust to a stable level.

A thorough mode switching analysis is pending the data analysis of the ongoing inflight PROX operations.

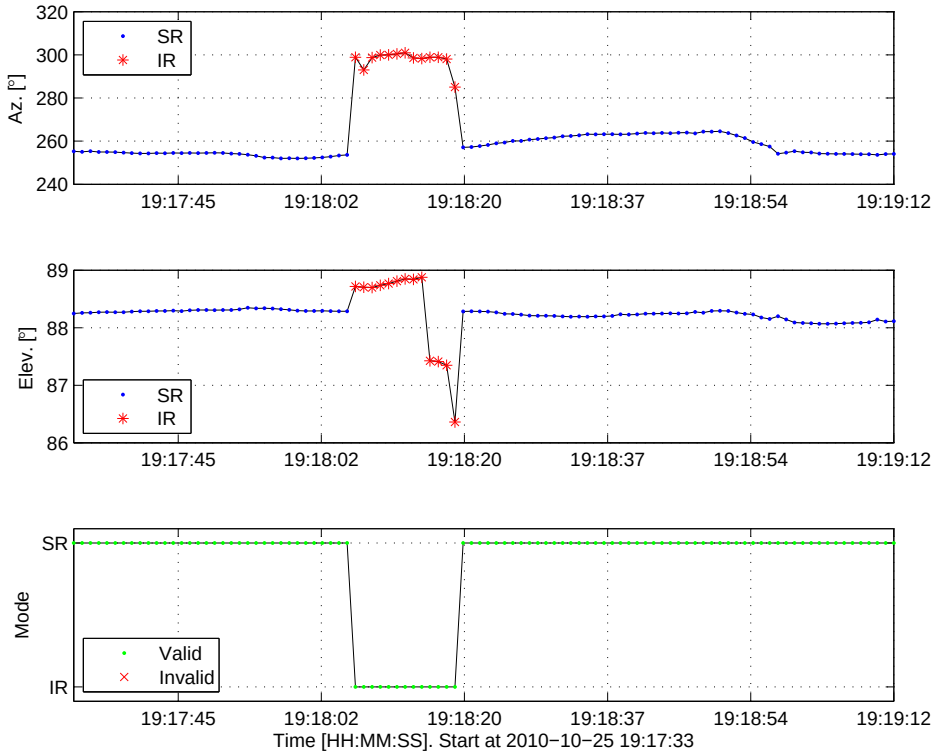

Figure 7.22. *Inflight SR↔IR mode transition. The two top plots illustrates the Apparent Direction result from the VBS packet in reference to the CHU coordinate frame, and the bottom plot illustrates the mode and validity flags from the VBS packet.*

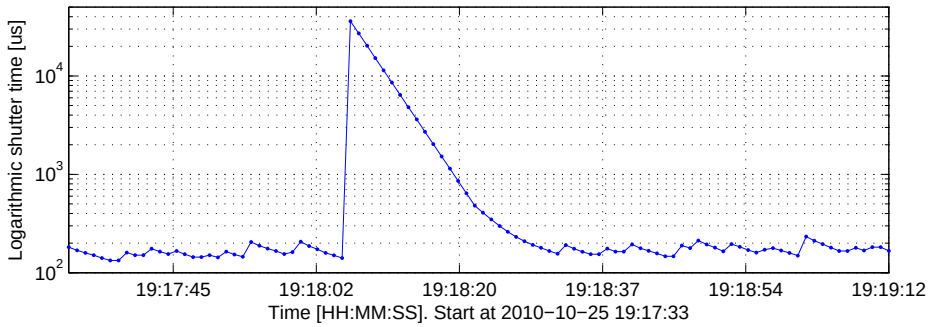

Figure 7.23. *Shutter time during mode transition.*

7.6 Summary

This chapter has presented the very first inflight results of the VBS system, acquired during the Early Harvest phase of the PRISMA mission. The inflight data has shown both desired and undesired behavior for a wide range of different scenarios, where the critical undesired behaviors have been corrected for and verified on the inflight VBS system.

Most aspects of the VBS performance range have been covered during the Early Harvest and the PROX operations, though the data analysis, the performance characterization and parameter tunings of the inflight VBS system have only begun and are ongoing and continuous during the entire PRISMA mission lifetime.

Chapter 8

Concluding Comments

The dissertation in hand has in fully described a vision based navigation sensor system which can support formation flying spacecraft to perform rendezvous and docking maneuvers.

The design and development of the Vision Based Sensor (VBS) has been based on thorough scenario analysis, which created the design parameters and requirements for the system. Furthermore, the implementation and realization of the VBS onto the already space-qualified μ-Advanced Stellar Compass, together with the needed hardware changes and support hardware, has been described into details.

The functionalities of the VBS system has been verified in realistic on-ground scenarios, which have focussed on both full coverage of the wide dynamic range, system robustness and solution availability. This has led to a performance analysis with respect to the expected noise figures and mode-switching capabilities of the VBS system.

Finally, the VBS system has been integrated on the platform of the technical demonstration satellite mission, PRISMA, and launched into orbit. The very first inflight VBS data from the Early Harvest phase of PRISMA has been presented together with the preliminary data analysis on inflight performance, illustrating that the VBS system is capable of delivering navigation data in all its three main modes with correct transition during mode switching.

8.1 Future Work

The first inflight experience with the VBS system is provided by the system integrated into the technological demonstration platform of PRISMA.

Since the PRISMA mission only recently has entered its operational phase,

the future work aspect includes both the inflight experience gathering from PRISMA and preparations for upcoming missions.

8.1.1 PRISMA Data Analysis

Several performance and system aspects of the VBS system are still to be realized on the PRISMA mission. This includes a full performance characterization of the VBS system in the scenarios available, but also exploration of the outer perimeters such as detection of the tractor beam system during close-up operations.

The PRISMA mission will also be used for preparation of the Short Range Non-cooperative mode by providing inflight images of the scenario which will form the basis of the algorithm implementation to the VBS system.

Additional data analysis of the acquired inflight PRISMA VBS data is likewise planned for. This includes analysis of the sun pressure to the satellites and the mutual influence from thruster firing on the relative Main and Target movements.

8.1.2 Upcoming Missions

The relative short inflight experience with the VBS system has already led to revision of the on-ground verification methods used, which has shown critical for upcoming missions which features a VBS system.

These revisions include i.a. a redesign of the Far Range verification methods which is in need of moving the celestial sky and not just the Target object, and a redesign of the Intermediate Range verification methods featuring multiple objects.

Additionally, the algorithm implementations are taken up for revision with respect to lesson learned from the PRISMA mission, including investigation of methods for acquiring Target. E.g. include analysis of the Target orbit rotation vector into the FR-algorithms in order to exclude cross-passing objects in the FOV.

This dissertation hereby concludes the work performed on the realization of a Vision Based Sensor implementation in the μASC navigation system during the course of the PhD project period of November 2007 to October 2010 at Measurements and Instrumentation Systems, DTU Space.

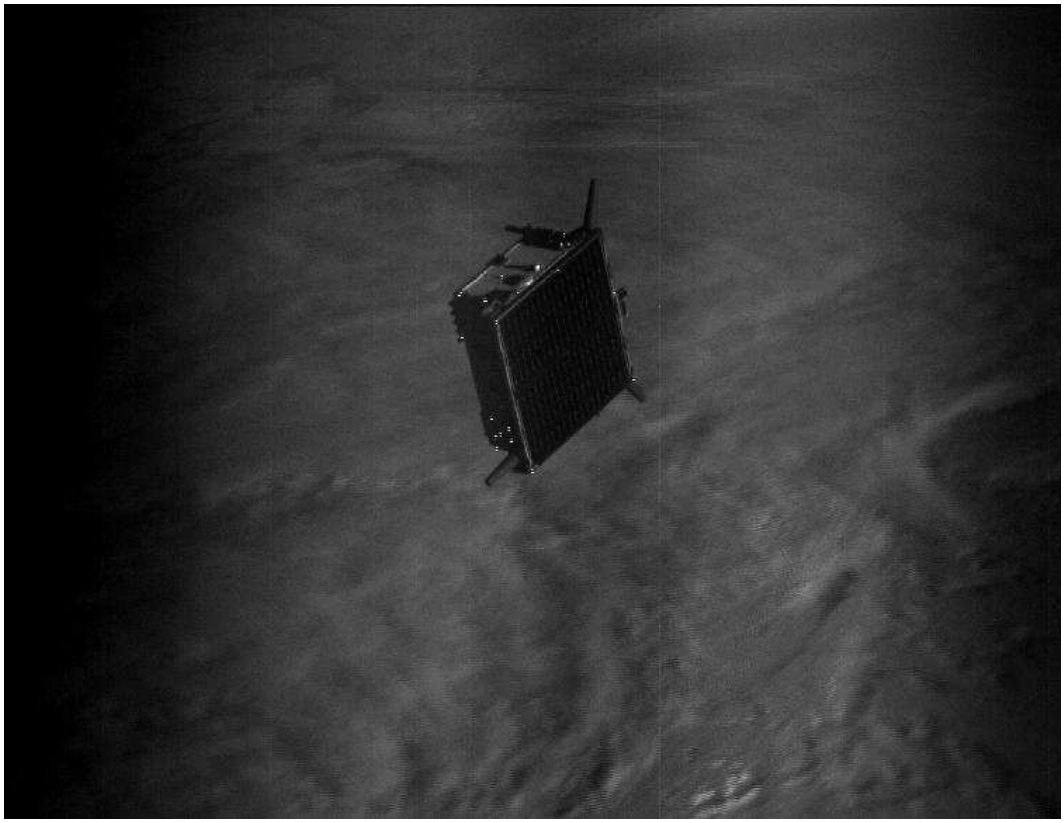

Figure 8.1. *View of Target from Short Range CHU with clouds in the background.*

"AD ASTRA PER ASPERA"
Surmounting adversity - reaching for the stars

October 31st, 2010

Bibliography

[Abidi1990] M.A. Abidi and T. Chandra. Pose Estimation for Camera Calibration and Landmark Tracking. *Robotics and Automation, 1990. Proceedings., 1990 IEEE International Conference on*, pages 420–426, 1990.

[Adams2006] Robert A. Adams. *Calculus: A Complete Course*. Pearson Addison Wesley, 6th edition, 2006.

[Baker2007] Martin John Baker. Euclidian Space - building a 3D world, 2007. http://www.euclideanspace.com/.

[Ballantyne1972] D.W.G Ballantyne and D.R. Lovett. *A Dictionary of Named Effects and Laws in Chemistry, Physics and Mathematics*. Science Paperback, 3rd edition, 1972.

[Benn2007] M. Benn. Design of a Visual Rendezvous and Docking Navigation Sensor. Master's thesis, Danish Technical University, September 2007.

[Benn2008a] Mathias Benn and John Leif Jørgensen. Short Range Pose and Position Determination of Spacecraft Using a μ-Advanced Stellar Compass. In *3rd International Symposium on Formation Flying, Missions and Technologies*. ESA, 2008. Presented at: International Symposium on Formation Flying, Missions and Technologies, Noordwijk, The Netherlands, 2008.

[Benn2008b] Mathias Benn and Jonas Bjarnø. VBS LED Solution, August 2008. Issue 1.5.

[Benn2008c] M. Benn. Led notes. Technical note 2, DTU Space, May 2008. Pages: 38.

[Benn2008d] M. Benn and F.E. Jørgensen. Target Diode Assembly Procedure. Technical report, DTU Space, 2008.

[Benn2009a] Mathias Benn and John Leif Jørgensen. Range Management of a Vision Based Rendezvous and Docking Navigation Sensor. In *Proceedings of the International Astronautical Conference, 2009.*

IAF, 2009. Presented at: International Astronautical Conference 2009, IAC, Daejeon, Korea, 2009.

[Benn2009b] Mathias Benn and Troelz Denver. TM/TC Delta Architectural Design Document, December 2009. Issue: 1.9.

[Benn2010a] M. Benn. Notes on Noise Measurements of the VBS Mock-up System. Technical note, DTU Space, March 2010.

[Bjarnoe2005] Jonas B. Bjarnø. Short Range Camera for Rendezvous in Space. Course: 31840 - Image Analysis on Microcomputer, December 2005.

[Bjarnoe2007] Jonas B. Bjarnø. Inertial Sensor Augmentation of Stellar Reference Units in the High Frequency Domain. Master's thesis, Danish Technical University, February 2007.

[Bjarnoe2010] J. Bjarnø. *Attitude Fusion Techniques for Spacecraft.* PhD thesis, DTU Space, August 2010.

[Denver2006a] Troelz Denver. Micro Advanced Stellar Compass - TM/TC Interface Control Document. Space Instrumentation Group, ASC-DTU-ICD-3004, Issue 2.1, September 2006.

[Denver2006b] T. Denver, J.L. Jørgensen, R. Michelsen, and P.S. Jørgensen. MicroASC Star Tracker Generic Developments. In *Small Satellite Systems and Services - The 4S Symposium 2006*. ESA, 2006. Presented at: Small Satellite Systems and Services Symposium, Chia Laguna, Sardinia, Italy, 2006.

[Eberhard2007] Gill Eberhard, D'Amico Simone, and Montenbruck Oliver. Autonomous Formation Flying for the PRISMA Mission. *Journal of Spacecraft and Rockets*, 44(3):671–681, 2007.

[Fortescue2003] Peter Fortescue, John Stark, and Graham Swinerd. *Spacecraft Systems Engineering.* John Wiley and Sons, 3rd edition, 2003.

[Granholm2007] Leif Granholm. PRISMA Radiation Control Plan, December 2007. DOX-RBS-#41423-v1C.

[Hansen2004b] F. Hansen. Satellite Technology Course - Orbital Mechanics, 2004. Danish Space Research Institute.

[Hedden1960] W.A. Hedden, J.F. Kircher, and B.W. King. Investigation of Some Glasses for High-Level Gamma-Radiation Dosimeters. *Journal of the American Ceramic Society*, 43(8):413–415, August 1960.

[Hellman2007] Hans Hellman. PRISMA Spacecraft Mechanical Layout, April 2007. DOX-RBS-#60708-v4.

[Inaba2000] N. Inaba and M. Oda. Autonomous Satellite Capture by a Space Robot: World First On-orbit Experiment on a Japanese Robot Satellite ETS-VII. *Robotics and Automation, 2000. Proceedings. ICRA '00. IEEE International Conference on*, 2:1169–1174, 2000.

[Janesick2001] J.R. Janesick. *Scientific Charge-Coupled Devices*. SPIE - The International Society for Optical Engineering, 2001.

[Joergensen2008] J. L. Jørgensen. PRISMA RVD Short Range Camera Performance Optimization. Technical report, DTU Space, 2008.

[Johnston2000] A.H. Johnston and T.F. Miyahira. Characterization of Proton Damage in Light-Emitting Diodes. *IEEE Transactions on Nuclear Science*, 47(6):2500–2507, 2000.

[Kasai1999] T. Kasai, M. Oda, and T. Suzuki. Results of the ETS-7 Mission: Rendezvous Docking and Space Robotics Experiments. *iSAIRAS'99. Fifth International Symposium on Artificial Intelligence, Robotics and Automation in Space (ESA SP-440)*, pages 299–306, 1999.

[Leinz2008] Manny R. Leinz, Chih-Tsai Chen, Michael W. Beaven, Thomas P. Weismuller, David L. Caballero, William B. Gaumer, Peter W. Sabasteanski, Peter A. Scott, and Mark A. Lundgren. Orbital express autonomous rendezvous and capture sensor system (arcss) flight test results. volume 6958, page 69580A. SPIE, 2008.

[Madsen2008] Kaj Madsen and Hans Bruun Nielsen. *Introduction to Optimization and Data Fitting*. DTU Informatics - IMM, August 2008.

[Massaro2010a] A. S. Massaro. Pharos Module for the Star Field Stimulator. Technical Note. Vers.2.0, DTU Space, March 2010.

[Massaro2010b] A. S. Massaro. Pharos Module for the Star Field Stimulator. Test Report. Vers.2.0, DTU Space, March 2010.

[Michelsen2006] R. Michelsen. micro Advanced Stellar Compass - General Information. Space Instrumentation Group, ASC-DTU-PRP-3000, Issue: 1.1, December 2006.

[Mortensen2005] M. Mortensen. micro-Advanced Stellar Compass - User's Manual. Space Instrumentation Group, ASC-DTU-MA-3001, Issue 1.2, September 2005.

[Murray2001] C. D. Murray and S. F. Dermott. *Solar System Dynamics*. Cambridge University Press, 2001.

[NASA1966] Gemini VII Mission Evaluation Team. Gemini Program Mission Report - Gemini VII, January 1966. NASA, Manned Spacecraft Center.

[Nocedal2006] Jorge Nocedal and Stephen J. Wright. *Numerical Optimization*. Springer, 2nd edition, 2006.

[Ochi1996] S. Ochi, T. Iizuka, M. Hamasaki, Y. Sato, T. Narabu, H. Abe, Y. Kagawa, and K. Kato. *Charge-coupled Device Technology*, volume 30(A). Gordon and Breach Publishers, 1996. ISBN: 90-5699-001-2.

[Persson2006a] Staffan Persson. Prisma Mission Requirements Document, November 2006. DOX-RBS-#60685-v2D.

[Persson2006b] Staffan Persson, Per Bodin, Eberhard Gill, Jon Harr, and John Jorgensen. PRISMA - An Autonomous Formation Flying Mission. *European Space Agency, (Special Publication) ESA SP*, 625 SP, 2006.

[Portree1995] David S. F. Portree. Mir Hardware Heritage, March 1995. NASA RP 1357.

[Rasc2007] RASC Royal Astronomical Society of Canada. The Stellar Magnitude System, September 2007. http://cobalt.golden.net/∼kwastro/.

[Rotenberger2008] Scott Rotenberger, David SooHoo, and Gabriel Abraham. Orbital express fluid transfer demonstration system. volume 6958, page 695808. SPIE, 2008.

[Schubert2006] E. F. Schubert. *Light-Emitting Diodes*. Cambridge University Press, 2nd edition, 2006.

[Sidi2002] Marcel J. Sidi. *Spacecraft Dynamics & Control*. Cambridge Aerospace Series 7. Cambridge, 2002.

[Soda1961] Reisuka Soda. Infrared Absorption Spectra of Quartz and Some other Silica Modification. *Bulletin of the Chemical Society of Japan*, 34(10):1491–1495, 1961.

[Spenvis2007] Belgian Institute for Space Aeronomy. SPENVIS - The Space Environment Information System, 2007. http://www.spenvis.oma.be.

[Thuesen2007] G. Thuesen. Sr90 Irradiation of LEDs. Technical report, DTU Space, 2007.

[Wertz2002] James R. Wertz. *Spacecraft Attitude Determination and Control*. Kluwer Academic Publishers, 2002.

Appendices

Appendix A

Datasheet of LED SMC735

Marubeni

SMC735 High Performance infrared SMD LED on ceramics

SMC735 consists of an AlGaAs LED mounted on the ceramics package
and is sealed with silicone or epoxy resin.
It emits a spectral band of radiation at 735nm.

♦Specifications

1) Product Name	SMD type infrared LED
2) Type No.	SMC735
3) Chip	
(1) Chip Material	AlGaAs
(2) Peak Wavelength	735nm typ.
4) Package	
(1) Package	Ceramics
(2) Lens	Silicone or Epoxy resin

♦Outer dimension (Unit : mm)

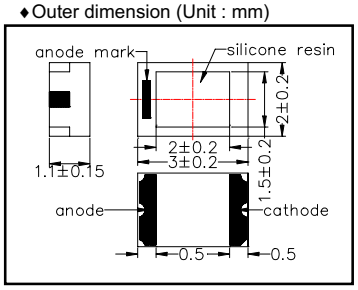

♦Absolute Maximum Ratings

Item	Symbol	Maximum Rated Value	Unit	Ambient Temperature
Power Dissipation	P_D	200	mW	Ta=25°C
Forward Current	I_F	100	mA	Ta=25°C
Pulse Forward Current	I_{FP}	500	mA	Ta=25°C
Reverse Voltage	V_R	5	V	Ta=25°C
Operating Temperature	T_{OPR}	-20 ~ +80	°C	
Storage Temperature	T_{STG}	-30 ~ +80	°C	
Soldering Temperature	T_{SOL}	240	°C	

‡Pulse Forward Current condition: Duty=1% and Pulse Width=10us.
‡Soldering condition: Soldering condition must be completed within 3 seconds at 240°C

♦Electro-Optical Characteristics [Ta=25°C]

Item	Symbol	Condition	Minimum	Typical	Maximum	Unit
Forward Voltage	V_F	I_F=50mA		1.85	2.00	V
Reverse Current	I_R	V_R=5V			10	uA
Total Radiated Power	P_O	I_F=50mA	4.0	10.0		mW
Radiant Intensity	I_E	I_F=50mA	2.0	5.0		mW/sr
Peak Wavelength	λ_P	I_F=50mA		735		nm
Half Width	$\Delta\lambda$	I_F=50mA		30		nm
Viewing Half Angle	$\theta_{1/2}$	I_F=50mA		±55		deg.
Rise Time	tr	I_F=50mA		80		ns
Fall Time	tf	I_F=50mA		80		ns

‡Total Radiated Power is measured by Photodyne #500
‡Radiant Intensity is measured by Tektronix J-6512.

Marubeni America Corporation
3945 Freedom Circle, Suite 1000, Santa Clara, CA 95054
408-330-0650 (Ext. 323), 408-330-0655 (Fax), sales@tech-led.com

Figure A.1. *Datasheet of LED SMC735 (Source: www.tech-led.com).*

Appendix B

Characterization of LED SMC735

The LED used to provide the feature points on the PRISMA Target model is of the type SMC735. This section presents the results from characterization of the thermal effects on the wavelength stability of the LED. For this purpose a test bench was setup based on following equipment:

- The LED under test fixated to an aluminium bracket with similar thermal characteristics as the LED aluminium housing.
- Thermal resistor heater mounted on backside of aluminium bracket, enabling temperature increase control.
- PT100 temperature detector element placed in close proximity with the LED.
- Laser Spectrum Analyzer with a spectral response range of 350-1000nm.
- Collimating lens system in front of the LED in order to focus the light into the spectrum analyzer.

In Figure B.1 this test bench illustrated. In the following figures, from Figure B.2 to B.11, is the spectrum analyzer output to the oscilloscope illustrated. Here the trig-arrow indicates the 735nm mark, the 1st dataset indicates wavelength with each tick as 1nm and the 2nd dataset indicates the detected intensity for the given wavelength.

Each of the oscilloscope screenshots are captured with different test setup settings as indicated by the figure text. Discussion and analysis is given in Section 3 based on the presented data.

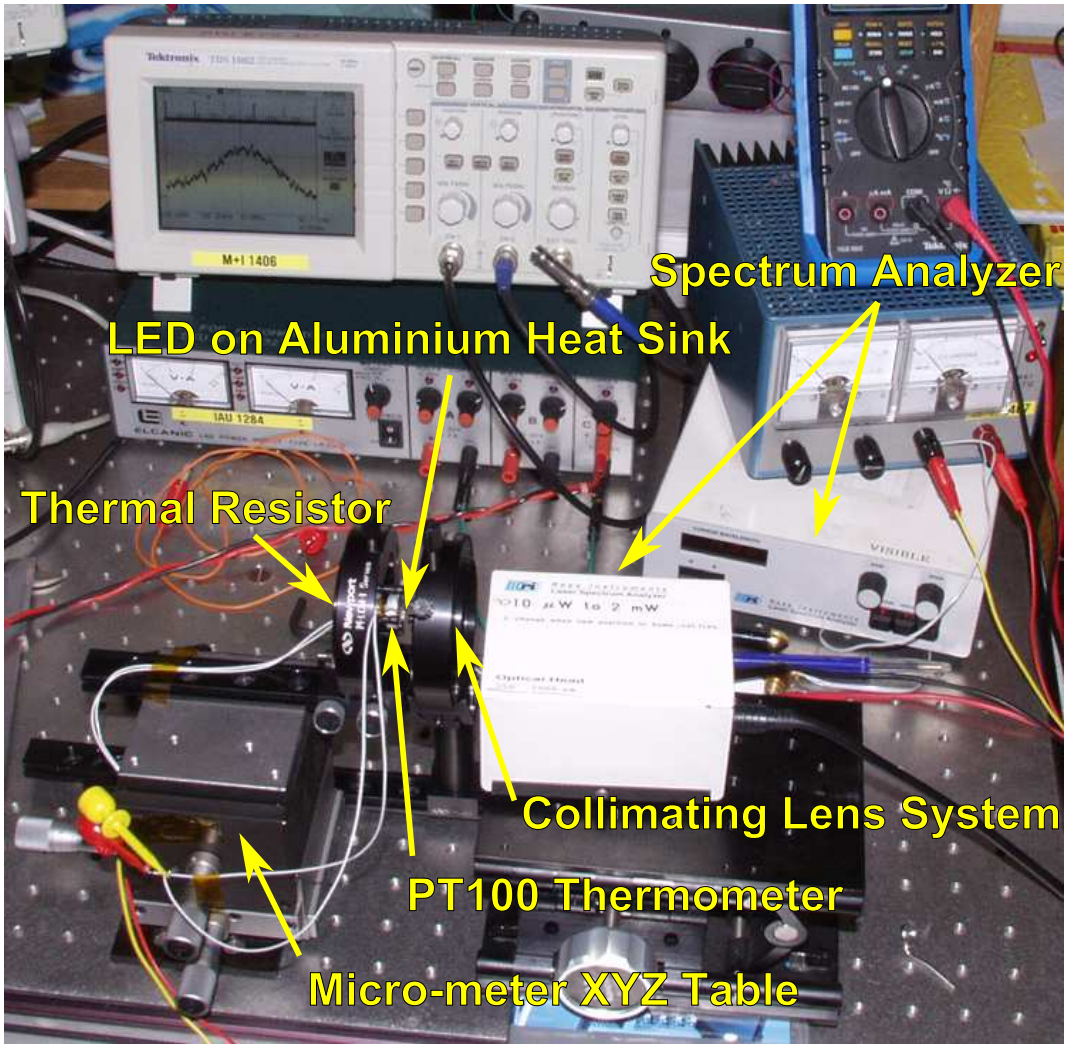

Figure B.1. *Test bench for thermal characterization of the SMC735.*

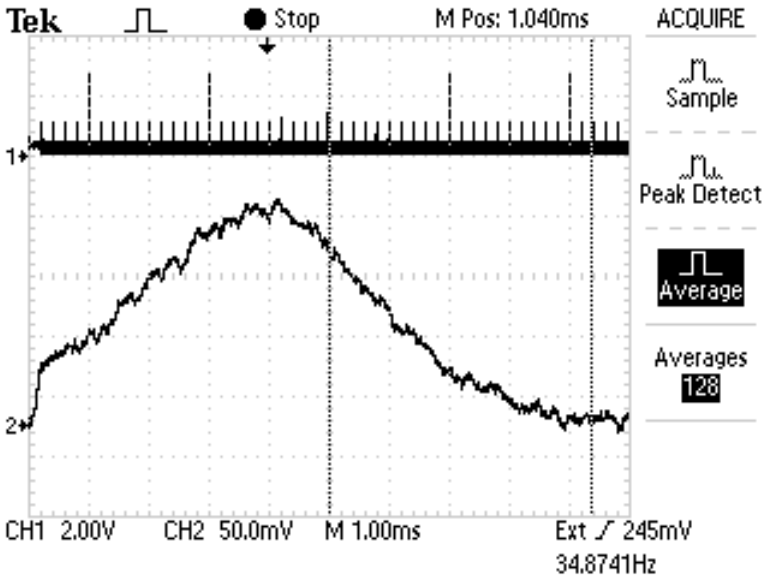

Figure B.2. *LED pulsed with 2.0*V *in 2*ms *at a 1*s *cycle. Peak wavelength at 735*nm.

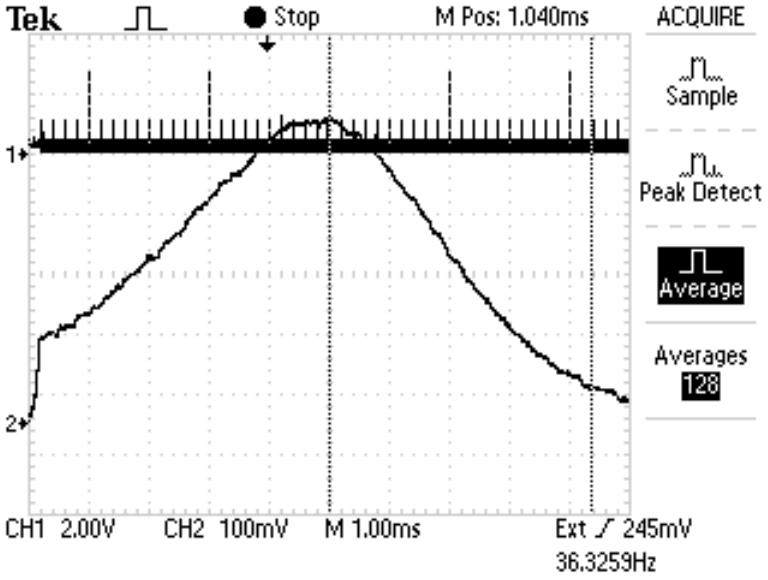

Figure B.3. *LED pulsed with 3.2*V *in 2*ms *at a 1*s *cycle. Peak wavelength at 739*nm.

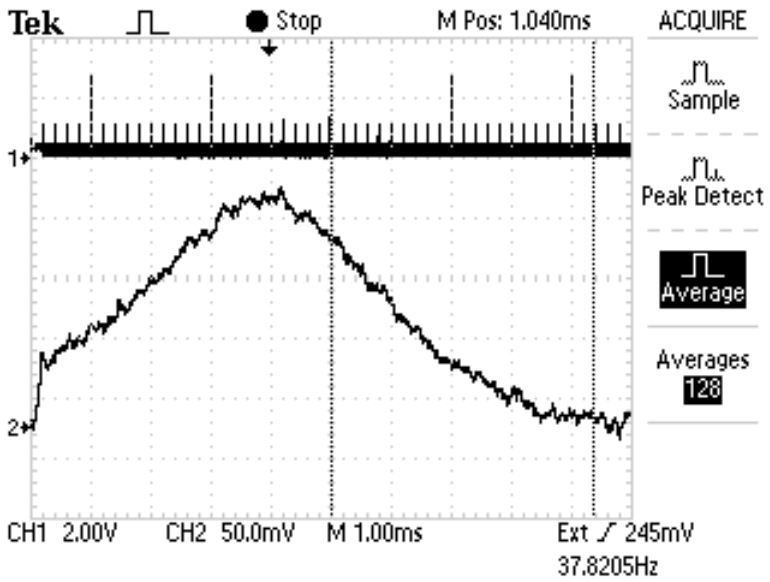

Figure B.4. *LED pulsed with 2.0*V *in 5*ms *at a 1*s *cycle. Peak wavelength at 735*nm.

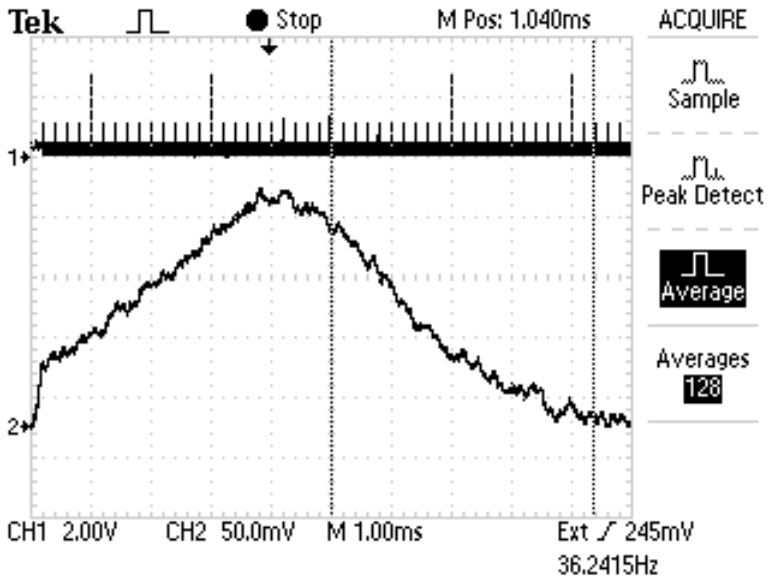

Figure B.5. *LED pulsed with 2.0*V *in 8*ms *at a 1*s *cycle. Peak wavelength at 736*nm.

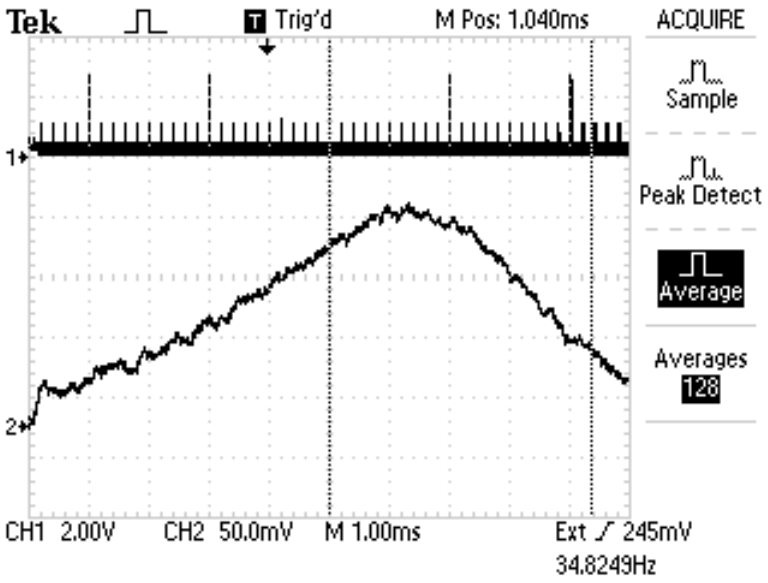

Figure B.6. *LED powered with 2.0*V *continuously. Peak wavelength at 748*nm.

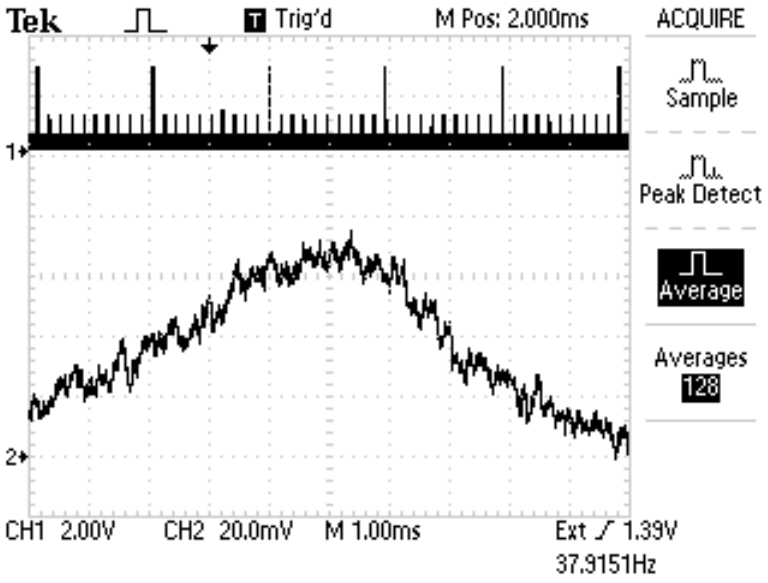

Figure B.7. *PT100 at temperature 27*°C*. LED powered with 1.85*V *continuously. Peak wavelength at 745*nm.

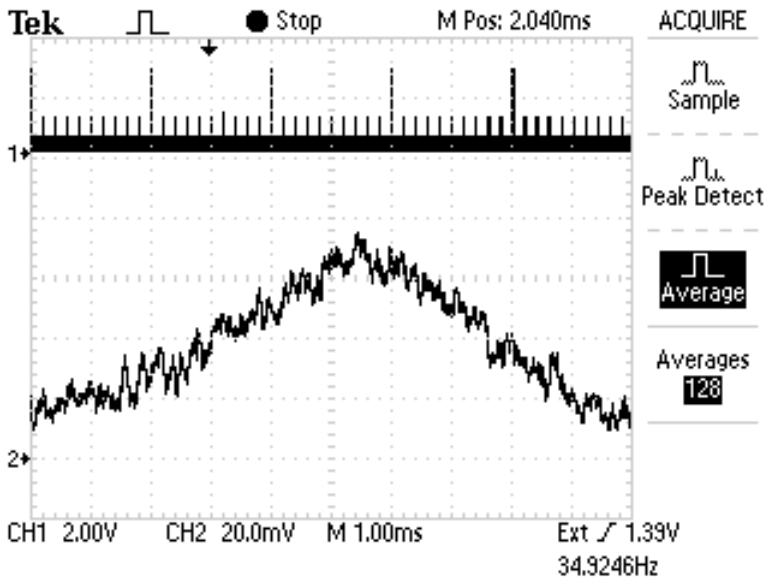

Figure B.8. *PT100 at temperature 38*°C*. LED powered with 1.85*V *continuously. Peak wavelength at 747*nm*.*

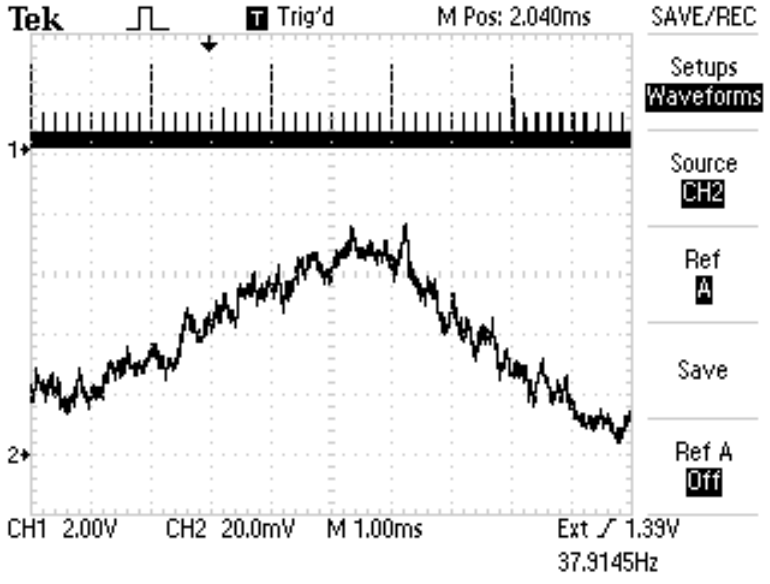

Figure B.9. *PT100 at temperature 50*°C*. LED powered with 1.85*V *continuously. Peak wavelength at 749*nm*.*

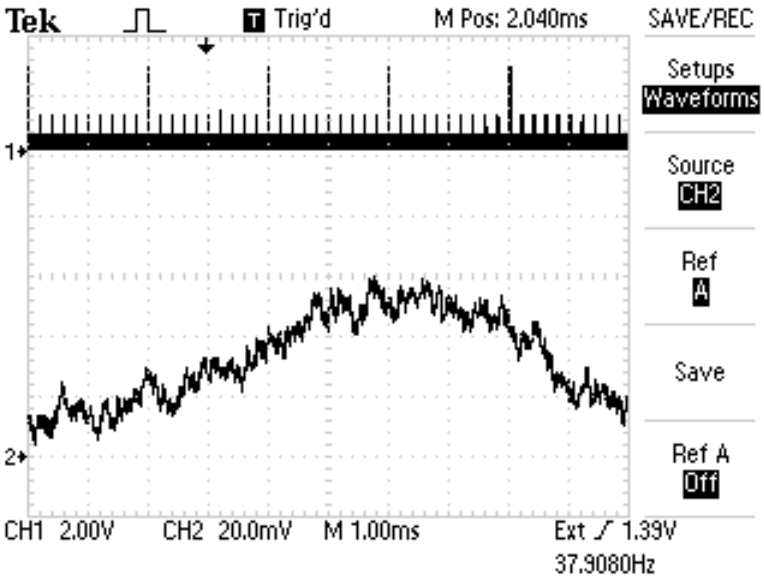

Figure B.10. *PT100 at temperature 74*°C*. LED powered with 1.85*V *continuously. Peak wavelength at 752*nm*.*

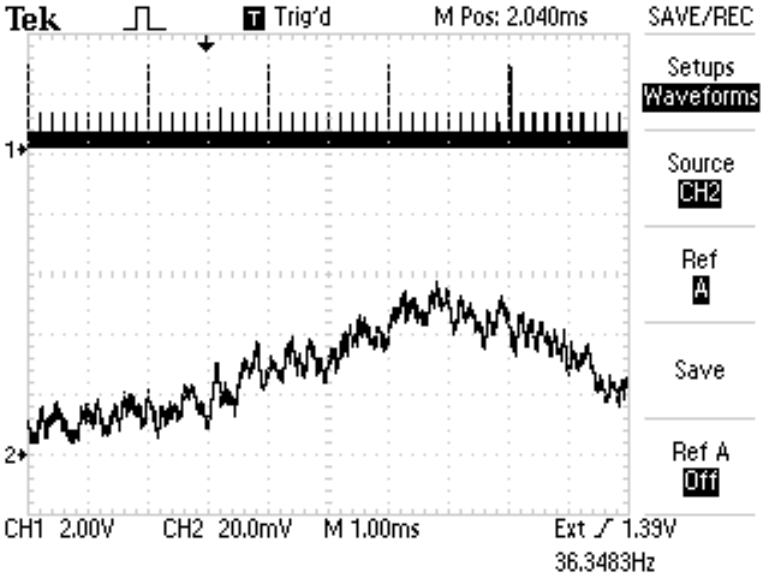

Figure B.11. *PT100 at temperature 91*°C*. LED powered with 1.85*V *continuously. Peak wavelength at 755*nm*.*

Appendix C

PRISMA FM LEDs

This note-set was created in order to compare the quality and the radiation pattern in between the LEDs used for the PRISMA mission.

The radiation pattern was measured using the μASC with an EM SR CHU having fixed integration time, capturing centroids while rotating around each individual LED in both the yz- and xz-plane.

This document has been used to group the LEDs based on similarities in their characteristics. Each group represent a panel of the Target satellite, and has been used to determine the final wiring and the finalization of the LED placement model description given in [Benn2008b].

LED Notes

Mathias Benn

May 13th 2008

Id A

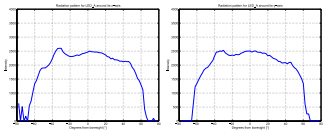

Figure 1: Radiation pattern of LED in yz- and xz-plane respectively.

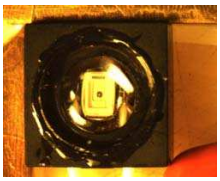

Figure 2: Photo of LED from above.

Remarks:

- Ok.

Id B

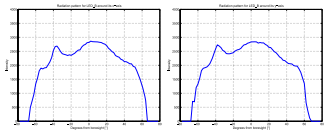

Figure 3: Radiation pattern of LED in yz- and xz-plane respectively.

Figure 4: Photo of LED from above.

Remarks:

- Ok.

Id C

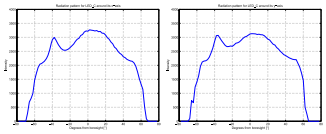

Figure 5: Radiation pattern of LED in yz- and xz-plane respectively.

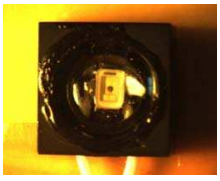

Figure 6: Photo of LED from above.

Remarks:

- Ok.

Id D

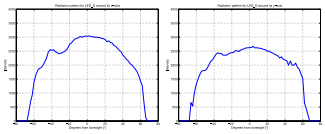

Figure 7: Radiation pattern of LED in yz- and xz-plane respectively.

Figure 8: Photo of LED from above.

Remarks:

- Ok.

5

Id E

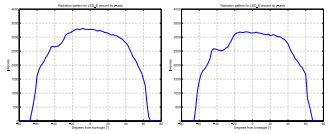

Figure 9: Radiation pattern of LED in yz- and xz-plane respectively.

Figure 10: Photo of LED from above.

Remarks:

- Ok.

6

Id F

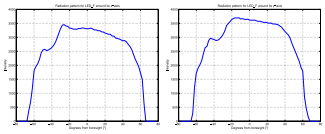

Figure 11: Radiation pattern of LED in yz- and xz-plane respectively.

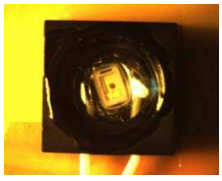

Figure 12: Photo of LED from above.

Remarks:

- Ok.

7

Id G

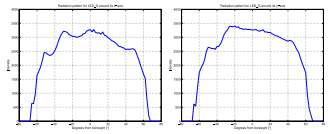

Figure 13: Radiation pattern of LED in yz- and xz-plane respectively.

Figure 14: Photo of LED from above.

Remarks:

- Ok.

8

Id H

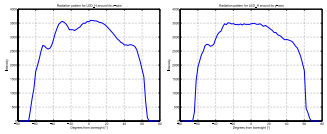

Figure 15: Radiation pattern of LED in yz- and xz-plane respectively.

Figure 16: Photo of LED from above.

Remarks:

- Ok.

9

Id I

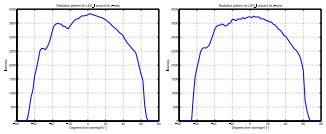

Figure 17: Radiation pattern of LED in yz- and xz-plane respectively.

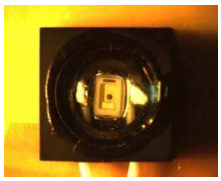

Figure 18: Photo of LED from above.

Remarks:

- Ok.

10

Id J

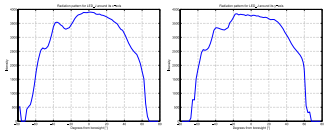

Figure 19: Radiation pattern of LED in yz- and xz-plane respectively.

Figure 20: Photo of LED from above.

Remarks:

- Ok.

11

Id K

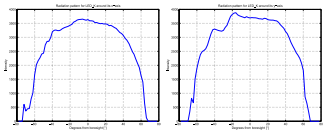

Figure 21: Radiation pattern of LED in yz- and xz-plane respectively.

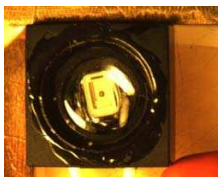

Figure 22: Photo of LED from above.

Remarks:

- Ok.

12

Id L

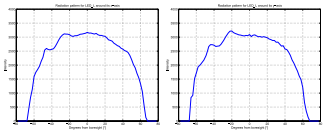

Figure 23: Radiation pattern of LED in yz- and xz-plane respectively.

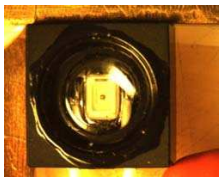

Figure 24: Photo of LED from above.

Remarks:

- Ok.

13

Id M

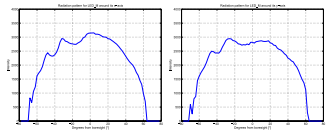

Figure 25: Radiation pattern of LED in yz- and xz-plane respectively.

Figure 26: Photo of LED from above.

Remarks:

- Ok.

14

Id N

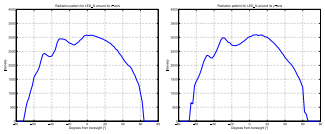

Figure 27: Radiation pattern of LED in yz- and xz-plane respectively.

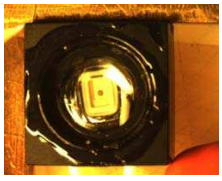

Figure 28: Photo of LED from above.

Remarks:

- Ok.

15

Id O

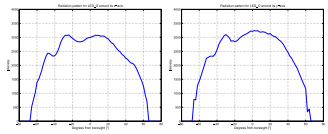

Figure 29: Radiation pattern of LED in yz- and xz-plane respectively.

Figure 30: Photo of LED from above.

Remarks:

- Ok.

16

Id P

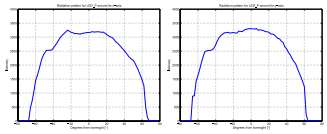

Figure 31: Radiation pattern of LED in yz- and xz-plane respectively.

Figure 32: Photo of LED from above.

Remarks:

- Ok.

17

Id Q

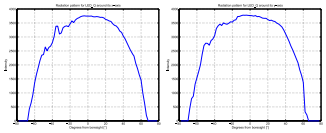

Figure 33: Radiation pattern of LED in yz- and xz-plane respectively.

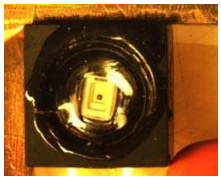

Figure 34: Photo of LED from above.

Remarks:

- Ok.

18

Id R

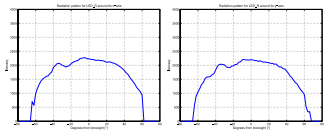

Figure 35: Radiation pattern of LED in yz- and xz-plane respectively.

Figure 36: Photo of LED from above.

Remarks:

- Ok.

19

Id a

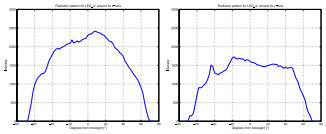

Figure 37: Radiation pattern of LED in yz- and xz-plane respectively.

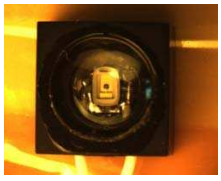

Figure 38: Photo of LED from above.

Remarks:

- Cable extended. Use LED as spare.

20

Id b

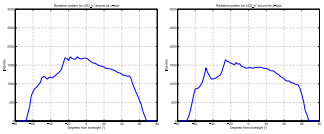

Figure 39: Radiation pattern of LED in yz- and xz-plane respectively.

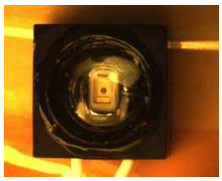

Figure 40: Photo of LED from above.

Remarks:

- Cable extended. Use LED as spare.

21

Id c

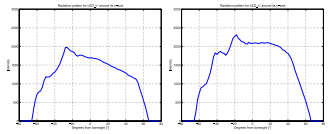

Figure 41: Radiation pattern of LED in yz- and xz-plane respectively.

Figure 42: Photo of LED from above.

Remarks:

- Ok.

22

Id d

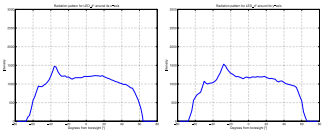

Figure 43: Radiation pattern of LED in yz- and xz-plane respectively.

Figure 44: Photo of LED from above.

Remarks:

- Ok.

23

Id e

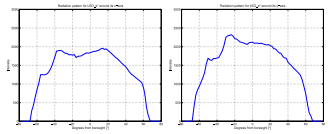

Figure 45: Radiation pattern of LED in yz- and xz-plane respectively.

Figure 46: Photo of LED from above.

Remarks:

- Ok.

24

Id f

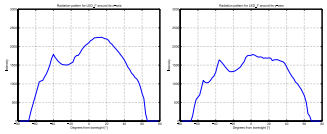

Figure 47: Radiation pattern of LED in yz- and xz-plane respectively.

Figure 48: Photo of LED from above.

Remarks:

- Ok.

25

Id g

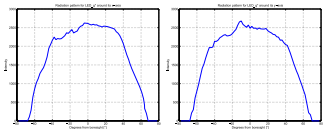

Figure 49: Radiation pattern of LED in yz- and xz-plane respectively.

Figure 50: Photo of LED from above.

Remarks:

- Ok.

26

Id h

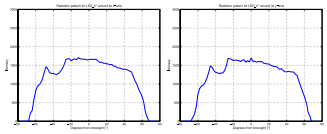

Figure 51: Radiation pattern of LED in yz- and xz-plane respectively.

Figure 52: Photo of LED from above.

Remarks:

- Ok.

27

Id i

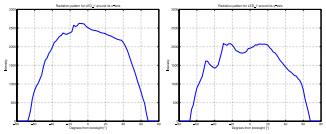

Figure 53: Radiation pattern of LED in yz- and xz-plane respectively.

Figure 54: Photo of LED from above.

Remarks:

- Ok.

28

Id j

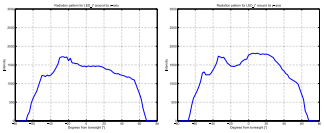

Figure 55: Radiation pattern of LED in yz- and xz-plane respectively.

Figure 56: Photo of LED from above.

Remarks:

- Ok.

29

Id k

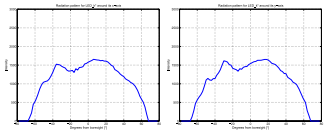

Figure 57: Radiation pattern of LED in yz- and xz-plane respectively.

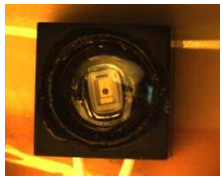

Figure 58: Photo of LED from above.

Remarks:

- Ok.

30

Id l

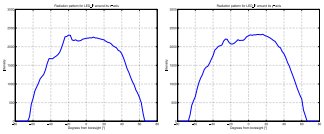

Figure 59: Radiation pattern of LED in yz- and xz-plane respectively.

Figure 60: Photo of LED from above.

Remarks:

- Ok.

31

Id m

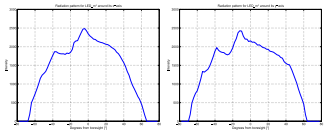

Figure 61: Radiation pattern of LED in yz- and xz-plane respectively.

Figure 62: Photo of LED from above.

Remarks:

- Ok.

32

Id n

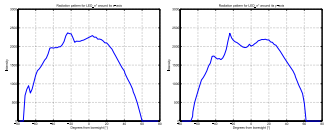

Figure 63: Radiation pattern of LED in yz- and xz-plane respectively.

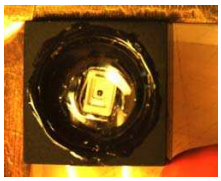

Figure 64: Photo of LED from above.

Remarks:

- Ok.

33

Id o

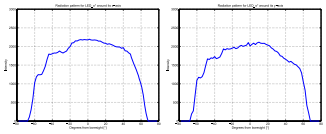

Figure 65: Radiation pattern of LED in yz- and xz-plane respectively.

Figure 66: Photo of LED from above.

Remarks:

- Ok.

34

Id p

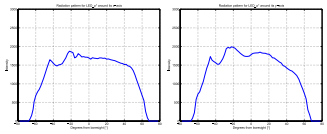

Figure 67: Radiation pattern of LED in yz- and xz-plane respectively.

Figure 68: Photo of LED from above.

Remarks:

- Ok.

35

Id q

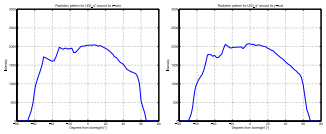

Figure 69: Radiation pattern of LED in yz- and xz-plane respectively.

Figure 70: Photo of LED from above.

Remarks:

- Ok.

36

Id r

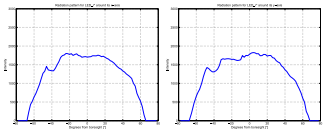

Figure 71: Radiation pattern of LED in yz- and xz-plane respectively.

Figure 72: Photo of LED from above.

Remarks:

- Ok.

37

Id s

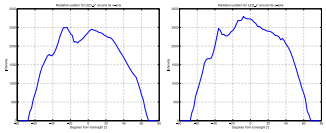

Figure 73: Radiation pattern of LED in yz- and xz-plane respectively.

Figure 74: Photo of LED from above.

Remarks:

- Ok.

38

Appendix D

LED Placement on STEP Model

Appendix – LED placement on STEP model

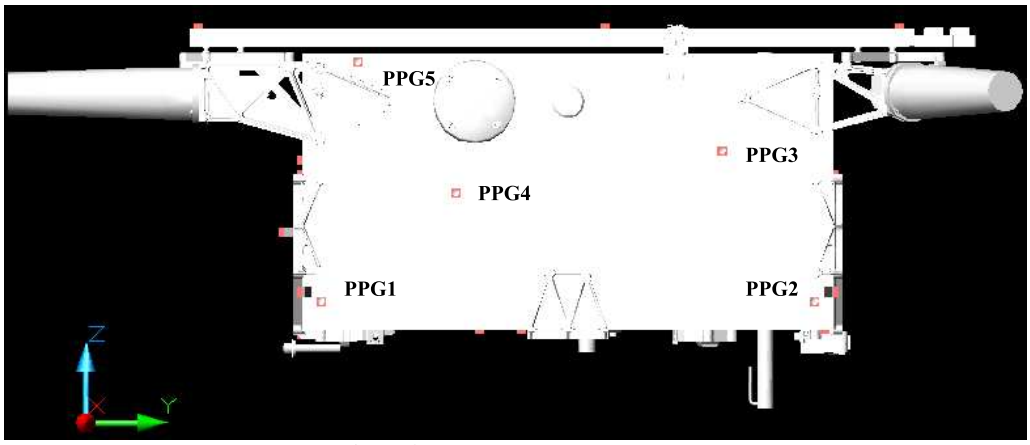

Figure 6: LED placement on +X panel.

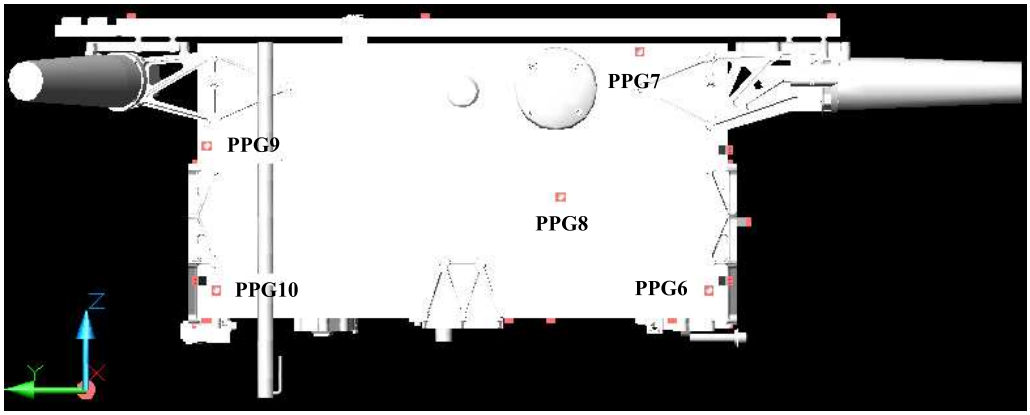

Figure 7: LED placement on -X panel.

This document contains information that may not be disclosed, reproduced or distributed without prior approval from DNSC-DTU

Figure 8: LED placement on +Y panel.

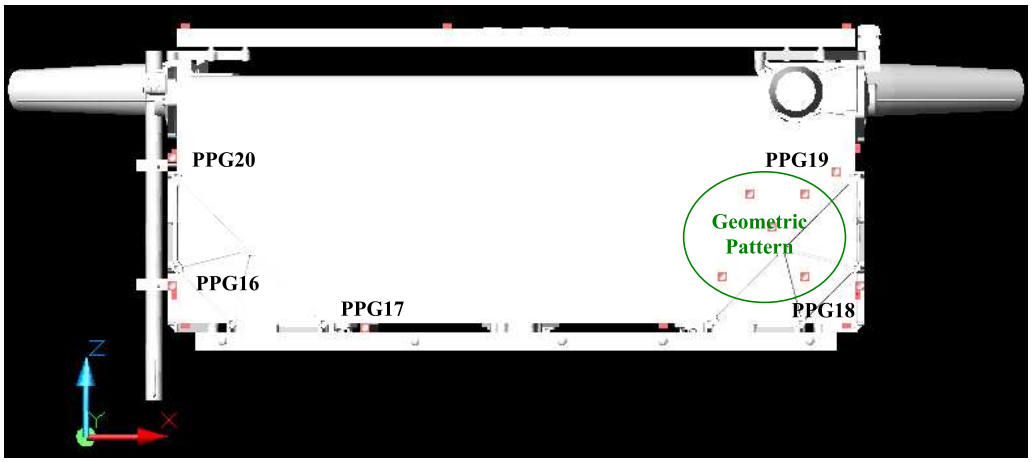

Figure 9: LED placement on -Y panel. See Figure 12 for the Geometric Pattern.

This document contains information that may not be disclosed, reproduced or distributed without prior approval from DNSC-DTU

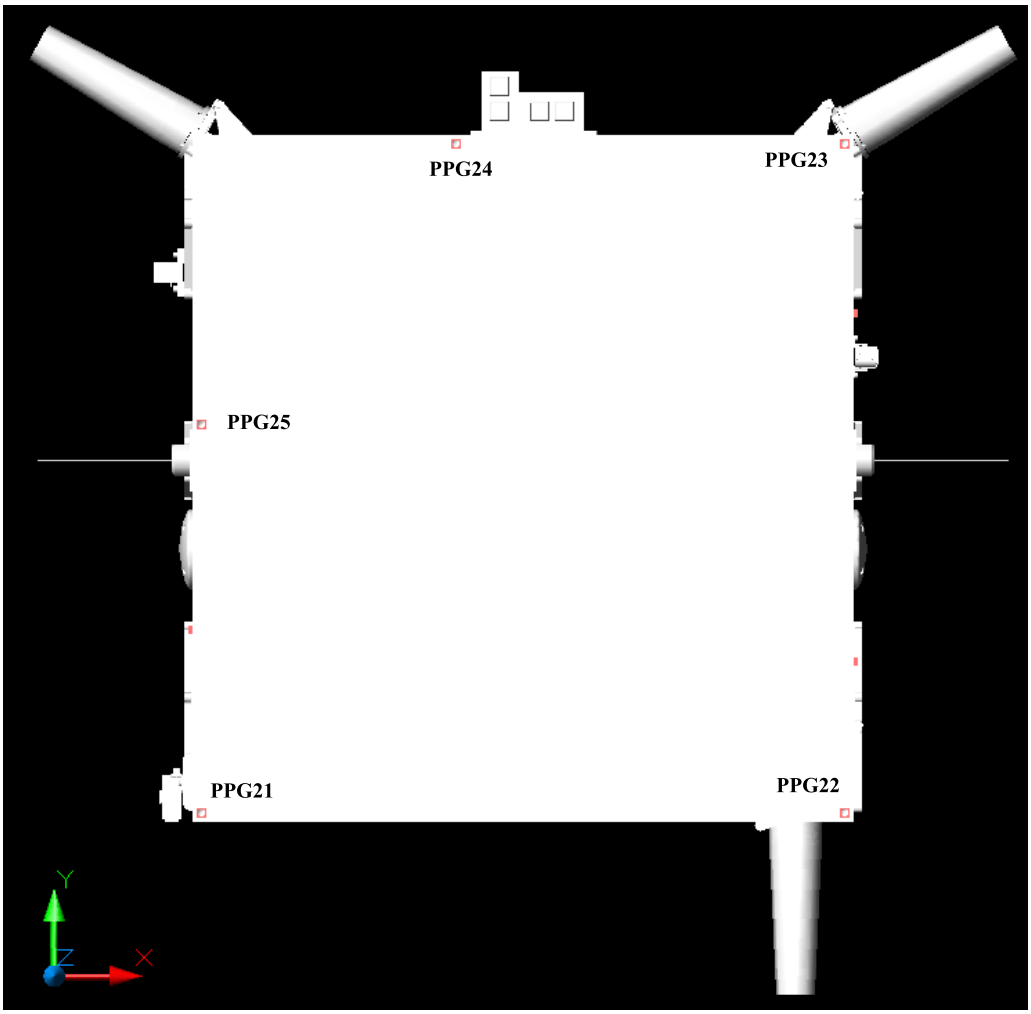

Figure 10: LED placement on +Z panel.

This document contains information that may not be disclosed, reproduced or distributed without prior approval from DNSC-DTU

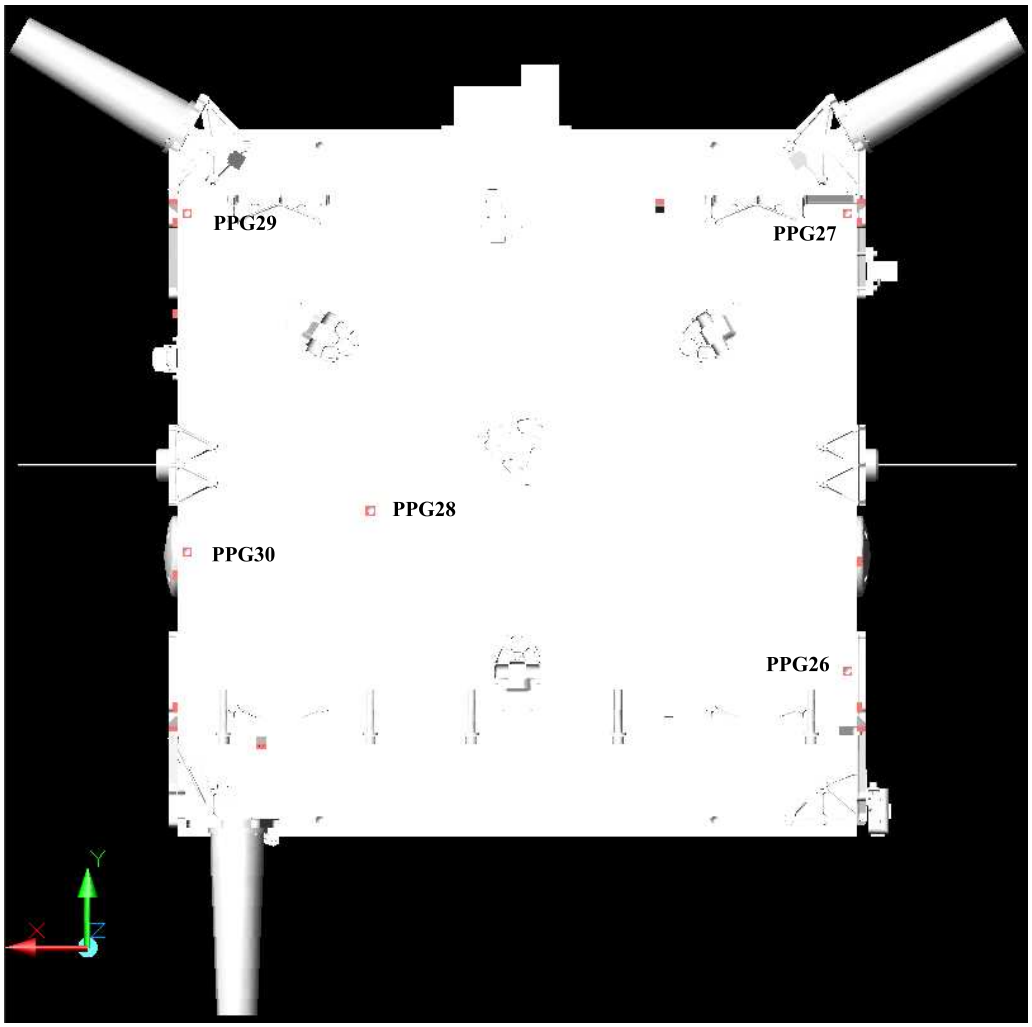

Figure 11: LED placement on -Z panel.

This document contains information that may not be disclosed, reproduced or distributed without prior approval from DNSC-DTU

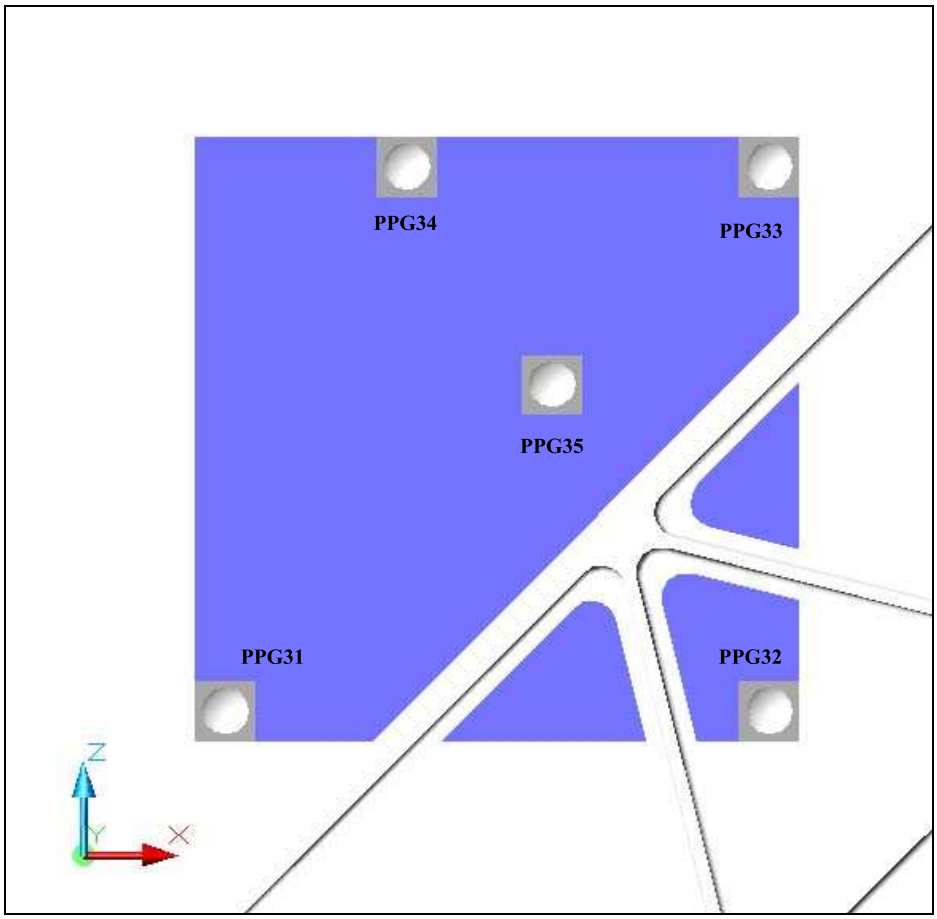

Figure 12: Placements of the LEDs on the Geometric Pattern.

This document contains information that may not be disclosed, reproduced or distributed without prior approval from DNSC-DTU

Appendix E

μASC CHU Timing

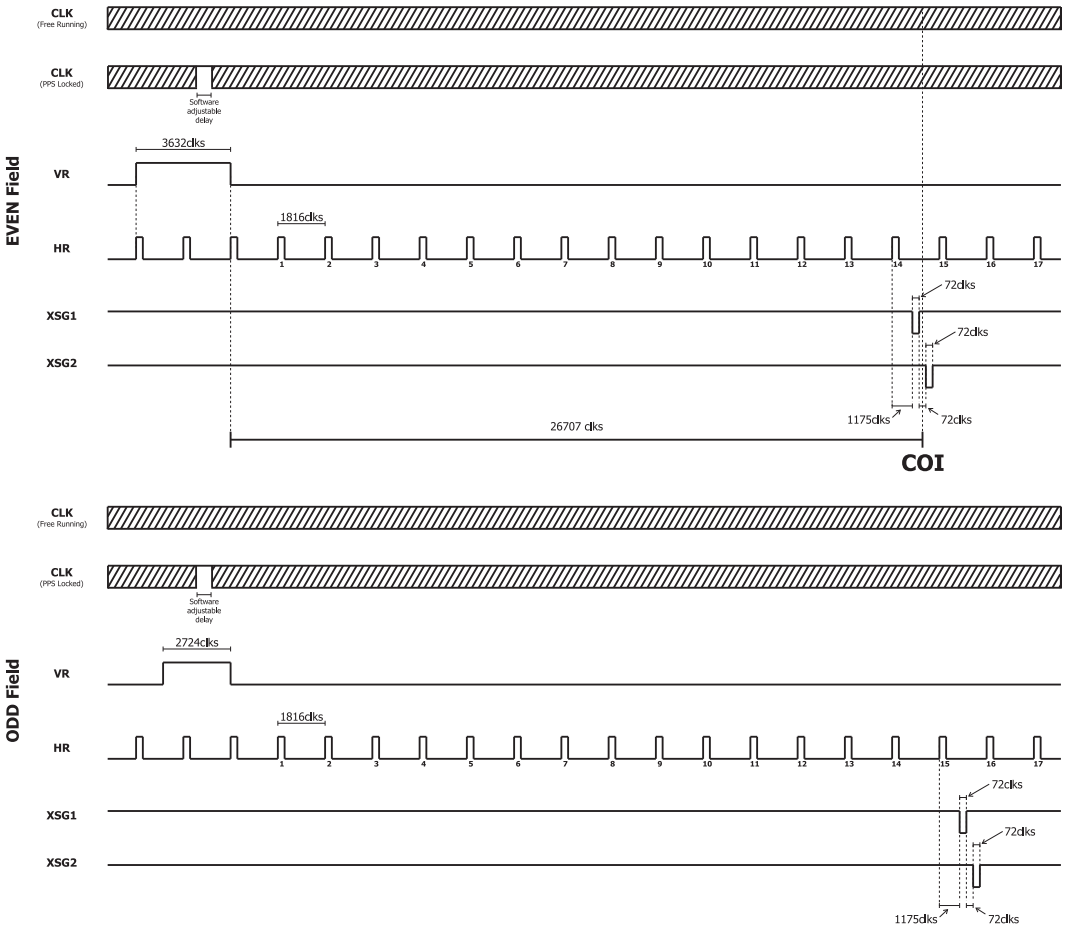

Figure E.1. *μASC Center of Integration Timing with respect to VR trailing edge. [Bjarnoe2010]*

Appendix F

P4P Solution Method

The following section describes the solution method of the P4P problem as used by the VBS. The text and equations are partly extracted from [Benn2007].

The P4P problem can be solved using a geometric model based on volume calculations of the four tetrahedra defined by the Camera Center, C_C, and three of the four points [Abidi1990]. Taking a pinhole projection into consideration, the projection of four points, P_i for $i = 1..4$, are as described in Figure F.1 where the points on the CCD are described by P_i', assuming that the projected points have been corrected for lens distortion. The C_C indicates the center of the camera and f describes the focal length.

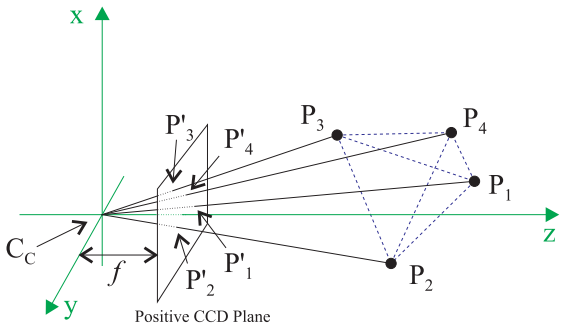

Figure F.1. *Definition of pinhole projection of four points.*

Again, the projected points on the CCD can be described on the unit sphere of the CHU providing the following relation between the projected points, P_i' and the real points, P_i:

$$\overrightarrow{u_i} = \frac{\overrightarrow{C_C P_i'}}{F_i} = \frac{\overrightarrow{C_C P_i}}{d_i} \tag{F.1}$$

where:
$\overrightarrow{u_i}$: describes the unit vector of the point P_i.
F_i: describes the distance from C_C to the projected point P_i' defined as $\sqrt{(x_i')^2 + (y_i')^2 + f^2}$.
d_i: describes the unknown distance from the Camera Center to the point P_i.

Since the camera center, C_C, is in the origin of the defined coordinate system $(0, 0, 0)$, the vectors $\overrightarrow{C_C P_i'}$ and $\overrightarrow{C_C P_i}$ will be written as $\overrightarrow{P_i'}$ and $\overrightarrow{P_i}$, respectively.
Defining the bases of the four possible tetrahedra, spanned by the Camera Center and three of the four points, as being placed in the plane of the four coplanar points infers that the height, h, of each tetrahedron describes the distance from the plane to C_C, and are the same for all bases. Using the definitions from Figure F.1 the base area spanned by triangle $\triangle P_1 P_2 P_3$ can be defined by:

$$A_1(\triangle P_1 P_2 P_3) = \tfrac{1}{2} \left| \overrightarrow{P_1 P_2} \times \overrightarrow{P_1 P_3} \right| \tag{F.2}$$

Furthermore, the base areas can be described using Heron's Formula based on the side lengths of a triangle [Ballantyne1972]. Again for triangle $\triangle P_1 P_2 P_3$:

$$A_1 = \tfrac{1}{4} \sqrt{\left(s_{12}^2 + s_{13}^2 + s_{23}^2\right)^2 - 2(s_{12}^4 + s_{13}^4 + s_{23}^4)} \tag{F.3}$$

where:
s_{ij}: describes the distance between the two points P_i and P_j.

The volume of a tetrahedron can be determined as for any pyramid or cone by $V = \frac{1}{3} A \cdot h$, but can furthermore also be expressed as a sixth of the volume of the parallelepiped span of the vectors forming the tetrahedron. The volume V_1 of the tetrahedron $\blacktriangle C_C P_1 P_2 P_3$ can therefore be described by the following, with the definitions in Equation (F.1) implemented:

$$\begin{aligned} V_1 &= \tfrac{1}{3} A_1 \cdot h \\ &= \tfrac{1}{6} \left| \overrightarrow{P_1} \bullet (\overrightarrow{P_2} \times \overrightarrow{P_3}) \right| \\ &= \tfrac{1}{6} d_1 d_2 d_3 \left| \overrightarrow{u_1} \bullet (\overrightarrow{u_2} \times \overrightarrow{u_3}) \right| \end{aligned} \tag{F.4}$$

Using the procedures in Equation (F.2), (F.3) and (F.4) the base area and the volume for each tetrahedra can be determined. Combining the procedures used in these three equations and Equation (F.1) the following expressions for the distances d_2, d_3 and d_4 can be derived [Abidi1990]:

$$d_2 = \frac{B_3}{A_3}\frac{A_4}{B_4}\frac{F_2}{F_1}d_1 = C_{12}\frac{F_2}{F_1}d_1 \tag{F.5}$$

$$d_3 = \frac{B_2}{A_2}\frac{A_4}{B_4}\frac{F_3}{F_1}d_1 = C_{13}\frac{F_3}{F_1}d_1 \tag{F.6}$$

$$d_4 = \frac{B_1}{A_1}\frac{A_4}{B_4}\frac{F_4}{F_1}d_1 = C_{14}\frac{F_4}{F_1}d_1 \tag{F.7}$$

where:
B_i: describes twice the area of the projected triangles on the CCD, which can be determined by the cross product of the vectors spanning the projected triangles.

From these equations describing the three last of the four distances, it is seen that they all can be expressed from the first distance of the four, namely the distance between C_C and P_1 denoted d_1. Therefore, an expression for this instance is needed. In [Abidi1990], the knowledge of the line sections of which the point P_1 is a part and at which points these line segments crosses other line segments, is used in order to describe the d_1 distance. This results in the following six different expressions for d_1:

$$d_1 = \frac{s_{12}F_1}{\sqrt{H_{12}^2+f^2(1-C_{12})^2}} \tag{F.8}$$

$$= \frac{s_{13}F_1}{\sqrt{H_{13}^2+f^2(1-C_{13})^2}} \tag{F.9}$$

$$= \frac{s_{14}F_1}{\sqrt{H_{14}^2+f^2(1-C_{14})^2}} \tag{F.10}$$

$$= \frac{s_{23}F_1}{\sqrt{H_{23}^2+f^2(1-C_{23})^2\cdot C_{12}}} \tag{F.11}$$

$$= \frac{s_{24}F_1}{\sqrt{H_{24}^2+f^2(1-C_{24})^2\cdot C_{12}}} \tag{F.12}$$

$$= \frac{s_{34}F_1}{\sqrt{H_{34}^2+f^2(1-C_{34})^2\cdot C_{13}}} \tag{F.13}$$

where:
$H_{ij}^2 = \left(x_i' - C_{ij}x_j'\right)^2 + \left(y_i' - C_{ij}y_j'\right)^2$ and where the values (x_i', y_i') and (x_j', y_j') describes the projected coordinates on the CCD plane for the points P_i' and P_j', respectively.

These six equivalent expressions for d_1 should all produce the same result, assuming that the projected points and the distances in between the points are correct. Since this is hardly the case for points exposed to lens distortion, centroiding and measurement inaccuracy, an average of these six expressions are taken into consideration.

From a combination of the expressions in Equation (F.8-F.13) and from the expression in Equation (F.5-F.7), all distances from the camera center to

the points can be determined, providing only the distances s_{ij} in between the points and the projected coordinate points. From Equation (F.1) the location of the points can now be expressed by:

$$P_i = \overrightarrow{P_i} = d_i \overrightarrow{u_i} \tag{F.14}$$

It must be noted that this solution method assumes that the reference between the projected points and which point is projected are known beforehand. Placing the points in unique asymmetric patterns will result in only one solution fit where the six equations of d_1 will result in similar results.

In order to describe the translation and the rotation of the point positions with respect to the coordinate system of the camera, a definition of a coordinate system with respect to the points has to be described. Defining that the point P_1 is the origin of the points coordinate system, the x-axis is described by the pointing of the vector between P_1 and P_2, $\Rightarrow \overrightarrow{P_1P_2}$, and the z-axis is the normal vector of the plane in which all the points are coplanar. This results in a translation matrix $\underline{\underline{T}}$ equal to the coordinates of position P_1 and a rotation matrix $\underline{\underline{R}}$ describing the rotation needed to align the defined xyz-axes of the points coordinate system with the coordinate system of the camera. Figure F.2 illustrates this.

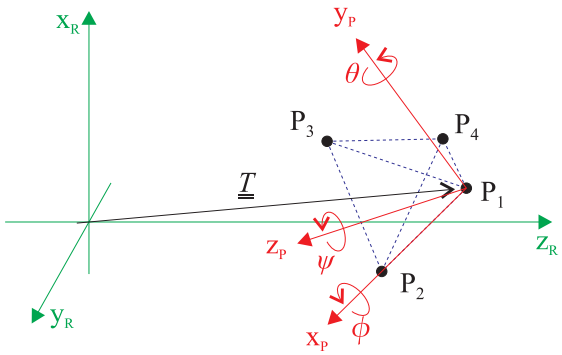

Figure F.2. *Mapping between frames performed by a translation and rotations.*

The rotation angles ϕ, θ and ψ denote the rotation around the x-, y- and z-axis, respectively. Each of these rotations can be described using rotation matrices defined as follows [Fortescue2003]:

$$\underline{\underline{R}}_\phi = \begin{bmatrix} 1 & 0 & 0 \\ 0 & \cos\phi & -\sin\phi \\ 0 & \sin\phi & \cos\phi \end{bmatrix}, \quad \underline{\underline{R}}_\theta = \begin{bmatrix} \cos\theta & 0 & \sin\theta \\ 0 & 1 & 0 \\ -\sin\theta & 0 & \cos\theta \end{bmatrix}, \quad \underline{\underline{R}}_\psi = \begin{bmatrix} \cos\psi & -\sin\psi & 0 \\ \sin\psi & \cos\psi & 0 \\ 0 & 0 & 1 \end{bmatrix} \tag{F.15}$$

Where a complete rotation matrix, representing the entire rotation, can be determined by multiplying the rotation matrices for each rotation:

$$\underline{\underline{R}} = \underline{\underline{R}}_{\psi}\underline{\underline{R}}_{\theta}\underline{\underline{R}}_{\phi} = \begin{bmatrix} \cos\psi\cos\theta & -\sin\psi\cos\phi + \cos\psi\sin\theta\sin\phi & \sin\psi\sin\phi + \cos\psi\sin\theta\cos\phi \\ \sin\psi\cos\theta & \cos\psi\cos\phi + \sin\psi\sin\theta\sin\phi & -\cos\psi\sin\phi + \sin\psi\sin\theta\cos\phi \\ -\sin\theta & \cos\theta\sin\phi & \cos\theta\cos\phi \end{bmatrix} \tag{F.16}$$

As such, from knowing the positions of the points on Target and the mapping from the points to the Target frame, the translation and rotation of the Target frame in the reference CHU frame can thereby be determined.

This solution method takes the input arguments $\underline{\underline{s}}$, $\underline{\underline{q}}$ and $focal\_length$ respectively describing the distances between the investigated points, their projected coordinates on the CCD and the focal length of the camera. The parameters $\underline{\underline{s}}$ and $\underline{\underline{q}}$ are matrices defined as:

$$\underline{\underline{s}} = \begin{bmatrix} s_{11} & s_{12} & s_{13} & s_{14} \\ s_{21} & s_{22} & s_{23} & s_{24} \\ s_{31} & s_{32} & s_{33} & s_{34} \\ s_{41} & s_{42} & s_{43} & s_{44} \end{bmatrix}, \ \underline{\underline{q}} = \begin{bmatrix} q1_x & q2_x & q3_x & q4_x \\ q1_y & q2_y & q3_y & q4_y \end{bmatrix} \tag{F.17}$$

where:
s_{ij}: describes the distances between the points P_i and P_j. Note that $s_{ij} = s_{ji}$ and that $s_{ii} = 0$.
qi_x, qi_y: describes the xy-coordinates of the projected coordinates of the points P_i onto the CCD.

As output the solutions of the positions P_{1-4} in the xyz-coordinate system is given, based on the input parameters:

$$\underline{\underline{P}} = \begin{bmatrix} P1_x & P1_y & P1_z \\ P2_x & P2_y & P2_z \\ P3_x & P3_y & P3_z \\ P4_x & P4_y & P4_z \end{bmatrix} \tag{F.18}$$

The presented solution method of the P4P application is only capable of handling solutions for four diodes at a time, corresponding to four detected LEDs on one side of Target. Determination of the best fitted solution is based on the variance occurring from the six different expressions of the d_1 distance given in Equation (F.8-F.13), where the variance is denoted σ^2 and defined as:

$$\sigma^2 = \frac{1}{6}\sum_{n=1}^{6}\left(d_1(n) - \bar{d_1}\right)^2 \tag{F.19}$$

where:
$d_1(n)$: describes the n-th solution of the six expressions for d_1.
$\bar{d_1}$: describes the mean value of all the six d_1 expressions.

This gives an indication of the best fit since only the correctly chosen sequence of centroids will result in a small value of the variance. The solution calculated by the P4P application providing the smallest variance is therefore marked as the result of the P4P application.

Appendix G

Short Range Cooperative LED Fitting

The Short Range Cooperative mode use iterative fitting of the back-projected LED model versus the detected centroids. This chapter describes the fitting method implemented in the μASC.

The iterative solution is executed as soon as an initial guess is estimated for the Target Pose and Position. The initial guess can either be estimated by the P4P method or having the previous solution and drift information.

When fitting the Target Pose and Position, the total error is determined by the residual value calculated as the squared difference in distance between the projected LEDs and the detected centroids.

The fitting relies on the fact that each distribution can be estimated by a quadratic function in the form of:

$$f(x) = a \cdot x^2 + b \cdot x + c \tag{G.1}$$

Where the minimum of the function, the vertex, describes the best fitting. The vertex is placed at:

$$x = \frac{-b}{2a} \tag{G.2}$$

For simplicity reasons and what is achievable in the μASC, the rotation and translation parameters are minimized individually.

In Figure G.1 and G.1 are illustrated how the fitting for each of the variables can be estimated by fitting a quadratic function to this. Additionally, the VBS system determines the fitting using only three points of the system in order to minimize the calculation time, where these three points are illustrated as `'fitbase'`. Table G.1 details that the three points are sufficient to determine the minimum vertex of Equation (G.1)

Fitting	VBS est. minimum	Real minimum	Difference
rotX	$x = -3.3958$	$x = -3.3958$	$1.4067 \cdot 10^{-5}$
rotY	$x = -6.5786$	$x = -6.5794$	$7.9564 \cdot 10^{-4}$
rotZ	$x = -0.4497$	$x = -0.4497$	$6.9940 \cdot 10^{-8}$
transX	$x = -0.3429$	$x = -0.3429$	$-1.3616 \cdot 10^{-6}$
transY	$x = -0.0398$	$x = -0.0398$	$1.4690 \cdot 10^{-8}$
transZ	$x = 2.1890$	$x = 2.1890$	$6.9449 \cdot 10^{-5}$

Table G.1. *Real minimum vs. estimated VBS minimum.*

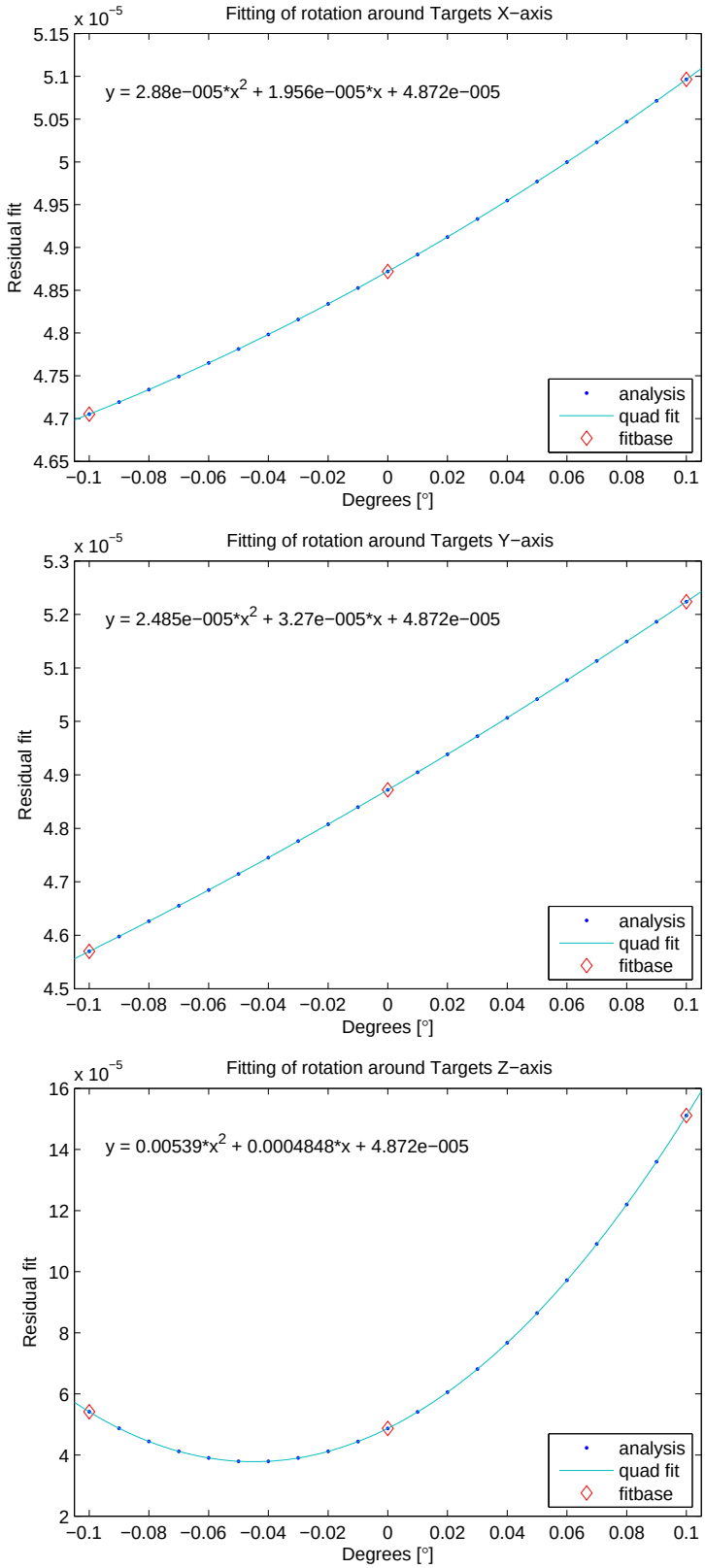

Figure G.1. *Fitting of the Target rotations around the x-,y- and z-axis of the Target.*

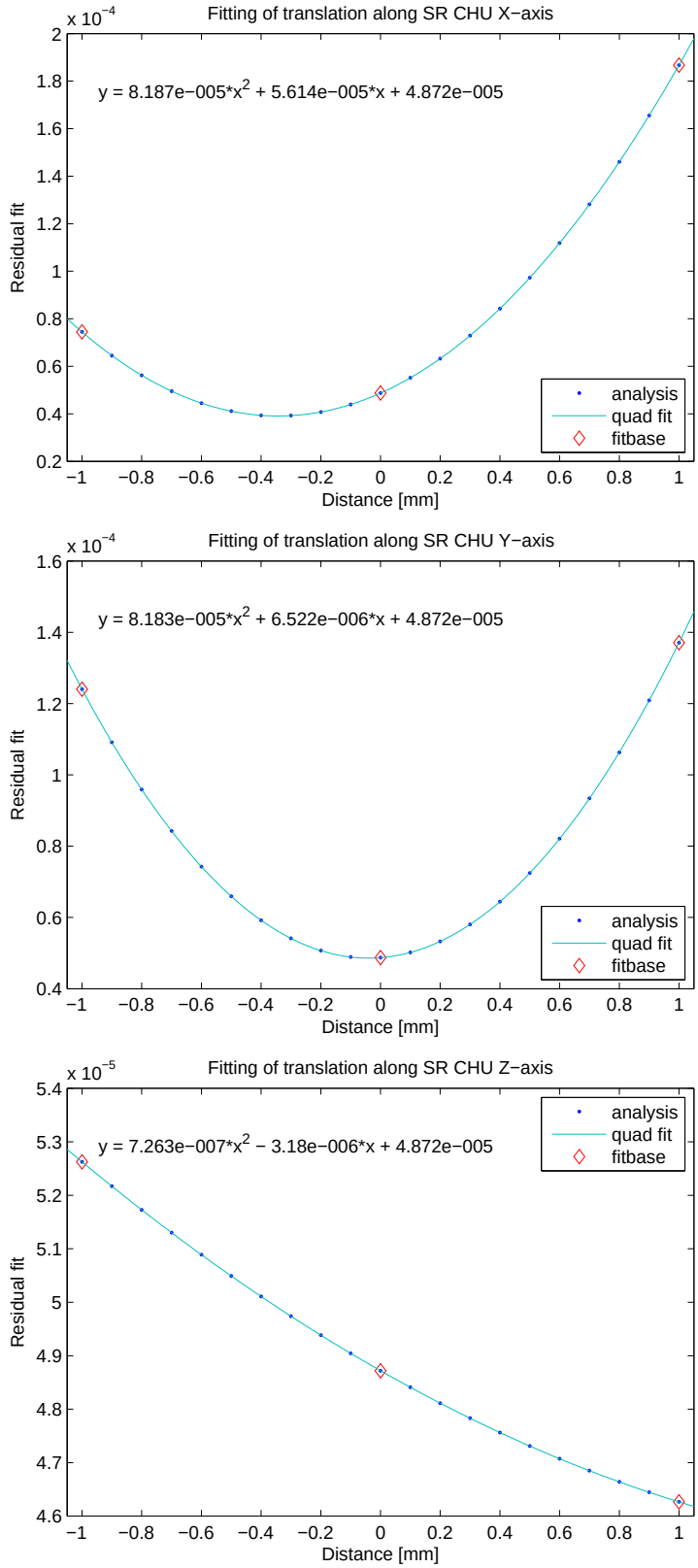

Figure G.2. *Fitting of the Target translations in reference to the x-,y- and z-axis of the SR CHU.*

Appendix H

PPS vs. LED Pulsing

Measurements of the PPS signal vs. the LED pulsing taken on the FM PRISMA satellites on test campaign PRISMA_20090624 at SSC, Solna, Stockholm.

The test setup consisted of a VTB1113 Photodiode placed directly on top of one LED on the Target spacecraft. The LED was pulse-powered by the onboard GPS system on Target S/C, and the photodiode connected to an oscilloscope together with a reference from the GPS system on Main S/C.

For the oscilloscope screenshots presented, the following channels are represented as:

CH1: MAIN satellite, Connector: CORE nom P2 pin 2-, 7+. (PPS puls from core board).

CH2: TARGET satellite, DTU optical device connected to one LED.

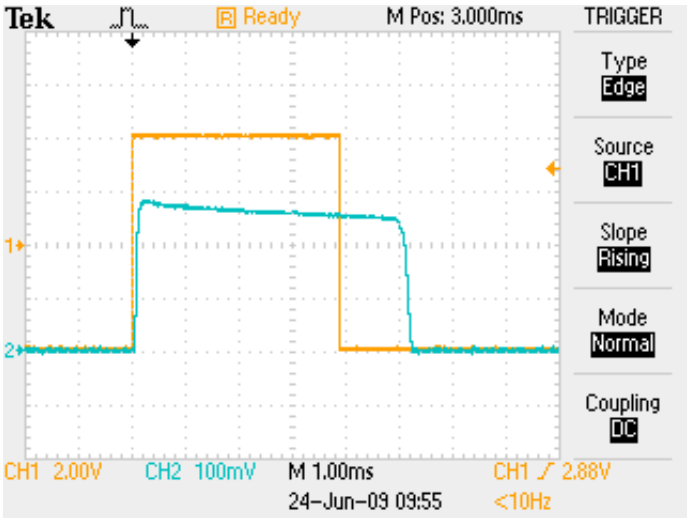

Figure H.1. *PPS pulse vs. LED pulse.*

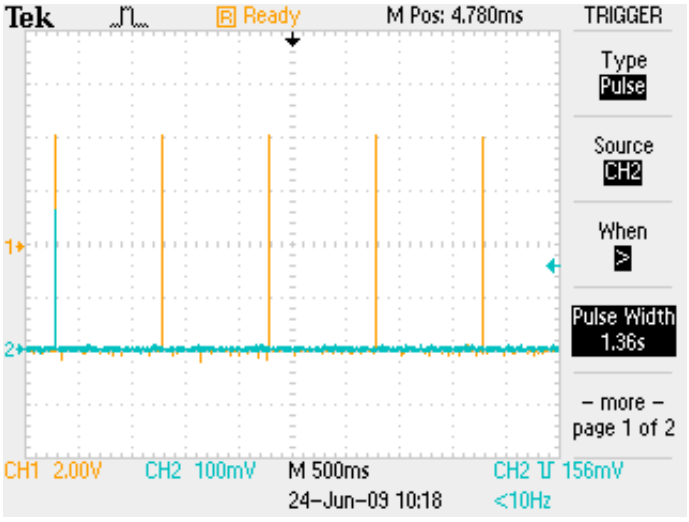

Figure H.2. *PPS and LED frequency.*

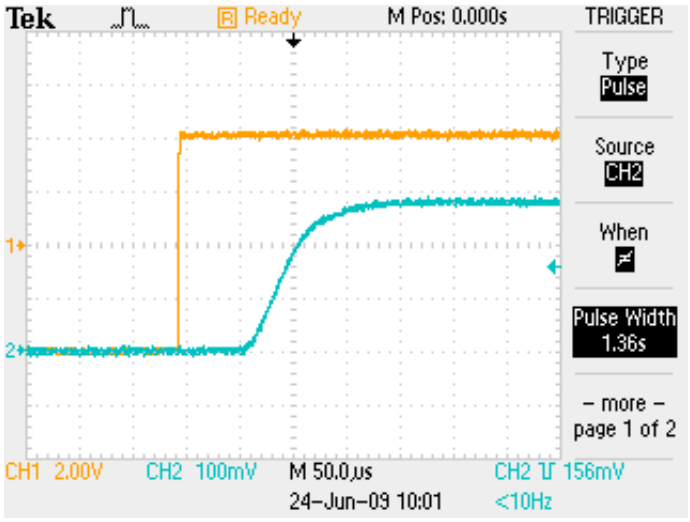

Figure H.3. *Leading edge of PPS and LED pulses.*

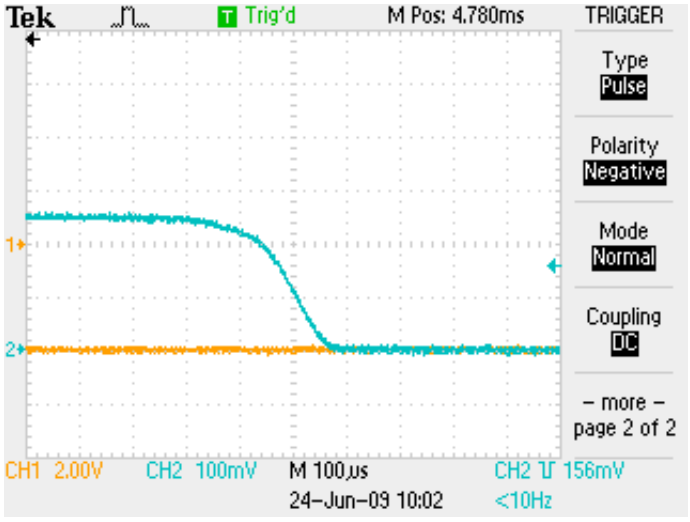

Figure H.4. *Trailing edge of LED pulse.*

Appendix I

Notes on Noise Measurements of the VBS Mockup

Notes on Noise Measurements of the VBS Mock-up System

Mathias Benn – DTU Space

1 Intro

These notes present the noise measurements of the VBS systems performance on the PRISMA mock-up test bench.
The measurements are performed using a dolly setup for the VBS Short Range camera and a rotation stand for the PRISMA Target satellite. The satellite has been pictured from different fixed angles whereas the dolly has been moved to a set of different fixed positions.
The dolly setup is pictured in Figure 1, and each different setup is illustrated in leading of each section.

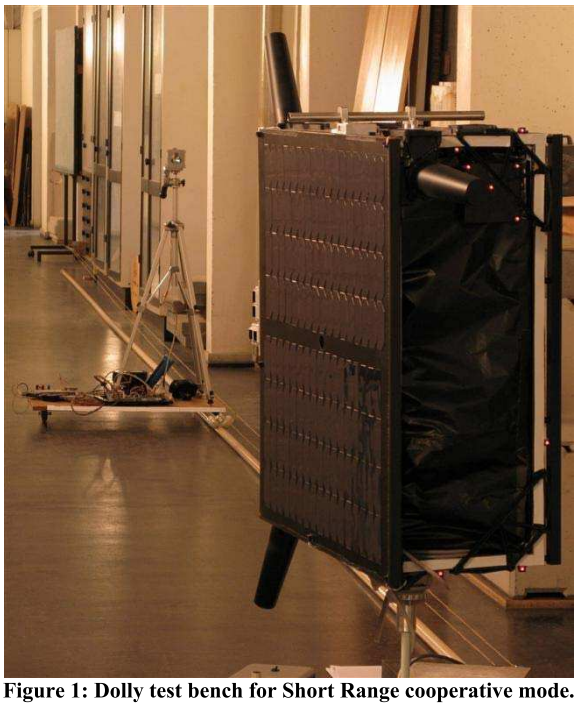

Figure 1: Dolly test bench for Short Range cooperative mode.

Four different rotation positions have been considered, and four different distances have been measured for each rotation position. The following sections describe the measurements for the four rotation positions, where the four different distances are given in subsections. For each measurement group the standard deviation has been calculated using Eq. (1), and all standard deviations are compared for the full overview in Section 6.

$$\sqrt{\frac{1}{n}\sum_{i=1}^{n}(x_i - \bar{x})^2} \qquad (1)$$

This document contains information that may not be disclosed, distributed or reproduced without written approval by MIS at National Space Institute – DTU.

2 +Y Panel (~0 deg)

Figure 2: Satellite orientation for measurements on +Y panel (~0 deg).

2.1 Distance1 (~5.2m)

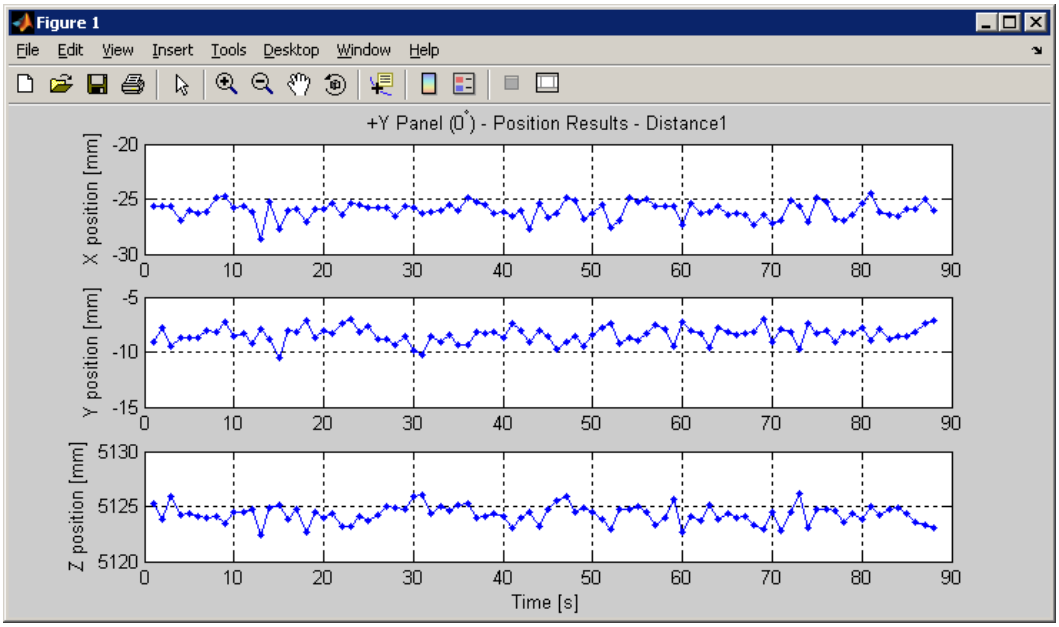

This document contains information that may not be disclosed, distributed or reproduced without written approval by MIS at National Space Institute – DTU.

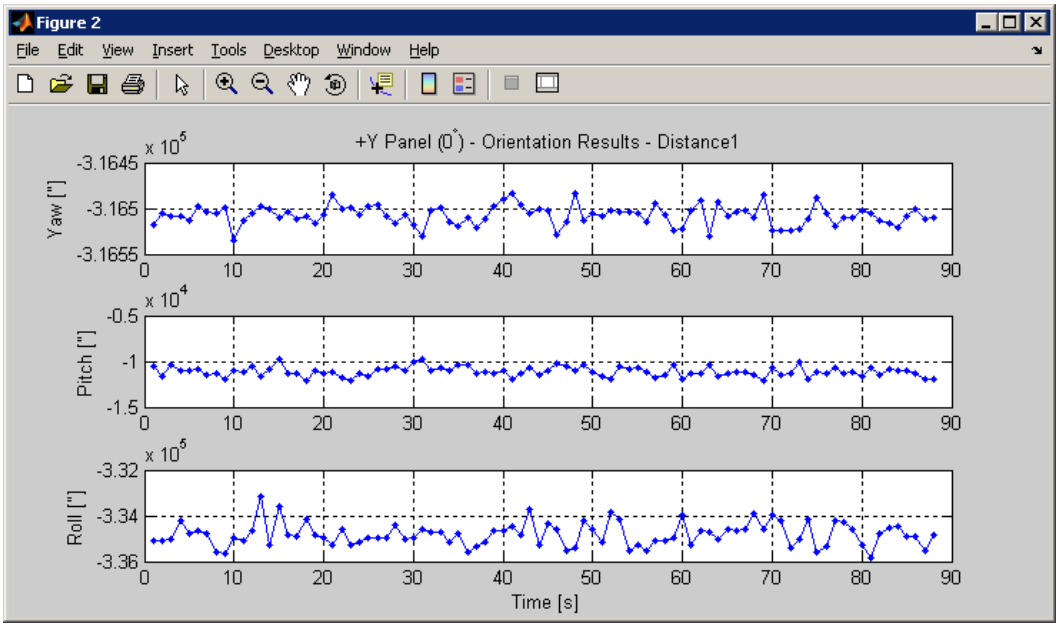

Std(posX) [mm]	Std(posY) [mm]	Std(posZ) [mm]	Std(yaw) ["]	Std(pitch) ["]	Std(roll) ["]
0,763	0,728	0,815	10,783	530,432	507,062

This document contains information that may not be disclosed, distributed or reproduced without written approval by MIS at National Space Institute – DTU.

2.2 Distance2 (~8.2m)

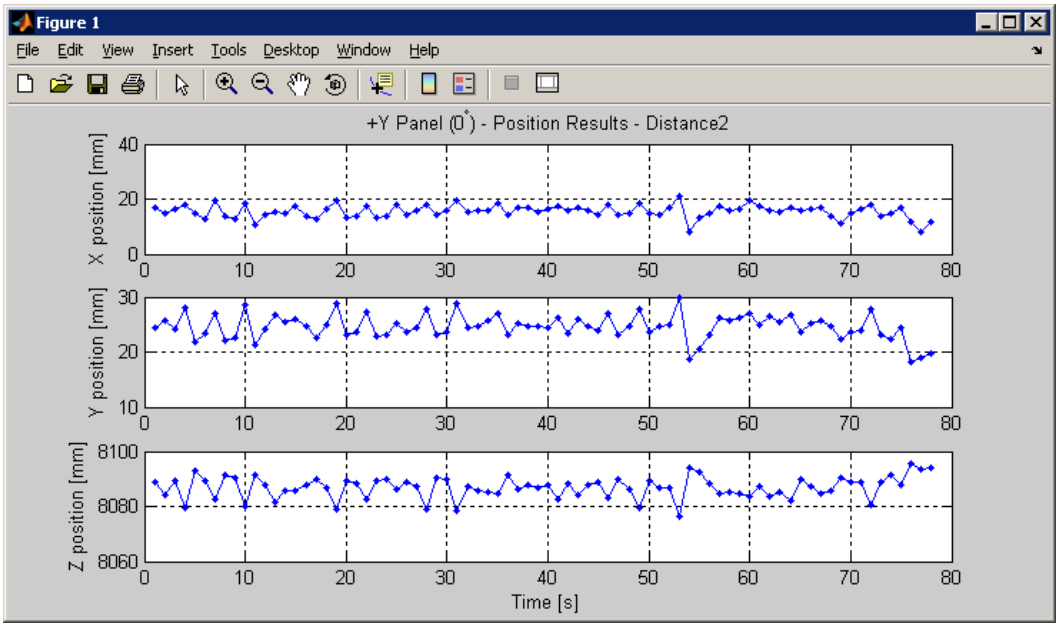

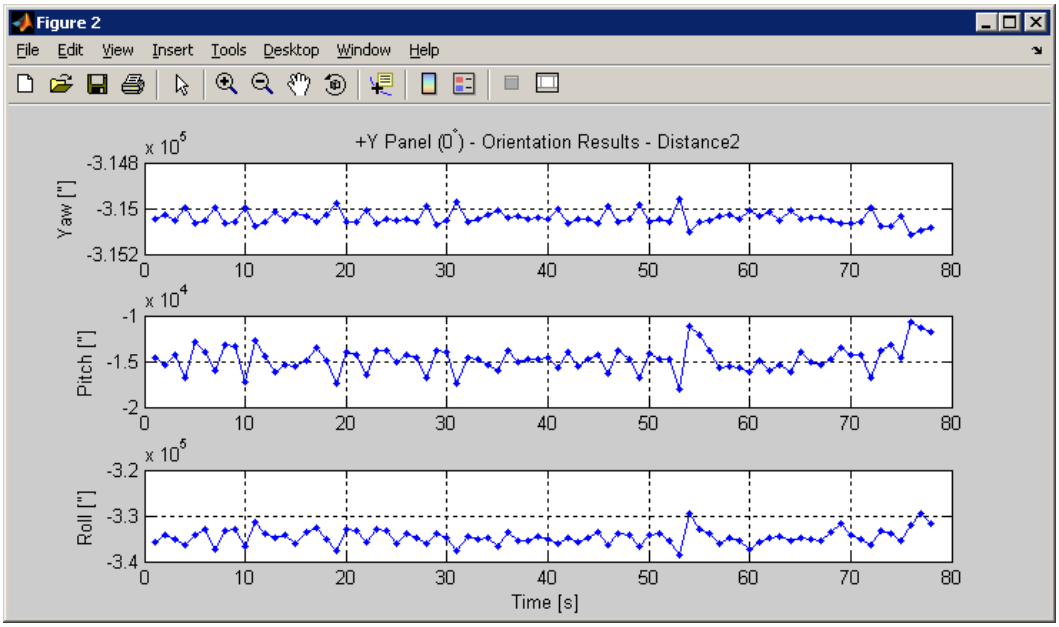

Std(posX) [mm]	Std(posY) [mm]	Std(posZ) [mm]	Std(yaw) ["]	Std(pitch) ["]	Std(roll) ["]
2,396	2,269	3,947	29,858	1414,285	1659,188

This document contains information that may not be disclosed, distributed or reproduced without written approval by MIS at National Space Institute – DTU.

2.3 Distance3 (~11.2m)

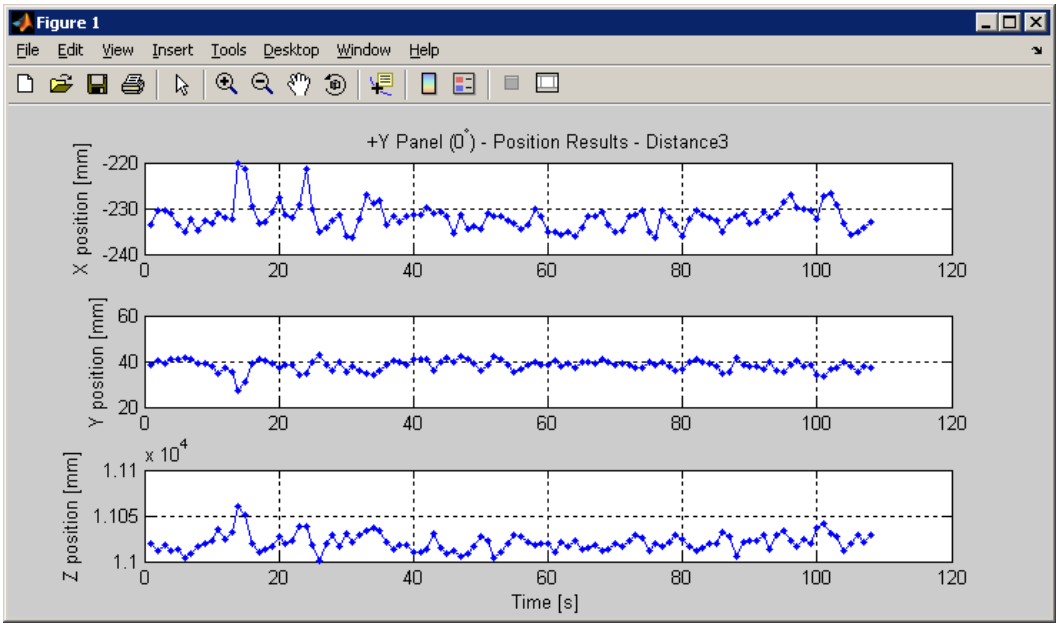

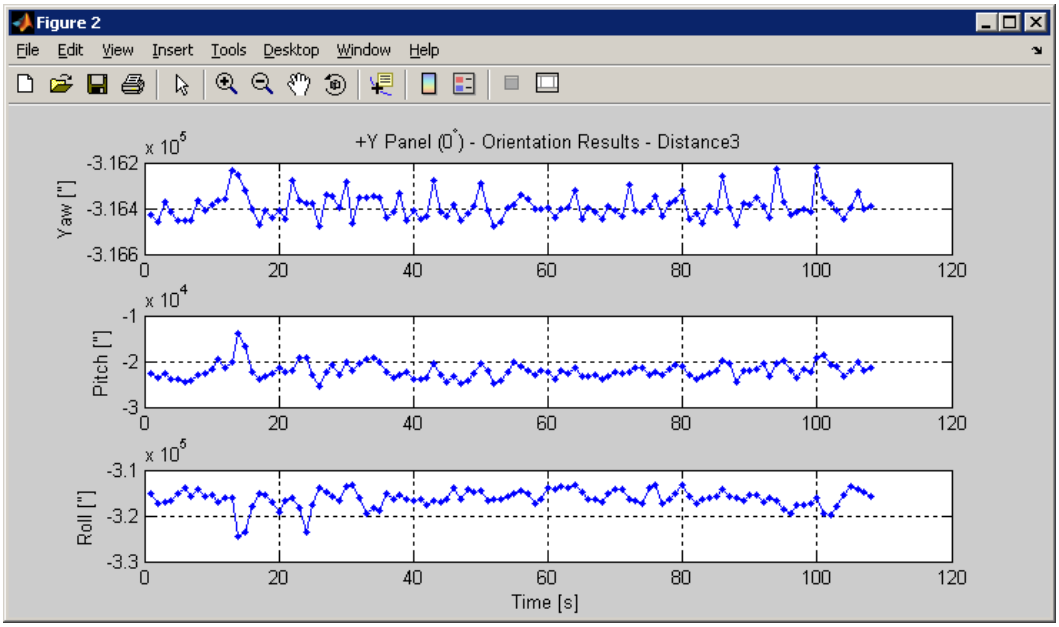

Std(posX) [mm]	Std(posY) [mm]	Std(posZ) [mm]	Std(yaw) ["]	Std(pitch) ["]	Std(roll) ["]
2,875	2,444	9,557	55,547	1752,901	1969,919

This document contains information that may not be disclosed, distributed or reproduced without written approval by MIS at National Space Institute – DTU.

2.4 Distance4 (~15.2m)

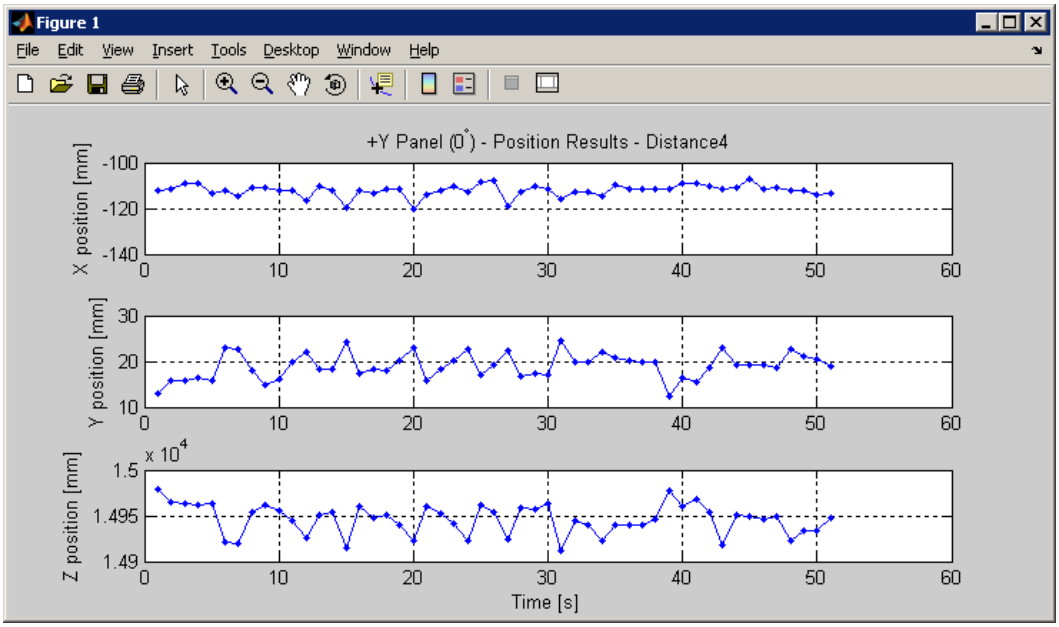

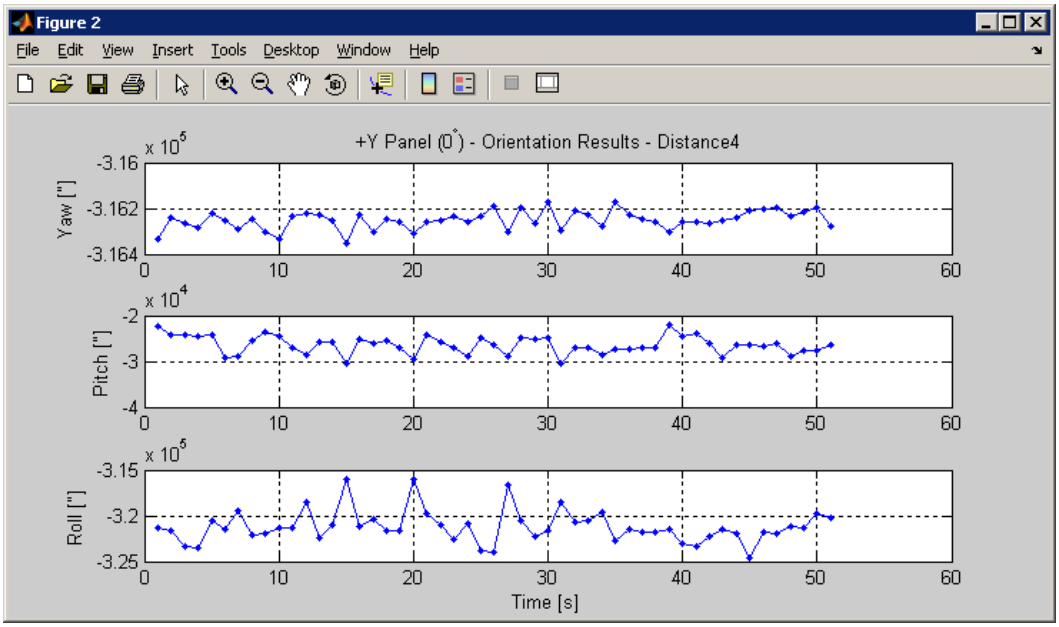

Std(posX) [mm]	Std(posY) [mm]	Std(posZ) [mm]	Std(yaw) ["]	Std(pitch) ["]	Std(roll) ["]
2,648	2,744	16,341	40,476	1963,994	1768,507

This document contains information that may not be disclosed, distributed or reproduced without written approval by MIS at National Space Institute – DTU.

3 Slanted +Y Panel (~22.5 deg)

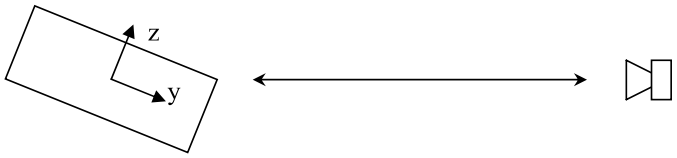

Figure 3: Satellite orientation for measurements on slanted +Y panel (~22.5 deg).

3.1 Distance1 (~5.2m)

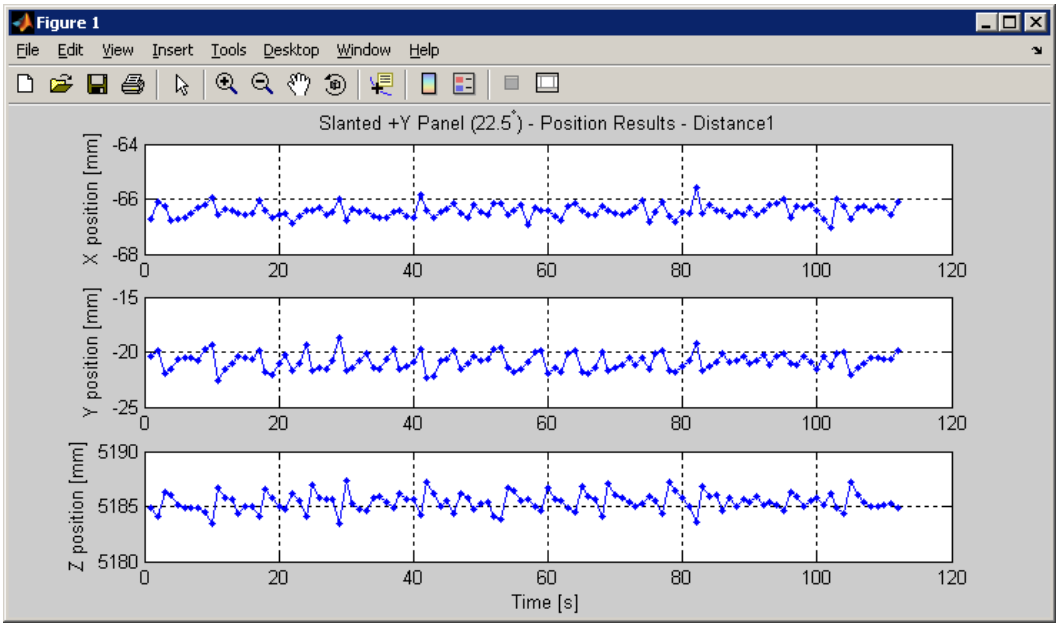

This document contains information that may not be disclosed, distributed or reproduced without written approval by MIS at National Space Institute – DTU.

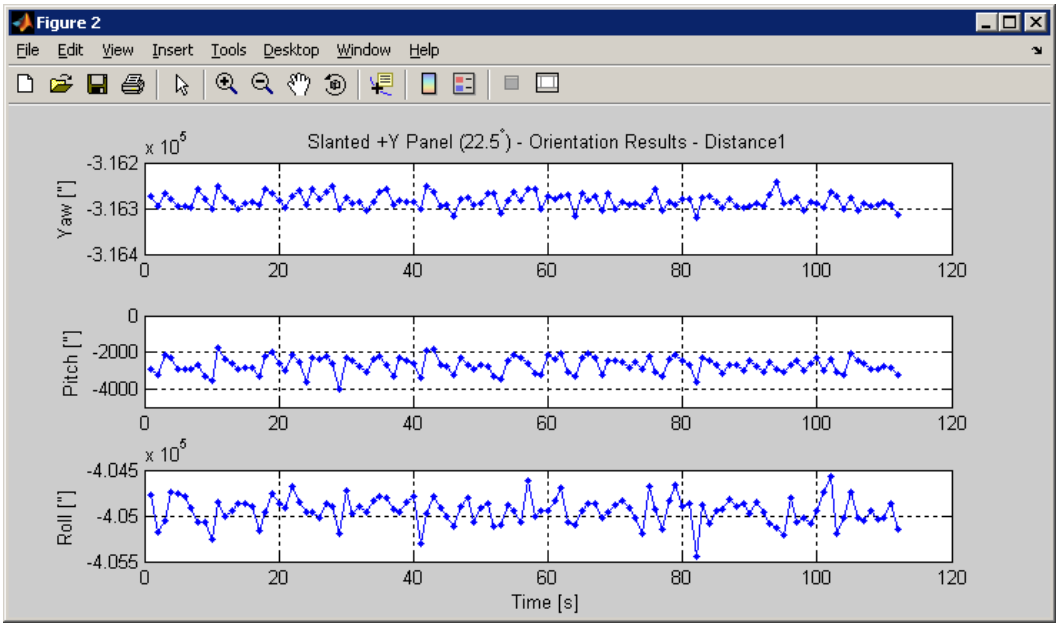

Std(posX) [mm]	Std(posY) [mm]	Std(posZ) [mm]	Std(yaw) ["]	Std(pitch) ["]	Std(roll) ["]
0,236	0,759	0,845	15,582	434,924	147,047

This document contains information that may not be disclosed, distributed or reproduced without written approval by MIS at National Space Institute – DTU.

3.2 Distance2 (~8.2m)

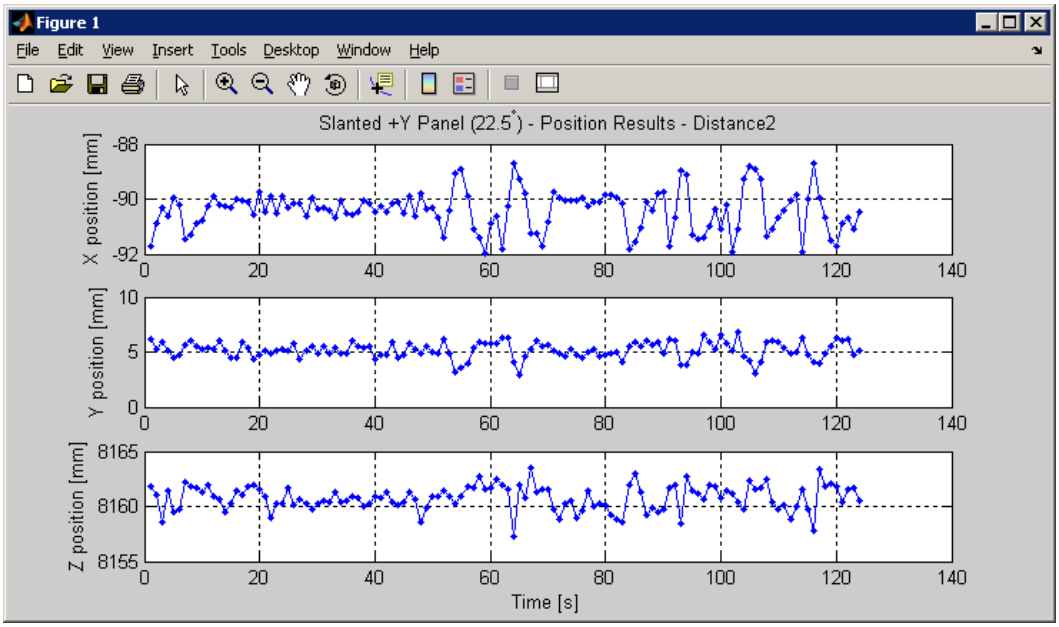

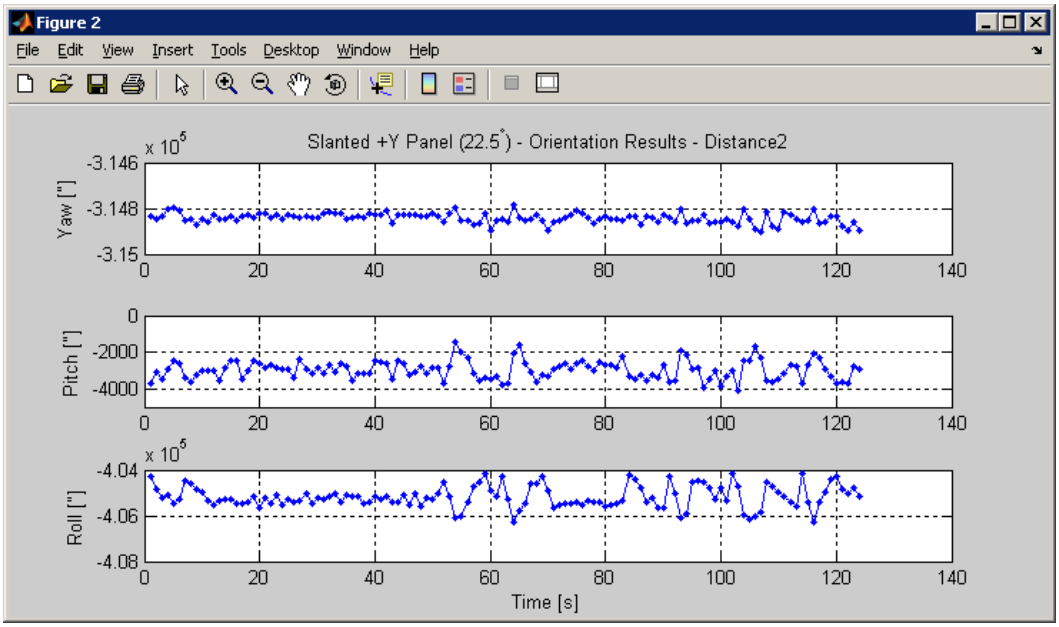

Std(posX) [mm]	Std(posY) [mm]	Std(posZ) [mm]	Std(yaw) ["]	Std(pitch) ["]	Std(roll) ["]
0,724	0,735	1,133	22,243	513,676	475,110

This document contains information that may not be disclosed, distributed or reproduced without written approval by MIS at National Space Institute – DTU.

3.3 Distance3 (~11.2m)

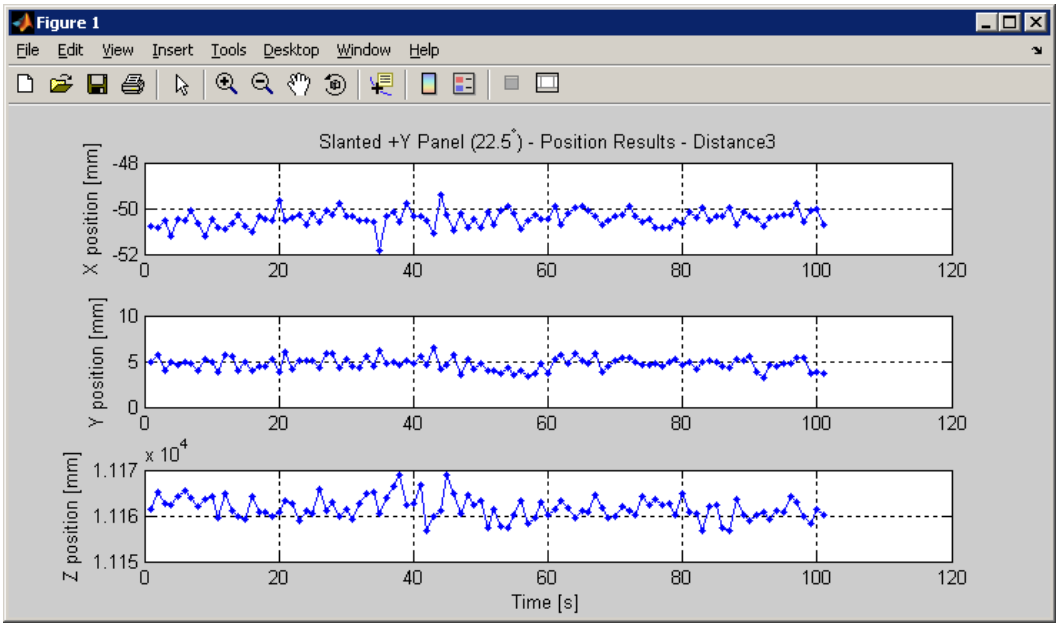

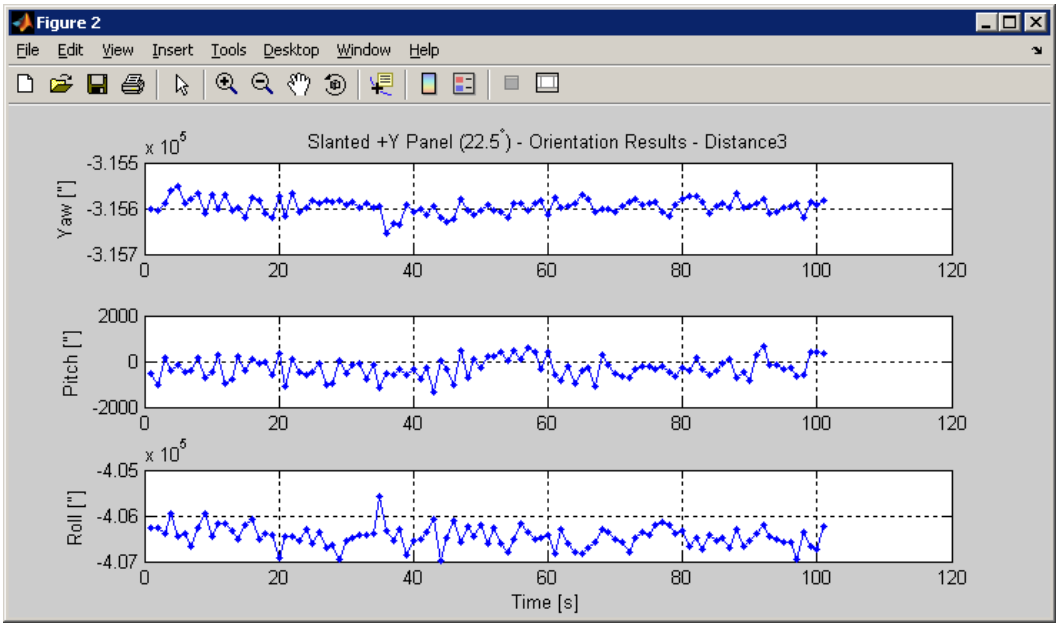

Std(posX) [mm]	Std(posY) [mm]	Std(posZ) [mm]	Std(yaw) ["]	Std(pitch) ["]	Std(roll) ["]
0,363	0,680	2,463	17,018	438,005	231,292

This document contains information that may not be disclosed, distributed or reproduced without written approval by MIS at National Space Institute – DTU.

3.4 Distance4 (~15.2m)

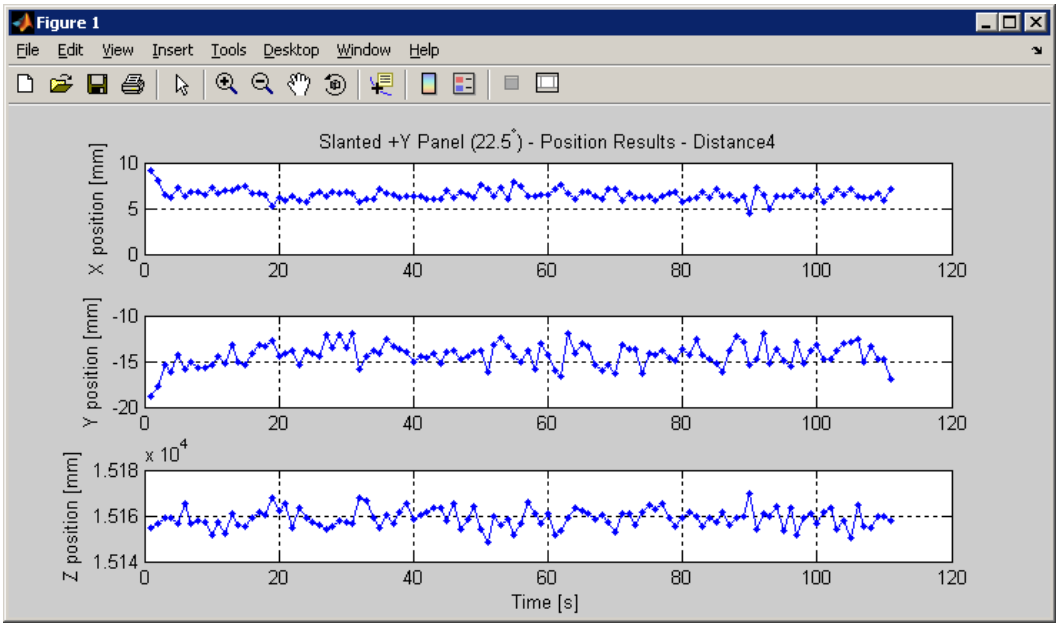

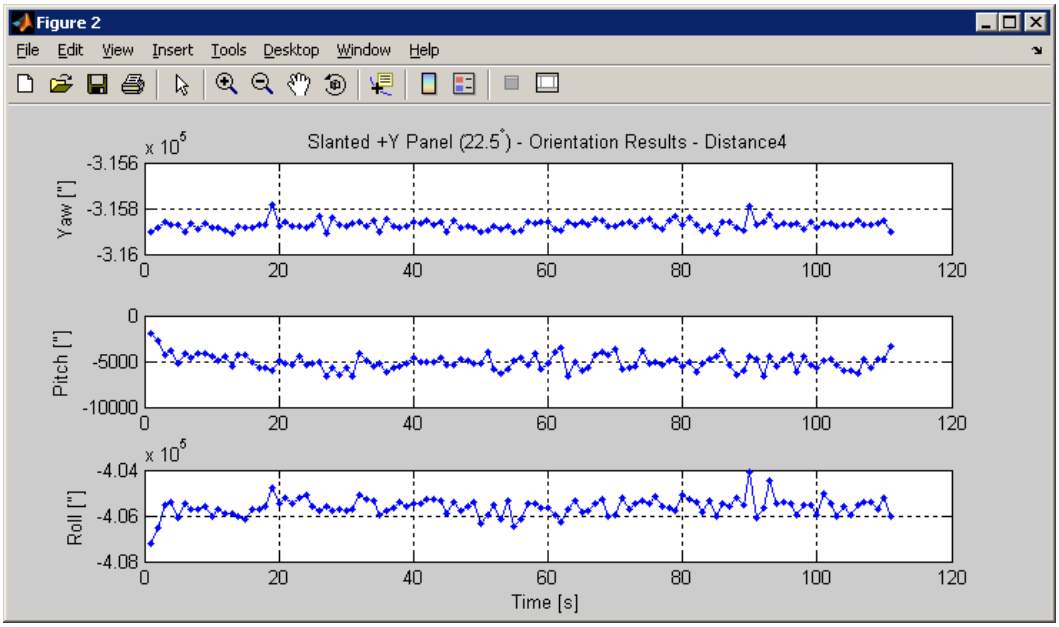

Std(posX) [mm]	Std(posY) [mm]	Std(posZ) [mm]	Std(yaw) ["]	Std(pitch) ["]	Std(roll) ["]
0,605	1,241	4,097	20,837	835,524	391,715

This document contains information that may not be disclosed, distributed or reproduced without written approval by MIS at National Space Institute – DTU.

4 +Y +Z Panel (~45 deg)

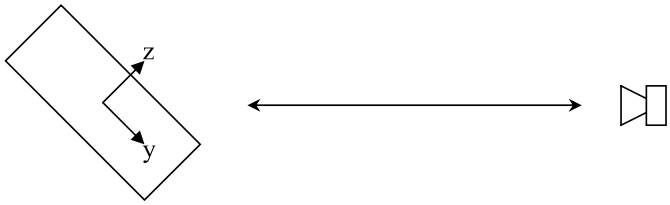

Figure 4: Satellite orientation for measurements on +Y +Z panel (~45 deg).

4.1 Distance1 (~5.2m)

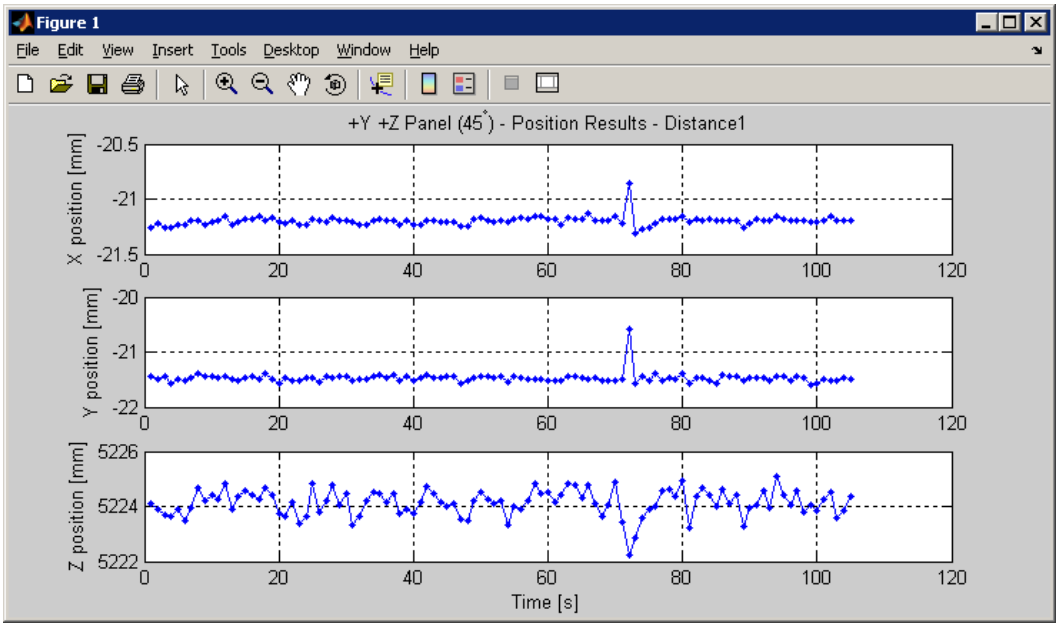

This document contains information that may not be disclosed, distributed or reproduced without written approval by MIS at National Space Institute – DTU.

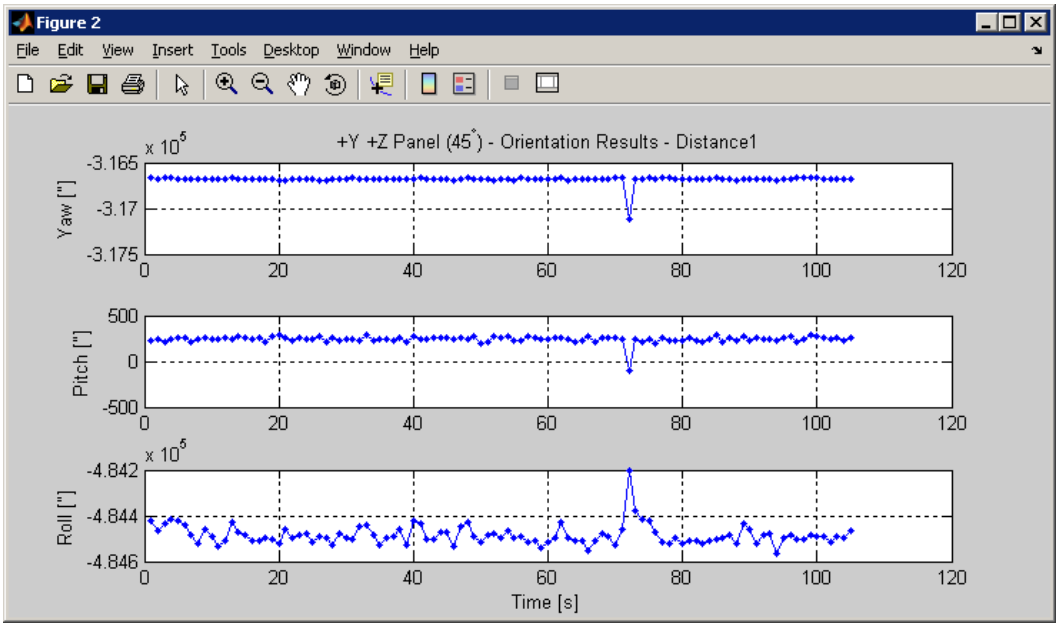

Std(posX) [mm]	Std(posY) [mm]	Std(posZ) [mm]	Std(yaw) ["]	Std(pitch) ["]	Std(roll) ["]
0,044	0,097	0,473	43,601	39,123	43,384

This document contains information that may not be disclosed, distributed or reproduced without written approval by MIS at National Space Institute – DTU.

4.2 Distance2 (~8.2m)

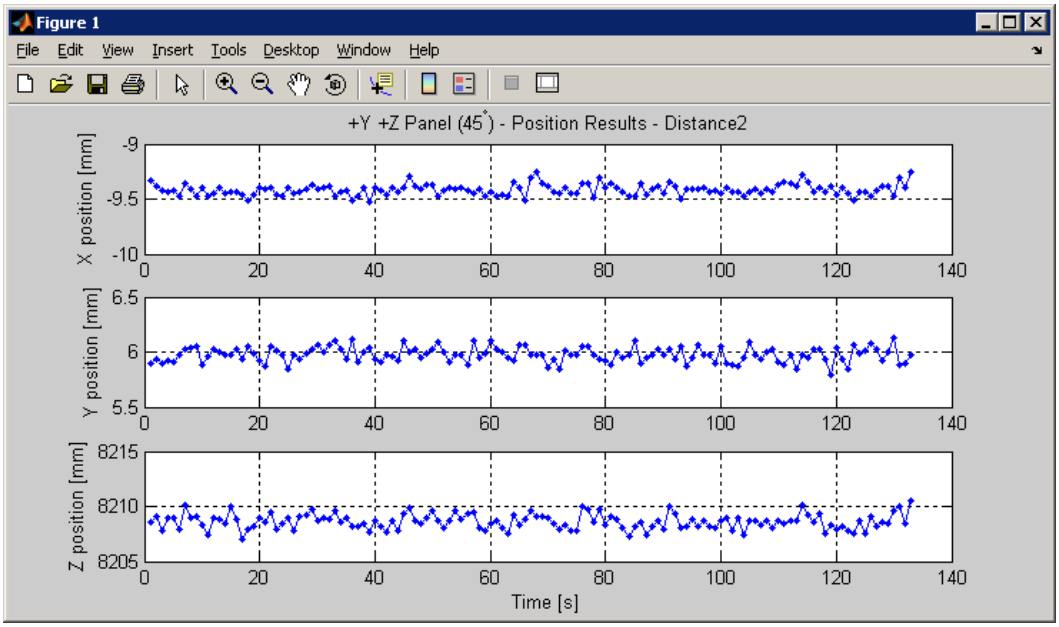

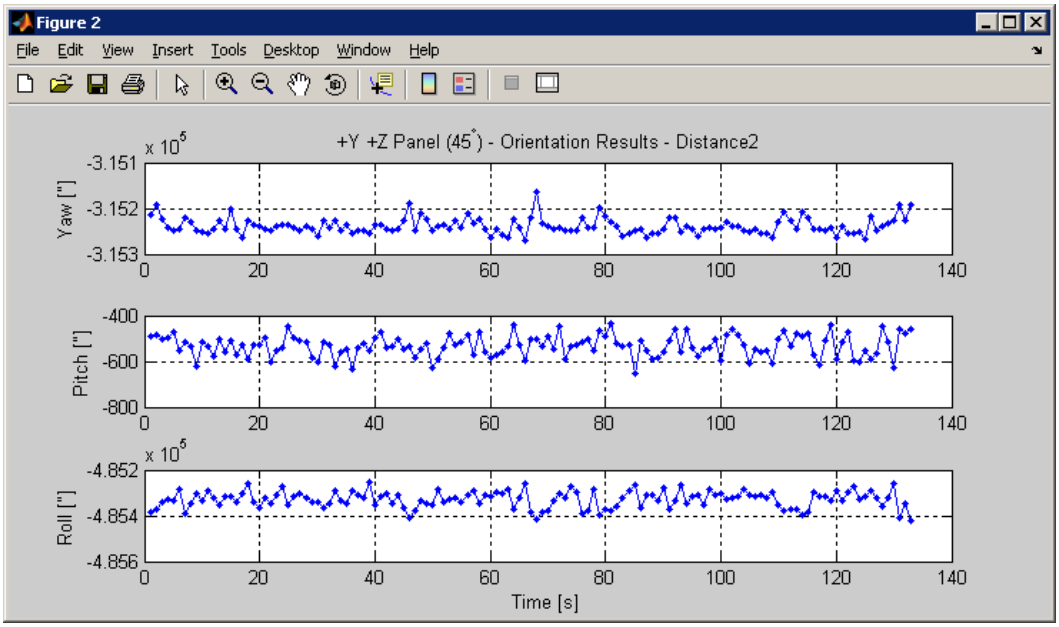

Std(posX) [mm]	Std(posY) [mm]	Std(posZ) [mm]	Std(yaw) ["]	Std(pitch) ["]	Std(roll) ["]
0,051	0,068	0,691	17,389	47,301	36,376

This document contains information that may not be disclosed, distributed or reproduced without written approval by MIS at National Space Institute – DTU.

4.3 Distance3 (~11.2m)

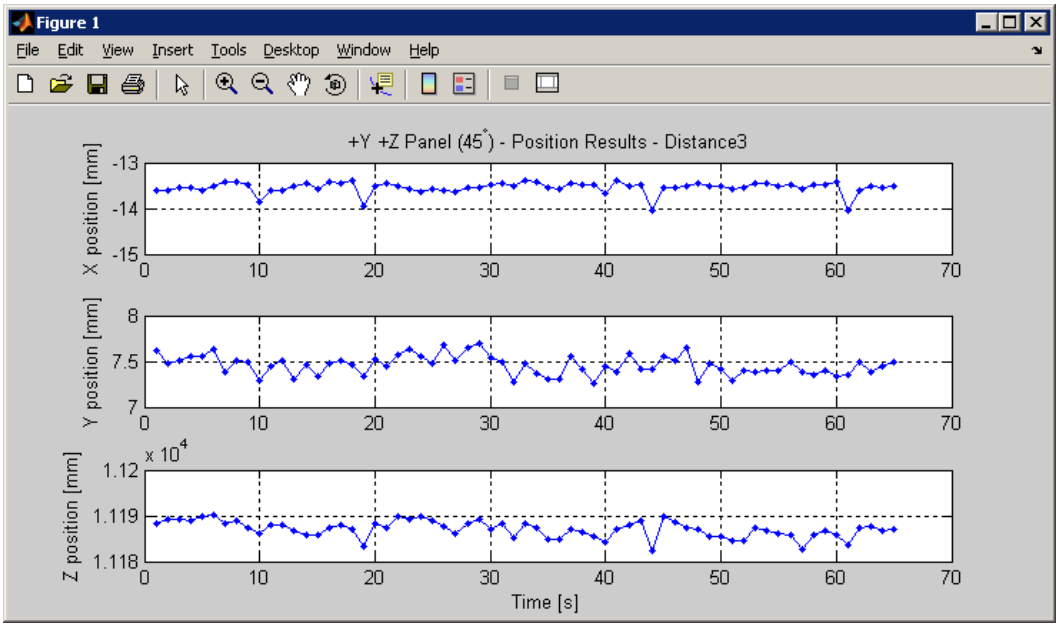

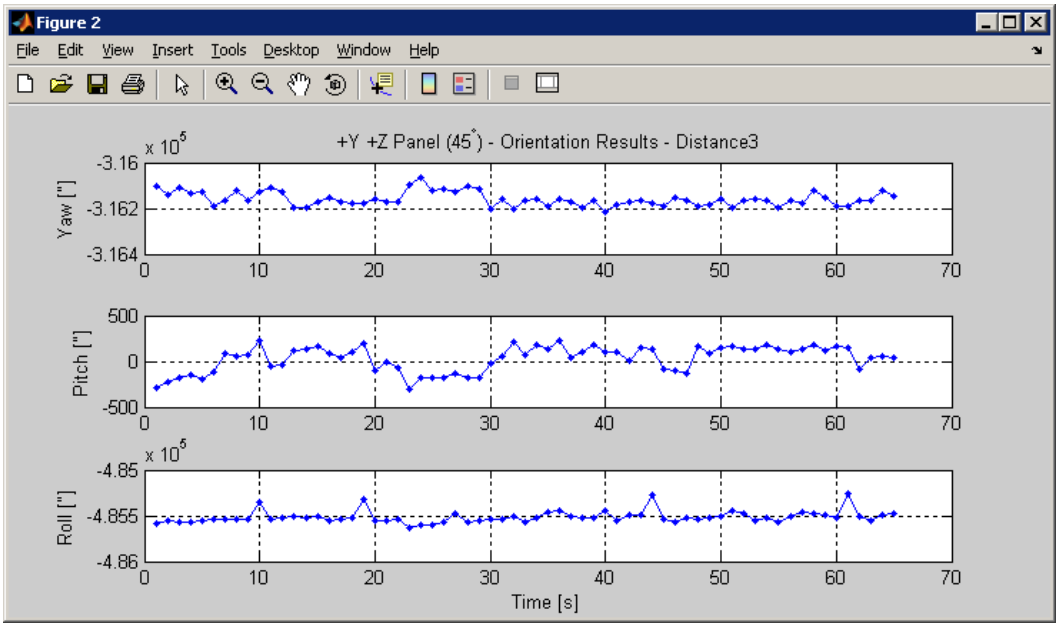

Std(posX) [mm]	Std(posY) [mm]	Std(posZ) [mm]	Std(yaw) ["]	Std(pitch) ["]	Std(roll) ["]
0,130	0,107	1,786	31,160	139,614	67,345

This document contains information that may not be disclosed, distributed or reproduced without written approval by MIS at National Space Institute – DTU.

4.4 Distance4 (~15.2m)

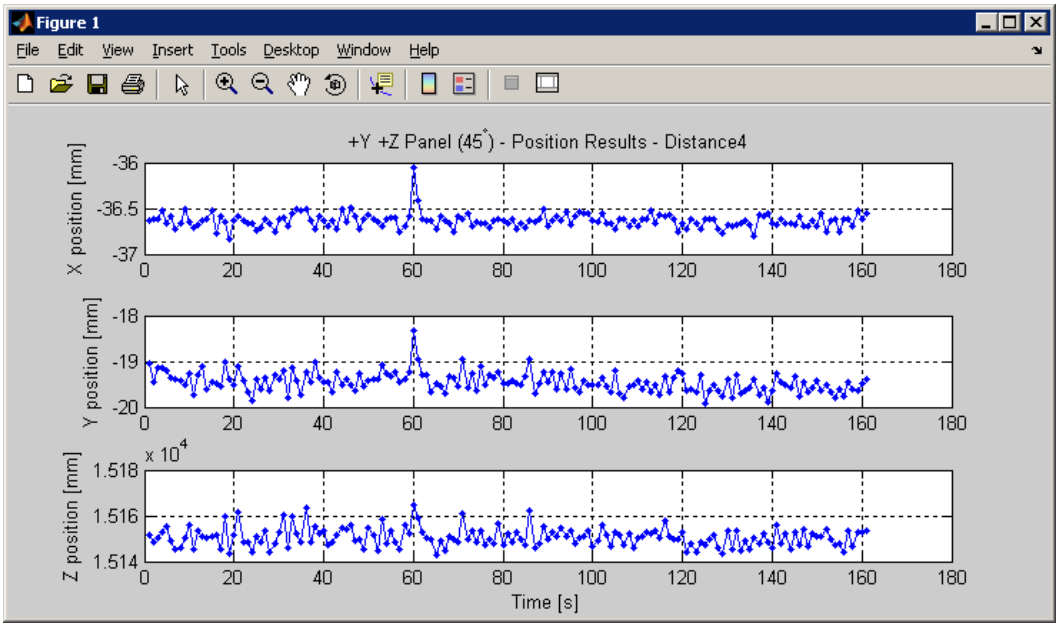

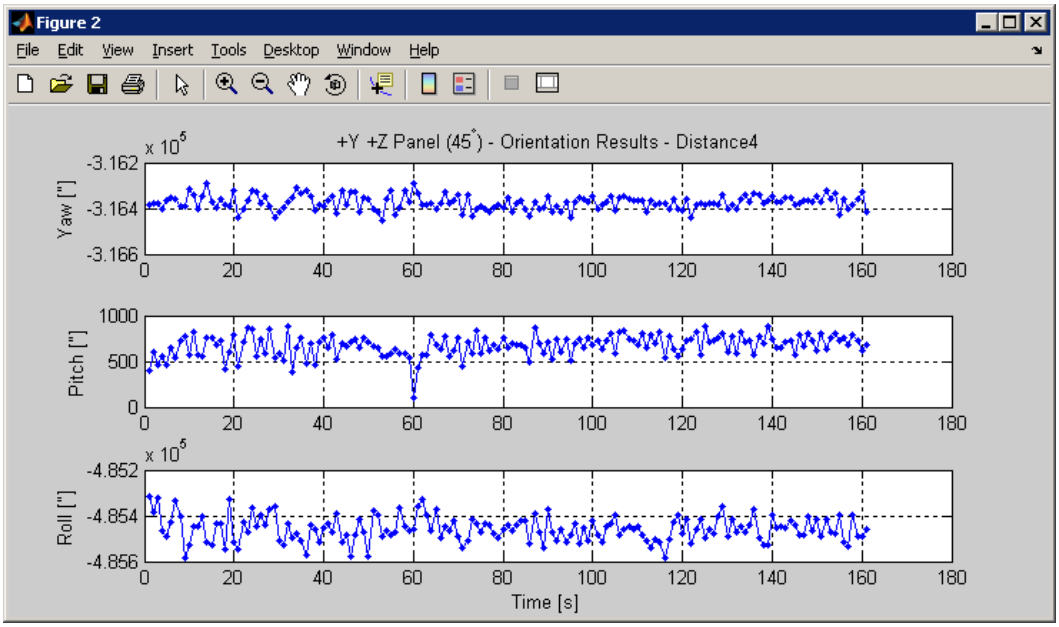

Std(posX) [mm]	Std(posY) [mm]	Std(posZ) [mm]	Std(yaw) ["]	Std(pitch) ["]	Std(roll) ["]
0,082	0,220	4,202	31,569	117,874	54,536

This document contains information that may not be disclosed, distributed or reproduced without written approval by MIS at National Space Institute – DTU.

5 +Z Panel (~90 deg)

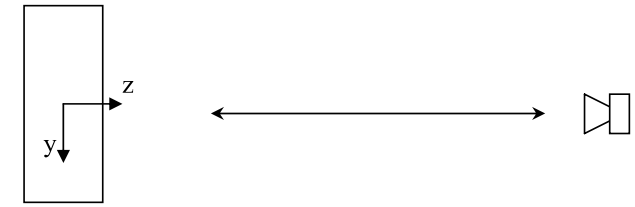

Figure 5: Satellite orientation for measurements on +Z panel (~90 deg).

5.1 Distance1 (~5.2m)

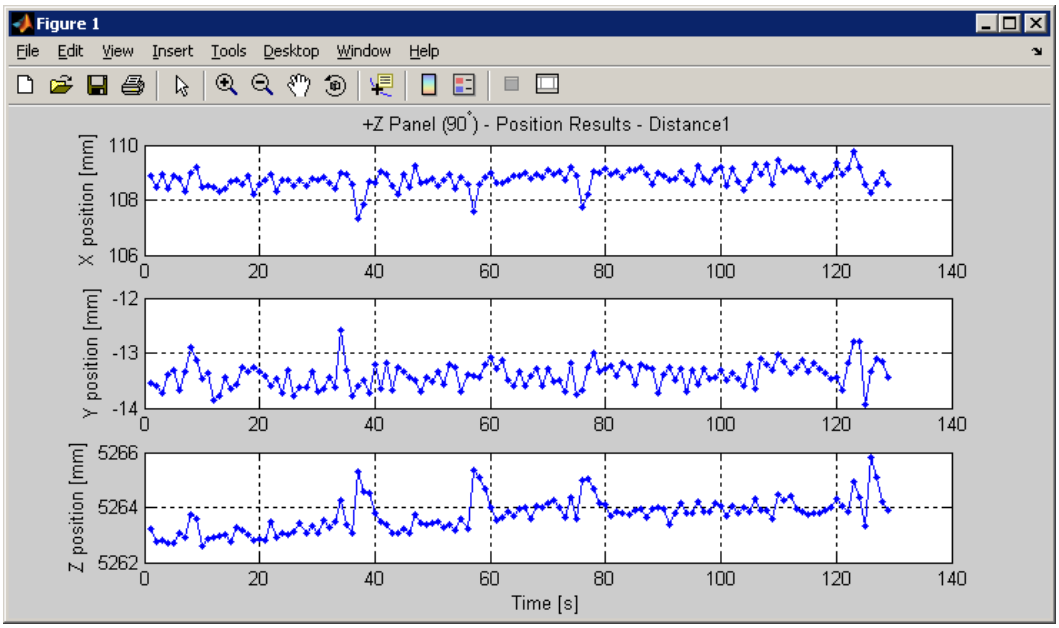

This document contains information that may not be disclosed, distributed or reproduced without written approval by MIS at National Space Institute – DTU.

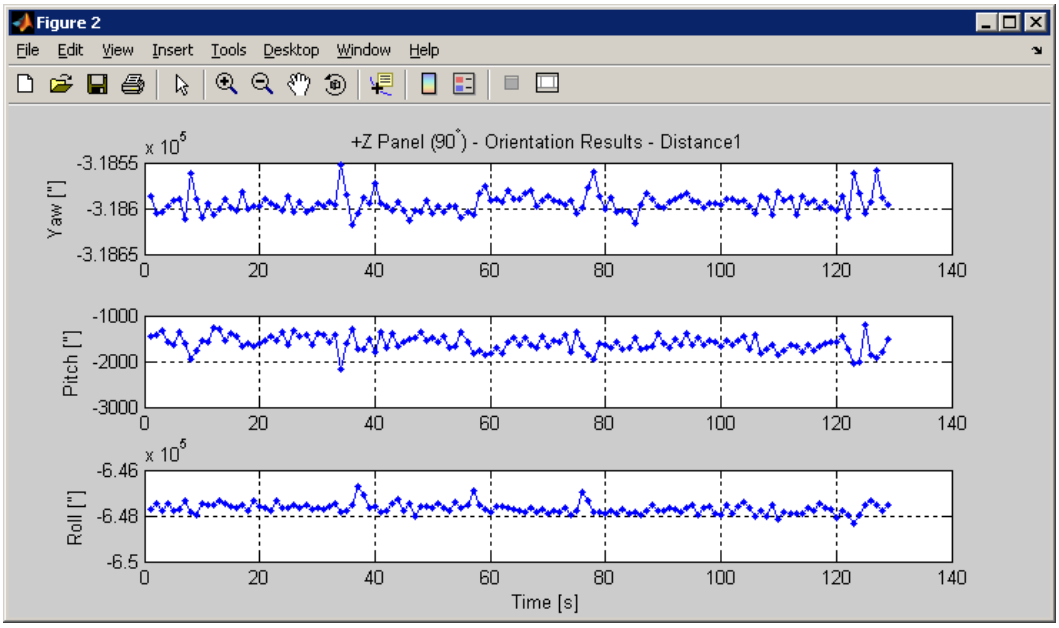

Std(posX) [mm]	Std(posY) [mm]	Std(posZ) [mm]	Std(yaw) ["]	Std(pitch) ["]	Std(roll) ["]
0,346	0,226	0,614	10,918	171,195	230,341

This document contains information that may not be disclosed, distributed or reproduced without written approval by MIS at National Space Institute – DTU.

5.2 Distance2 (~8.2m)

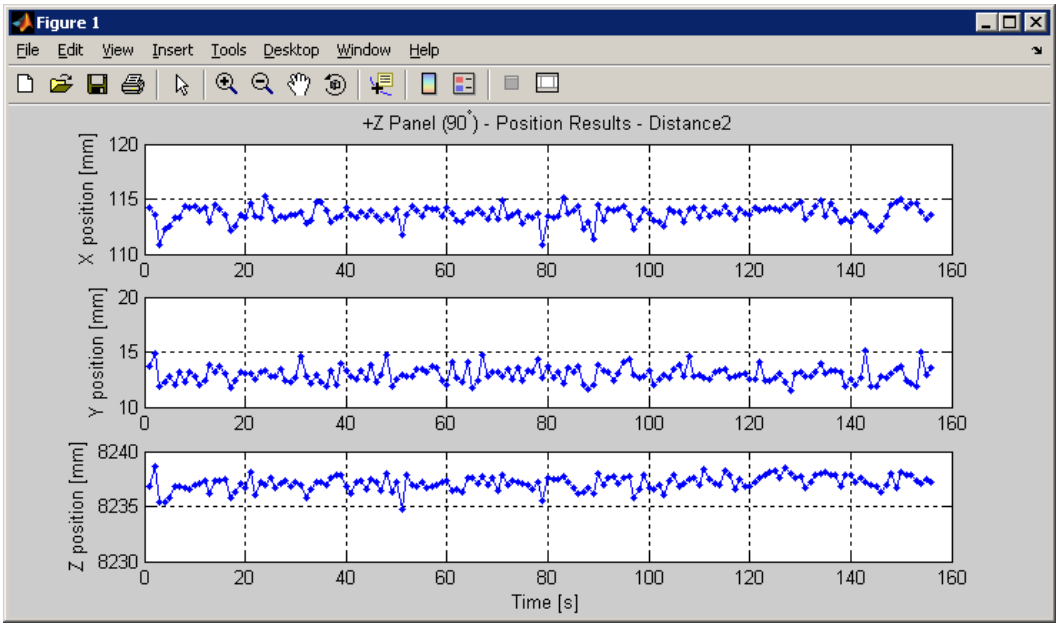

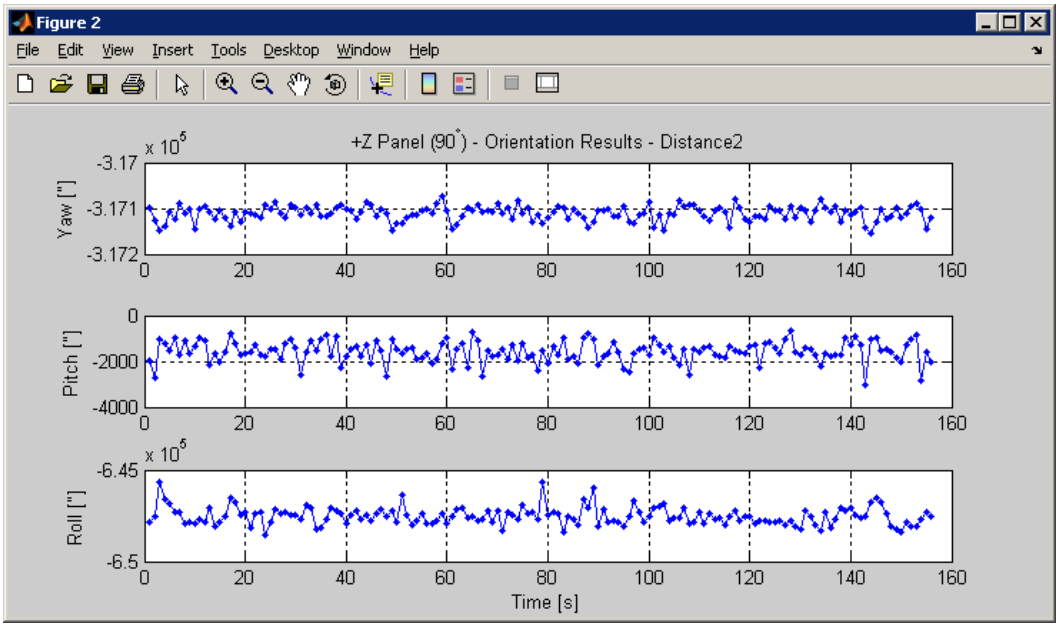

Std(posX) [mm]	Std(posY) [mm]	Std(posZ) [mm]	Std(yaw) ["]	Std(pitch) ["]	Std(roll) ["]
0,745	0,720	0,666	16,299	459,545	489,119

This document contains information that may not be disclosed, distributed or reproduced without written approval by MIS at National Space Institute – DTU.

5.3 Distance3 (~11.2m)

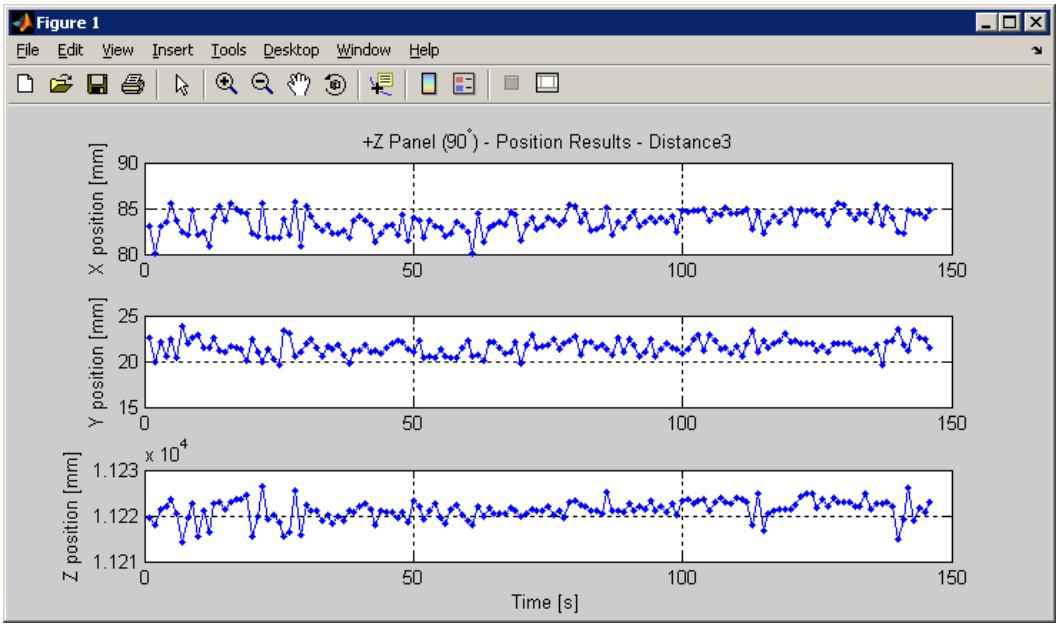

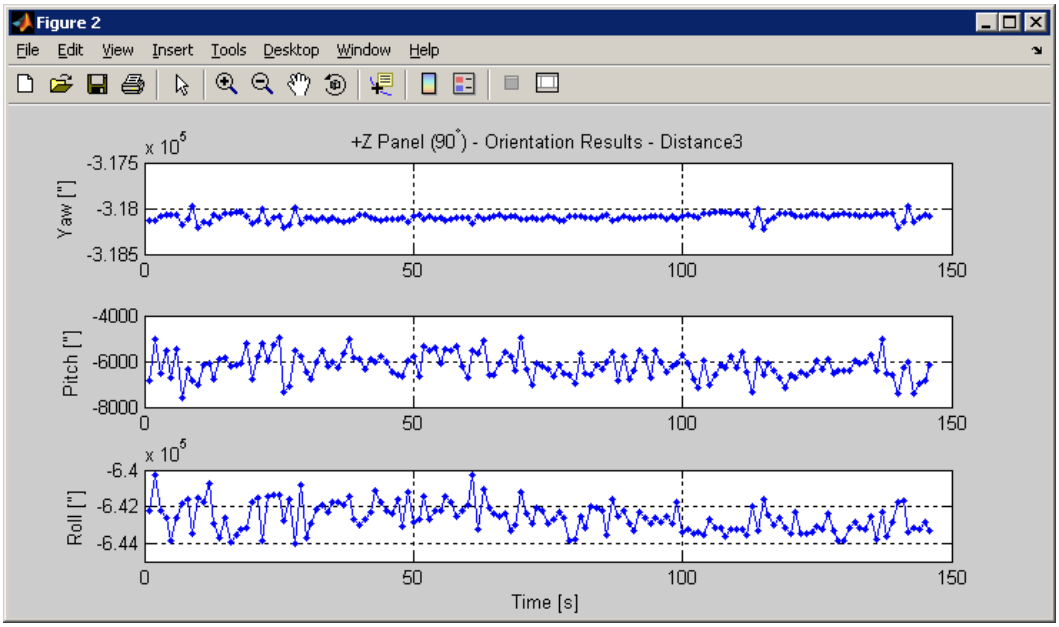

Std(posX) [mm]	Std(posY) [mm]	Std(posZ) [mm]	Std(yaw) ["]	Std(pitch) ["]	Std(roll) ["]
1,196	0,846	2,241	41,938	551,414	803,172

This document contains information that may not be disclosed, distributed or reproduced without written approval by MIS at National Space Institute – DTU.

5.4 Distance4 (~15.2m)

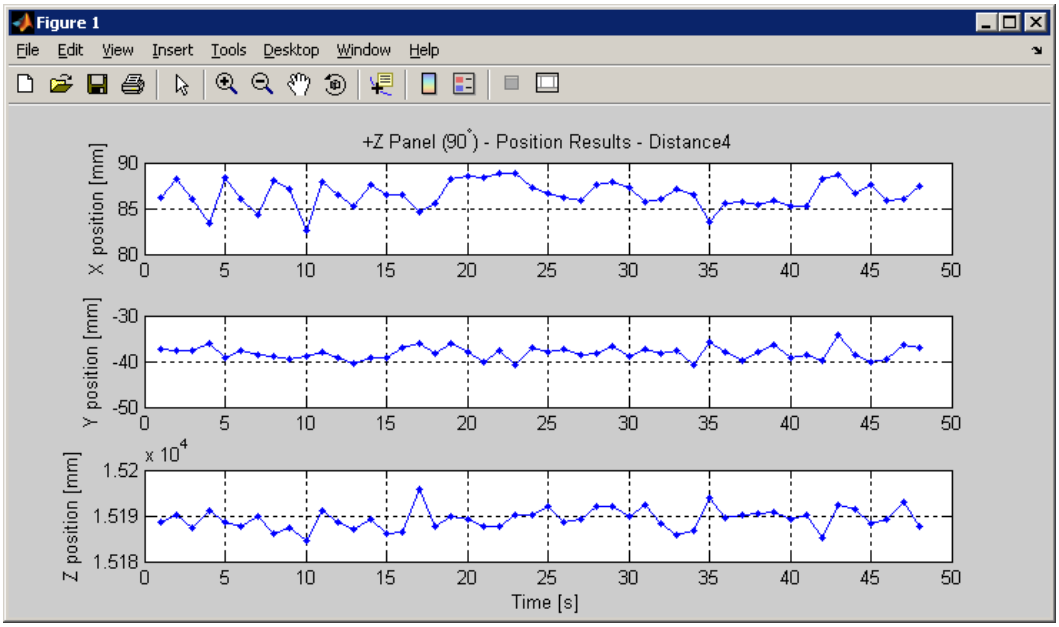

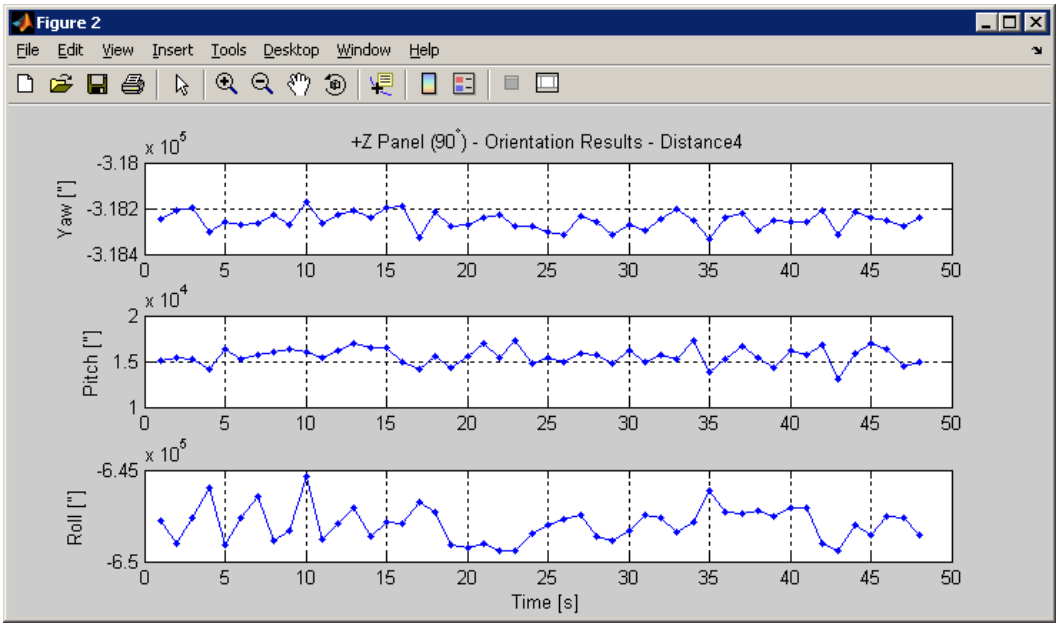

Std(posX) [mm]	Std(posY) [mm]	Std(posZ) [mm]	Std(yaw) ["]	Std(pitch) ["]	Std(roll) ["]
1,457	1,371	2,306	37,838	928,311	940,587

This document contains information that may not be disclosed, distributed or reproduced without written approval by MIS at National Space Institute – DTU.

6 Standard Deviation Comparison

This section compares the listed standard deviation values listed in the previous sections. The approximated distance values are used in order to plot the distance and rotation influences on the noise of the VBS system.

Ori	Dist	Std(posX) [mm]	Std(posY) [mm]	Std(posZ) [mm]	Std(yaw) ["]	Std(pitch) ["]	Std(roll) ["]
0 deg	Dist1	0,763	0,728	0,815	10,783	530,432	507,062
	Dist2	2,396	2,269	3,947	29,858	1414,285	1659,188
	Dist3	2,875	2,444	9,557	55,547	1752,901	1969,919
	Dist4	2,648	2,744	16,341	40,476	1963,994	1768,507
22.5deg	Dist1	0,236	0,759	0,845	15,582	434,924	147,047
	Dist2	0,724	0,735	1,133	22,243	513,676	475,110
	Dist3	0,363	0,680	2,463	17,018	438,005	231,292
	Dist4	0,605	1,241	4,097	20,837	835,524	391,715
45 deg	Dist1	0,044	0,097	0,473	43,601	39,123	43,384
	Dist2	0,051	0,068	0,691	17,389	47,301	36,376
	Dist3	0,130	0,107	1,786	31,160	139,614	67,345
	Dist4	0,082	0,220	4,202	31,569	117,874	54,536
90 deg	Dist1	0,346	0,226	0,614	10,918	171,195	230,341
	Dist2	0,745	0,720	0,666	16,299	459,545	489,119
	Dist3	1,196	0,846	2,241	41,938	551,414	803,172
	Dist4	1,457	1,371	2,306	37,838	928,311	940,587

The noise distribution for the different determined pose and position variables are respectively plotted in the following figures.

This document contains information that may not be disclosed, distributed or reproduced without written approval by MIS at National Space Institute – DTU.

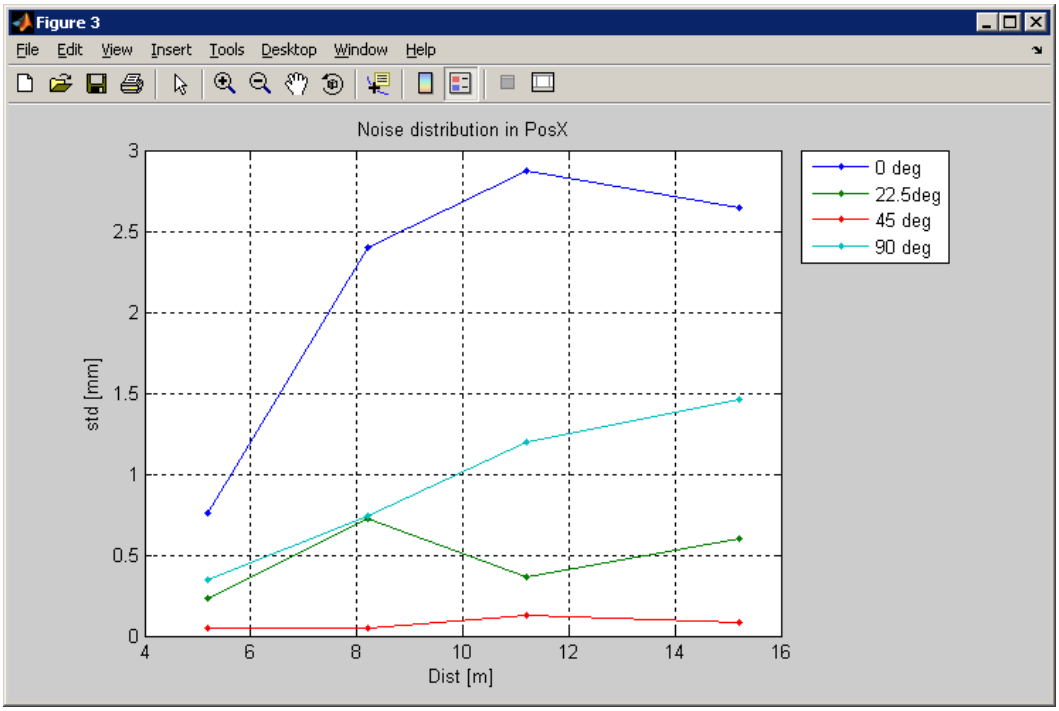

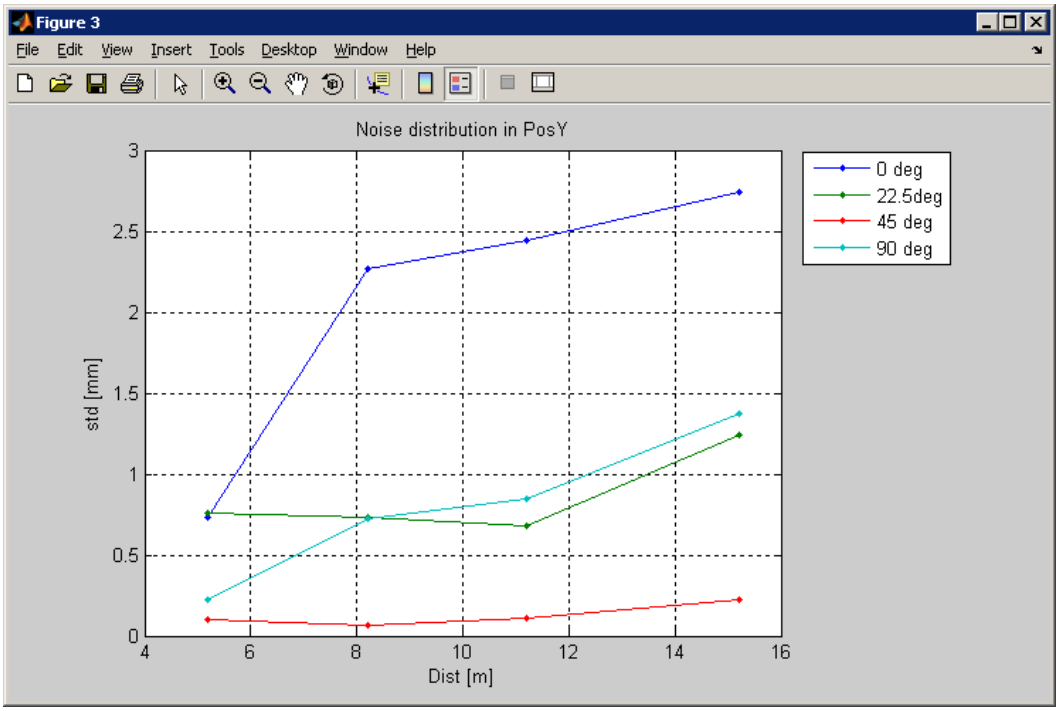

This document contains information that may not be disclosed, distributed or reproduced without written approval by MIS at National Space Institute – DTU.

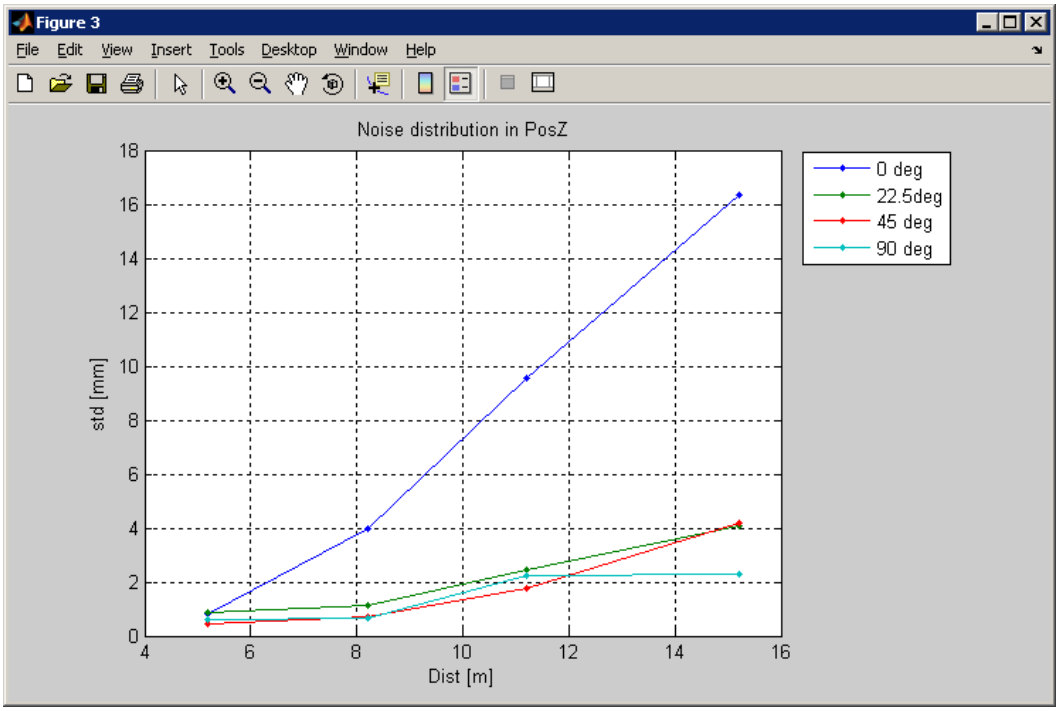

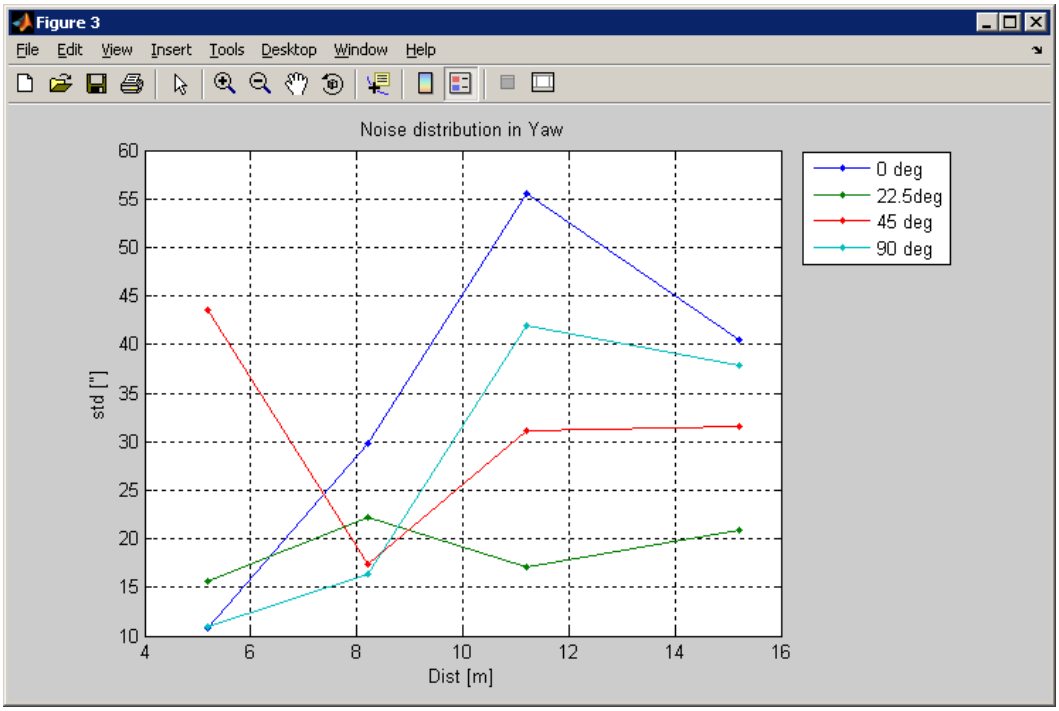

This document contains information that may not be disclosed, distributed or reproduced without written approval by MIS at National Space Institute – DTU.

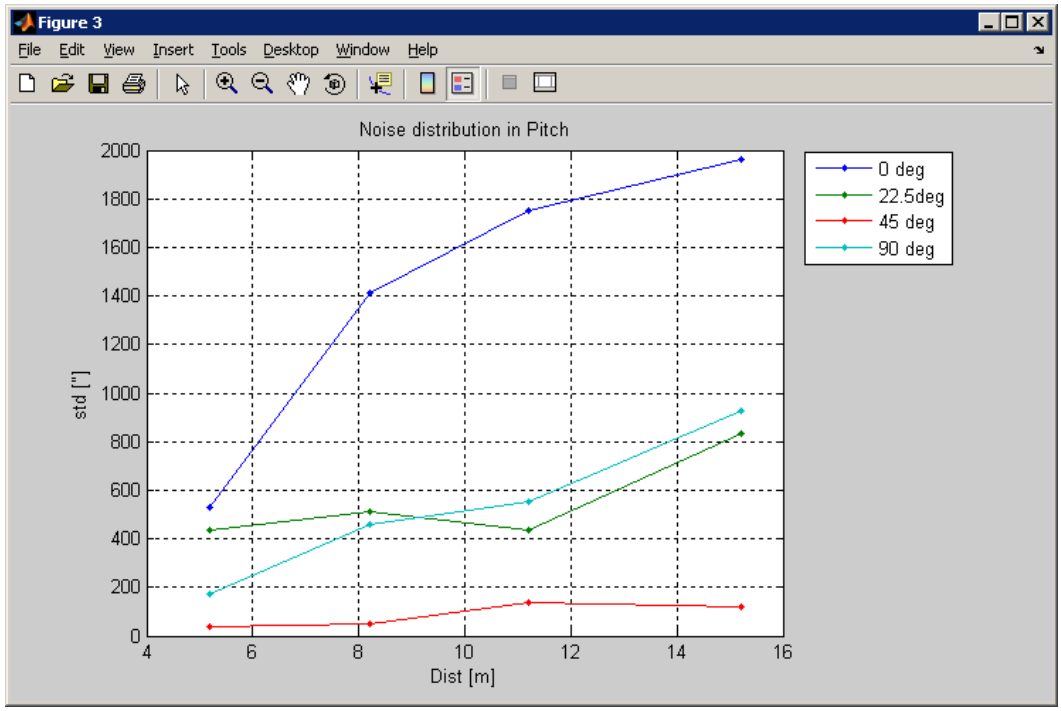

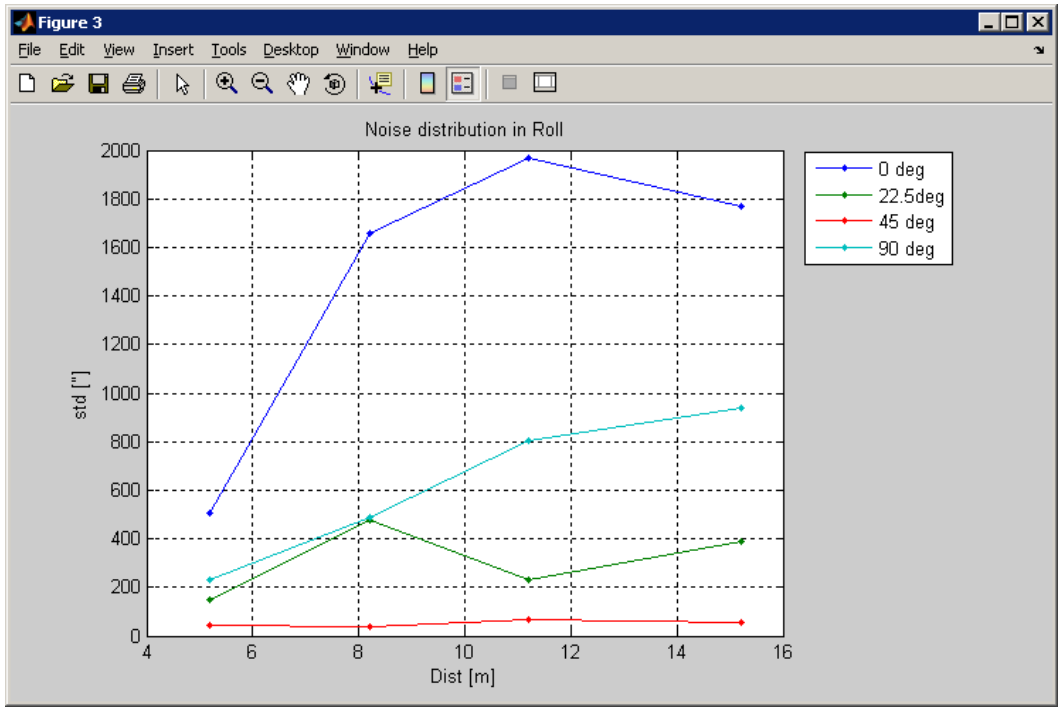

This document contains information that may not be disclosed, distributed or reproduced without written approval by MIS at National Space Institute – DTU.

7 Conclusion

It is seen that the noise distribution of the normal view on +Y panel (0 deg) is notably greater than for the other measured panel views. It is believed that this effect is due to a combination of the narrow spacing between the LEDs and the influence of centroiding noise when viewing from normal. Similar effect is for example not seen at same level when viewing the +Z panel from its normal, nor seen when +Y panel is slightly slanted.

It has to be noted that cross correlation between the position values and the pose values have been observed for a main part of the measurements and can give an increase in the standard deviation results. Cross correlations can occur due to the fact that the reference point of the Target satellite is placed offset of the measurement points on the panels.

Not all the plotted standard deviations follow the exponential growing as would be expected. It is believed that several additional measurements are needed in order to make a clearer assumption on such a distribution of all the standard deviations.

This document contains information that may not be disclosed, distributed or reproduced without written approval by MIS at National Space Institute – DTU.

Appendix J

Test Report of the Final PRISMA SW Load Campaign

Test Report of the Final PRISMA SW Load Campaign. December 3-4, 2009

A.Massaro, J.L.Jørgense, M.Benn

1. Upload new SW

The software release dated **20091201** consists of updated TOPS, MAXIHOP and SYSVAR. Additionally is included a new LEDMODEL based on measurements from previous SW campaign. First task consisted of upload the three first SW modules, verify the upload by checksum, reboot the DPU and initiate the VBS mode.

In order to check for any improvements, changes or solution issues for the SR_Coop mode, upload of the new LEDMODEL was awaited until verification of a solution by the new software modules.

The software modules were verified by checksum, having the following parameters:

Name:	Address:	Length:	ISO:
TOPS	0x01015000	29716	0x2f8f
MAXIHOP	0x0102A000	149524	0xe70d
LEDMODEL	0x01387000	516	0x4a0f

Setting up Main and Target in fixed position enabled the VBS to provide solution of pose and position of Target based on the old LEDMODEL. The following data is extracted from the binary TM file: 'OPS_TM_VC0_1936_ST_DPU_B_20091203-132203_20091203-143054.RAC'.

The Target position output of the VBS system is given as follow:

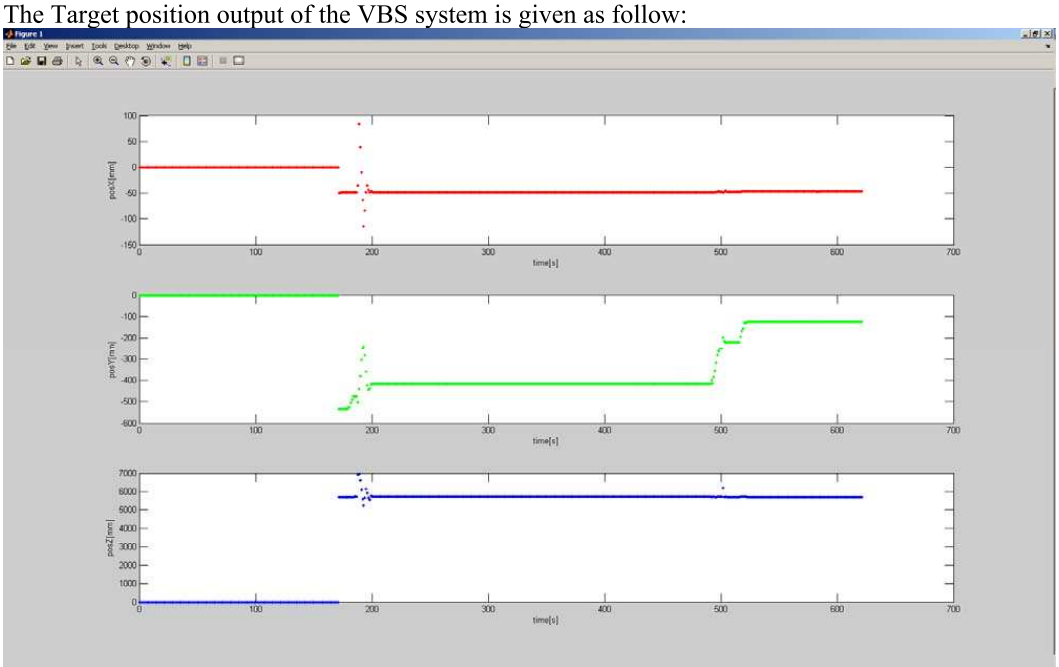

This document contains information that may not be disclosed, distributed or reproduced without written approval by MIS at National Space Institute – DTU.

The AGC control of the shuttertime:

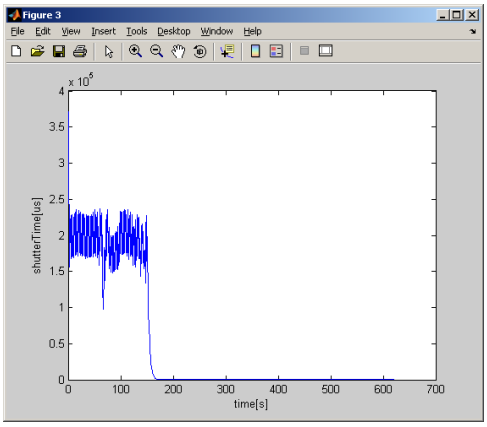

The VBS status flags:

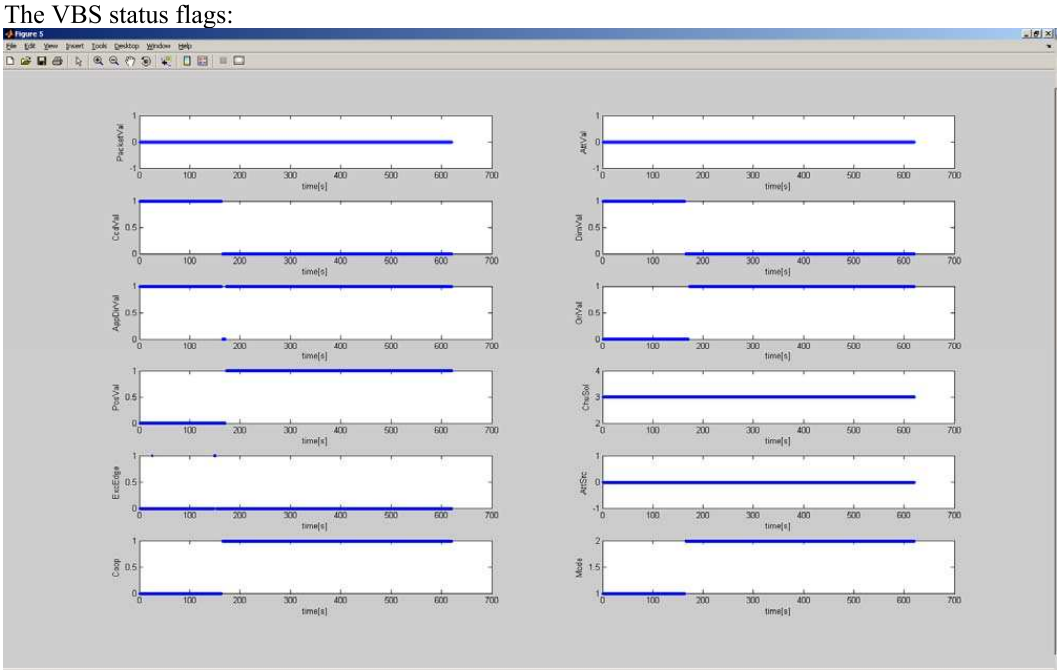

And the VBS status values:

This document contains information that may not be disclosed, distributed or reproduced without written approval by MIS at National Space Institute – DTU.

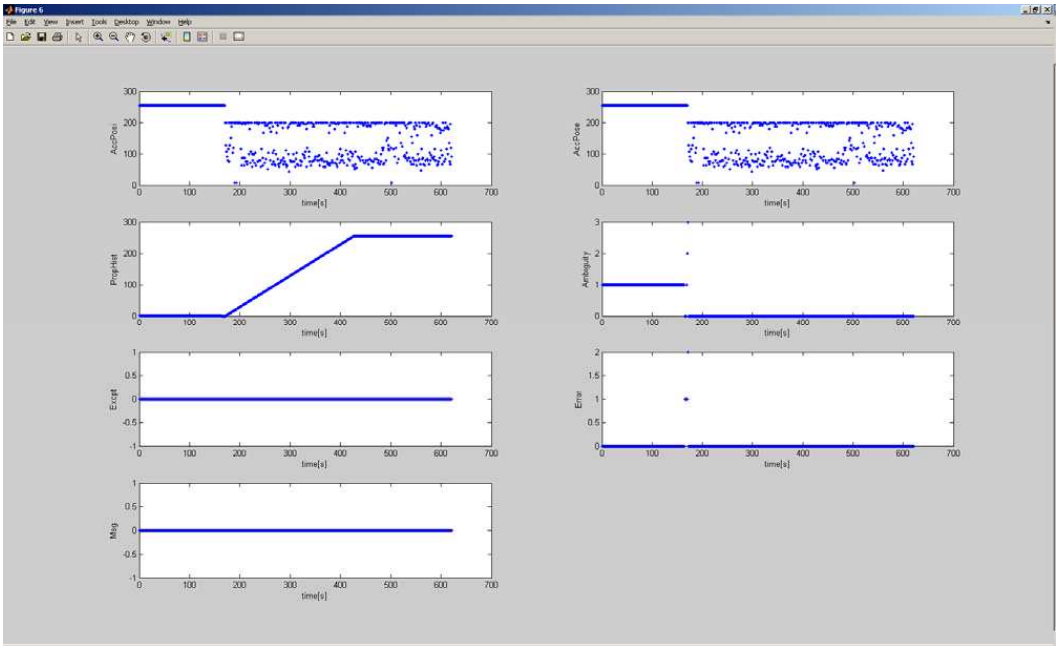

In order to analyze the noise figure of the VBS results, the last 50 samples are analyzed since it is seen that the AGC control has acquired a stable level in the end of the test.

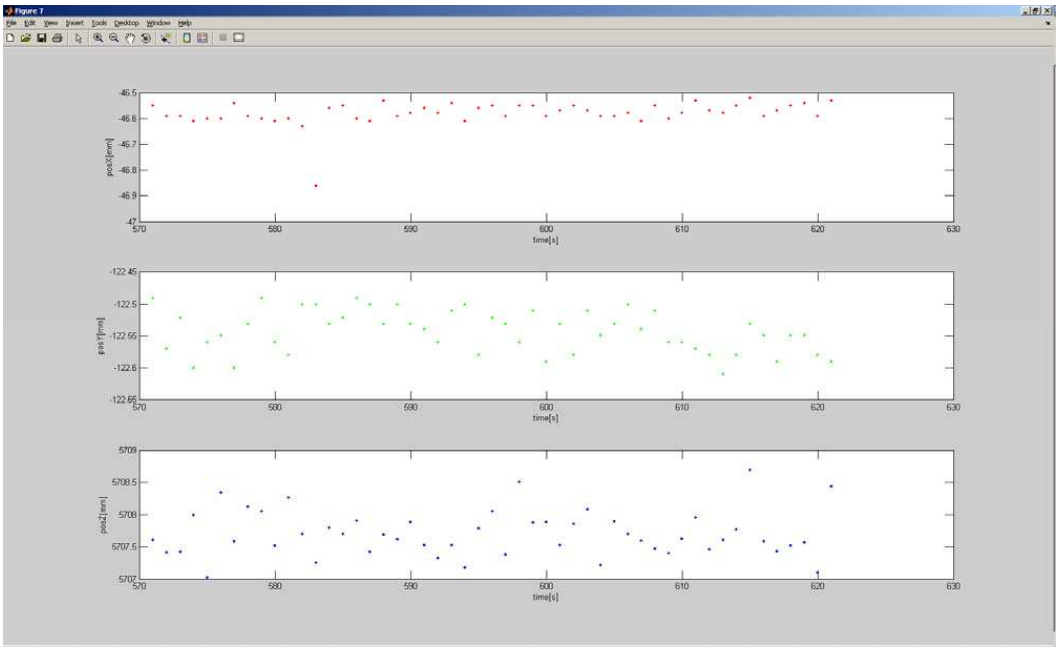

This document contains information that may not be disclosed, distributed or reproduced without written approval by MIS at National Space Institute – DTU.

Mean and Standard Deviation for the given dataset is given as:

Param:	Mean[mm]:	Std[mm]:
PosX	-46.58	0.04736
PosY	-122.54	0.03317
PosZ	5707.70	0.35365

It is seen that the noise in both PosX and PosY is below 0.05mm in standard deviation and below 0.5mm in PosZ. This already shows an improvement from previous SW versions, and is mainly due to a more stable AGC control providing better centroid fixes of the LEDs. The last 50 values of the shutter time are likewise given here:

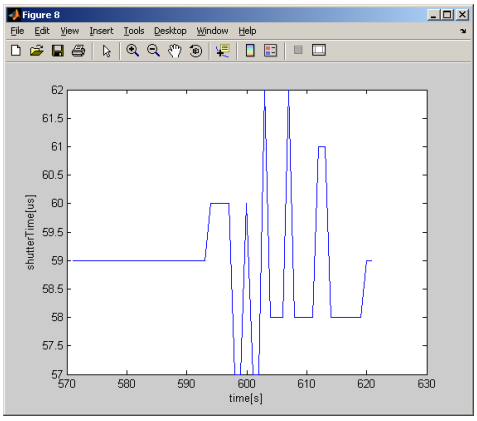

In order to compare the previous LEDMODEL with the new LEDMODEL, the same measurements are performed on the exact same setup with the new LEDMODEL uploaded to the system. The following data is extracted from the binary TM file: 'OPS_TM_VC0_1936_ST_DPU_B_20091203-144542_20091203-150557.RAC'.

Again, the last 50 samples of the Target position output of the VBS system are given:

This document contains information that may not be disclosed, distributed or reproduced without written approval by MIS at National Space Institute – DTU.

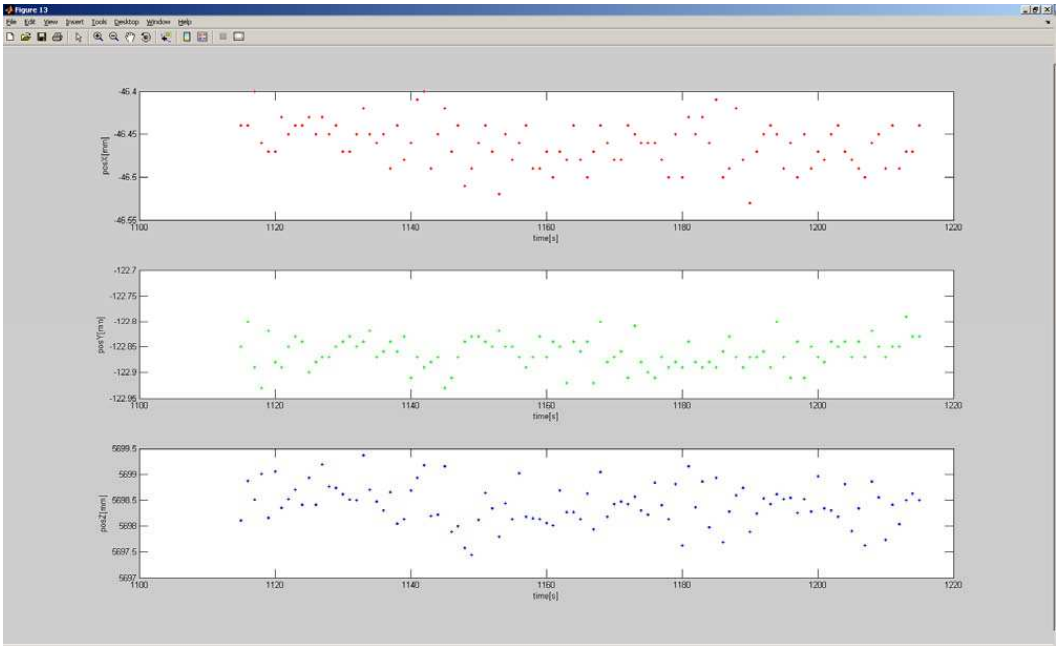

With the corresponding shutter times:

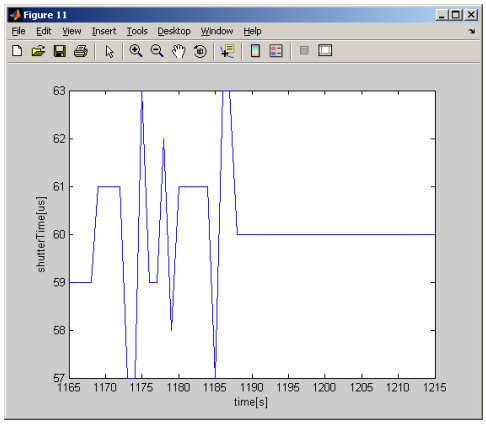

The Mean and Standard Deviation for the new LEDMODEL have the following values:

Param:	Mean[mm]:	Std[mm]:
PosX	-46.47	0.02431
PosY	-122.86	0.02980
PosZ	5698.40	0.35955

It is seen that the noise figures for the new LEDMODEL are improved for PosX and PosY, and similar for PosZ. This indicates that the new LEDMODEL is an improvement from the previous version, though only for the current visible panels in the fixed setup between Main and Target.

This document contains information that may not be disclosed, distributed or reproduced without written approval by MIS at National Space Institute – DTU.

Likewise, a bias shift is seen in the Mean values due to the changes in the LEDMODEL. This is expected since the panels have been adjusted in correlation to each other, and the new result is believed to be a better solution due to the lower noise figures and the better fit of the centroids.

2. Analysis of LEDMODEL

In order to analyse the new LEDMODEL uploaded, the Target satellite is rotated around one axis while the VBS system is providing solutions. The following data is extracted from the binary TM file: 'OPS_TM_VC0_1936_ST_DPU_B_20091203-152805_20091203-154755.RAC'.
All centroids detected during the rotation are illustrated given in CCD coordinates for x and y respectively:

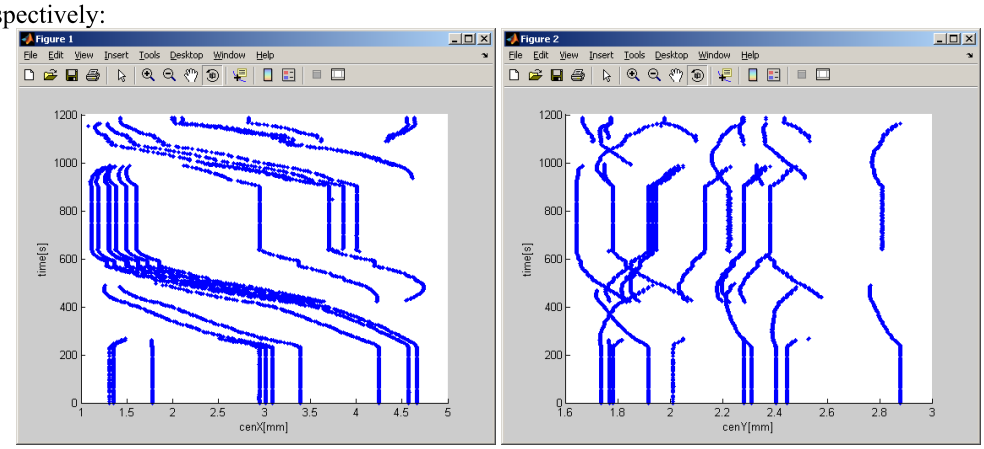

During this rotation the VBS system provided following results for the position:

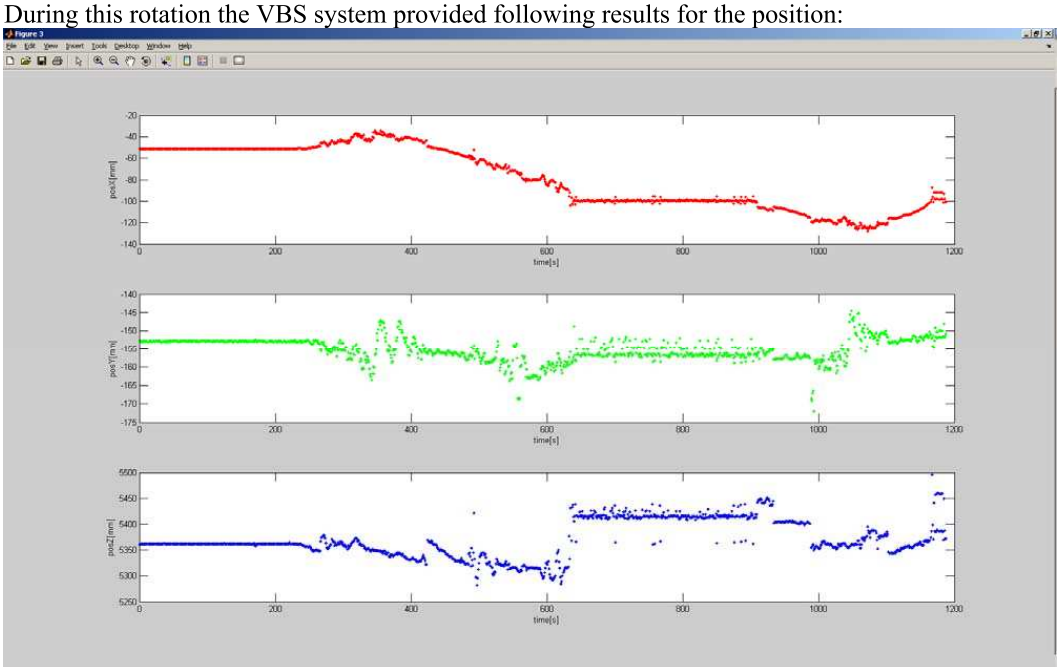

This document contains information that may not be disclosed, distributed or reproduced without written approval by MIS at National Space Institute – DTU.

And the following pose:

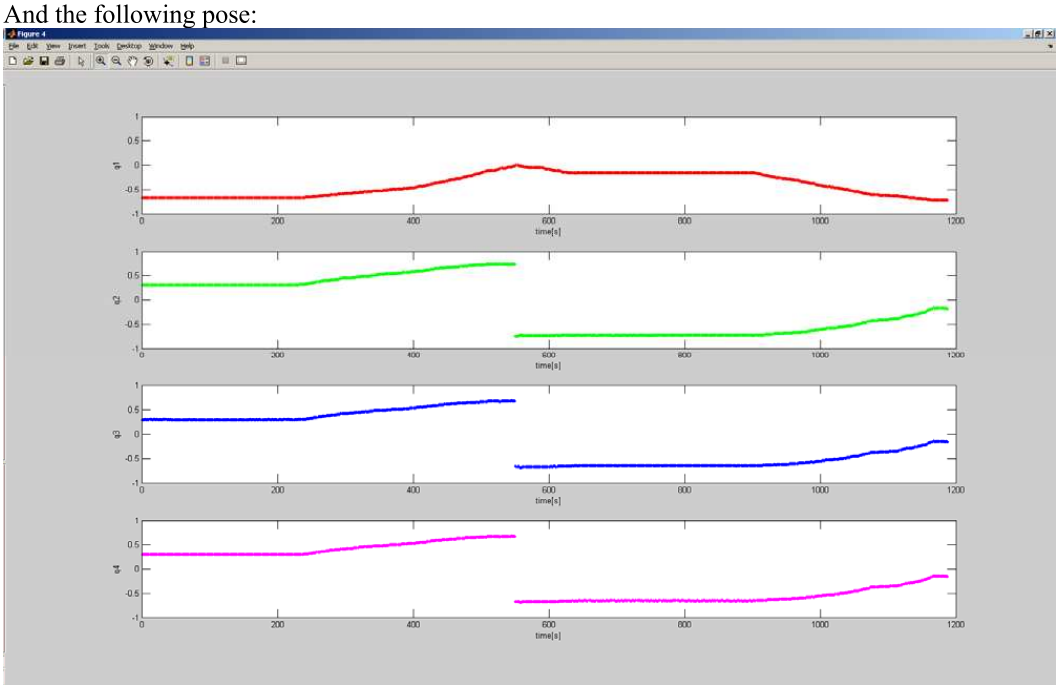

During the rotation it was observed that the mapping between panel -Y +X and +X +Y went smoother with the new LEDMODEL, while the mapping between panel +Y -X and -X -Y were uneven and provided noisy results. This indicates that the –X panel is not yet correctly aligned to the other panels.

3. No GPS fix on Target

During the tests it was observed that when Main had a good GPS fix and Target did not have a GPS fix, the VBS system (LEDs on Target and DPU on Main) was still performing during several minutes. This was due to the fact that the Target satellite was capable of keeping the LED pulsing period without drifting too much compared to the Main satellite.
The PPS period of the unfixed Target satellite is though believed to vary differently when in-flight where different temperatures will be experienced for the two satellites.

4. Exceeding Edge Flag

The Exceeding Edge flag in SR Coop mode has been implemented since the latest SW release. Therefore a test was performed in order to confirm correct flagging in the current mode. The following data is extracted from the binary TM file: 'OPS_TM_VC0_1936_ST_DPU_B_20091204-091649_20091204-103742.RAC'.
The test sequence consisted of having full Target in FOV showing that the Exceeding Edge flag was not set. Thereafter the SR CHU was blinded, forcing it out of lock, and the Target satellite moved to a position where at least one LED is out of the FOV of the SR CHU. The blinding cover was

This document contains information that may not be disclosed, distributed or reproduced without written approval by MIS at National Space Institute – DTU.

thereby removed, and it was observed that a solution was acquired as soon as the AGC levels had adjusted where the Exceeding Edge flag was correctly set.
The centroids taken during the test setup is illustrated, where the blue centroids indicate invalid VBS solutions, green centroids indicate valid VBS solution without Exceeding Edge flag and the red centroids indicate valid VBS solution with the Exceeding Edge flag:

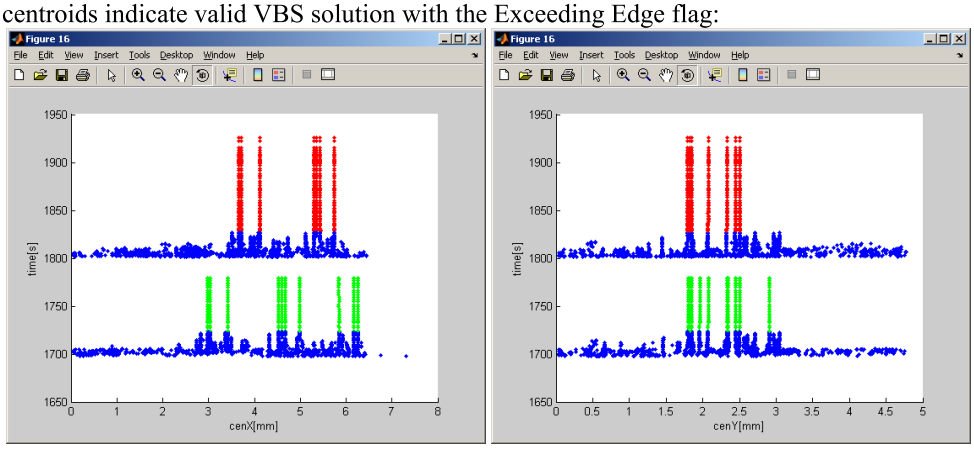

The Exceeding Edge flag thereby performs as expected.

5. Pharos module testing

The testing of the FR and IR modes was performed with the Pharos module attached on the FR camera's baffle, using a customized interface plate.
Two designs with differing features were developed and validated for the test instrument. While both are able to create a moving target within a static stars background, Pharos 1.0 allows for limited swing amplitude of about 25" on a single axis, whereas Pharos 2.0 can move the target along two axis on a radius of 1 degree around the center of the image plane.
Pharos was also used for testing mode switching FR-IR/IR-FR.

This document contains information that may not be disclosed, distributed or reproduced without written approval by MIS at National Space Institute – DTU.

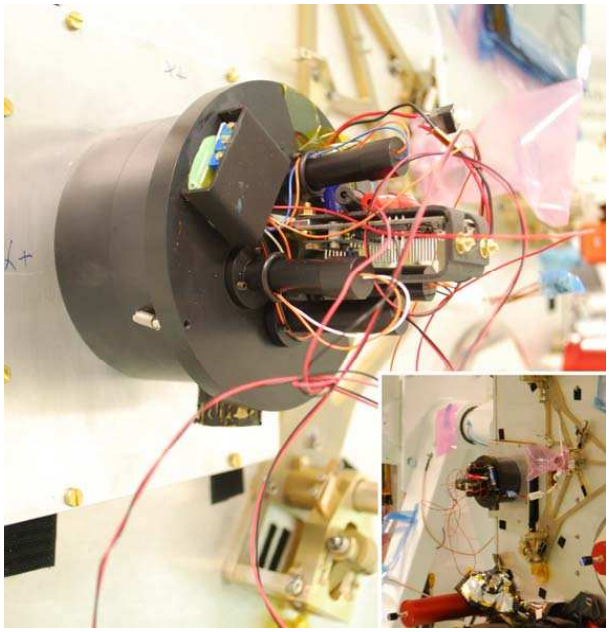

Testing setup

Mounting procedure:

- Mount Pharos module on the interface plate
- Mount module on the baffle
  - Make sure that the mirrors axis is vertical, with the fixed mirror below the moving one
- Connect power cables (stars, Target, control board)
- Connect USB interface cable from control board to PC
- Power up the module
  - **5V** on stars
  - **1.3V** (or 10mA) on Target
  - **3V** (battery pack) on Pharos control board
- Verify, via SW-EGSE, that the 9 stars and Target are powered
  - Reposition Target if it's out of the field of view (software controlled)

Below is shown a snapshot from the far range camera with all stars and Target powered on. Target appears in the lower area of the frame, closer to the "line" stars group.

This document contains information that may not be disclosed, distributed or reproduced without written approval by MIS at National Space Institute – DTU.

In these conditions, the module is ready for testing. The data documented in this report is extracted from the file *OPS_TM_VC0_1936_ST_DPU_B_20091204-113014_20091204-132401.RAC*.

Test FR

The testing consisted of two phases:

a. test FR Target lock
b. test out of range motion and verify that Target is not locked

Procedure:

- Perform update cycle
- Set min and max Target speed range in sysvar table at 600 and 1000 "/s
- Set Target speed at about 800 "/s
- Test target acquisition and validity during its motion
- Set Target at minimum speed (about 400 "/s)
- Observe invalid solution

Outcome:
The speed range parameters were correctly loaded in the system and Target lock in FR mode, after a stimulator update, has been continuously validated with Pharos 1.0. Target is "not locked" (invalid solution) when the speed range is outside the defined values, as expected.
On the other hand, Pharos 2.0 showed a non linear motion of the Target, which made it tricky for the system to maintain a continuous lock. This behavior is supposedly caused by the current Pharos design, which relies on open loop control of the drive motors, resulting in a variable speed and motion direction of the Target.

This document contains information that may not be disclosed, distributed or reproduced without written approval by MIS at National Space Institute – DTU.

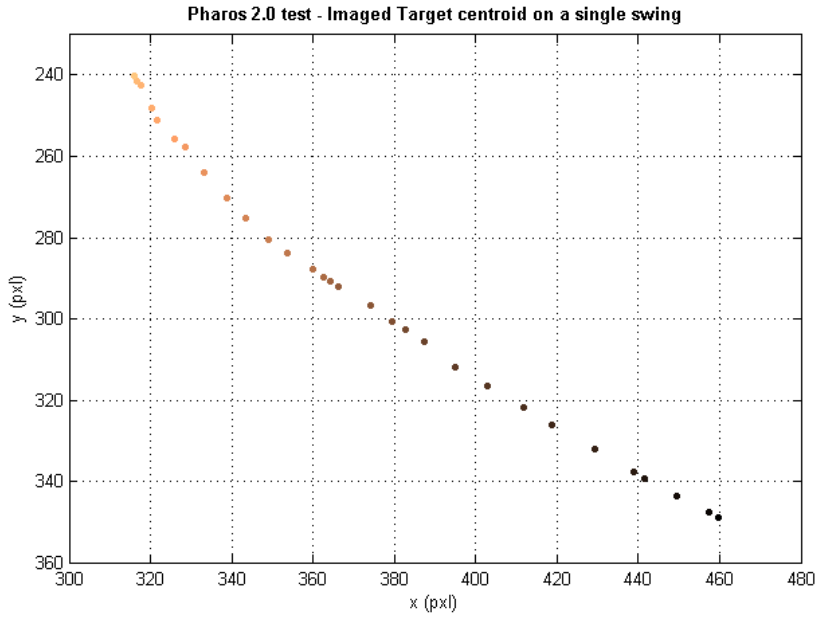

A test segment has been plotted below. The Target lock during motion happens at sporadic instants, which alternate to losses of contact. This can be seen in the time intervals 4900 ÷ 4950 s and 5010 ÷ 5050 s. Between 4950 s and 5010 s, Target was out of the field of view, thus no data is retrieved.

This document contains information that may not be disclosed, distributed or reproduced without written approval by MIS at National Space Institute – DTU.

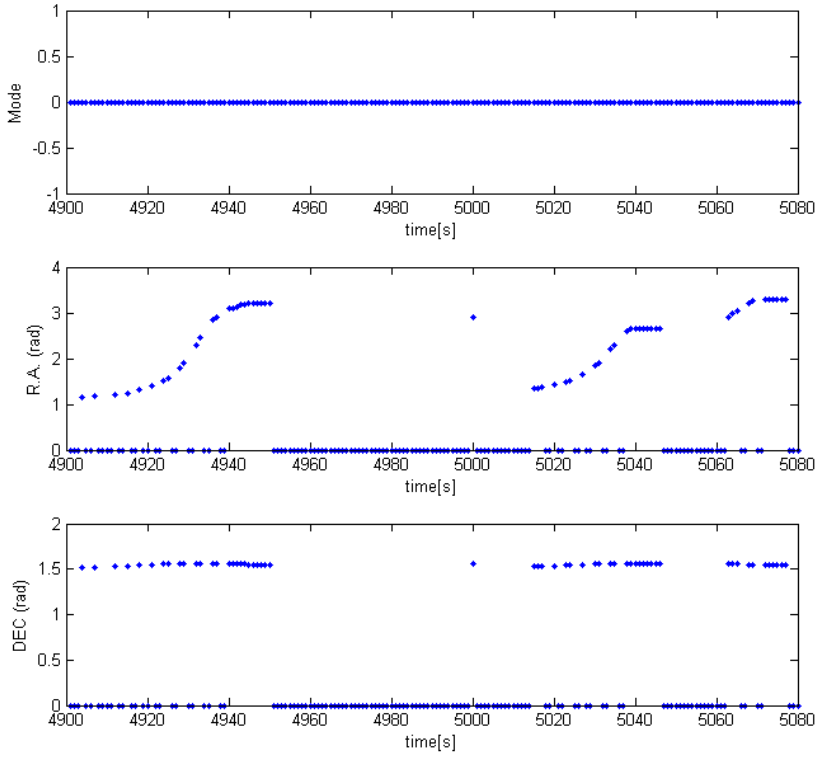

Test IR

Procedure:

- Turn off Pharos stars
- Verify that Target is the only object visible and that the SW is able to lock on it, providing its relative direction (RA and DEC)

Outcome:
RA and DEC calculation have been verified. As shown in the following plots, when mode is 1 (IR) a valid pair of right ascension and declination is output.

This document contains information that may not be disclosed, distributed or reproduced without written approval by MIS at National Space Institute – DTU.

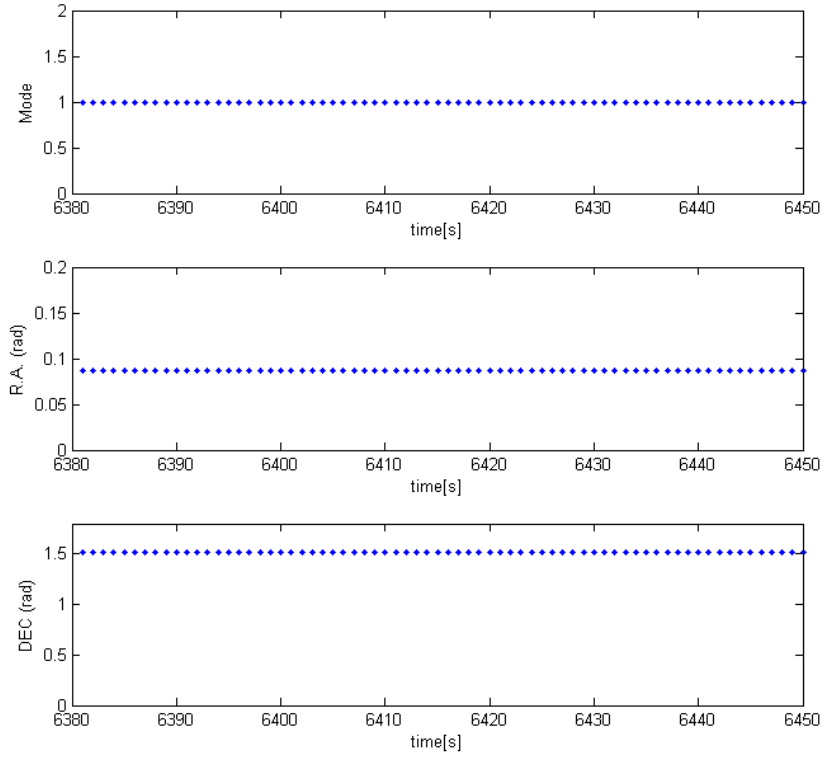

Test switching FR -> IR and IR -> FR

Procedure:

- Mount Pharos (see 6)
- Set system on far range mode
- Verify switching
  a. Increase Target brightness until IR mode switching occurs. Decrease Target brightness to verify restoring of FR mode.
  b. Turn off stars and verify switching to IR. Turn on stars and verify restoring of FR mode.

Outcome:
The mode switching has been verified by turning off and on the stars on Pharos. A mode switching stimulated by gradual brightness variation could not be verified since the Target's maximum brightness relative to the stars' is not sufficient to bloom the camera and trigger the switch.
Mode switching in and out of IR has been verified and plotted in figure below. The plots show that when mode switches from 0 to 1 (FR to IR), RA and DEC are shifted of a constant value. This shift is due to the fact that in IR mode the camera loses track of the firmament, thus calculating the

This document contains information that may not be disclosed, distributed or reproduced without written approval by MIS at National Space Institute – DTU.

values of RA and DEC relative to the camera coordinate system. Acknowledging this factor, the values of RA and DEC are unchanged when a mode switching occurs.

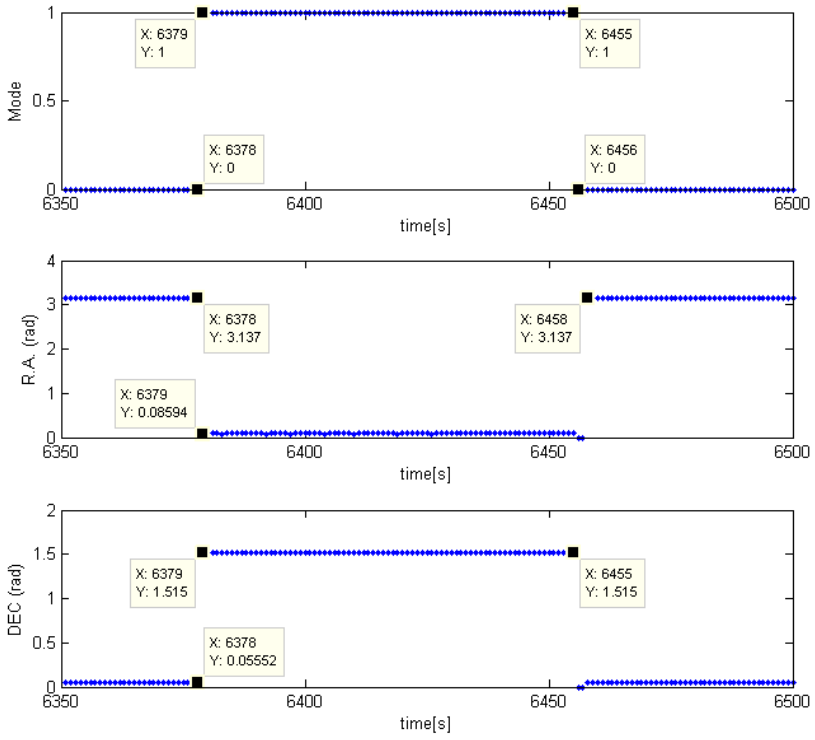

After the IR to FR mode switching, there are two measurements returning null values of relative direction. This happens because the stars are back in the field of view, and the Target needs to pass through the FR filters and be tracked for at least three following snapshots before being identified.

6. Timestamping

Previous software load campaign showed issues regarding correct time stamping of the VBS TM packets. This was due to the PPS latch fluctuations, and therefore a more robust detection system is implemented in the latest SW release.
A test sample has been taken from the binary TM file:
'OPS_TM_VC0_1936_ST_DPU_B_20091203-132203_20091203-143054.RAC', where the difference between all VBS packages have been illustrated:

This document contains information that may not be disclosed, distributed or reproduced without written approval by MIS at National Space Institute – DTU.

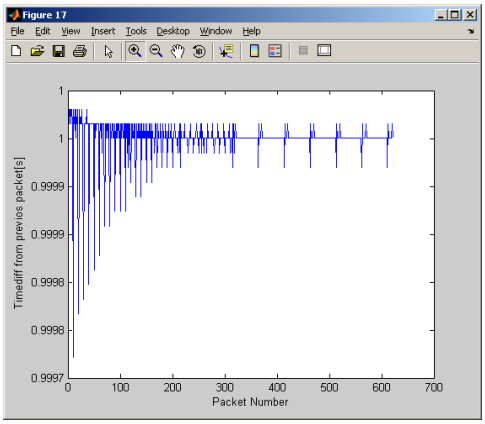

This shows that the half second variation is not longer present in the current data set. Though, the PPS latch fluctuation is seen as a drifting into a stable level. This drifting could be due to the fact that the GPS had just fixed onto satellites and was thereby still stabilizing its accuracy.

7. Conclusion on NCRs

The following NCRs have been handled during the SW load and subsequent tests:

NCR-429: Calculation of R.A. and Dec was inconsistent between IR and FR mode. This has now been corrected and verified.

NCR-449: Correct setting of the Exceeding Edge flag during SR cooperative mode has been verified.

NCR-451: Half second difference in VBS timestamps are not longer detected due to the more robust implementation of PPS detection by the µASC DPU.

NCR-453: Along with the new software release a new Delta TM/TC ICD was released as well, which includes requested actions.

NCR-454: During the RA and Dec validation it was observed that the Dimension information was inconsistent. This needs to be investigated by DTU.

NCR-455: Related to NCR-429.

This document contains information that may not be disclosed, distributed or reproduced without written approval by MIS at National Space Institute – DTU.

Appendix K

Docking Pattern Calibration

Images captured of the Docking Pattern placed on the $-Y$ panel of the Target spacecraft. These measurements were taken on the FM PRISMA satellites, with the FM VBS system integrated, on test campaign PRISMA_20090929 at SSC, Solna, Stockholm.

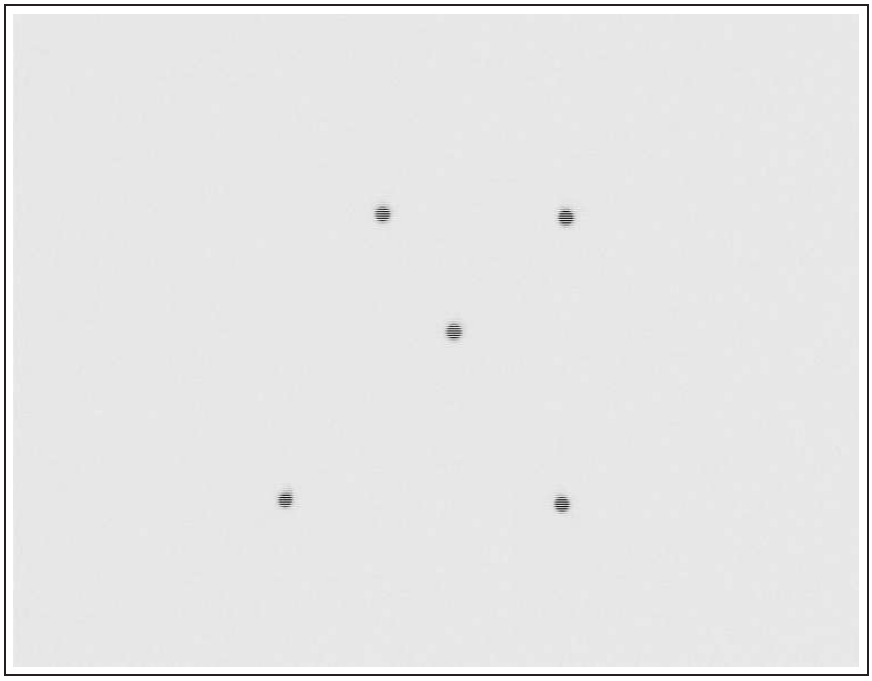

Figure K.1. *Docking Pattern captured normal to boresight with the SR CHU. Image is inverted and enhanced for printing.*

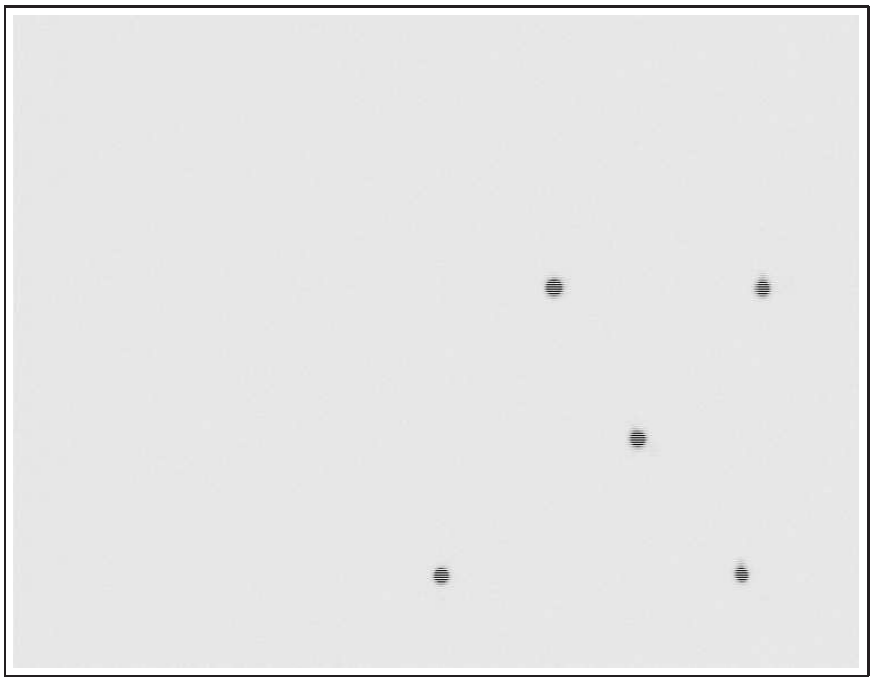

Figure K.2. *Docking Pattern captured at 45deg pitch to boresight around Target x-axis. Image is inverted and enhanced for printing.*

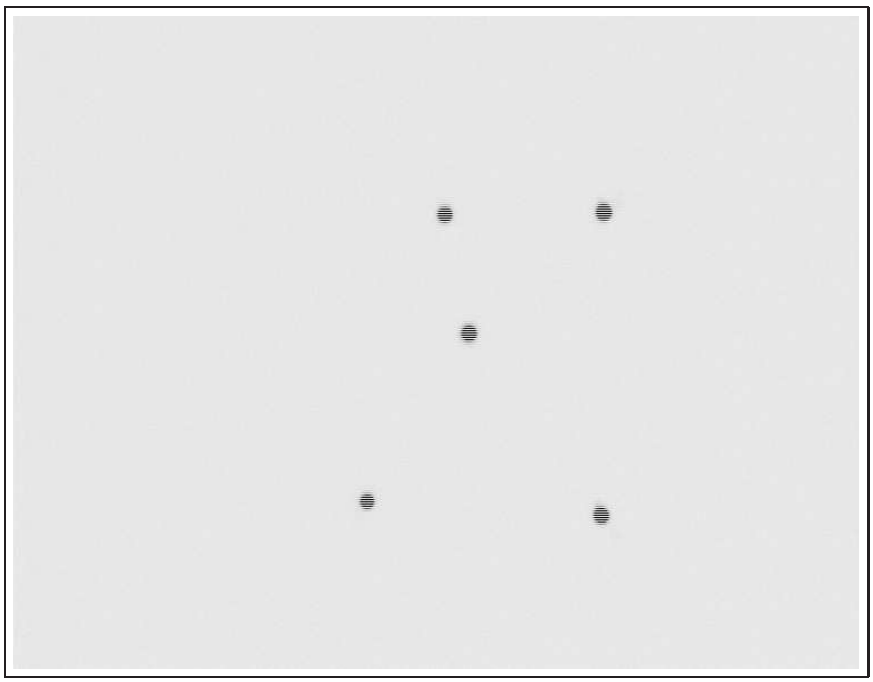

Figure K.3. *Docking Pattern captured at 45deg turn to boresight around Target z-axis. Image is inverted and enhanced for printing.*

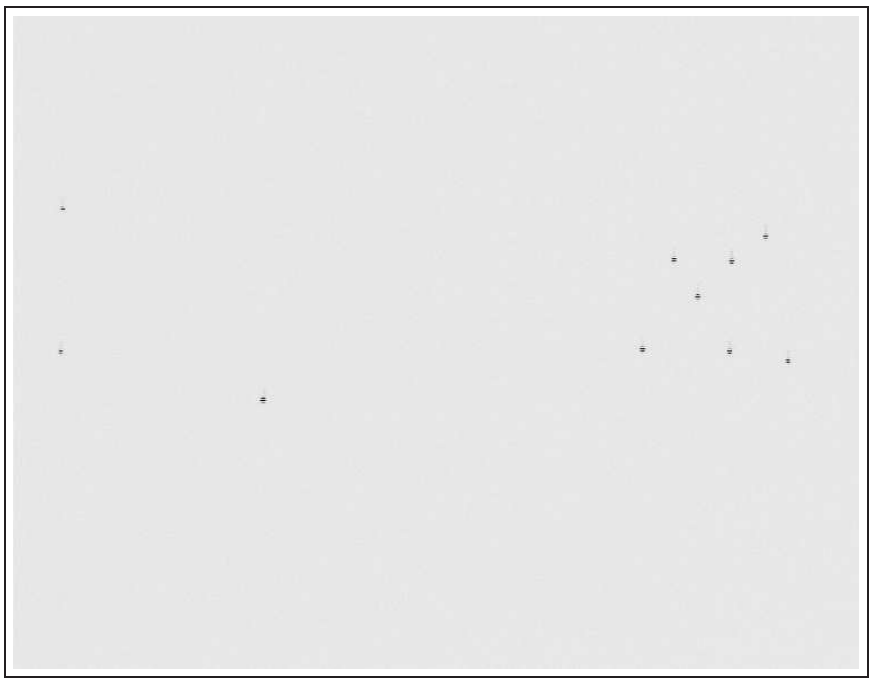

Figure K.4. *Full −Y panel of Target captured normal to boresight with the SR CHU. Image is inverted and enhanced for printing.*

Appendix L

Inflight Data Analysis

This chapter describes the first data analysis of the inflight Early Harvest Phase for the PRISMA VBS system after the first software revision. The following sections describes the background for several of the parameter and variable adjustments needed for optimizing the VBS inflight performance, as well as verification of corrections made to the outputted VBS solutions.

L.1 FR AGC and Detection Threshold Settings

During the Early Harvest for the VBS system it was found that the shutter control of the AGC for the FR CHU was not performing at desired. In Figure 1 it is seen that the powerful blooming from the Target spacecraft provides unwanted lens reflections and halo effects, all making correct centroiding difficult.

Based on these facts a series of different settings for the aggressiveness of the AGC shutter control were performed and is illustrated in the images below. To the left a 200x200pxl image segment of the detected Target spacecraft is shown, and to the right a logarithmic histogram of the given segment. The shown histograms are based on the JPEG images, which will give deviations from true values.

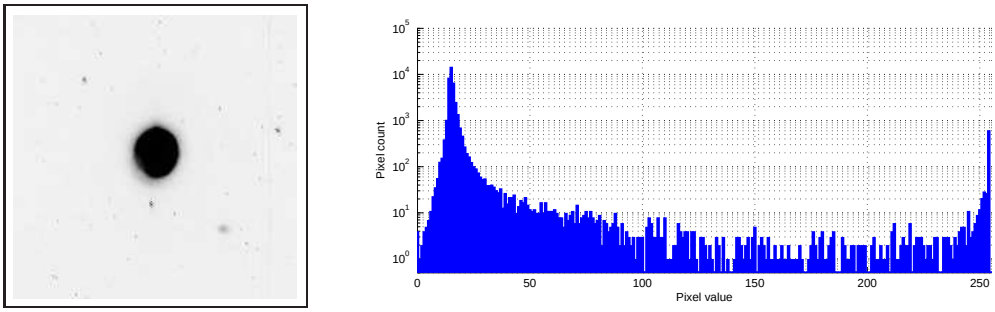

Figure L.1. *Image segment for AGC setting 5000 from inverted image IMC_967247853.878632.jpg, together with the belonging logarithmic histogram.*

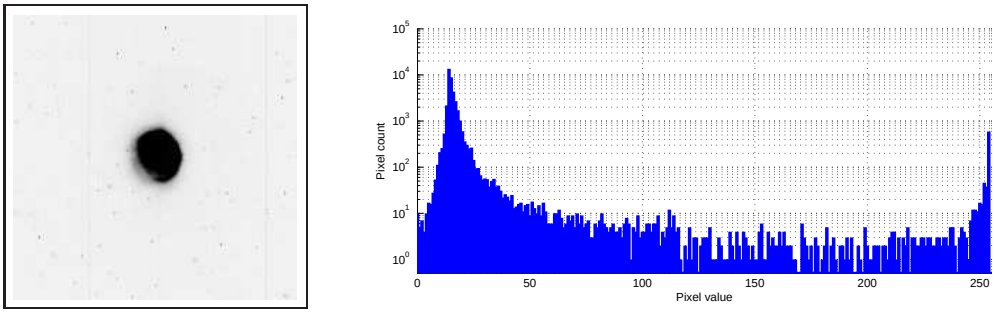

Figure L.2. *Image segment for AGC setting 400 from inverted image IMC_967314711.878632.jpg, together with the belonging logarithmic histogram.*

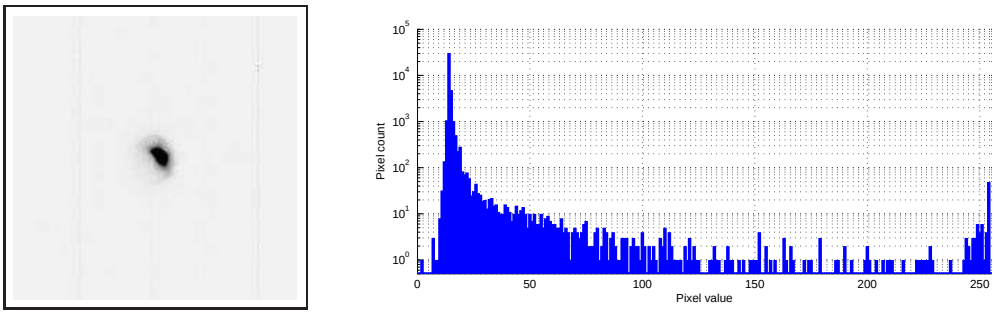

Figure L.3. *Image segment for AGC setting 40 from inverted image IMC_967308111.878632.jpg, together with the belonging logarithmic histogram.*

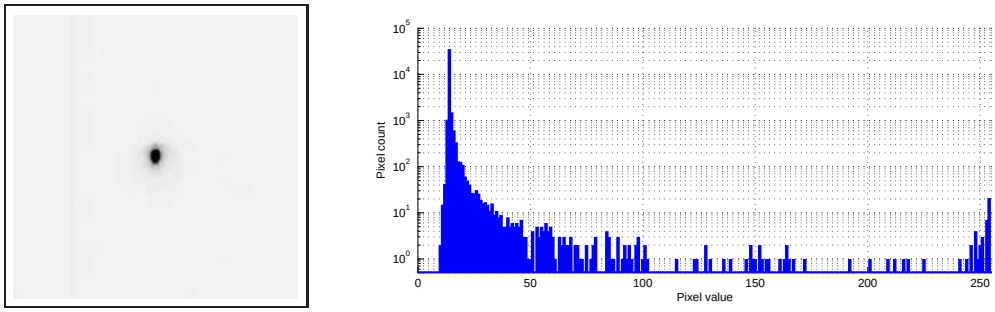

Figure L.4. *Image segment for AGC setting 20 from inverted image IMC_967387390.878632.jpg, together with the belonging logarithmic histogram.*

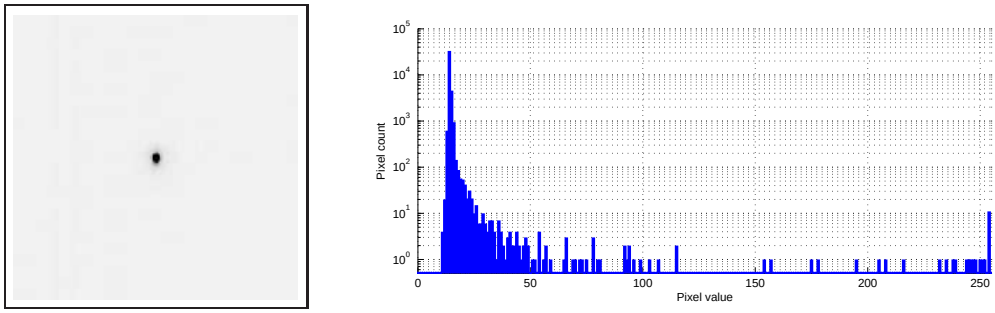

Figure L.5. *Image segment for AGC setting 10 from inverted image IMC_967392190.878632.jpg, together with the belonging logarithmic histogram.*

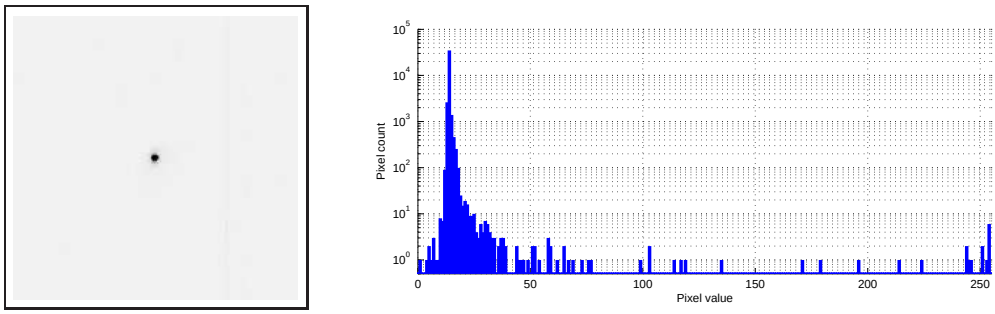

Figure L.6. *Image segment for AGC setting 5 from inverted image IMC_967401189.878632.jpg, together with the belonging logarithmic histogram.*

It is seen that the halo and lens reflections are clearly present for AGC settings 5000, 400 and 40. At 20 the halo effect is toning out, and for 10 and 5 only Target self is present. Since the FR CHU needs to detect stars in order for Far Range mode to be executed, the AGC aggressiveness should be set as high as possible. On the other hand the very same setting needs to be low enough to avoid halo effects and lens reflections.

The value of 20 is a feasible value for the AGC shutter control if the detection threshold likewise is increased to lie above the pixel values of the halo ($\sim$100). This increase in the detection threshold corresponds to the fact that the earth shine experienced by the FR CHU needs to be neglected. In Figure L.7 the Earth Shine effect is illustrated in the left side of the image, having pixel values above 50 for the undesired area.

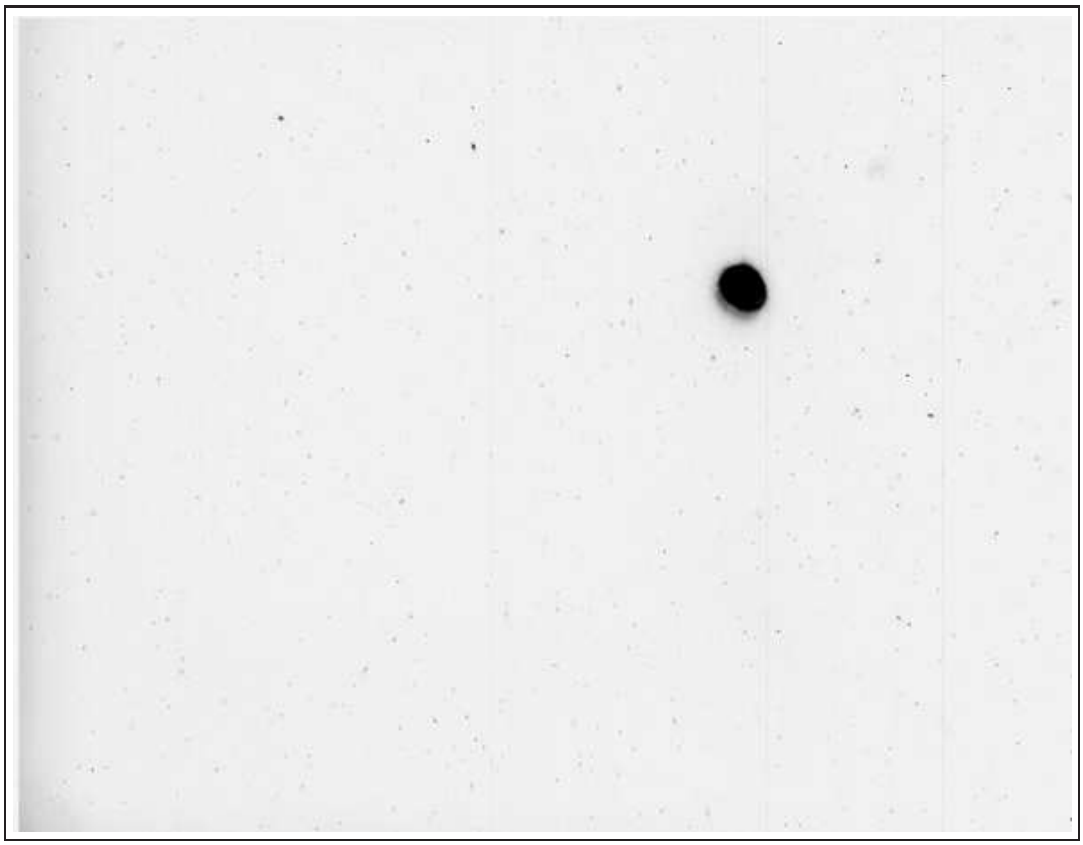

Figure L.7. *Inverted image illustrating the Earth Shine in the left side.*

Since the FR mode will accept great detected objects as a false Target, this Earth Shine needs to be handle by increasing the threshold detection level.

L.2 IR Mode Validation for FR CHU

Input file: VBSFR_968844243.830704.txt

This section discusses the validity of the IR mode for the FR CHU after the latest software release dated: 17/9-10. Additionally, validation of correct flag and info settings are discussed.

L.2.1 FR Valid Flags

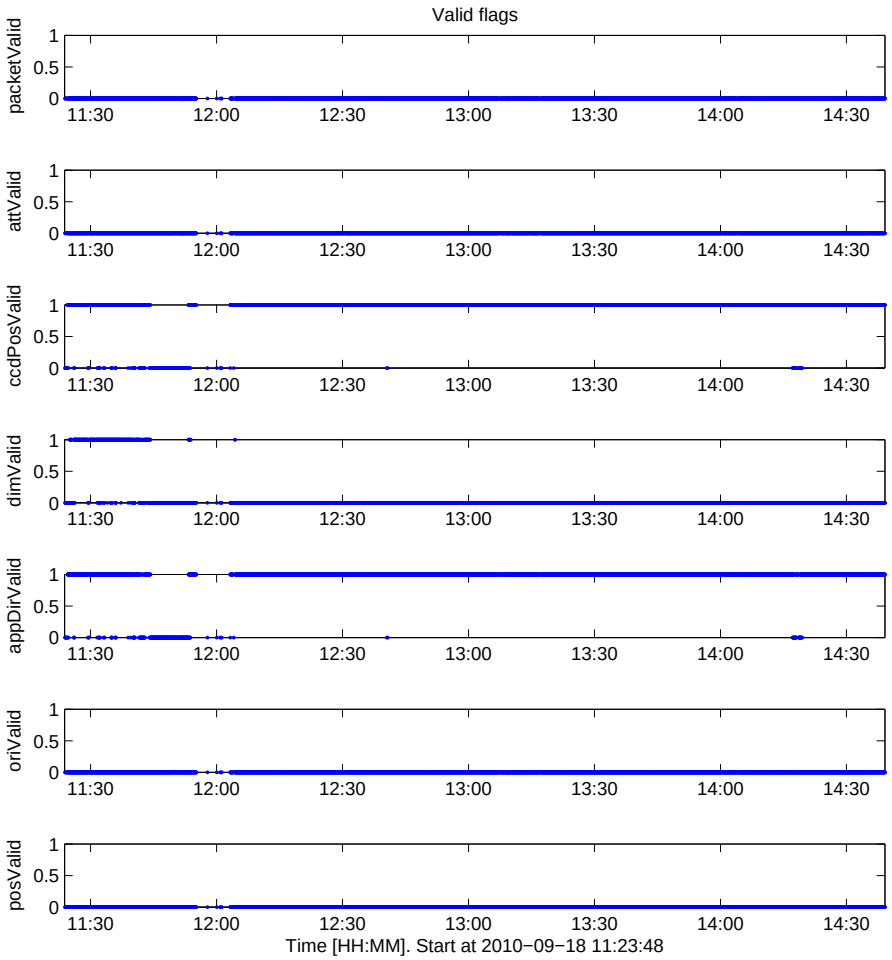

Figure L.8. *Valid flags for IR mode on FR CHU.*

The valid flags of the Apparent Direction and CCD Position now corresponds to each other when running in IR mode.

L.2.2 FR Info Flags

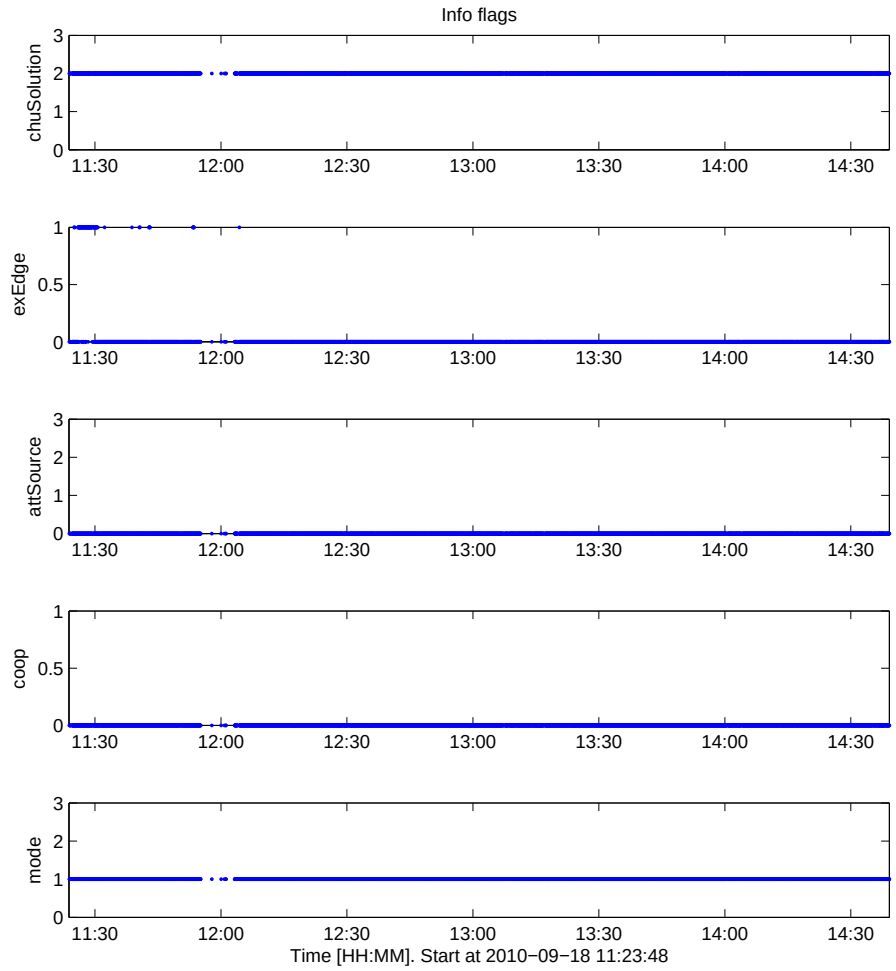

Figure L.9. *Info flags for IR mode on FR CHU.*

L.2.3 FR Solution Info

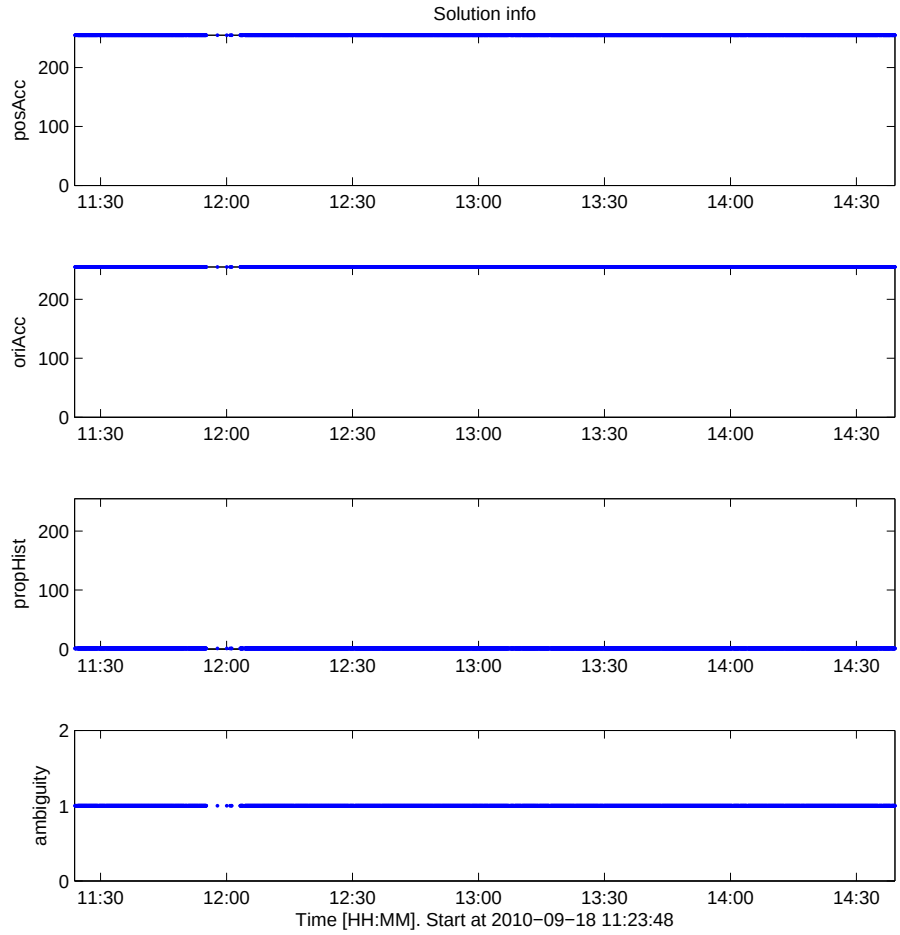

Figure L.10. *Solution info fields for IR mode on FR CHU.*

The values indicating accuracy is always set to 255, even when solution is good. This needs to be redesigned. Likewise, the propagation history is not increasing even though the determined solution is the same, and the ambiguity level needs to be set if multiple objects are present.

L.2.4 FR Apparent Direction

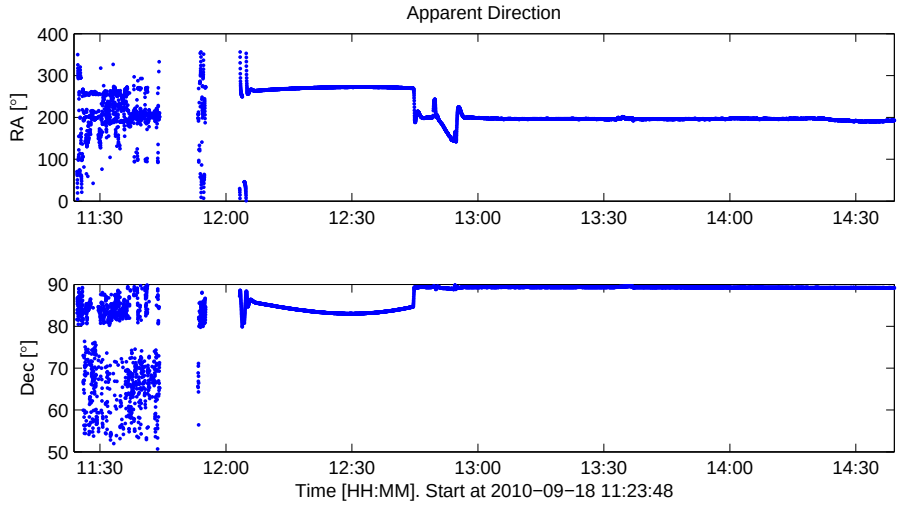

Figure L.11. *Apparent Direction marked valid for IR mode on FR CHU.*

The Apparent direction field of the VBS TM packet does not correspond with the expected pointing given from the onboard GNC. Apparent Direction needs to be verified against correct attitude mapping and is under investigation.

L.2.5 FR CCD Position

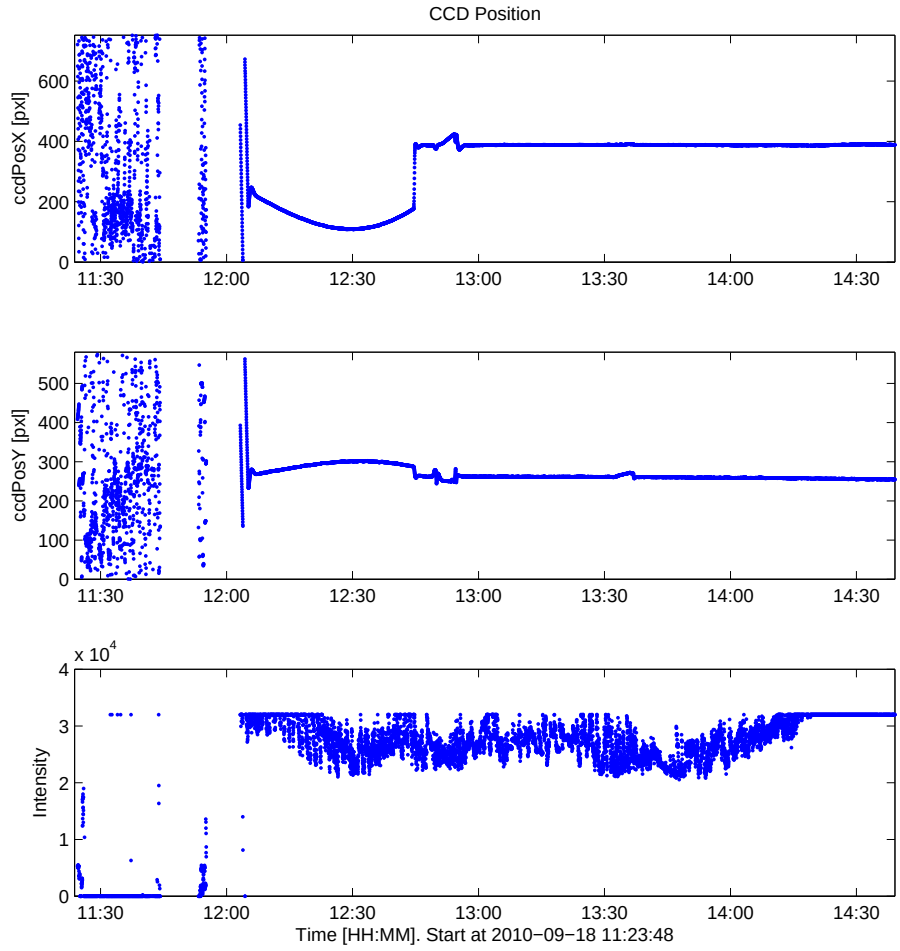

Figure L.12. *CCD positions marked valid for IR mode of FR CHU.*

The CCD Position of the IR solution is now always available even though multiple bright objects are detected. The Target is detected as soon as it enters the FOV and the AGC control adjusts. The high intensity and low shutter value indicates that the satellites are in close operations, extending the detected object. The shutter values are given in Figure L.15.

L.2.6 FR CCD Position - x vs. y

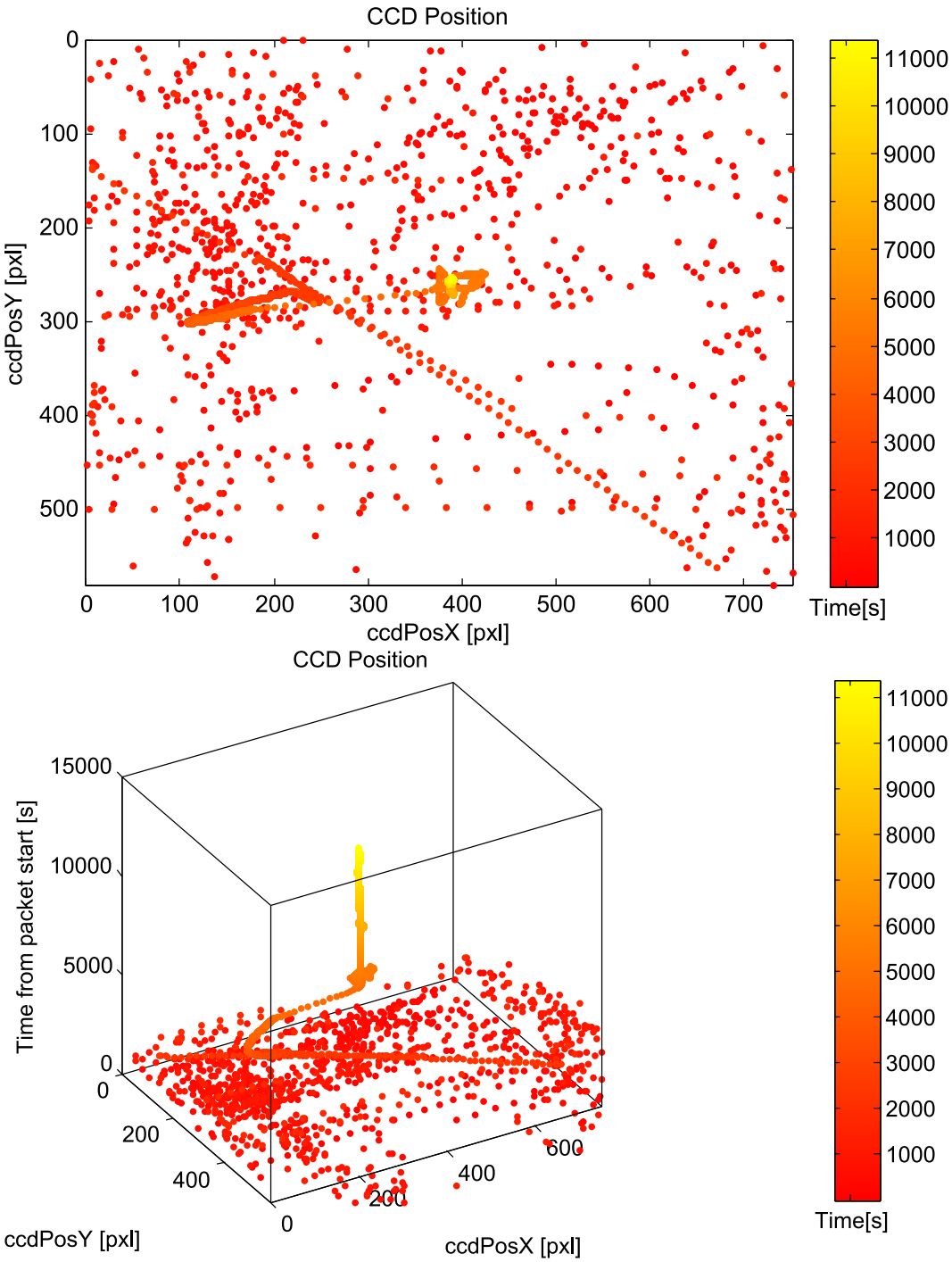

Figure L.13. *CCD positions marked valid for IR mode of FR CHU.*

L.2.7 FR Target Dimension

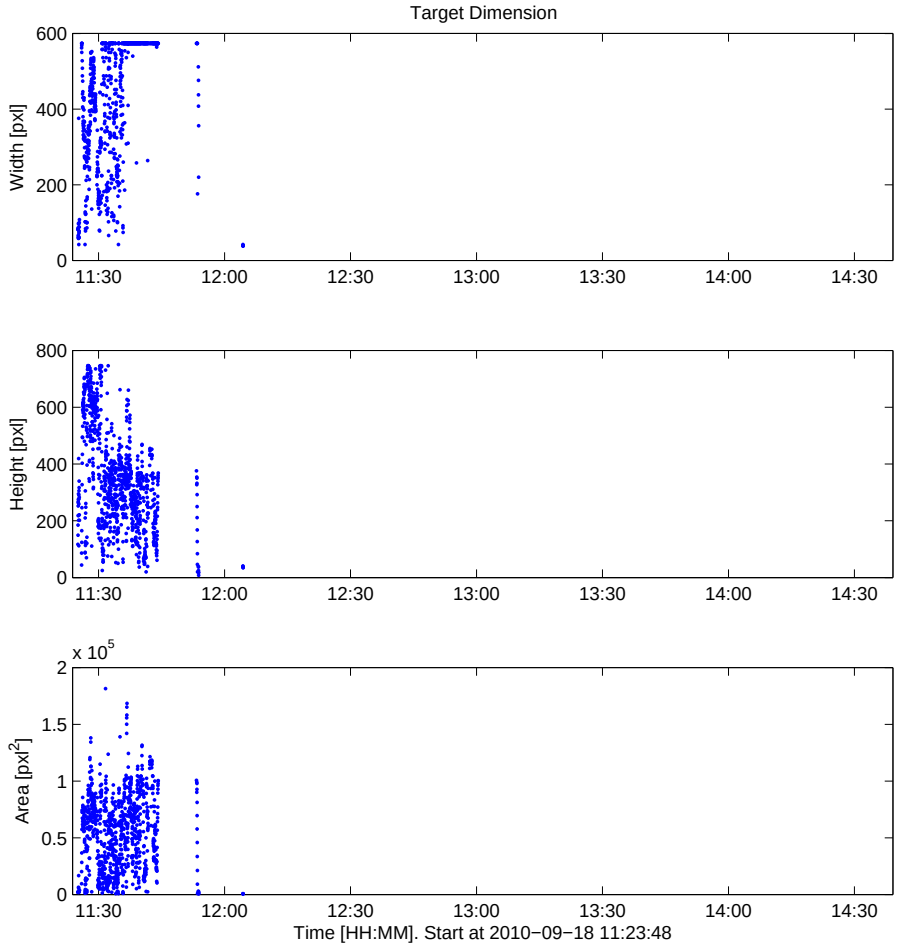

Figure L.14. *Target dimensions marked valid for IR mode of FR CHU.*

The Target Dimension is now reported correct and corresponds to the valid flag. The Dimension is only reported when a BBO is detected, which here indicates that the Target is not a BBO using the current AGC and centroid threshold setting.

L.2.8 FR HK Shutter Time

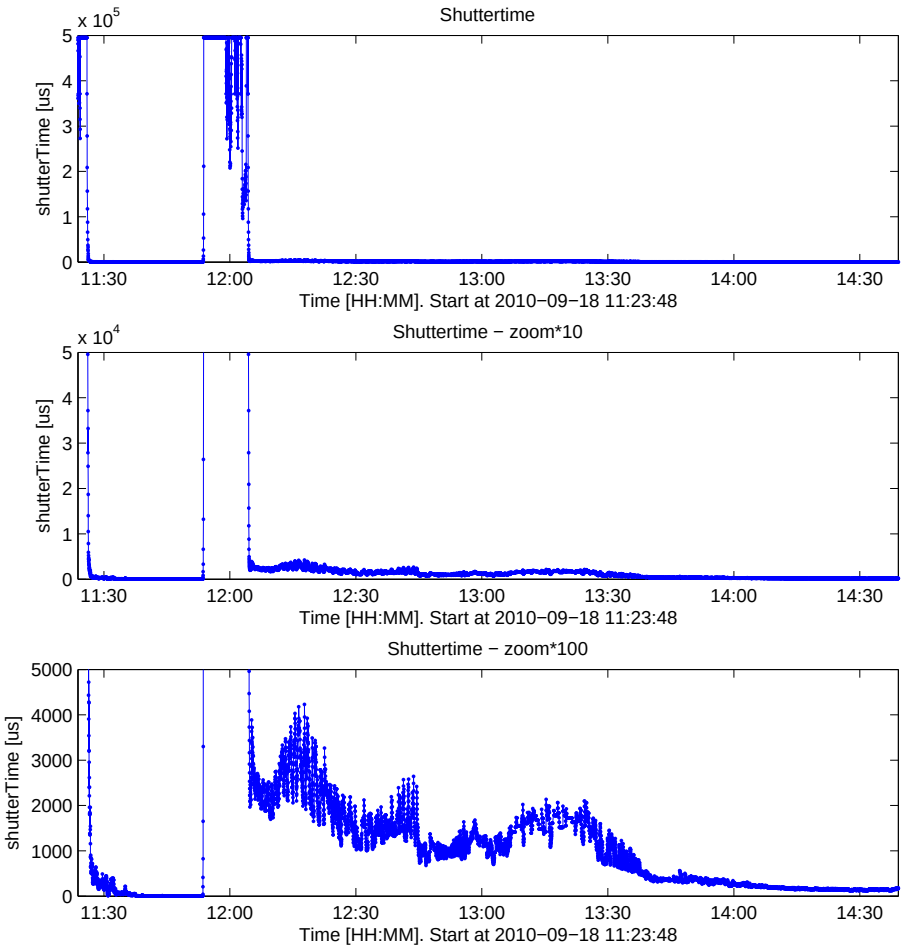

Figure L.15. *Shutter times for the FR CHU.*

The very low shutter time for the first ∼25min indicates that the FR CHU is pointing towards a BBO, e.g. the Earth. Afterwards, a pass of ∼10min where the AGC adjust onto the stars. And finally a fast transition of the AGC control when Target is entering the FOV.

L.3 IR Mode Validation for SR CHU

Input file: VBSSR_968844243.844818.txt

L.3.1 SR CCD Position

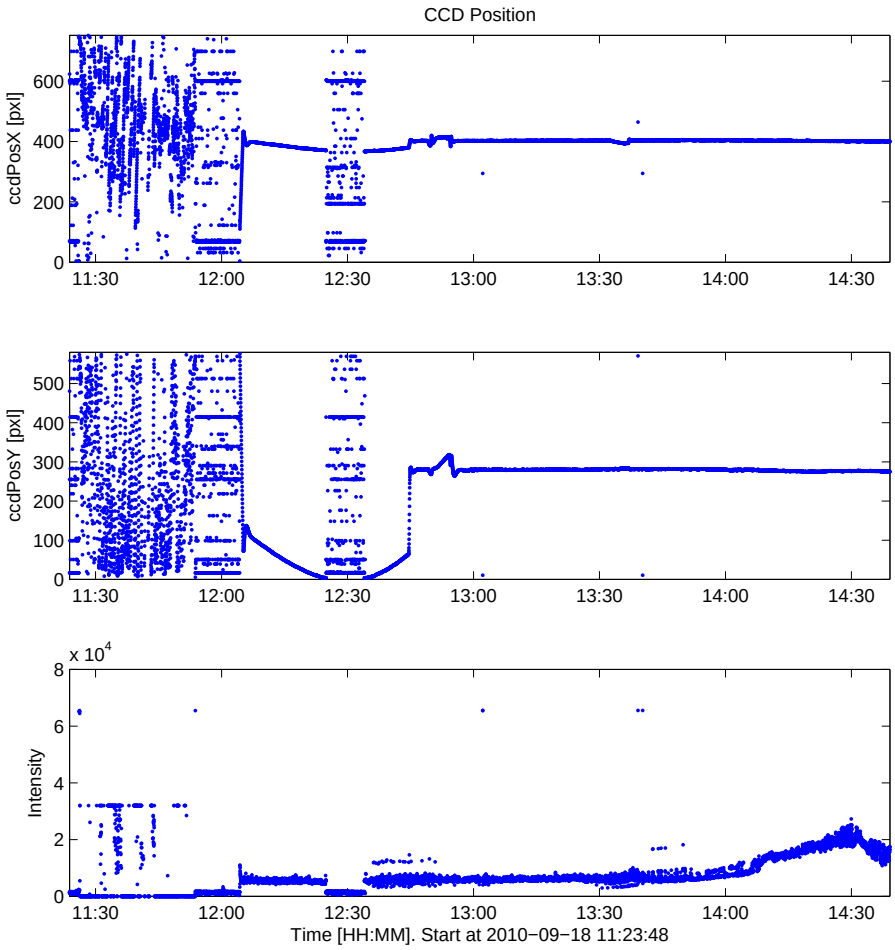

Figure L.16. *CCD positions marked valid for IR mode of SR CHU.*

IR mode for the SR camera is able to provide stable solutions as soon as Target is in FOV. When compared to the detected centroids of the FR CHU, given in Figure 12, indicates that the same object is detected. It is seen that $SR_Y \approx FR_X$ and $SR_X \approx -FR_Y$, describing the $\sim 90°$ rotation between the two VBS CHUs.

L.3.2 SR CCD Position - x vs. y

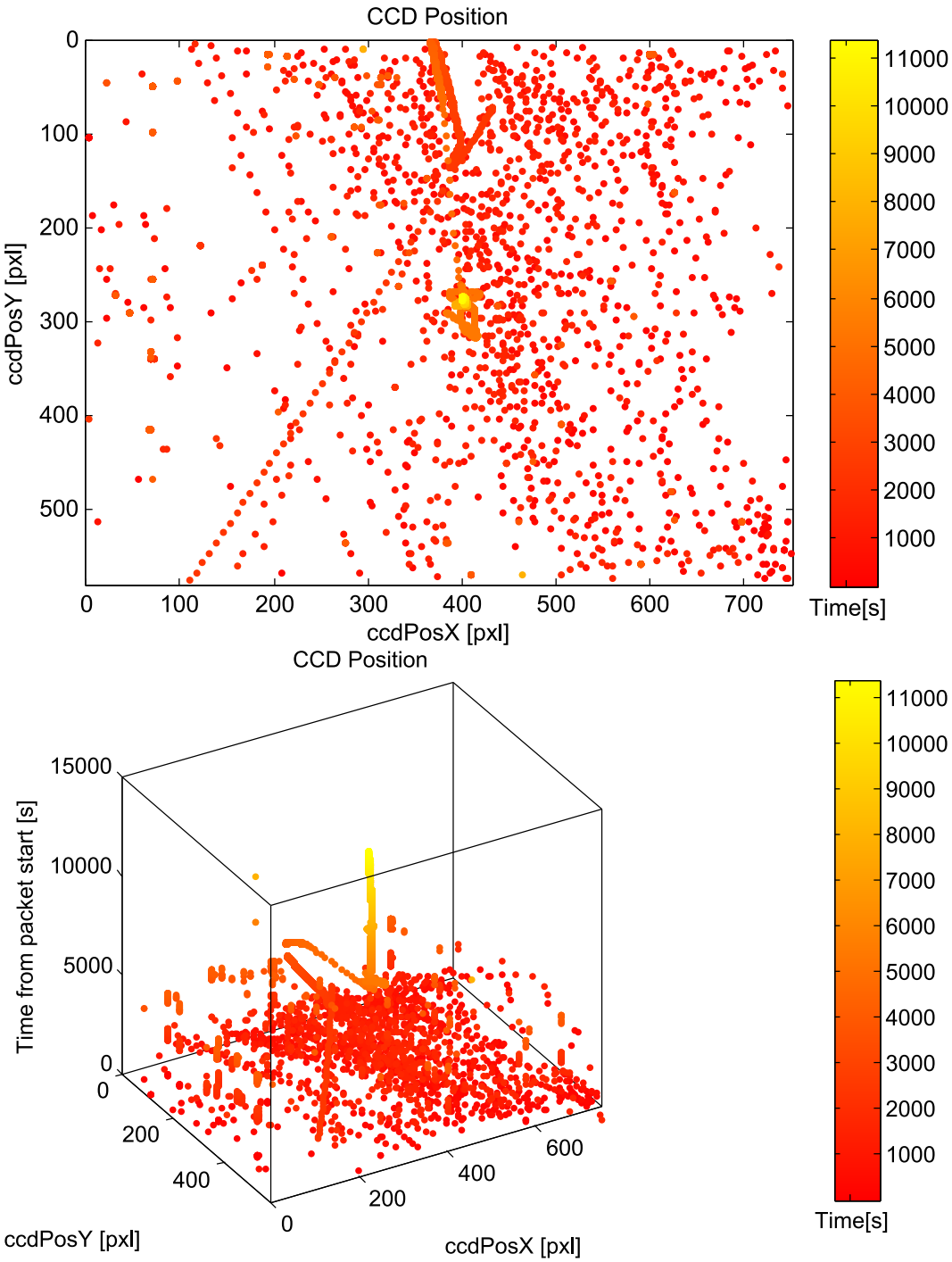

Figure L.17. *CCD positions marked valid for IR mode of SR CHU.*

L.3.3 SR Target Dimension

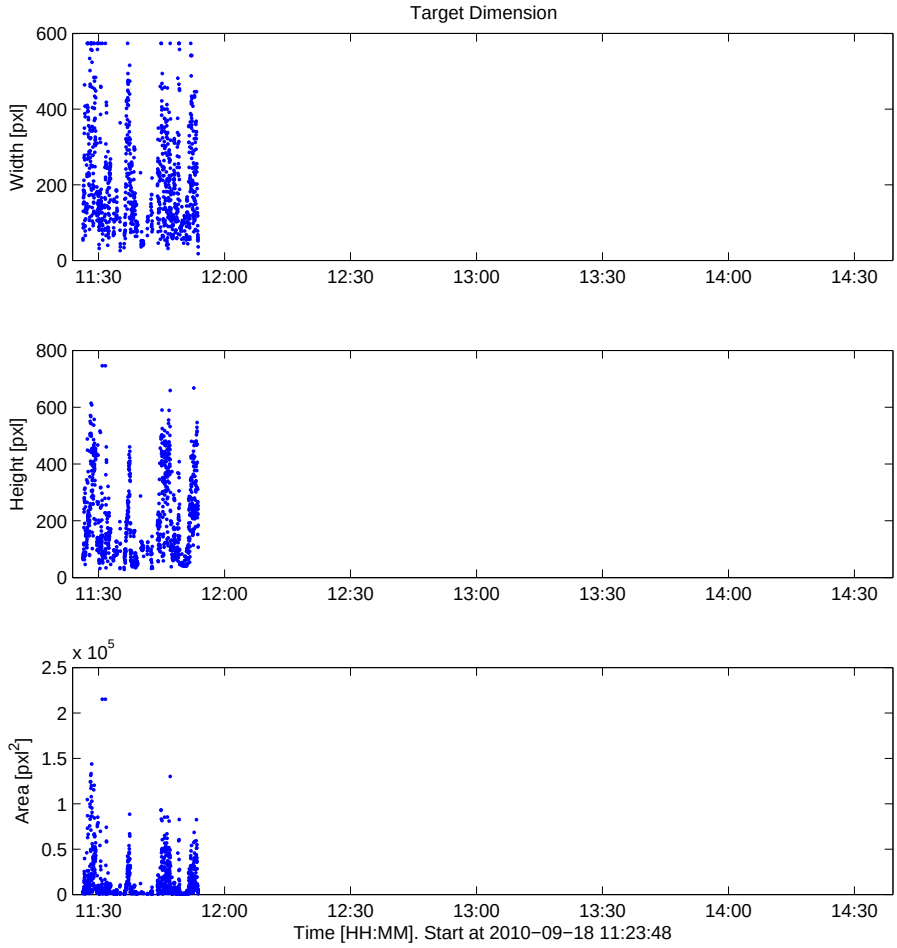

Figure L.18. *Dimensions marked valid for IR mode of SR CHU.*

Likewise as for the FR CHU, the SR CHU only provides the Dimension when Target is detected as a BBO.

L.3.4 SR HK Shutter Time

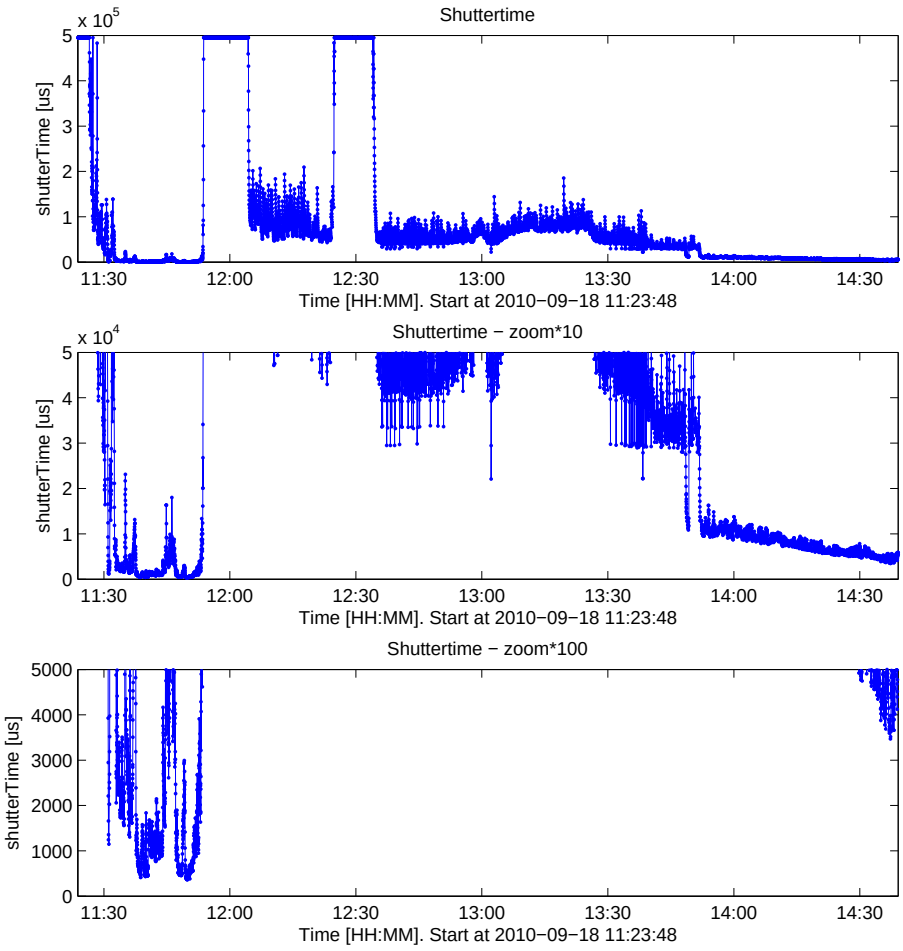

Figure L.19. *Shutter times for the SR CHU.*

L.4 CHU Alignment

Alignment between each of the CHUs needs to be determined. When known for all the CHU, attitude determined by only one CHU can support the rest with their attitude pointing. This gives the VBS system the ability to provide Target pointing in inertial coordinates.

L.4.1 CHU A+B Alignment with CHU C

Based on valid attitude data packets the following alignment rotations have been determined, used for mapping the attitudes from CHU A and B into the attitude of CHU C, respectively.

$$q_{B2C} = \begin{bmatrix} 0.892648 \\ 0.108352 \\ -0.283797 \\ 0.333012 \end{bmatrix} \Rightarrow \begin{array}{rcr} rot_z & = & 0.3112^\circ \\ rot_y & = & 35.3674^\circ \\ rot_x & = & 139.1821^\circ \end{array} \tag{L.1}$$

$$q_{A2C} = \begin{bmatrix} 0.891719 \\ -0.105216 \\ 0.285599 \\ 0.334960 \end{bmatrix} \Rightarrow \begin{array}{rcr} rot_z & = & 0.2597^\circ \\ rot_y & = & -35.4387^\circ \\ rot_x & = & 138.7412^\circ \end{array} \tag{L.2}$$

L.4.2 VBS CHU Alignment between CHU C and D

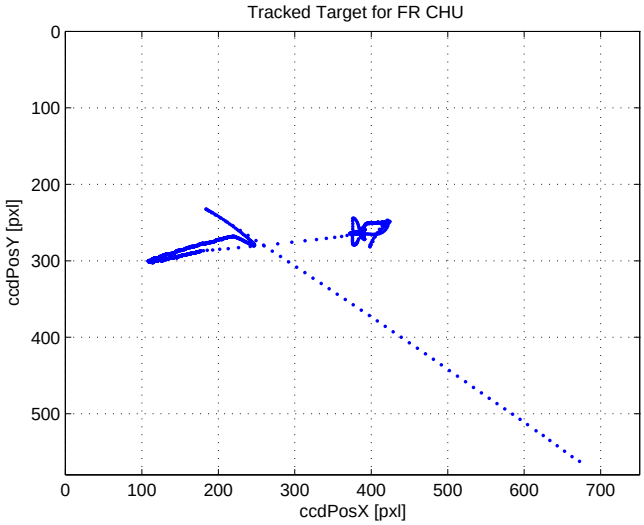

Figure L.20. *Tracked Target for the FR CHU.*

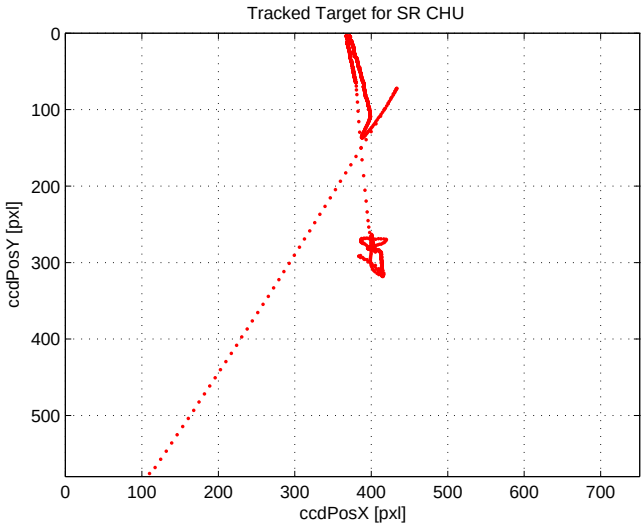

Figure L.21. *Tracked Target for the SR CHU.*

Based on chosen data from i.a. the IR data illustrated in Figure L.12 and L.16, the inter-alignment can be estimated. The 90° rotation inbetween the two VBS CHUs is clearly illustrated in Figure L.20 and L.21. This is an ongoing process in time of writing.

Appendix M

FR Bandpass and Edge Stray Analysis

An analysis of which objects the FR VBS mode locks onto has been performed on inflight data. This appendix includes the VBS solution results for the CCD position field at which the VBS system has locked onto. First all detected centroids are listed, then the true solution with Target in the centroid file. Afterwards, the true Target centroid has been removed from the centroid files, where different bandpass settings has been analyzed together with removal of the Edge Stray BBO object.

The given dataset for analysis is taken from the binary file from PDC: OPS_TM_VC1_1936_ST_DPU_B_20100903-210906_20100903-211808.RAC

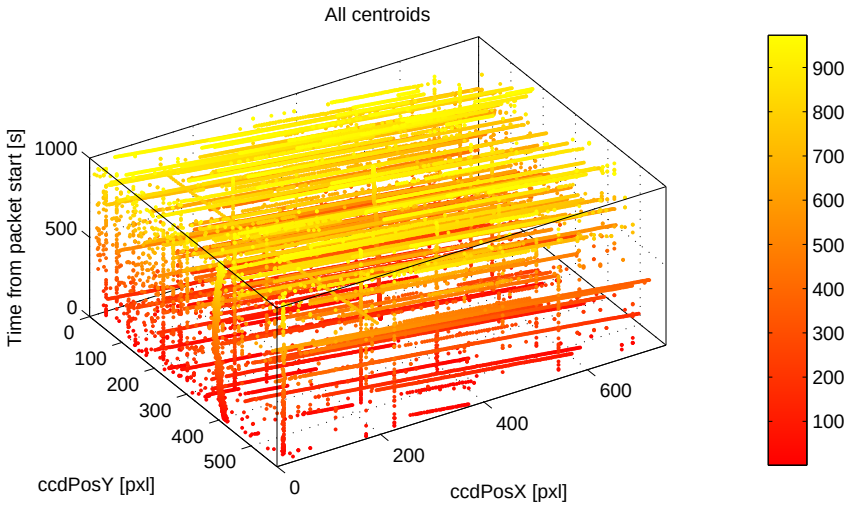

Figure M.1. *All detected centroids used for the current analysis.*

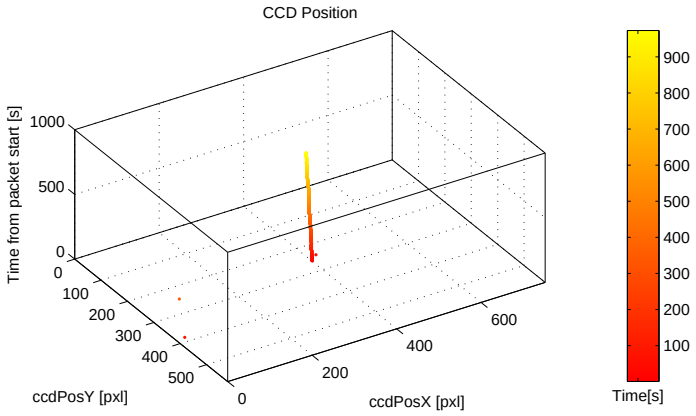

Figure M.2. *VBS FR solutions with Target. Bandpass:150-290"/s*

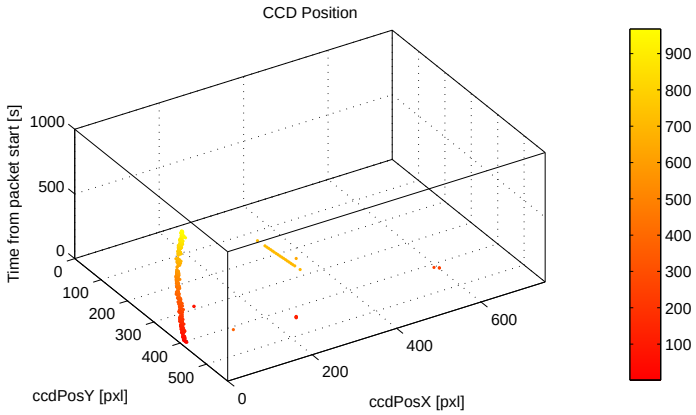

Figure M.3. *VBS FR solutions when Target is not contained in the centroid list. Bandpass:150-290"/s*

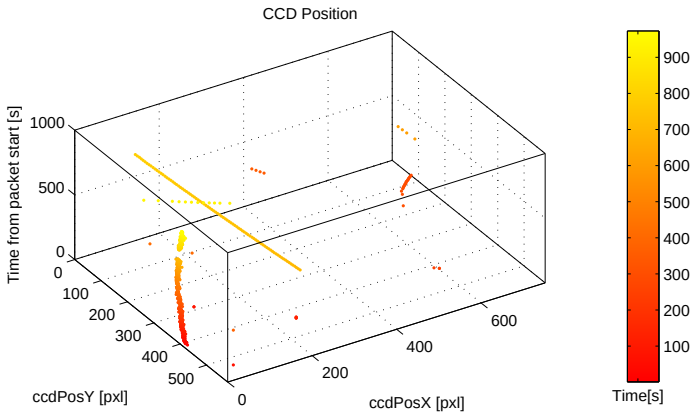

Figure M.4. *VBS FR solutions when Target is not contained in the centroid list. Bandpass:150-1000"/s*

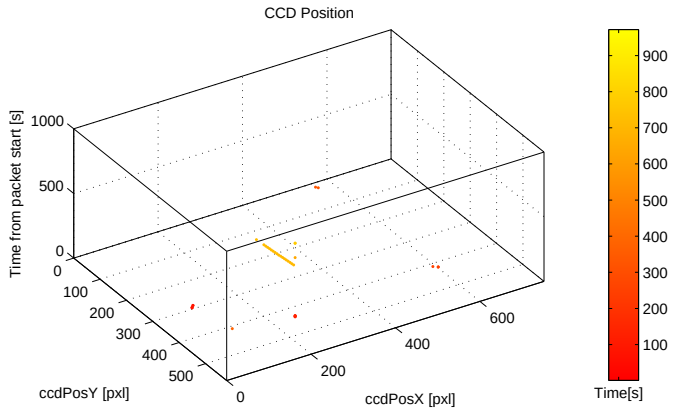

Figure M.5. *VBS FR solutions when Target and Edge Stray are not contained in the centroid list. Bandpass:15-290"/s*

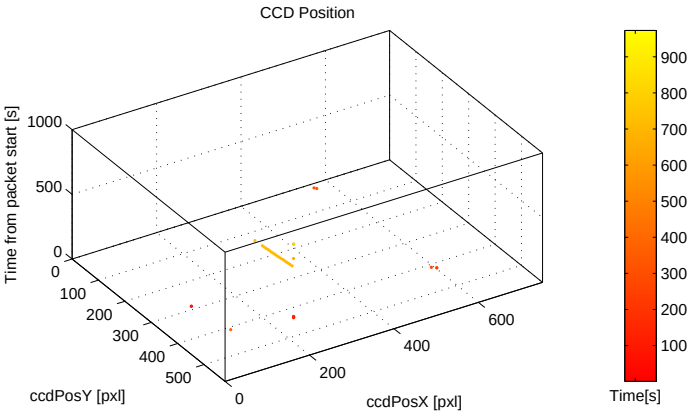

Figure M.6. *VBS FR solutions when Target and Edge Stray are not contained in the centroid list. Bandpass:150-290"/s*

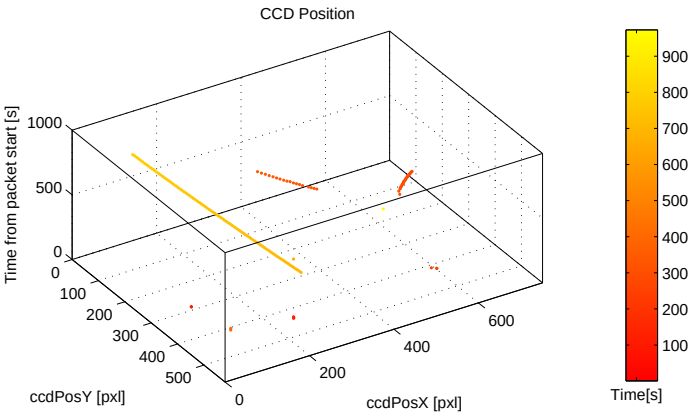

Figure M.7. *VBS FR solutions when Target and Edge Stray are not contained in the centroid list. Bandpass:150-500"/s*

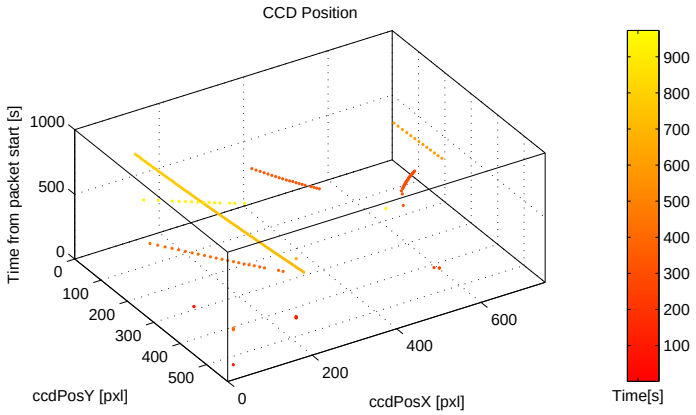

Figure M.8. *VBS FR solutions when Target and Edge Stray are not contained in the centroid list. Bandpass:150-1000"/s*

Appendix N

VBS Performance During Orbit Correction

During the VBS Early Harvest phase of the PRISMA mission, the first data-sets were taking with the FR CHU turned on pointing towards the Target satellite.

The scenario consisted of an orbit transfer where Main is approaching Target, and performs orbit corrections and transitions in order to keep Target in FOV of the FR CHU. The data-set presented involves Main and Target distances going from $\sim$ 1000m down to $\sim$ 750m, resulting in Intermediate Range solutions for the VBS system.

The boresight of the CHU (z-axis) is Target pointing and the x-axis (aligned with the CCD x-axis) is Nadir pointing.

The analyzed dataset is acquired from the binary data packet:
`OPS_TM_VC1_1936_ST_DPU_B_20100901-192139_20100901-205848.RAC`

This section describes shortly the performance of the VBS system at the presented scenario and the reaction to continuous orbit corrections.

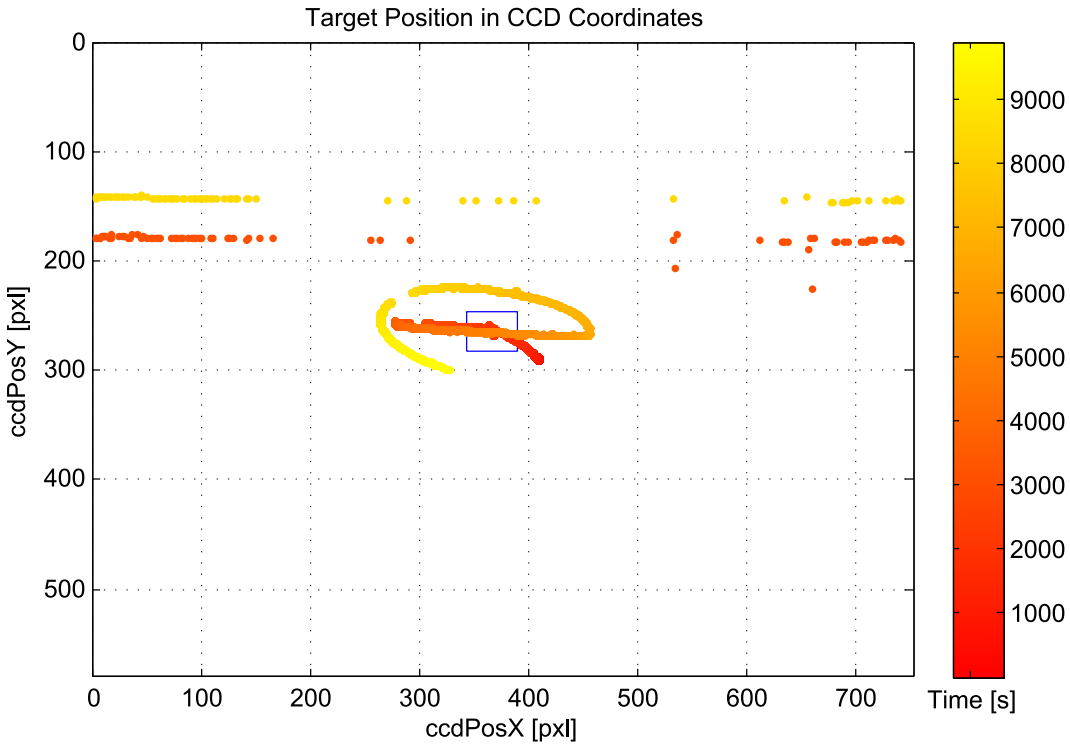

Figure N.1. *Detected Target in CCD Coordinates with color gradient representing time domain. Blue square indicates zoom area for Figure N.3.*

In Figure N.1 is illustrated the CCD coordinates of the VBS solution, i.e. the detected Target. In the beginning of the solution stream Target is detected in the center of the CCD, whereupon the orbit transition initiates, creating the spiraling movement of the Target satellite.

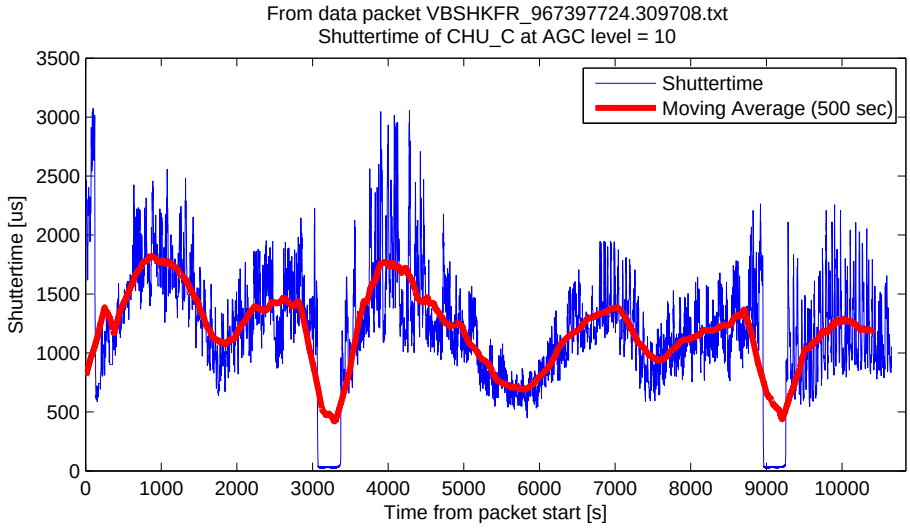

Figure N.2. *Shutter time of the FR CHU during VBS.*

The horizontal lines in Figure N.1 is the Moon entering the FOV of the FR CHU while orbiting the Earth. This is clearly illustrated in Figure N.2 where the shutter time of the FR CHU is given. The Moon passings are seen at $T \approx 3100$s and $T \approx 9000$s where the shutter time is at a minimum. During these passes the Target is undetectable, why the VBS system tracks the Moon instead due to the fact that this is the best Target candidate in the given time frames.

Looking at the trend of the shutter times, the Target illumination is clearly fluctuating which the AGC Shutter Control continuously adjust for. This fluctuation is due to the magnetourqer regulation of Target, creating wavering attitude pointings while orbiting the Earth.

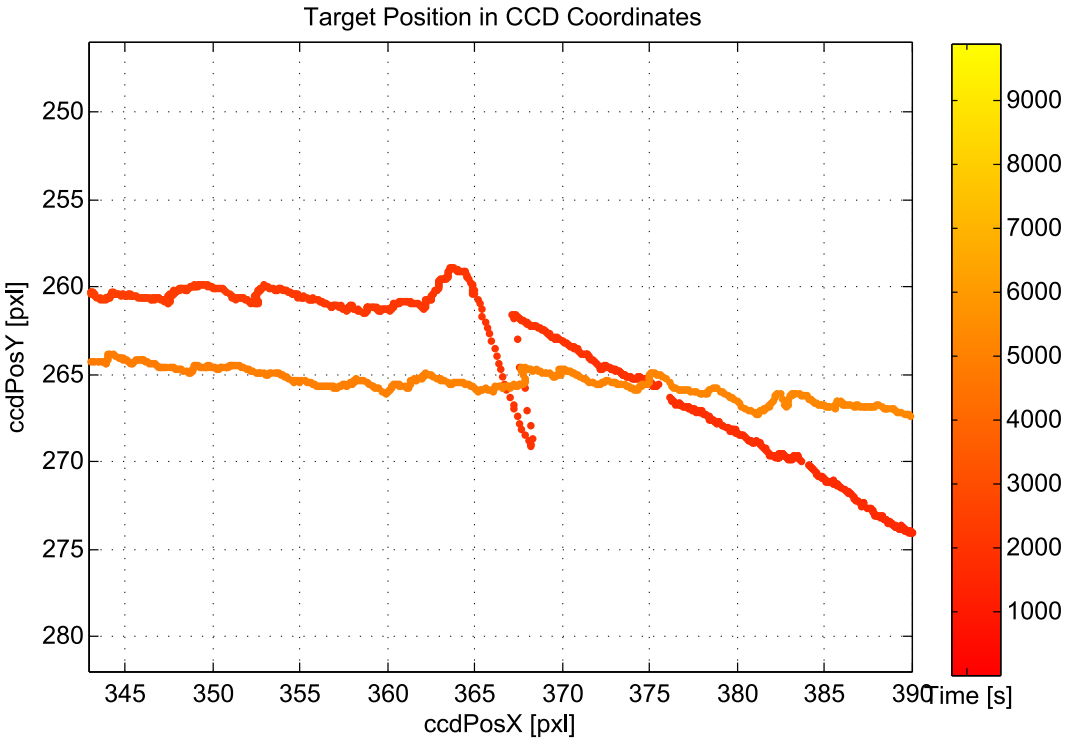

Figure N.3. *Zoomed area of detected Target from Figure N.1, where Main satellite performs orbit correction.*

The zoomed area from Figure N.1 is illustrated in Figure N.3. Here is seen how the orbit corrections performed by the Main satellite influence on the detection of the Target centroiding on the CCD. The data presented is from the IR mode of the VBS, saying that the VBS CHU is unable to determine its own pointing. Though, the attitude pointing from the normal startrackers are available, from where it is desired to determine the inertial attitude pointing towards Target, neglecting the orbit corrections performed by Main.

In the very beginning of the Early Harvest phase, the interalignment between the two normal startrackers and the VBS FR CHU where determined,

from where the attitude pointing of the FR CHU can be estimated based on attitude information from one of the standard startrackers.

In Figure N.4 is illustrated the pointing attitude of CHU B and the estimated attitude of CHU C based on mapping of the attitude from CHU B.

The plots are focussed on the orbit correction maneuver which occurs in the dataset given in Figure N.3.

The mapping has been performed using the quaternion rotation given as:

$$q_C = q_B \; q_{B \to C} \tag{N.1}$$

where: $\mathbf{q_B}$: describes the attitude pointing of CHU B.
$\mathbf{q_{B \to C}}$: describes the rotation mapping from CHU B to CHU C.
$\mathbf{q_C}$: describes the estimated attitude pointing of CHU C.

Based on the detected CCD coordinates, the pointing towards Target has been calculated in reference to the internal CHU C coordinate system. This Target pointing is given as Azimuth and Elevation with respect to the CHU C boresight, and is illustrated in Figure N.5.

Additionally is the residual error of linear fittings presented in the same figure. This gives a representation of the displacement of the Target pointing due to the orbit correction maneuver.

The Target pointing given in the CHU C coordinate system has been mapped with the estimated CHU C attitude pointing, giving the Target pointing in inertial coordinates. These are illustrated in Figure N.6 as Right Ascension and Declination.
Likewise, the residual error of linear fittings to Right Ascension and Declination are given, showing that the orbit correction maneuvers are not represented in the inertial pointing towards Target.

From this it can be concluded that the VBS system can provide reliable and precise pointing for the IR mode, regardless of satellite maneuvering. The only criteria is that attitude information is available from either of the two standard startrackers, since the VBS system is running in IR mode on the FR CHU (i.e. The FR CHU is unable to determine its own attitude due to Target blinding.).

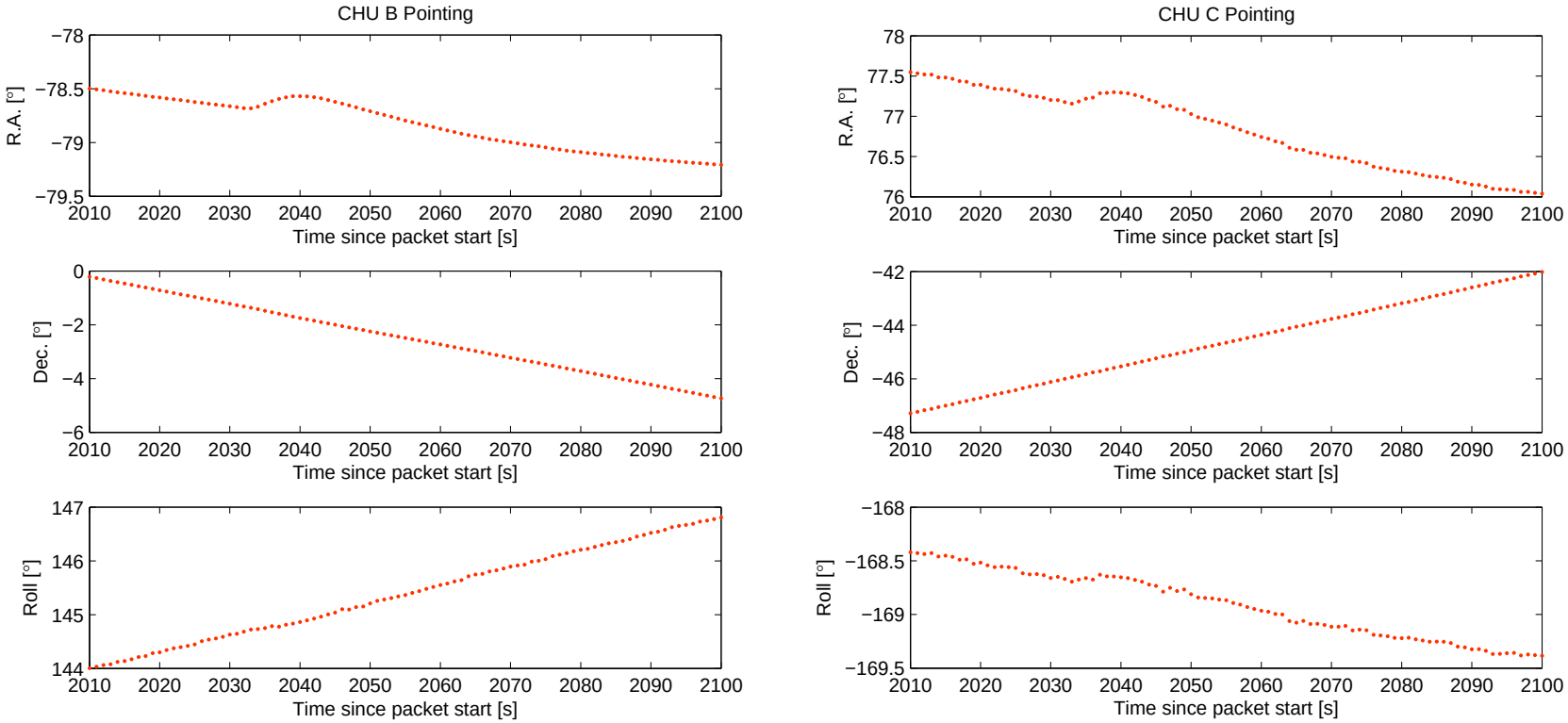

Figure N.4. *Pointing attitude of CHU B to the left, and the mapped attitude into the VBS CHU C on the right.*

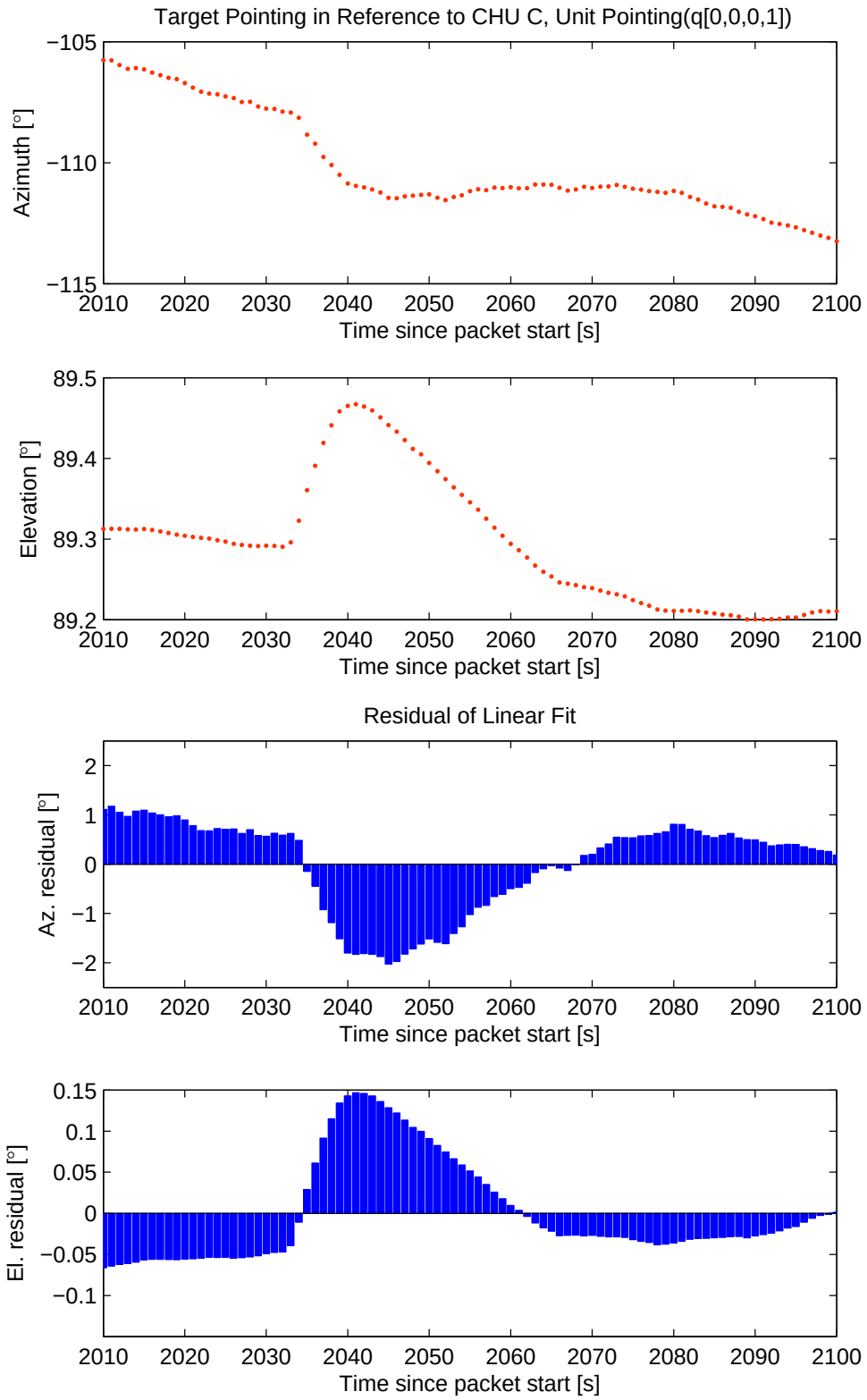

Figure N.5. *Target pointing given in the internal camera coordinate system of CHU C. The two top graphs shows the Azimuth and Elevation in respect to CHU C boresight, and the two bottom graphs shows the residual error of linear fitting of Azimuth and Elevation, respectively*

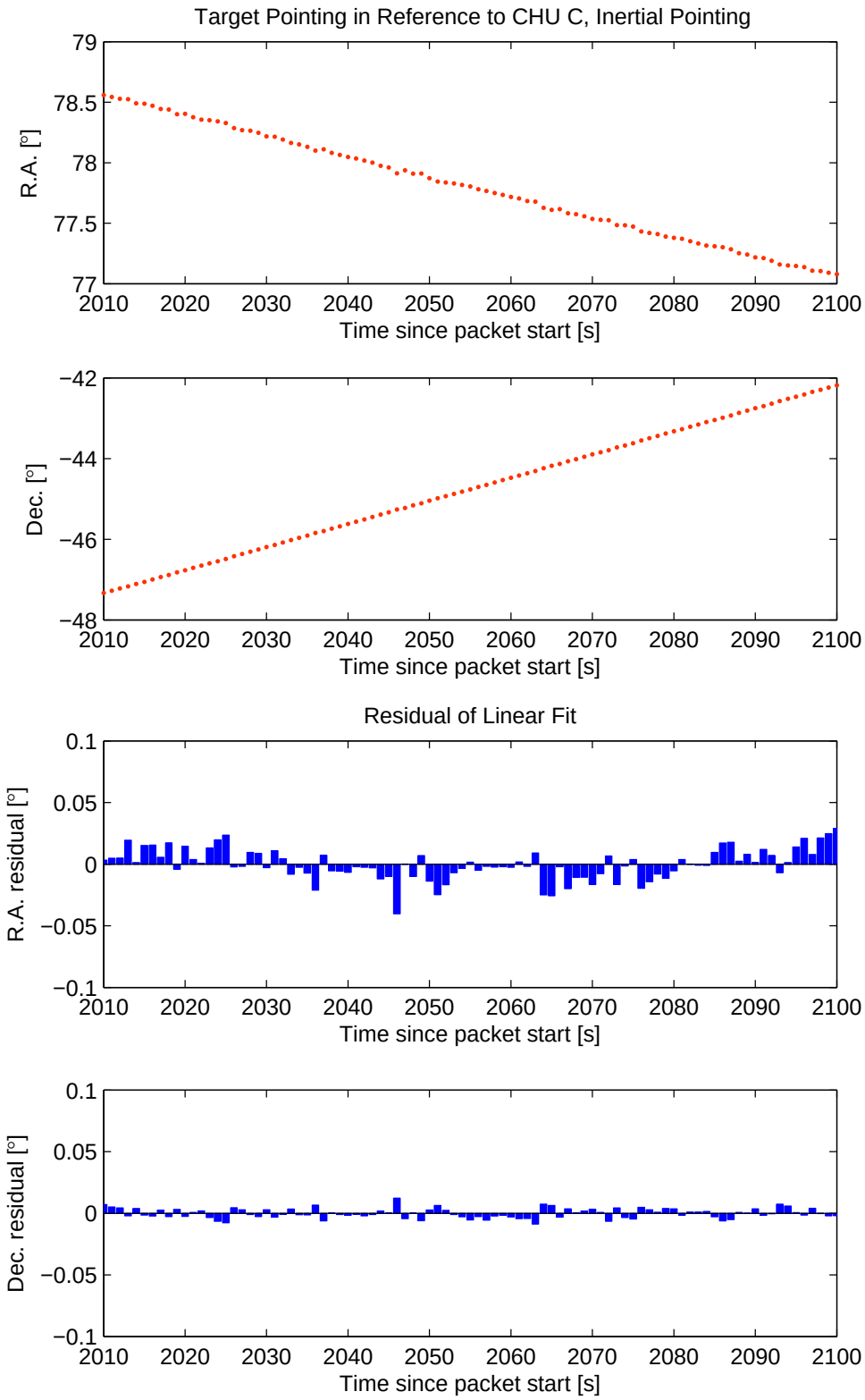

Figure N.6. *Target pointing given in inertial coordinates. The two top graphs shows the Right Ascension and Declination, and the two bottom graphs shows the residual error of linear fitting of Right Ascension and Declination, respectively*